DTU Library

# Turbulent boundary layer trailing-edge noise: Theory, computation, experiment, and application

**Lee, Seongkyu; Ayton, Lorna; Bertagnolio, Franck; Moreau, Stephane; Chong, Tze Pei; Joseph, Phillip**

*Published in:*
Progress in Aerospace Sciences

*Link to article, DOI:*
10.1016/j.paerosci.2021.100737

*Publication date:*
2021

*Document Version*
Publisher's PDF, also known as Version of record

Progress in Aerospace Sciences 126 (2021) 100737

Contents lists available at ScienceDirect

Progress in Aerospace Sciences

journal homepage: www.elsevier.com/locate/paerosci

# Turbulent boundary layer trailing-edge noise: Theory, computation, experiment, and application

Seongkyu Lee [a,*], Lorna Ayton [b], Franck Bertagnolio [c], Stephane Moreau [d], Tze Pei Chong [e], Phillip Joseph [f]

[a] University of California, Davis, 1 Shields Ave, Davis, CA 95616, USA
[b] University of Cambridge, Wilberforce Road, CB3 0WA, UK
[c] Technical University of Denmark, Frederiksborgvej 399, 4000 Roskilde, Denmark
[d] Université de Sherbrooke, Sherbrooke, J1K2R1, QC, Canada
[e] Brunel University London, Uxbridge, England UB8 3PH, United Kingdom
[f] University of Southampton, Southampton, SO17 1BJ, UK

ARTICLE INFO

*Keywords:*
Trailing-edge noise
Aeroacoustics
Turbulent boundary layer

ABSTRACT

When the pressure fluctuations caused by turbulence vorticity in the boundary layer are scattered by a sharp trailing edge, acoustic energy is generated and propagated to the far field. This trailing edge noise is emitted from aircraft wings, turbomachinery blades, wind turbine blades, helicopter blades, etc. Being dominant at high frequencies, this trailing-edge noise is a key element that annoys human hearing. This article covers virtually the entire landscape of modern research into trailing-edge noise including theoretical developments, numerical simulations, wind tunnel experiments, and applications of trailing-edge noise. The theoretical approach includes Green's function formulations, Wiener–Hopf methods that solve the mixed boundary-value problem, Howe's and Amiet's models that relate the wall pressure spectrum to acoustic radiation. Recent analytical developments for poroelasticity and serrations are also included. We discuss a hierarchy of numerical approaches that range from semi-empirical schemes that estimate the wall pressure spectrum using mean-flow and turbulence statistics to high-fidelity unsteady flow simulations such as Large Eddy Simulation (LES) or Direct Numerical Simulation (DNS) that resolve the sound generation and scattering process based on the first-principles flow physics. Wind tunnel experimental research that provided benchmark data for numerical simulations and unravel flow physics is reviewed. In each theoretical, numerical, and experimental approach, noise control methods for mitigating trailing-edge noise are discussed. Finally, highlights of practical applications of trailing-edge noise prediction and reduction to wind turbine noise, fan noise, and rotorcraft noise are given. The current challenges in each approach are summarized with a look toward the future developments. The review could be useful as a primer for new researchers or as a reference point to the state of the art for experienced professionals.

## 1. Introduction

Aeroacoustics is a study of flow-induced noise. This noise is generated by either aerodynamic forces acting on a surface or flow turbulence that may or may not interact with a surface. When flow turbulence interacts with a surface, the flow turbulence generates chaotic or random pressure fluctuations on this surface. When this turbulence-induced pressure fluctuations have a sudden change in the boundary condition, energy scattering occurs. This phenomenon is exemplified when a turbulent boundary layer flow passes by a sharp edge of a finite flat surface or an airfoil. During this process, strong turbulent kinetic energy is converted into acoustic energy, which propagates to the far field, as shown in Fig. 1. This aerodynamic noise is called turbulent boundary layer trailing-edge noise or simply trailing-edge noise.

Trailing-edge noise has received a lot of attention in engineering applications such as wind turbine noise, marine propeller noise, rotorcraft noise, automobile fan noise, etc. In some cases, trailing-edge noise is the most dominant noise source. For others, trailing-edge noise is a floor of noise, which is still important when this noise floor is higher than background noise and other noise sources are reduced below background noise.

* Corresponding author.
*E-mail address:* skulee@ucdavis.edu (S. Lee).

https://doi.org/10.1016/j.paerosci.2021.100737
Received 7 January 2021; Received in revised form 14 May 2021; Accepted 14 May 2021
Available online 24 June 2021
0376-0421/

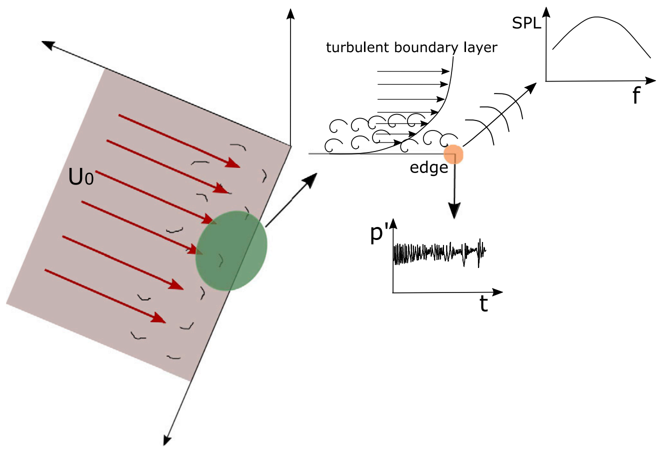


**Fig. 1.** Schematic of trailing-edge noise generation and physics: turbulent boundary layer eddies near the trailing edge generates stochastic and unsteady pressure fluctuations on the surface. The pressure fluctuations are scattered by a sharp trailing edge and the hydrodynamic turbulent energy is converted into far-field radiating sound waves.

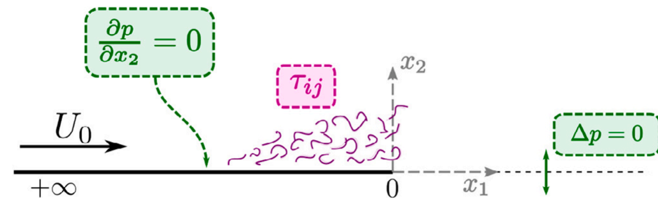


**Fig. 2.** Sketch for rudimentary trailing-edge noise models with the corresponding boundary conditions.

Although trailing-edge noise is broadband noise, it has a distinct peak frequency where noise becomes maximum. For example, the peak frequency that is estimated based on the energetic fluctuations in the boundary layer near the trailing-edge is expressed as $f\delta^*/U_\infty = 0.06 - 0.08$ [1] where $f$ is a frequency, $\delta^*$ is a boundary layer displacement thickness, and $U_\infty$ is a freestream velocity.

Trailing-edge noise is considered as non-compact, which means that the wavenumber of noise of interest is shorter than the characteristic length of a surface such as an airfoil chord length, $c$. For example, the acoustic wavelength at the peak frequency scales as $\lambda/c = \alpha\frac{\delta^*/c}{M_\infty}$ where a constant $\alpha$ ranges 13–18 and $M_\infty$ is a flow Mach number [1]. For a high speed condition, $\lambda/c = 0.4 - 0.6$, which demonstrates the non-compactness. Even for low Mach number where $\lambda/c > 1$, high-frequency noise contents are still in non-compact range.

To authors' best knowledge, the first paper that presented trailing-edge noise is Powell's paper [2] in 1959. He analyzed the scaling of noise source and acoustic power and postulated that trailing-edge noise scales with the velocity raised to between the fourth and fifth power and it is predominantly important at low speeds. Since this first paper, the physics of trailing-edge noise has been extensively studied for several decades. However, the last two decades have seen a large volume of research papers on this area being published. In particular, significant progress has been made in all scientific disciplines including theoretical, numerical, and experimental aspects.

The only comprehensive review paper about trailing-edge noise available is one written by Howe [3] in 1978. However, this review paper covers only theoretical aspects of trailing-edge noise. Another review paper was written by Doolan and Moreau [4], which only covers a subset of experimental research and data with specific applications to wind turbine noise. Since these earlier review papers are narrowly focused and do not contain recent advances, we believe that it is a right time to summarize recent technical developments of trailing-edge noise in theoretical, numerical, and experimental areas. These technical developments include sophisticated analytic models that could handle complex geometries; development of low-fidelity numerical models for industrial design purposes and of high-fidelity numerical models that are capable of revealing complex flow physics; and experimental techniques to identify noise source characteristics and explore noise reduction techniques.

In this review paper, the state-of-the-art on trailing-edge noise generation from turbulent boundary layers is broadly reviewed, where we focus on recent analytical developments and new insights from numerical simulations and experimental campaigns. Passive noise control and the applications driven by trailing-edge noise are focal points of the review, and each major section provides an outlook for future developments and contemporary challenges. The review covers virtually the entire landscape of modern research into trailing-edge noise. The review could be useful as a primer for new researchers or as a reference point to the state of the art for experienced professionals.

We start by presenting governing equations and theoretical approaches to solve the scattering of the incident pressure fields by a trailing edge in Section 2. The Green's function approach as well as Amiet's and Howe's models are discussed as semi-infinite models. Then, extended versions of the Green's function approach and the Wiener–Hopf technique for the finite chord length are presented. Notably, recent analytical developments to deal with complex geometries such as serrations are reviewed. This section includes a theory of the surface pressure spectra as well. These theoretical developments serve as the backbone of many semi-empirical models, which is part of Section 3. Semi-empirical and statistical models are introduced in conjunction with steady Reynolds-Averaged Navier–Stokes (RANS) solvers. High-fidelity Computational Fluid Dynamics (CFD), such as Large Eddy Simulations (LES) and Direct Numerical Simulations (DNS), are discussed in detail. We then present the detailed wind-tunnel test activities in Section 4. Significant efforts and various ideas toward noise reduction are reviewed. In Section 5, engineering applications of trailing-edge noise including wind turbine noise, fan noise, rotorcraft and propeller noise are discussed. Specific noise characteristics and design considerations are discussed for each application problem. At the end of the paper, in Section 6, we provide concluding remarks on each approach.

## 2. Theoretical approach

In this section we aim at reviewing the basic theoretical models which can be implemented to predict trailing-edge noise. The models all emanate from the classic assumptions laid out by Lighthill [5] who supposed that in an aeroacoustic setting the surrounding fluid is inviscid and isentropic and thus the total pressure, $p$, satisfies

$$\frac{1}{c^2}\frac{D^2 p}{Dt^2} - \nabla^2 p = \frac{\partial T_{ij}^2}{\partial x_i \partial x_j} \tag{1}$$

where $T_{ij}$ is the Lighthill stress tensor approximated by

$$T_{ij} = \rho u_i u_j, \tag{2}$$

where $\boldsymbol{u}$ is the fluid velocity, $c$ is the speed of sound, and $\rho$ is the total fluid density such that $p = c^2(\rho - \rho_0)$ with $\rho_0$ the mean density, and $D/Dt$ is the material derivative. Here we have assumed unsteady fluctuations in the Mach number are small and the Reynolds number is large, which simplifies this turbulent source term. The fundamentals of a theoretical prediction of noise scattered by the trailing edge of an airfoil thus have two primary concerns; how does one solve Eq. (1) (subject to the relevant boundary conditions), and how does one model the source, $T_{ij}$?

With regards to the relevant boundary conditions, we begin with the most rudimentary models sketched in Fig. 2 supposing the airfoil is a semi-infinite flat plate lying in the region $x_1 \le 0$, $x_2 = 0$, with $x_3$ being an infinite spanwise direction, and that the surrounding fluid has a steady uniform flow parallel to the plate of velocity magnitude $U$ [6,7]. In such a case the governing equation for the pressure is supplemented by a boundary condition enforcing no through-flow;

$$\left.\frac{\partial p}{\partial x_2}\right|_{x_2=0} = 0 \qquad x_1 < 0, \tag{3}$$

and a supposed flat vortex sheet extending for $x_2 = 0$, $x_1 > 0$ over which the pressure is continuous;

$$\Delta p|_{x_2=0} = 0 \qquad x_1 > 0. \tag{4}$$

We will therefore open this theoretical section by discussing the early fundamental solutions to Eq. (1) with these boundary conditions. The first solution by Ffowcs Williams and Hall (FW–Hall) is obtained via a Green's function formulation [6], which allows for any source term, $T_{ij}$ and as such we do not yet address the question of modeling $T_{ij}$. The second solution by Howe [3] uses an alternative formulation of the governing equation (for enthalpy rather than pressure), but follows a similar Green's function construction.

An alternative approach based on the Wiener–Hopf technique will then be discussed which, rather than relying on a Green's function, decomposes the turbulence into surface pressure waves of a given frequency. This approach fundamentally decomposes the source term, $T_{ij}$, into single-frequency waves thus we will also discuss how one takes these single-frequency building blocks and recreates realistic boundary layer turbulence: since the theory here is linear, we can simply sum (integrate) the relevant single-source solutions for the scattered noise in the same manner as we do the sources themselves to recreate the initial turbulence. This decomposition of the source is also utilized by Amiet [8] who, rather than relying on the full Wiener–Hopf method, exploits the Schwartzchild solution to obtain the scattered surface pressure distribution on the plate and from there propagates a finite section of this surface pressure to the far-field via Curle's integral. In doing so, Amiet introduces the first influences of finite chord length.

This section next also extends both the Green's function and Wiener–Hopf frameworks to consider the effects of finite chord and discuss two new approaches which enable rapid calculation of the scattered noise in this case. Finite chord effects are important both for acoustically compact, $ka \ll 1$, and non-compact, $ka \geqslant O(1)$, interactions, which are distinguished by their Helmholtz number, $ka$, comprising of a typical frequency, $k$, and typical body length scale, $a$. Naturally, when considering a semi-infinite body, no matter how low one chooses the frequency of interaction one cannot investigate the compact regime. However, perhaps more subtly, finite chord effect can also be important for accurate prediction of high-frequency/non-compact interactions; at high-frequencies the interference of a trailing-edge source with a leading-edge effect leads to modulation of the overall acoustic far-field. Noise reduction techniques can seek to exploit this to create optimal destructive interference [9]. This section ends with a discussion of some of these bio-inspired noise reduction models, including trailing-edge serrations and porosity, and how one may adapt the aforementioned theoretical approaches to these new more complex boundaries.

### 2.1. Analytic models

#### 2.1.1. Green's function approach

A Green's function is particularly useful when the source is complex and cannot be easily manipulated analytically as may be the case arising in Eq. (1). It is most conveniently found in the frequency domain by defining the Fourier transform

$$\tilde{p}(\boldsymbol{x},\omega) = \int_{-\infty}^{\infty} p(\boldsymbol{x},t)e^{i\omega t}\,dt \tag{5}$$

The transformed Green's function, $\tilde{G}(\boldsymbol{x};\boldsymbol{y})$ in the case of zero mean flow should therefore satisfy

$$\nabla^2\tilde{G} + k^2\tilde{G} = -4\pi\delta(\boldsymbol{x}-\boldsymbol{y}), \tag{6}$$

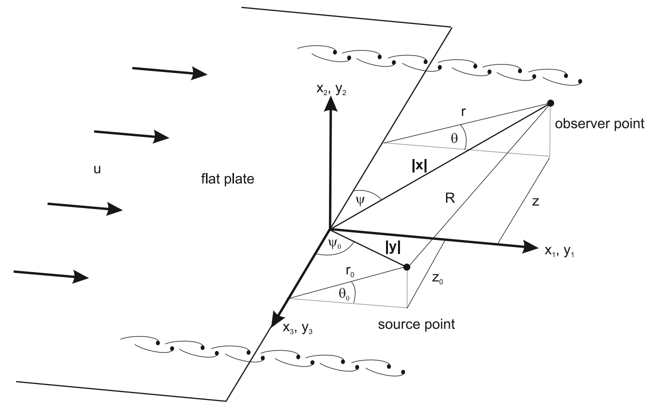


**Fig. 3.** Coordinate system for the half-plane Green's function. *Source:* Adapted from [6].

for $k = \omega/c$, and requires $\frac{\partial\tilde{G}}{\partial y_2} = 0$ on the rigid half-plate.[1] This is given by [11] as

$$\tilde{G} = \frac{e^{\pi i/4}}{\sqrt{\pi}}\left(\frac{e^{-ikR}}{R}\int_{-\infty}^{u_R} e^{-iu^2}du + \frac{e^{-ikR'}}{R'}\int_{-\infty}^{u_{R'}} e^{-iu^2}du\right), \tag{7}$$

where

$$u_R = 2\left(\frac{krr_0}{D+R}\right)^{1/2}\cos\left(\frac{\theta-\theta_0}{2}\right), \tag{8a}$$

$$u_{R'} = 2\left(\frac{krr_0}{D+R'}\right)^{1/2}\cos\left(\frac{\theta+\theta_0}{2}\right), \tag{8b}$$

and

$$R = (r^2 + r_0^2 - 2rr_0\cos(\theta-\theta_0) + (z-z_0)^2)^{1/2} \tag{8c}$$

is the separation between the source (subscript $_0$) and observer, and

$$R' = (r^2 + r_0^2 - 2rr_0\cos(\theta+\theta_0) + (z-z_0)^2)^{1/2} \tag{8d}$$

is the separation between the image source and the observer. Finally

$$D = ((r+r_0)^2 + (z-z_0)^2)^{1/2} \tag{8e}$$

is the shortest distance between the source and observer by traveling via the edge of the plate. These coordinates are illustrated in Fig. 3. One must pay careful attention that $R \neq r$ for comparison of the various models discussed in this section.

Using this Green's function one may recover the total pressure by integrating over the volume sources,

$$\tilde{p}(\boldsymbol{x},\omega) = \int_V \tilde{T}_{ij}\frac{\partial^2\tilde{G}}{\partial y_1\partial y_2}dV(\boldsymbol{y}). \tag{9}$$

Numerous asymptotic regimes can be investigated analytically from this result, including the far-field pressure due to compact turbulence of volume $\Lambda$ located close to the edge given by [3] as

$$|p| \approx \frac{\rho v U M}{\pi}\frac{\delta}{R}\frac{\Lambda}{\delta^3}\sin(\theta/2)\sqrt{\sin\alpha} \tag{10}$$

where $v$ is the mean turbulent fluctuation velocity, $\delta$ the characteristic turbulence correlation scale, and $\alpha$ the (azimuthal) angle between the observer direction and the edge of the half-plate. Here we see a $\sin(\theta/2)$ directivity pattern emerging for the scattered pressure.

The general scaling law of trailing-edge noise may also be obtained from this result [6]; the sound intensity in the far-field due to a near-field isolated eddy is $I \sim \rho U^3 M^2\delta^2/R^2$, which scales with velocity as

[1] The factor of $-4\pi$ multiplying the Dirac delta function is here due to Fourier transform conventions. This convention and subsequent definitions follows Jones [10] exactly and thus contains this extra factor.

$U^5$. This is $O(M^{-3})$ larger than the sound generated by an identical eddy far from the edge.

For 2D subsonic flows including the unsteady Kutta condition, or 3D flows neglecting the Kutta condition, half-plate Green's functions have also been found [12,13], which may simply replace $\tilde{G}$ in Eq. (9). Whilst more complex, these Green's functions can aid in the calculation of flap side-edge noise.

#### 2.1.2. An alternative Green's function formulation

Howe [3] suggested, that rather than starting from Lighthill's equation, we should reformulate the acoustic analogy to be suited to an arbitrary mean flow where the density may not be expressed only as a function of pressure. Instead we use the ideal gas relation

$$p = \rho RT \tag{11}$$

where $R$ is the specific gas constant, and $T$ temperature, and reformulate the governing equations based on enthalpy, $B$, defined as

$$B = \int \frac{dp}{\rho} + \frac{1}{2}v^2. \tag{12}$$

This results in a general wave equation for $B$ given by [14, Eq. (4.14)]

$$\begin{aligned}\left[\frac{D}{Dt}\left(\frac{1}{c^2}\frac{D}{Dt}\right) + \frac{1}{c^2}\frac{D\boldsymbol{v}}{Dt}\cdot\nabla - \nabla^2\right]B = \nabla\cdot(\boldsymbol{\omega}\times\boldsymbol{v} - T\nabla S)\\ - \frac{1}{c^2}\frac{D\boldsymbol{v}}{Dt}\cdot(\boldsymbol{\omega}\times\boldsymbol{v} - T\nabla S) + \frac{D}{Dt}\left(\frac{T}{c^2}\frac{DS}{Dt}\right) + \frac{\partial}{\partial t}\left(\frac{1}{c_p}\frac{DS}{Dt}\right),\end{aligned} \tag{13}$$

where $S$ is entropy, $\boldsymbol{v}$ is the total fluid velocity, $\boldsymbol{\omega}$ is the vorticity, and $c_p$ is the specific heat at constant pressure. Note, here the material derivative involves the actual fluid flow, not only the mean flow. Should heat conduction be negligible, $DS/Dt = 0$ hence the final two terms on the RHS disappear.

Howe used this formulation to evaluate the noise generated by a line vortex passing over the edge of a semi-infinite half plane in low Mach number flow at constant temperature. By linearizing about the mean flow, Eq. (13) becomes

$$\left(\frac{1}{c^2}\frac{\partial^2}{\partial t^2} - \nabla^2\right)B = \nabla\cdot(\boldsymbol{\omega}\times\boldsymbol{v}), \tag{14}$$

with $\boldsymbol{\omega} = \kappa\delta(\boldsymbol{x} - \boldsymbol{x}_0(t))\hat{\boldsymbol{e}}_3$, and $\boldsymbol{v} = \dot{\boldsymbol{x}}_0(t)$ denoting the velocity of the vortex whose center is at $\boldsymbol{x}_0(t)$ and has strength $\kappa$.

The path of the vortex about the edge is given in polar coordinates, $(r_0, \theta_0)$ by

$$r_0 = a\sec(\theta_0/2) \tag{15}$$

where $r_0$ and $\theta_0$ are measured from the edge of the half plane, and $a$ is the closest distance between the vortex and the plate.

A Green's function, as discussed previously, can then be employed to obtain the solution for $B = p/\rho_0$, which then yields a far-field pressure

$$p \approx \frac{\rho_0\kappa\sin(\theta/2)}{\pi\sqrt{r}}\left[\frac{D\Psi}{Dt}\right] \tag{16}$$

where $\Psi = -\sqrt{r_0}\cos(\theta_0/2)$ corresponds to the streamfunction of an ideal source-free two-dimensional potential flow around a half plane, and $[.]$ denotes evaluation at the retarded time, $t - r/c$. As the vortex crosses the streamlines of the flow on approach to the edge, noise is increased proportionally to the rate at which the vortex crosses these lines.

We recover through this approach the familiar form of the far-field noise, $\sim \sin(\theta/2)r^{-1/2}$. Note of course differences in how the 'incident' field is defined results in different overall scalings of this fundamental scattered form. Of course, Howe's method can also be used to predict the far-field noise due to simulated turbulent flow rather than just a single vortex by suitably adapting the source term.

#### 2.1.3. Wiener–Hopf approach

The Wiener–Hopf approach, developed by Wiener and Hopf [15] but later made popular by Noble [16], is most convenient when the unsteady turbulent source can be characterized by a simple decomposition into planar pressure waves on the upper surface of the plate. In such a case, the total pressure may be decomposed into its incident and scattered parts, $p = p_i + p_s$ respectively. The so-called incident part, taken for a single planar pressure wave

$$p_i = P_0 e^{ik_1x_1 + ik_3x_3 - i\omega t}, \tag{17}$$

deals with the source term of the governing equation leaving the scattered term to satisfy;

$$\frac{1}{c^2}\frac{D^2 p_s}{Dt^2} - \nabla^2 p_s = 0 \tag{18a}$$

subject to

$$\left.\frac{\partial p_s}{\partial x_2}\right|_{x_2=0} = 0 \qquad x_1 < 0, \tag{18b}$$

and

$$\Delta p_s|_{x_2=0} = -\Delta p_i|_{x_2=0} \qquad x_1 > 0. \tag{18c}$$

We assume the pressure convects with velocity $U_c$ which is less than the external flow velocity, $U$, hence $k_1 = \omega/U_c$.

These equations simplify for the given incident field under the following transformation

$$p_s = P_0\,\phi(x_1, x_2)e^{-ikMx_1/\beta^2 + ik_3x_3 - i\omega t}, \tag{19a}$$

and a Prandtl–Glauert transformation

$$x_1 \to x_1/\beta, \tag{19b}$$

to give

$$\nabla^2_{x_1,x_2}\phi + w^2\phi = 0 \tag{20a}$$

subject to

$$\left.\frac{\partial \phi}{\partial x_2}\right|_{x_2=0} = 0 \qquad x_1 < 0, \tag{20b}$$

and

$$\Delta\phi_s|_{x_2=0} = -e^{i\delta x_1} \qquad x_1 > 0, \tag{20c}$$

where $M$ is the Mach number of the background steady flow, $\beta = \sqrt{1 - M^2}$, $k = \omega/c$, $w^2 = (k/\beta)^2 - k_3^2$, and $\delta = (k_1 + kM\beta^{-2})\beta$.

Eqs. (20) form a familiar mixed-boundary condition problem which may immediately be solved via the Wiener–Hopf technique to yield;

$$p_s(\boldsymbol{x}, t) = P_0\frac{\sqrt{-\delta - w}}{4\pi i}\int_{-\infty}^{\infty}\frac{e^{-i\lambda x_1 - \sqrt{\lambda^2 - w^2}|x_2|}}{(\lambda + \delta)\sqrt{\lambda - w}}\,d\lambda\, e^{-ikMx_1/\beta^2 + ik_3x_3 - i\omega t} \tag{21}$$

presented in the Prandtl–Glauert transformed space. The method of steepest descents may be applied to obtain an analytic solution for the far-field scattered noise, or one may evaluate the integral numerically to recover the scattered pressure field throughout the whole domain. The analytic far-field approximation is given by

$$p_s(r, \theta, x_3, t) \sim P_0\frac{\sqrt{-\delta - w}\sin(\theta/2)}{4\sqrt{\pi}(\delta - w\cos\theta)}\frac{e^{iwr}}{\sqrt{r}}e^{-\pi i/4 - ikMr\cos\theta/\beta^2 + ik_3x_3 - i\omega t}, \tag{22}$$

where $(r, \theta, x_3)$ are stretched cylindrical coordinates centered on the trailing edge of the plate. This provides a far-field functional form of

$$p_s \approx C\sin\left(\frac{\theta}{2}\right)\frac{e^{iwr}}{\sqrt{kr}}, \tag{23}$$

where $C$ is a constant dependent on $\delta$ and $w$. Like the Green's function, the directivity has the functional form of $\sin(\theta/2)$.

We mention here, for the reader familiar with the classical Wiener–Hopf solution from Jones [10], that this setup differs from Jones'

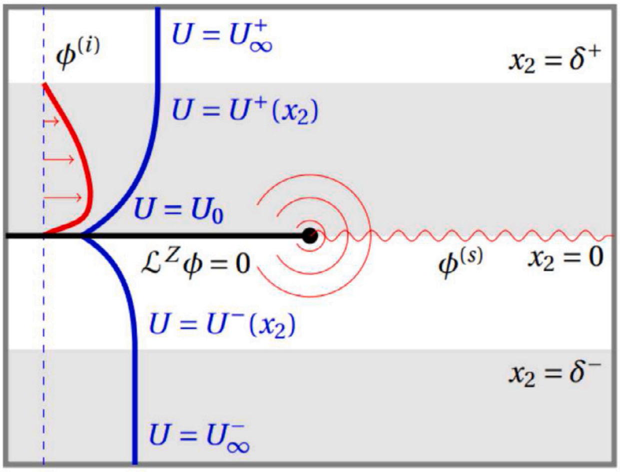


**Fig. 4.** Setup for Wiener–Hopf scattering off a semi-infinite plate in the presence of background shear flow.
*Source:* Reproduced with permission from [18].

traditional setup, since there the convection speed of the surface pressure wave is assumed to be the same as the external mean flow speed, $U = U_c$. Such an assumption tidies the algebra, although significantly reduces the accuracy of the model since it is well documented that surface waves convect at sub-freestream speeds [17].

The Wiener–Hopf method has recently been extended to include the effects of the boundary layer shear profile [18], as illustrated in Fig. 4, although due to the more complex setup a numerical factorization must be performed. The acoustic source in this case is taken to be a vortex sheet at a given height above the half-plate, which is an extension to the above gust-type source specified only on the surface. Since a numerical factorization is used, impedance boundary conditions have also be considered with relative ease.

These solutions, both in uniform flow and shear flow, use a simplistic single-frequency source. To consider fully turbulent flows, one must integrate over all waves that generate the required turbulence on the surface. We refer to this as integrating over the surface pressure spectrum, which accounts for the various pressure fluctuations on the surface due to a turbulent boundary layer. We discuss the exact formulation of the surface pressure spectrum, denoted by $\Pi(k_1, k_3, \omega)$, and this integration at the end of this section.

### 2.1.4. Amiet approach

Amiet [19] first imposed a surface pressure along $x_2 = 0$ corresponding to that of the basic surface wave. Then, by extending the plate to upstream infinity, he found a scattered solution that cancels the incorrect surface wave imposed along the downstream wake. He thus considered the diffraction of a semi-infinite flat plate by invoking the Schwarzschild solution to the general problem

$$\frac{\partial^2 \Phi}{\partial x_1^2} + \frac{\partial^2 \Phi}{\partial x_2^2} + \mu^2 \Phi = 0 \tag{24a}$$

$$\Phi(x_1, 0) = f(x_1) \qquad x_1 \geq 0 \tag{24b}$$

$$\frac{\partial \Phi}{\partial x_2}(x_1, 0) = 0 \qquad x_1 \leq 0 \tag{24c}$$

This solution provides the values of $\Phi(x_1, 0)$ along $x_1 < 0$ as

$$\Phi(x_1, 0) = \frac{1}{\pi}\int_0^\infty G(x_1, \xi, 0) f(\xi) d\xi \tag{25}$$

where

$$G(x, \xi, 0) = \sqrt{\frac{-x}{\xi}}\,\frac{e^{-i\mu(\xi - x)}}{\xi - x} \tag{26}$$

This solution provides only the unknown $\Phi$ along the boundary $x_2 = 0$, $x_1 < 0$, and is equivalent to evaluating the Wiener–Hopf solution here. The benefit of the Schwarzschild solution is that it is simpler to implement for an arbitrary $f(x_1)$, whereas in the Wiener–Hopf approach one would have to 'split' this function which may require numerical contour integration.

The jump in total (scattered and initial) surface pressure along the plate lying in the region $x_1 < 0$ is then given by

$$\Delta P(x_1, \omega, U_c) = P_0\left((1 + i)E^*\left(-x_1\left[(1 + M)\mu + k_1\right]\right) - 1\right)e^{-ik_1 x_1} \tag{27}$$

where recall $U_c$ is the convection speed of the surface pressure wave, and $k_1 = \omega/U_c$. We further define $\mu = M\omega/U\beta^2$. The Fresnel function $E^*$ is given by

$$E^*(x) = \int_0^x (2\pi\xi)^{-1/2} e^{-i\xi} d\xi. \tag{28}$$

This is equivalent to the semi-infinite Wiener–Hopf approach.

The total far-field noise, $p = p_i + p_s$ is obtained from the jump in total surface pressure, $\Delta P$, via Curle's analogy yielding the radiation integral [8]

$$p(\boldsymbol{x}, \omega) = \frac{-i\omega x_3}{4\pi c_0 S_0^2}\int_{-2}^{0}\int_{-L/2}^{L/2} \Delta P e^{i\omega R_t/c_0}\, dy\, dx \tag{29}$$

where $(x_1, x_2, x_3)$ denotes the observer locations with the origin at the trailing edge, and $L$ denotes the finite span of the plate which is non-dimensionalized with respect to the plate semi-chord. The terms $S_0$ and $R_t$ denote radial directions to the observer which account for convection. Given the expression Eq. (27) for $\Delta P$, one can evaluate this integral to obtain a transfer function from the initial single-frequency gust, to its far-field acoustics, and from there integrate over a turbulent spectrum (discussed later) to approximate the far-field noise as

$$S(\omega) = \left(\frac{\omega x_2}{2\pi c_0 \sigma^2}\right)^2 l_3(\omega)\, L\, |\mathcal{L}|^2\, \Phi_{pp}(\omega) \tag{30}$$

where $\sigma^2 = x_1^2 + \beta^2 x_2^2$, $\beta^2 = 1 - M^2$, $|\mathcal{L}|$ is the norm of the transfer function of the airfoil at the location $(x_1, x_2)$, and $\Phi_{pp}(\omega)$ is the surface pressure spectrum near the trailing-edge. The quantity:

$$l_3(\omega) = \frac{1}{\Phi(\omega, 0)}\int_0^\infty \Phi(\omega, x_3)\, dx_3 \tag{31}$$

is a spanwise length scale for the surface pressure turbulence. Further discussion of the surface pressure spectrum will be given at the end of this section. Roger and Moreau [20] added a factor of 2 in $\Delta P$ in Eq. (29) to account for the scattering effect from the opposite side. This yields a factor of 4 in the acoustic spectrum or Eq. (30).

### 2.1.5. Howe's approach

Howe similarly calculated the surface pressure using his alternative formulation [3] for a single surface pressure wave and determined a similar expression for the far-field acoustic spectrum in terms of the surface pressure spectrum.

$$S(\omega) = \frac{M_c L \sin\bar{\alpha}\sin^2(\theta/2)\Phi(\omega, k\cos\bar{\alpha})}{\pi R^2(1 + M_{0r})^2(1 - M_{cr})^2(1 - M_{wr})^2(1 - M_c\sin\bar{\alpha})} \tag{32}$$

where $M_{0r} = M_0 x_1/R, M_{cr} = M_c x_1/R, M_{wr} = M_w x_1/R$ are the relative Mach numbers in the direction of the observer, with $M_0$ the Mach number of the external mean flow, $M_c$ the Mach number of the convective boundary layer flow, and $M_w$ the Mach number in the wake.

In the limit of low Mach number, $M_0 \ll 1$, and high frequency, $k \gg 1$, Howe's solution and Amiet's solution of acoustic power spectra generated from each surface of an airfoil, which is measured at 90 degrees from a trailing edge, can be shown to both converge to the following equation:

$$S(\omega) = \frac{1}{4}\left(\frac{L}{\pi^2 R^2}\right)\left(\frac{M_c}{1 - M_c}\right) l_3(\omega)\Phi_{pp}(\omega) \tag{33}$$

Then, the total noise is calculated from the two surfaces.

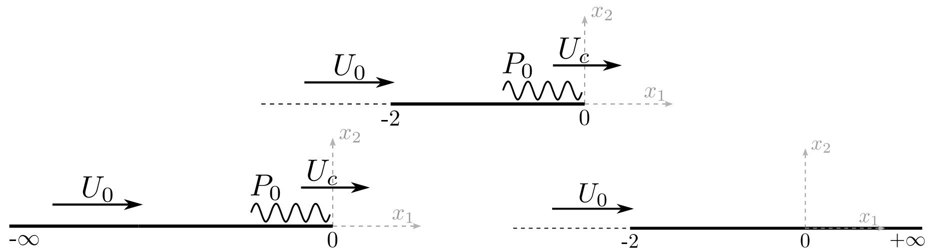


**Fig. 5.** Trailing-edge noise model. Incident gust on a finite-chord airfoil (top), main scattering half-plane problem (bottom left) and leading-edge correction (right). Coordinates made non-dimensional by the half chord, reference at the trailing edge.

### 2.1.6. Further advances for finite chord

Amiet [8] was the first to consider the finite-chord effects for the leading-edge noise mechanism. Amiet composed two semi-infinite Schwarzschild solutions based on the velocity potential for this noise mechanism. Roger and Moreau [20] used the same principle for trailing-edge noise as illustrated in Fig. 5. Indeed, to account for the finite nature of the plate, the far-field acoustics is calculated *only* from the surface pressure induced within the region $-2 < x_1 < 0$. Thus in the upstream region, $x_1 < -2$, there is an unphysical pressure jump that is ignored. By doing so, all dominant features of scattering at the trailing edge are accounted for, but only partial features of scattering at the leading edge are accounted for. One then corrects the unphysical pressure jump arising in this solution by introducing a so-called back scattering term. This involves adding another semi-infinite plate solution in the region $x_1 > -2$, which corrects the pressure along the upstream direction. To obtain a true finite-chord solution, one would, however, need to continue indefinitely with semi-infinite plate corrections to ensure the appropriate boundary conditions along each of the three sections $x_1 < -2$, $-2 < x_1 < 0$ and $x_1 > 0$ as, by correcting the upstream once, an incorrect pressure jump occurs in the downstream. The first backscattering correction term has been calculated by Roger and Moreau [20] and Moreau and Roger [21], which is shown to be an influential modifier to Amiet's solution at low frequencies.

In addition to these initial considerations of finite-chord effects, further advances for finite-chord have been made using Green's functions. Howe [22] constructed an asymptotic Green's function (in the Fourier Transformed domain) for a chord of length $l$ through successive solutions of edge corrections, as is the idea behind extending Amiet's approach [20]. Importantly, Howe included the infinite series of terms required to obtain the correct boundary conditions along the whole of $x_2 = 0$. In the limit of high frequency, Howe's result yields

$$\tilde{G}(\boldsymbol{x},\boldsymbol{y},\omega) = \tilde{G}_1(\boldsymbol{x},\boldsymbol{y},\omega) + \tilde{G}_{LE}(\boldsymbol{x},\boldsymbol{y},\omega) + \tilde{G}_{TE}(\boldsymbol{x},\boldsymbol{y},\omega), \tag{34}$$

where

$$\tilde{G}_1(\boldsymbol{x},\boldsymbol{y},\omega) \approx \frac{-\mathrm{sgn}(x_2)\phi^*(\boldsymbol{y})e^{\pi i/4}}{(2\pi)^2\sqrt{\pi}} \int_{-\infty}^{\infty}\int_{-\infty}^{\infty} \frac{e^{i(kx_1+k_3x_3)}}{\sqrt{\kappa+k}}\,dk\,dk_3, \tag{35}$$

$$\tilde{G}_{LE}(\boldsymbol{x},\boldsymbol{y},\omega) \approx \frac{\sqrt{\kappa}\sqrt{\sin\psi}\,\phi^*(\boldsymbol{y})e^{i\kappa(|\boldsymbol{x}'|+l\sin\psi)}}{2} i\pi^{3/2}|\boldsymbol{x}|(1+e^{2i\kappa l\sin\psi}/2\pi i\kappa l\sin\psi) \times \mathcal{F}\left(2\sqrt{\frac{\kappa l\sin\psi\cos^2(\theta/2)}{\pi}}\right), \tag{36}$$

$$\tilde{G}_{TE}(\boldsymbol{x},\boldsymbol{y},\omega) \approx \frac{-\phi^*(\boldsymbol{y})e^{i\kappa(|\boldsymbol{x}|+2l\sin\psi)}}{\pi^2|\boldsymbol{x}|\sqrt{2il}(1+e^{2i\kappa l\sin\psi}/2\pi i\kappa l\sin\psi)} \times \mathcal{F}\left(2\sqrt{\frac{\kappa l\sin\psi\sin^2(\theta/2)}{\pi}}\right), \tag{37}$$

where $\kappa = \sqrt{k_0^2 - k_3^2}$, $\sin\psi = r/|\boldsymbol{x}|$, $\boldsymbol{x}' = (x_1+l, x_2, x_3)$ is a shifted coordinate system based on the leading edge, and $\phi^*(\boldsymbol{y})$, which is a function of source position of $\boldsymbol{y}$, is the velocity potential of an ideal incompressible flow around the edge. For a half plane, $\phi^*(\boldsymbol{y}) = \sqrt{r_y}\sin(\theta_y/2)$, where $y$ denotes polar coordinates for the source. Finally, $\mathcal{F}(x) = g(x) + if(x)$ where $f(x)$ and $g(x)$ are Fresnel integral auxiliary functions [23].

With this expression for the Green's function, Wang et al. [24] also generalized Ffowcs Williams and Hall's trailing-edge noise model described in Section 2.1.1. Indeed, one can integrate over the turbulent source via Eq. (9) to obtain the far-field acoustic pressure (see equations (14) and (15) in [24] or equation (3) in [25]).

We compare the various models in Fig. 6 against experimental data for the controlled diffusion (CD) airfoil at a reference angle of attack of 8° [21] (see Section 3.2). Inputs for Amiet and Howe's models came from the experimental wall-pressure statistics collected at Ecole Centrale de Lyon (ECL) [26]. Inputs for the Ffowcs Williams and Hall's model were taken from LES predictions with the CDP code developed at Stanford [27]. At low frequencies, the effects of backscattering are significant and bring the theoretical prediction into better agreement with the experimental data. Howe's model is seen to represent a high-frequency approximation of Amiet's model (without the humps from the Fresnel functions caused by the finite chord). All models agree over the frequency range of the measurements, but some distinct behavior is found at high frequencies, which will be explained in Section 3.3. Note also that the dominant geometric effects on the scattering of trailing-edge noise are from the finite chord, and not the precise geometry of the airfoil itself (e.g thickness and camber).

### 2.1.7. Wiener–Hopf approach for finite chord

Finally, for completeness of this section we discuss the extension of the Wiener–Hopf method to finite chord. This brings about a system of equations analogous to Eq. (20)

$$\nabla^2\phi + w^2\phi = 0 \tag{38a}$$

with

$$\Delta\phi|_{x_2=0} = 0 \qquad x_1 < -2 \tag{38b}$$

$$\left.\frac{\partial\phi}{\partial x_2}\right|_{x_2=0} = 0 \qquad -2 < x_1 < 0 \tag{38c}$$

$$\Delta\phi|_{x_2=0} = 2f(x_1) \qquad x_1 > 0 \tag{38d}$$

where here we now include the requirement that upstream of the plate, the pressure is continuous. For simplification we have labeled the pressure-jump forcing over the wake as $2f(x_1)$.

To cast as a Wiener–Hopf equation, we define the half-range Fourier Transforms

$$\Phi(\lambda, x_2) = \Phi_-^0(\lambda, x_2) + \Phi_+^0(\lambda, x_2) \tag{39a}$$

and

$$\Phi(\lambda, x_2) = (\Phi_-^{-2}(\lambda, x_2) + \Phi_+^{-2}(\lambda, x_2))e^{-2i\lambda} \tag{39b}$$

where

$$\Phi_-^a(\lambda, x_2) = \int_{-\infty}^{a} \phi(x_1, x_2)e^{i\lambda(x_1-a)}\,dx_1 \tag{39c}$$

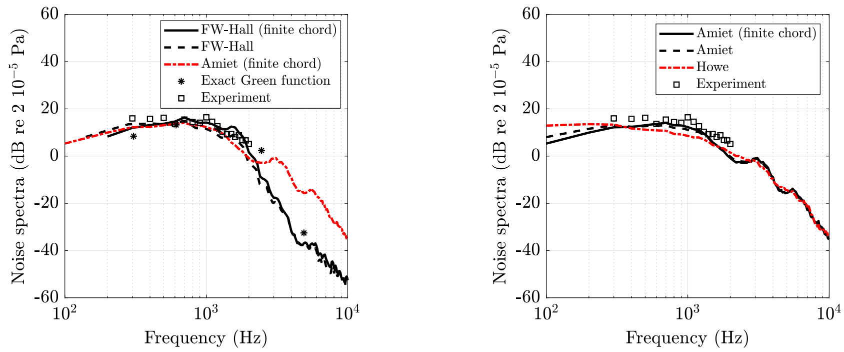


(a) (b)

**Fig. 6.** Trailing-edge noise model comparison on the CD airfoil against ECL experimental data [21,26]: (a) Ffowcs Williams and Hall's analogy with flat plate and exact Green's functions and Amiet's model and (b) Amiet's and Howe's models.

and

$$\Phi_+^a(\lambda, x_2) = \int_a^\infty \phi(x_1, x_2) e^{i\lambda(x_1 - a)} dx_1 \tag{39d}$$

such that the subscript $\pm$ denotes the region of the complex $\lambda$ plane where the functions are analytic. One may therefore use the relation $\Phi' = -\gamma\Phi$, where $\gamma = \sqrt{\lambda^2 - w^2}$, $'$ denotes differentiation with respect to $y$, and all functions are evaluated along $y = 0$, to obtain the matrix Wiener–Hopf equation

$$\begin{pmatrix} \Phi_+^{0\,\prime} \\ \Phi_+^{-2} \end{pmatrix} + \begin{pmatrix} \gamma & e^{-2i\lambda} \\ -e^{2i\lambda} & 0 \end{pmatrix} \begin{pmatrix} \Phi_-^0 \\ \Phi_-^{-2\,\prime} \end{pmatrix} = \begin{pmatrix} -F(\lambda)\gamma \\ e^{2i\lambda} F(\lambda) \end{pmatrix}. \tag{40}$$

Whilst this equation may be constructed with relative ease, obtaining a solution to such an equation is a difficult task particularly due to the exponential functions. Here we therefore discuss appropriate methods for solving such an equation, and also alternative approaches for solving Eq. (38), which have come about over the past few years.

First discuss a modern advance of the Wiener–Hopf technique which permits the solution to the matrix equation Eq. (40) to be found quickly and accurately. Fundamentally this approach from Priddin [28,29] relies on the notion of iterative corrections for back scattering adopted by [20] and [22], whereby each correction term is formally smaller than the term preceding it. Eq. (40) may be written generally as

$$H \begin{pmatrix} \Phi_-^{(1)} \\ \Phi_-^{(2)} \end{pmatrix} + G \begin{pmatrix} \Phi_+^{(1)} \\ \Phi_+^{(2)} \end{pmatrix} = F \tag{41}$$

where $H$ is a lower triangular matrix, and $G$ is an upper triangular matrix and the unknowns are now labeled simply as the respective coefficients of the vectors involved. The non-zero off-diagonal terms in $H$ and $G$ contain exponential functions, which relate physically to rescattering features of the acoustic field.

By initially setting these off-diagonal entries to zero, an initial approximation for the unknown $\Phi_\pm^{(m)}$, denoted as $\Phi_\pm^{(m)0}$, may be found

$$\Phi_-^{(m)0} + K\Phi_+^{(m)0} = F^{(m)} - \sum_{l<m} H^{(l,m)} \Phi_-^{(l)0} \tag{42}$$

for $m = 1$ then $m = 2$. Here $K$ is a known term arising in both $H$ and $G$. A fixed point iterative scheme is then created by solving at the $r$th step

$$\Phi_-^{(m)r} + K\Phi_+^{(m)r} = F^{(m)} - \sum_{l<m} H^{(l,m)} \Phi_-^{(l)r} - \sum_{l>m} G^{(m,l)} \Phi_+^{(l)r-1}. \tag{43}$$

Implementation, convergence, and efficiency of this approach is detailed in [28] and [29].

Next, we discuss obtaining separable solutions to problems of the form Eq. (38); however for ease we suppose the plate lies in the region $-1 < x_1 < 1$ as to align with the literature on this approach (such a shift may be obtained with a simple change of streamwise coordinate). Whilst reliant on ideas developed in the 1960s by McLachlan [30], it is only recently that this idea has been applied effectively for trailing-edge noise prediction in references [31,32]. Here, the authors transform from Cartesian coordinates, $(x_1, x_2)$, to elliptic coordinates, $(\nu, \tau)$ defined via

$$x_1 = \cosh(\nu)\cos(\tau) \qquad x_2 = \sinh(\nu)\sin(\tau) \tag{44}$$

The governing equation thus becomes

$$\frac{\partial^2 \phi}{\partial \tau^2} + \frac{\partial^2 \phi}{\partial \nu^2} + \frac{\cosh(2\nu) - \cos(2\tau)}{2} k_0^2 \phi = 0, \tag{45}$$

which separates into solutions of the form $V(\nu)W(\tau)$. Imposing, as in [29], a continuity requirement of $\phi(x_1, 0) = 0$ off the plate (as would be the case for the scattering of a quadrupole source), the solution in elliptic coordinates is given by

$$\phi(\nu, \tau) = \sum_{m=1}^\infty a_m se_m(\tau) H se_m(\nu) \tag{46}$$

where $se_m$ are sine-elliptic functions, and $Hse_m$ are Mathieu–Hankel functions. The coefficients $a_m$ are obtained by applying the relevant boundary condition on the plate.

Both approaches mentioned here have the benefit of being fundamentally independent of the boundary condition applied on the plate, and for progress they rely predominantly on the geometry of the boundary. Hence, these approaches can be readily applied to predict the effects of, for example, perforated and/or elastic plates, which we discuss in the next subsection.

### 2.2. Noise control

#### 2.2.1. Poroelasticity

Trailing-edge noise may be mitigated by a variety of typically bio-inspired adaptations. The first modern theoretical venture which kick-started interest in bio-inspired trailing-edge noise reduction was by Jaworski and Peake [33], who used the Wiener–Hopf technique to determine the noise generated by a near-field quadrupole source scattered by a semi-infinite porous elastic plate (referred to as a poroelastic plate). The solution is obtained through the principle of reciprocity, whereby the far-field acoustic response to a near-field source may be equivalently calculated as the near-field response to a far-field source. Jaworski and Peake, therefore, considered the scattering of a far-field incident sound wave, by a poroelastic plate in zero mean flow.

The plate is modeled as a wave-bearing half-plane with regular circular perforations [3]. Instead of the usual rigid boundary condition, two coupled conditions must be specified on the plate. The first determines the elastic deformation of the plate, $\eta$, along $x_2 = 0$, $x_1 < 0$

$$(1 - \alpha_H)\left(\bar{B}\nabla^4 + m\frac{\partial^2}{\partial t^2}\right)\eta = -\left(1 + \frac{4\alpha_H}{\pi}\right)\Delta p \tag{47}$$

in terms of the plate mass per unit area, $m$, effective stiffness, $\bar{B}$, and fractional open area $\alpha_H$. $\Delta p$ denotes the jump in pressure across the plate, $\Delta p = p(x_1, 0^+) - p(x_1, 0^-)$. The second equation is the kinematic boundary condition on the plate $x_2 = 0$, $x_1 < 0$, requiring the total acoustic potential, $\phi$, to satisfy

$$\frac{\partial \phi}{\partial x_2} = \frac{\partial}{\partial t}\left[(1-\alpha_H)\eta + \alpha_H \eta_a\right] \tag{48}$$

where $\eta_a$ is the fluid displacement in the apertures of the plate, which relates directly to $\Delta p$.

These boundary conditions, together with the governing Helmholtz equation, may be solved as a one-dimensional Wiener–Hopf equation although the kernel of such an equation must be factorized numerically. Jaworski and Peake [33] completed this factorization and were able to predict the relative scattering strengths of porous and elastic edges. We note here that older studies have also used the Wiener–Hopf technique to consider acoustic scattering by compliant screens (perforated but not wave-bearing) [34] and a finite impermeable elastic strip [35]. These previous papers, however, restrict factorization to different asymptotic regimes, and unlike Jaworski and Peake [33], cannot provide a full picture for the noise reduction across a wide range of frequencies.

Jaworski and Peake [33] concluded that edge porosity modifies the acoustic power radiated from a quadrupole source to a sixth-power velocity dependence at low frequencies (as also seen by [34]). Meanwhile edge elasticity modifies this power to an even weaker seventh-power dependence. These both produce weaker radiation than a rigid edge which exhibits a fifth-power dependence. Further, whilst porosity is deemed most effective at noise reduction at low frequencies, elasticity provides acoustic benefits at higher frequencies. The combined poroelastic edge, therefore, extends the frequency range over which a noise reduction is observed versus a rigid plate than would be possible by just a porous or just an elastic plate.

Following the success of Jaworski and Peake's model some extensions have been made, which permit a finite chord for porous and poroelastic plates, both theoretically through the Wiener–Hopf technique [36] and numerically through a boundary element method [37]. These introduce the important feature of elastic plate resonances, something which is lacking in a semi-infinite model, and can cause tonal noise increases. To mitigate such resonances, one could introduce a variation in the elastic parameters of the plate along the chord, however doing so prohibits the use of the Wiener–Hopf technique since the Fourier transform cannot readily be applied to Eq. (47). Instead, the modern approach via a Mathieu function expansion allows for an arbitrarily varying elasticity [32] or indeed porosity [9].

Variable elasticity has shown the ability to reduce or shift plate resonances, and to be able to propagate the dominant pressure fluctuations away from the trailing edge. Meanwhile, smoothly varying porosity from a relatively high fractional open area at the trailing edge, to zero at the leading edge may improve aerodynamic performance *and* reduce low-frequency noise for certain chord-wise variations versus that produced by a constant porosity plate. This is achieved by inducing a destructive back scattered field at the rigid leading edge.

### 2.2.2. Serrations

The first theoretical predictions for the noise generated by a plate with a serrated trailing edge were developed by Howe [38,39], wherein he considered both sawtooth and sinusoidal serrations. Fig. 7 is taken from [39] and illustrates the setup considered: surface pressure fluctuations scatter off a serrated edge along $x_1 = \zeta(x_3)$, where $\zeta(x_3)$ represents a periodic sinusoidal serration with amplitude $h$ and wavelength $\lambda$.

This problem is governed by the usual Helmholtz equation, and half-space boundary condition. Howe therefore obtained a solution by finding the relevant Green's function satisfying

$$(\nabla^2 + k_0^2)G = \delta(\boldsymbol{x} - \boldsymbol{y}), \tag{49a}$$

$$\frac{\partial G}{\partial x_2} = 0 \qquad x_2 = 0, \quad x_1 < \zeta(x_3). \tag{49b}$$

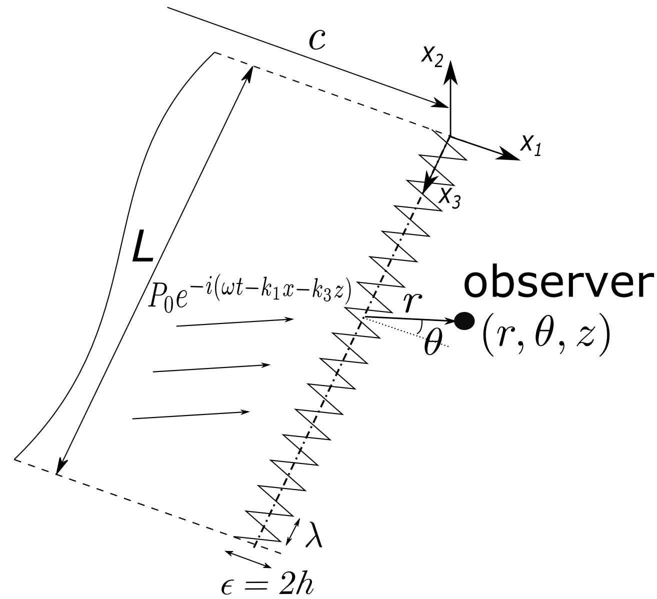


**Fig. 7.** Illustration of turbulent flow over a serrated edge as given in [39].

Through a change of variables $z_1 = y_1 - \zeta(y_3)$ Howe approximated the scattered field to be given by

$$p_s(\boldsymbol{x},\omega) = \frac{i}{2}\int_{-\infty}^{\infty} dy_3 \int_{-\infty}^{0} dz_1 \int_{-\infty}^{\infty} \gamma(K) G(\boldsymbol{x}, z_1 + \zeta(y_3), y_3 : \omega) p_{bl}(\boldsymbol{K},\omega) \times e^{i(K_1 z_1 + K_3 y_3 + K_1 \zeta(y_3))} d\boldsymbol{K} \tag{50}$$

where $K = |\boldsymbol{K}|$, and $\gamma(K) = \sqrt{k_0^2 - K^2}$. The term $p_{bl}$ denotes the source pressure in the boundary layer.

Howe defined the leading-order approximation for the acoustic pressure spectrum as $\propto \sin^2(\theta/2)\Psi(\omega)$ in the far field, where $\theta$ is the standard polar observer angle. If $\Psi_0$ is the spectrum for a straight edge, the spectrum for a serrated edge with $\lambda/h \lesssim 1$ is given by $\Psi_0/(2\pi h/\lambda)$, yielding less noise than the corresponding straight edge, and predicting that sharper serrations (larger $h/\lambda$) will produce less noise. Following this, Azarpeyvand et al. [40] used Howe's method to analytically predict the noise for a wider range of periodically serrated edges.

Upon comparison to experiments, however, Howe's solutions for sawtooth and sinusoidal edges significantly over-predict the noise reduction [40,41]. Therefore Lyu et al. [42] developed a more robust model based on the Schwarzschild solution. To do so, the change of variables $z_1 = x_1 - \zeta(x_3)$ is applied first to the governing equation and boundary conditions, ensuring the boundary condition is now specified in the half-space $z_1 < 0$ as required for the Schwartzchild method. The once simple Helmholtz equation is, however, transformed to a less straight-forward governing equation.

Through a Fourier series expansion in the spanwise coordinate $x_3$, the scattered pressure is given by the infinite series

$$P(z_1, x_2, x_3) = \sum_{n=-\infty}^{\infty} P_n(z_1, x_2) e^{i k_{3n} x_3}, \qquad k_{3n} = k_3 + 2n\pi/\lambda \tag{51}$$

where the wavenumber $k_3$ arises from supposing the acoustic source is a single gust of the form Eq. (17). When decomposed this way, the scattered modes are coupled, and so Lyu et al. developed an iterative method to obtain the approximate solution.[2] His zero-th order solution, assuming the modes are uncoupled, recovers the previous serration solution from Howe. However, after including the modal coupling, Lyu's solution predicts lower (and more realistic) levels of noise reduction versus straight edges.

Whilst Lyu's results are more accurate, the implementation of the iterative method means the process of obtaining solutions is slow. Ayton [43], therefore, developed an alternative method, applicable to any single-valued periodic serration shape. This method too uses the transform $z_1 = x_1 - \zeta(x_3)$, but does not decompose the solution into a Fourier series. Instead, following the Wiener–Hopf method, the streamwise Fourier transform is taken, mapping $z_1 \to \lambda$. In Fourier space, the governing equation is separable so that the scattered pressure may be written as $p = Y(x_2, \lambda)Z(x_3, \lambda)$. A modal solution is found

$$P(x_2, x_3, \lambda) = \sum_{n=-\infty}^{\infty} \frac{E_n(\lambda)\sqrt{-\delta - w_n}}{2i(\lambda + \delta)\sqrt{\lambda - w_n}} \mathrm{sgn}(x_2) e^{-|x_2|\sqrt{\lambda^2 - w_n^2}} Z_n(\lambda, x_3), \quad (52)$$

where $w_n^2 = (k/\beta)^2 - (k_3 + 2n\pi)^2$, and $\delta$ is as defined for the non-serrated case. The modal coefficients $E_n(\lambda)$ are functions of the serration geometry. This expression resembles precisely the scattering from a (straight-edged) half plane, and as serration height $h \to 0$ limits accordingly. The method of steepest descents may be applied to quickly recover the far-field noise for a single frequency gust and thus the overall far-field noise can be calculated rapidly. Either empirical models for boundary layer turbulence (discussed in the next section), or numerical boundary layer data can be input to predict the far-field noise.

Fig. 8 illustrates a comparison of the theoretical serration models [44]; boundary layer data and the appropriate surface pressure spectrum was provided by experimental measurements. Both Lyu and Ayton's models are more accurate than Howe's on predicting the noise reduction for a sawtooth serrated edge on comparison to numerical data, and Ayton's model captures the wider range of frequencies where a noise reduction is observed better than Lyu's model.

### 2.3. Surface pressure spectra

In this section we now discuss the modeling of the surface pressure fluctuations and how to incorporate this with the prior theoretical solutions, allowing us to then utilize the theoretical models to predict noise generated by fully turbulent flows.

#### 2.3.1. General considerations

Suppose the boundary layer turbulence convects with speed $U_c$ and generates the surface pressure $p_{bl}(x_1, x_3, t)$ where $x_1$ is the streamwise direction and $x_3$ the spanwise direction. Implicitly here, $x_2 = 0$ corresponds to the location of the airfoil surface.

The frequency spectrum of this surface pressure, $\Phi_{pp}(\omega)$, is defined by integrating over the wavenumber–frequency spectrum, $\Phi(k_1, k_3, \omega)$, as

$$\Phi_{pp}(\omega) = \int_{-\infty}^{\infty}\int_{-\infty}^{\infty} \Phi(k_1, k_3, \omega) dk_1 dk_3, \quad (53)$$

where

$$\Phi(k_1, k_3, \omega) = \frac{1}{(2\pi)^3}\int_{-T}^{T}\int_{-\infty}^{\infty}\int_{-\infty}^{\infty} E[p_{bl}(x_1, x_3, t), p_{bl}(x_1', x_3', t')] \times e^{i\omega\tau - ik_1\Delta x_1 - ik_3\Delta x_3} d\Delta x_1 d\Delta x_3 d\Delta\tau, \quad (54)$$

where $\Delta x_{1,3}$ and $\tau$ denote the difference between $x_{1,3}$, $t$ and $x_{1,3}'$, $t'$ respectively, $E[\cdot]$ denotes the expected value, and $T$ is some large time.

We wish to find the corresponding frequency spectrum of the scattered noise, $S_s(\omega)$. To do so we consider writing the boundary layer pressure as a double Fourier transform

$$p_{bl}(x_1, x_3, t) = \int_{-\infty}^{\infty}\int_{-\infty}^{\infty}\int_{-\infty}^{\infty} \tilde{\tilde{p}}_{bl}(k_1, k_3, \omega) e^{ik_1(x_1 - U_c t) + ik_3 x_3} dk_1 dk_3 d\omega, \quad (55)$$

thus we may write

$$\frac{\pi}{T} E[\tilde{\tilde{p}}_{bl}, \tilde{\tilde{p}}_{bl}'] = \Phi(k_1, k_3, \omega)\delta(k_1 - k_1')\delta(k_3 - k_3') \quad (56)$$

and equivalently the scattered pressure satisfies

$$\frac{\pi}{T} E[\tilde{\tilde{p}}_s, \tilde{\tilde{p}}_s'] = \Pi(k_1, k_3, \omega)\delta(k_1 - k_1')\delta(k_3 - k_3') \quad (57)$$

where $\Pi(k_1, k_3, \omega)$ is the scattered wavenumber–frequency spectrum.

We have now expressed the boundary layer pressure $p_{bl}$ in terms of components proportional to $P_0 e^{ik_1(x_1 - U_c t) + ik_3 x_3}$ (where we may view $\tilde{\tilde{p}}_{bl}(k_1, k_3, \omega)$ as $P_0$). The prior theoretical derivations, therefore, provide a far-field transfer function, $g$, between $\tilde{\tilde{p}}_{bl}$ and $\tilde{\tilde{p}}_s$ as

$$\tilde{\tilde{p}}_s = g(k_1, k_3, \omega)\tilde{\tilde{p}}_{bl}, \quad (58)$$

thus we can relate the scattered wavenumber–frequency spectrum to the boundary layer wavenumber–frequency spectrum

$$\Pi(k_1, k_3, \omega) = E[g, g']\Phi(k_1, k_3, \omega) \quad (59)$$

and hence the scattered noise is given by

$$S_s(\omega) = \int_{\infty}^{\infty}\int_{\infty}^{\infty} \Phi(k_1, k_3, \omega) E[g, g'] dk_1 dk_3. \quad (60)$$

To obtain the total far-field pressure, one would instead use the transfer function $g_T$ for the total field

$$\tilde{\tilde{p}} = g_T(k_1, k_3, \omega)\tilde{\tilde{p}}_{bl} \quad (61)$$

in the above expressions.

In the case of the Wiener–Hopf method, the scattered transfer function may be read from the derived far-field scattered solution. In the case of Amiet, the provided transfer function is in terms of the total surface pressure jump (thus provides the total noise), and must be radiated to the far-field via Curle's analogy to obtain the total far-field noise.

Whilst we may calculate the transfer function, $g$, from the boundary layer pressure to the far-field scattered noise theoretically, but the question remains; what is $\Phi$? A number of empirical and semi-empirical models have been created over the years to predict $\Phi$, many involving quantities which can only be obtained numerically. The problem of empirical models for $\Phi$ is discussed in Section 3.1.3.

#### 2.3.2. Relating turbulence to surface pressure

Before going into details, it is important to reflect on some key aspects of the physics involved. The goal here is to provide an input for the solution of the scattering problem, in form of a wall-pressure spectrum, such that the far-field acoustic spectrum can be related with measurable quantities of the hydrodynamic turbulent boundary layer flow. A distinction between hydrodynamic and acoustic quantities is made here. In essence, the turbulence within the boundary layer and the wall-pressure fluctuations that it creates can be described in the context of an incompressible fluid flow. In other words, the compressibility of the medium, which is a prerequisite for the existence of sound waves, does not play a role in this part of the mechanism. It is the interaction of these hydrodynamic fluctuations (denoted as the incident pressure field in Section 2.1.3 or $p_{bl}$ in the previous section) with the trailing edge that produces these sound waves, as a by-product through the scattering mechanism. Furthermore, it is fair to assume that the resulting sound waves do not have any impact back on the hydrodynamic flow that creates them in most cases.[3]

[2] This iterative method is not for inclusion of backscattering effects, but for Fourier mode coupling, which is a specific feature of a serrated edge.

[3] In the context of trailing-edge noise at relatively high Reynolds numbers as it is the case for most industrial applications, there is no feedback mechanism from the acoustic waves onto the boundary layer flow. However, this

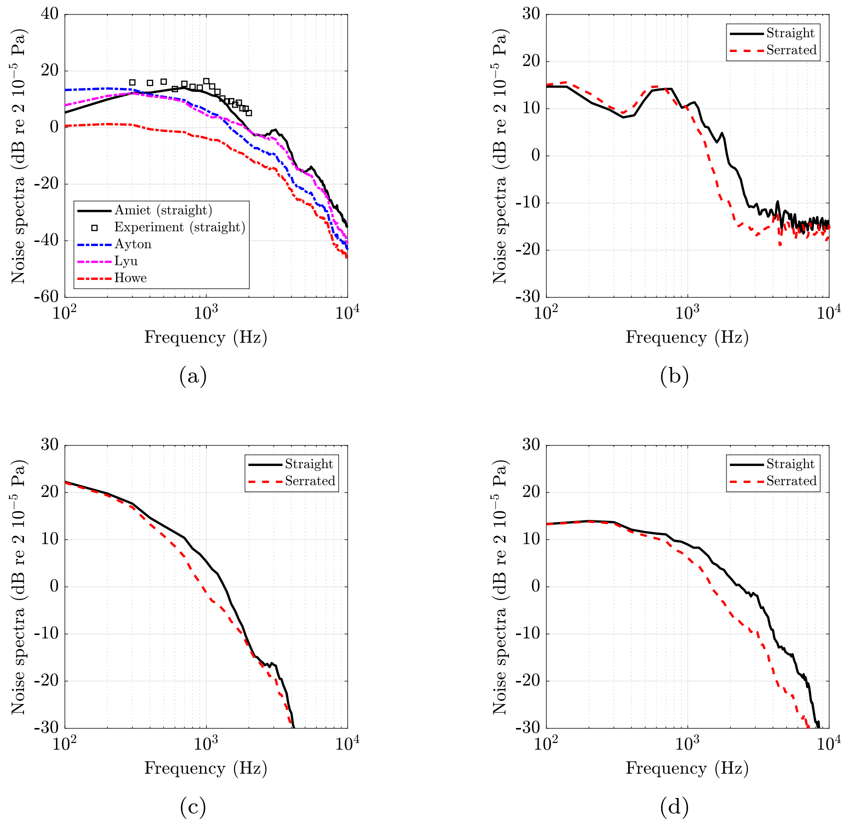


**Fig. 8.** Trailing-edge noise predictions on the CD airfoil with straight and serrated edges [44]: (a) comparison of all analytical models for serrations with ECL experimental data [45] and Amiet's model for a straight edge, (b) Direct numerical simulation,(c) Lyu's model, and (d) Ayton's model.

The basic idea behind the estimation of a wall-pressure spectral model is originally proposed by Kraichnan [49]. The first assumption consists in a simplification of the problem to the case a turbulent boundary layer over a flat plate, homogeneous in the direction of the flow. It may be argued that this is over-simplified. But as long as the airfoil is not highly cambered and the main flowfield is relatively smooth and not largely influenced by the presence of the trailing edge itself, it may be acceptable in the trailing-edge region. It is further assumed that the flow is incompressible, and that second-order turbulence–turbulence interactions are negligible. Under these assumptions, a 1D-differential equation for the turbulence pressure fluctuations within the turbulent boundary layer can be derived:

$$\frac{\partial^2 \tilde{\tilde{p}}_{bl}}{\partial x_2^2} - \lambda^2\, \tilde{\tilde{p}}_{bl}(k_1, x_2, k_3, \omega) = -2\rho\, \mathrm{i} k_1 \frac{\partial U_1(x_2)}{\partial x_2} \tilde{\tilde{u}}_2(k_1, x_2, k_3, \omega) \tag{62}$$

where the subscripts 1 and 3 refer to the direction parallel to the wall, along the flow and transverse to the flow respectively, and 2 to the direction perpendicular to the wall as shown in Fig. 3. $\lambda = \sqrt{k_1^2 + k_3^2}$ is the norm of the wavenumber vector spanning the plane parallel to the wall, $U_1(x_2)$ is the mean velocity across the boundary layer. The quantities $\tilde{\tilde{p}}_{bl}$ and $\tilde{\tilde{u}}_2$ are wavenumber–frequency spectral functions for the pressure and vertical velocity component, respectively at the distance $x_2$ from the wall. It is relatively easy to find a solution for the above equation (e.g. using Green's functions formalism as in appendix B of [50] or the method of variation of parameters as in appendix A of [51]), in particular on the wall surface, as:

$$\tilde{\tilde{p}}_{bl}(k_1, x_2 = 0, k_3, \omega) = 2\rho\, \frac{\mathrm{i} k_1}{\lambda} \int_0^{\delta} \frac{\partial U_1(x_2)}{\partial x_2}\, \tilde{\tilde{u}}_2(k_1, x_2, k_3, \omega)\, \mathrm{e}^{-\lambda |x_2|}\, \mathrm{d}x_2 \tag{63}$$

where $\delta$ is the boundary layer thickness and $x_2 = 0$ represents the surface location. Using ensemble average of the product of the previous equation by its complex conjugate yields a general solution for the wall-pressure spectrum [51–53]:

$$\begin{aligned}\Phi(k_1, k_3, \omega) \;=\; & 4\rho^2 \frac{k_1^2}{\lambda^2} \iint_0^{\delta} \frac{\partial U_1(x_2)}{\partial x_2} \frac{\partial U_1(x_2')}{\partial x_2}\, \varphi_{22}(k_1, x_2, x_2', k_3, \omega) \\ & \times \mathrm{e}^{-\lambda(x_2 + x_2')}\, \mathrm{d}x_2\, \mathrm{d}x_2'\end{aligned} \tag{64}$$

where $\varphi_{22}$ is the cross-spectrum of the vertical velocity fluctuations defined as:

$$\begin{aligned}&\varphi_{22}(k_1, x_2, x_2', k_3, \omega)\, \delta(k_1 - k_1')\, \delta(k_3 - k_3')\, \delta(\omega - \omega') \\ &\quad = E[\, \tilde{\tilde{u}}_2(k_1, x_2, k_3, \omega)\, \tilde{\tilde{u}}_2(k_1, x_2', k_3, \omega)\,]\end{aligned}$$

Note here that the dependence on $\omega$ and $k_1$ is often merged into one of these two variables by assuming frozen turbulence, which can be expressed as $K_c = \omega / U_c$ where $U_c$ is the convection velocity of wall-pressure turbulent fluctuations. A frequency spectrum for the wall-pressure fluctuations can then be obtained as [51]:

$$\Phi_{pp}(\omega) = \left( \int_{-\infty}^{+\infty} \Phi(K_c, k_3)\, \mathrm{d}k_3 \right) / U_c \tag{65}$$

where $\Phi$ on the right-hand side must be here interpreted as the wavenumber spectrum of the frozen turbulent surface pressure field, thus not depending on time. Semi-empirical or empirical models of $\Phi_{pp}(\omega)$ as well as their validity in trailing-edge noise will be presented

may occur for more sensitive aspects of the incompressible flowfield, such as laminar boundary layer instabilities [46–48].

in section 3.1.3. Panton and Linebarger [52] proposed to compute the cross-spectrum of vertical velocity fluctuations $\varphi_{22}$ in Eq. (64) as the double spatial Fourier transform of the normalized correlation coefficient in the plane defined by the wall $R_{22}$:

$$\varphi_{22}(k_1, x_2, x_2', k_3, \omega) = \frac{\sigma^2}{4\pi^2} \iint_{\infty}^{+\infty} R_{22}(r_1, r_2, r_3) \cos(k_1 r_1) \cos(k_3 r_3) \, \mathrm{d}r_1 \, \mathrm{d}r_3 \tag{66}$$

where $\sigma^2 = \sqrt{\overline{u_2^2}(x_2)\,\overline{u_2^2}(x_2')}$ and $r_i = |x_i - x_i'|$. A quintuple integration is then needed to compute the frequency spectrum of the wall-pressure fluctuations $\Phi_{pp}$ from Eqs. (64), (65) and (66). This can be achieved by a Monte Carlo method. Note that Grasso et al. showed that Eq. (66) can be reduced to a single integral (appendix A in [51]) yielding an even more efficient integration. Remmler et al. [53] successfully applied this more general method to flat plate and airfoil turbulent boundary layers.

Blake [54] provided some simplifications on the estimation of several parameters in Eq. (64), mainly concerning correlation between $u_2$ at two positions $x_2$ and $x_2'$ across the boundary layer (namely $R_{22}(r_1, r_3, x_2, x_2') = 0$ for $x_2 \neq x_2'$), as well as relaxing the hypothesis of frozen turbulence. The final result reads:

$$\Phi(k_1, k_3, \omega) = 4\rho^2 \frac{k_1^2}{\lambda^2} \int_0^{\delta} \left( \frac{\partial U_1}{\partial x_2}(x_2) \right)^2 L_2(x_2)\, \overline{u_2^2}\, \Phi_{22}(k_1, k_3) \times \Phi_m\big(\omega - U_1(x_2)\, k_1\big)\, \mathrm{e}^{-2\lambda x_2}\, \mathrm{d}x_2 \tag{67}$$

where $\Phi_{22}$ is the (normalized) diagonal term of the turbulence spectrum tensor corresponding to the direction perpendicular to the wall, and $\Phi_m$ is the moving-axis spectrum tensor characterizing the distortion of $\Phi_{22}$ during convection, and $L_2$ is the correlation length of the $u_2$ velocity fluctuation component in the direction perpendicular to the wall. It is found that $\Phi_m$ can be considered as a Dirac delta function (which is the equivalent to the frozen turbulence assumption) without significantly modifying the quantitative results in most cases. Note that the assumption on the normalized correlation coefficient, $R_{22}$, should be revised in the future as the recent high-fidelity LES and DNS presented in Sections 3.2 and 3.3 show that it does not hold (see Fig. 12 in [51]).

### 2.4. Outlook

Theoretical models remain a fruitful area of interest for understanding and controlling trailing-edge noise. Despite simplifications, their ability to swiftly predict the scattered noise over a wide parameter sweep aids in understanding noise-control mechanisms and can be used to design optimally quiet configurations, such as the ogee-shaped serration proposed by Lyu et al. [55], or the optimal iron-shape proposed by Avallone et al. [56]. As shown in Section 3.4, Kholodov and Moreau [57–59] further performed an optimization of the serration shape including slits based on the CD airfoil flow characteristics with and without aerodynamic constraints. Such an optimization could be generalized to other airfoil shape with additional flow or structural constraints for instance.

For straight trailing edges, Amiet's model [19] remains popular to this day due on the one hand to its simplicity and on the other hand to its flexibility. The model can be easily adapted for any surface pressure spectrum, either one modeled empirically or one determined experimentally or numerically. Inclusion of the backscattering correction by Roger and Moreau [20] extended Amiet's model and improved accuracy for low-frequency noise, ensuring the continued use of this model for quick trailing-edge noise prediction. Further extensions also include the effect of sweep to account for more general airfoil shapes [60].

For bio-inspired trailing edges, such as those with spanwise serrations or poroelasticity, new theoretical models have been produced over recent years which, like Amiet's model, can be used in conjunction with any surface pressure spectrum. Additionally, for edges with complicated surface conditions (acoustic liners/porosity/canopies etc.), theoretical work stemming from complex analysis has produced new rapid numerical tools [28,32] capable of predicting trailing-edge noise from these edges, and, hence, the possibly noise reduction versus a standard rigid impermeable edge. It is hoped these new developments prove as useful as Amiet's model for the continued study of trailing-edge noise, and can aid in the development of optimally quiet edges. A current unknown for this analysis, however, is the effect the altered surface has on the turbulent source and importantly the surface pressure spectrum.

## 3. Numerical approach

### 3.1. Empirical and semi-empirical models

In this section, a series of trailing-edge noise models based on different flow turbulence and noise scattering theories are reviewed. Their common feature is the fact that they are based on a number of geometrical and physical assumptions, and empirical tuning is used to various extents for most of them. These methods have been extensively used in the industry and research community alike as they are typically less computationally demanding than more advanced methods (see Sections 3.2 and 3.3).

#### 3.1.1. BPM model

One of the most popular and successful model for trailing-edge noise for the last 30 years is the so-called BPM model, denoted as such from the initials of the authors of the original report describing the methodology, namely Brooks, Pope and Marcolini [46]. This work was conducted in the perspective of earlier works on the subject (see e.g. [61,62]) as it was recognized that more accurate noise prediction models were required for the rapid developments in aeronautics.

In brief, the model is based on spectral scalings of various airfoil self-noise mechanisms[4] originating from theoretical results. Then, the model is tuned using an exhaustive experimental data set acquired in an anechoic wind tunnel. This data set consists of measurements of NACA0012 airfoil blade sections of different sizes and in various configurations that reproduce the various noise mechanisms and their dependencies to different physical parameters (such as the angle of attack). The measurement campaign also includes boundary layer flow measurements that contribute to characterize the boundary layer turbulence in these various configurations. The remaining of the present discussion on the BPM model concentrates on trailing-edge noise only. The derivations below are an abridged version of the actual model, only intended here to explain the methodology. The model implementation is detailed very accurately in the publicly available original report [46] and the latter should be used as reference if the reader wishes to implement it.

The basis for the BPM trailing-edge noise model is a scaling of the noise scattering of boundary layer turbulence by a sharp edge originally developed by Ffowcs Williams and Hall [6] (see Section 2.1.1 for more details). This analysis uses the well-known Lighthill analogy as a starting point for the derivation of a solution for the trailing-edge scattering problem. It is established that the acoustical power at an observer position located at a distance $r$ from the trailing-edge does scale as:

$$\langle p^2 \rangle \propto \rho^2 v'^2 \frac{U_c^3}{c_0} \frac{L\Lambda}{r^2} \overline{D} \tag{68}$$

where $\rho$ is the medium mean density, $v'^2$ the mean-square of turbulence velocity fluctuations, $U_c$ the convection speed of the turbulent vortices

[4] In addition to trailing-edge noise, the BPM model can predict vortex-shedding noise from laminar boundary layer instability and from a blunt trailing edge, separation-stall noise as well as tip noise.

passing by the trailing-edge, $c_0$ the speed of sound, $L$ the spanwise length of the emitting airfoil section, $\Lambda$ a characteristic turbulence length scale, and $\overline{D}$ a directivity factor depending on the observer position relative to the trailing-edge.[5] The quantities $v'^2$ and $\Lambda$ are a priori unknown. They are assumed to be linearly correlated with the boundary layer characteristics, that is the convection velocity $U_c$ and the boundary layer displacement thickness $\delta^*$, respectively.[6] Note that $U_c$ is proportional to the free-stream velocity $U$ and that $\delta^*$ is measured during the experimental campaign mentioned earlier. As a side comment, it is noteworthy that the above analysis yields this important general result: trailing-edge noise scales with the 5th power of the fluid velocity. Such a result can also be recovered rigorously from Amiet's model, Eqs. (30) and (33), at high frequencies and low Mach number:

$$S(\omega) \propto \langle p^2 \rangle \simeq \overline{D}\, St^{-5}\, L\, M^5\, \delta^*$$

with the Strouhal number $St = f\delta^*/U$. This corresponds to a non-compact dipole.

From the above derivation, the rationale behind the model is that a scaling law for the Sound Pressure Level (SPL) spectra in 1/3 octave bands for the trailing-edge noise, denoted as Scaled-$SPL_{1/3}$, can be written as:

$$\text{Scaled-}SPL_{1/3} = SPL_{1/3} - 10\log\left(M^5 \frac{\delta^* L\overline{D}}{r^2}\right) \tag{69}$$

where $M = U/C_0$ is the inflow Mach number. In the above equation, the logarithmic term stems directly from the proportionality formula of Eq. (68).

Furthermore, this scaled spectrum is in principle (at least within the limits of validity of the theoretical derivations and assumptions above) representative of trailing-edge noise independently of flow conditions and airfoil configurations. Thus, it is assumed that the scaled spectrum takes the following form:

$$\text{Scaled-}SPL_{1/3} = F(St) + K \tag{70}$$

where $F$ is a universal spectral shape function of the Strouhal number $St = f\delta^*/U$, and $K$ an empirical constant. The experimental data are used to precisely define $F$ and $K$ so that the model can reproduce the measured spectra.

An elaborate analysis of the measurement data based on the previous considerations (which is out of the scope of the present review, thus not reported here) leads to a fine-tuned model. Its main attributes are:

- 3 contributions for the overall model are distinguished: a suction side and a pressure side boundary layer contribution, as well as a contribution accounting for the effect of the angle of attack,
- the dependence on the Strouhal number is scaled so that the measured peak Strouhal numbers (i.e. where the spectra reach their maximum values) are used to tune the universal spectral shapes,
- for the above scalings, Strouhal numbers based on the boundary layer from the suction and pressure sides are separately defined depending on the considered contribution.

The spectral power of the 3 separate contributions must be added in order to recover the overall emitted power spectrum using the following formula:

$$SPL_{\text{TOT}} = 10\log\left(10^{SPL_s/10}\right) + 10\log\left(10^{SPL_p/10}\right) + 10\log\left(10^{SPL_\alpha/10}\right)$$

where the 3 terms on the right-hand sides correspond to contributions from the suction side, pressure side and angle of attack, respectively. The 3 SPL spectra $SPL_s$, $SPL_p$ and $SPL_\alpha$ can be expressed using Eqs. (69)–(70) for which the function $F$ and the constant $K$ are tuned using the analysis mentioned above. The angle of attack part or $SPL_\alpha$ was referred as separation noise in the BPM paper, and it was treated separately from trailing-edge noise. However, this separation is confusing to readers since this term should be considered as a part of trailing-edge in a physical sense; it is a contribution to trailing-edge noise from a non-zero angle of attack. The main part of the calculation procedure for the model can be summarized with these 3 formulas for each contribution:

$$SPL_s = 10\log\left(\frac{\delta_s^* M^5 L\overline{D}}{r^2}\right) + A\left(\frac{St_s}{St_1}\right) + (K_1 - 3) + \Delta K_1$$

$$SPL_p = 10\log\left(\frac{\delta_p^* M^5 L\overline{D}}{r^2}\right) + A\left(\frac{St_p}{St_1}\right) + (K_1 - 3)$$

$$SPL_\alpha = 10\log\left(\frac{\delta_s^* M^5 L\overline{D}}{r^2}\right) + B\left(\frac{St_p}{St_2}\right) + K_2$$

where $\delta_s^*$ and $\delta_p^*$ are displacement thicknesses on the suction and pressure sides, respectively. The Strouhal numbers $St_s$ and $St_p$ are defined accordingly. The functional forms $A$ and $B$ stand for the previous function $F$, but these are defined differently for the suction/pressure sides and angle of attack dependency contributions. Two different tuning parameters $K_1$ and $K_2$, as well as two different tuning parameters $St_1$ and $St_2$ for the Strouhal scalings are also defined. The latter parameters are tuned depending on a number of physical parameters, such as Reynolds number, angle of attack, etc. The actual procedure and implementation of the BPM model is quite intricate and the reader is referred to the original report [46] for details.

To close the model, a number of input data are required to calculate the immission noise spectra in the previous formulas. In addition to obvious quantities such as the airfoil geometry, the observer position to calculate the directivity factor, and the atmospheric conditions (e.g. yielding the speed of sound), the required information amount to: the inflow velocity, the displacement thicknesses near the trailing-edge on both suction and pressure sides and the angle of attack. These latter quantities are typically calculated using an airfoil flow solver such as the panel code XFOIL [63] or any CFD-RANS code, or possibly experimental data in certain cases.

Examples of the predictions obtained using the Brooks et al. [46] method converted to PSD are given in Figs. 9 and 10 compared against the spectrum measured at the University of Southampton at a single microphone located 1 m and 90 degree to the trailing edge of a NACA 0012 airfoil with 0.45 m span and 0.15 m chord [66]. Fig. 9 shows the comparison at a flow speed of 17.1m/s and AoA = 0° and 35.5 m/s and AoA = 15°. Agreement is generally good except at the highest speed below about 1 kHz where jet noise dominates. A distinguishing feature in these spectra is the presence of a number of narrow peaks distributed over a broad hump, which the Brooks et al. [46] scheme in the 1/3 octave bands is unable to capture. The noise spectra for the tripped turbulent boundary layer is generally lower than for the untripped case at the same flow speed, since the rms velocities in the turbulent boundary layer are generally less than that due to the unstable modes in the laminar boundary layer. As the BPM model provides only 1/3 octave band predictions, the comparison of the trailing-edge

[5] The spatial shape of the directivity factor is varying with frequency. It has the form of a classical dipole directivity pattern toward low frequencies, reaching its maximum directly above the trailing edge and being 0 in the airfoil plane. Toward higher frequencies, it progressively takes the general form of a cardioid with a maximum when looking from the region upstream of the airfoil, slowly decreasing when moving to the position above the trailing edge, and more rapidly going to 0 when moving back in the airfoil plane but in the downstream direction. Note however the existence of complex spatial patterns with multiple lobes also varying with frequency (see e.g. Fig. 22(b)).

[6] In the original analysis of Ffowcs Williams and Hall [6], the boundary layer thickness is used to evaluate the turbulence length scale, but in the BPM model, better scaling laws can be established using the displacement thickness instead.

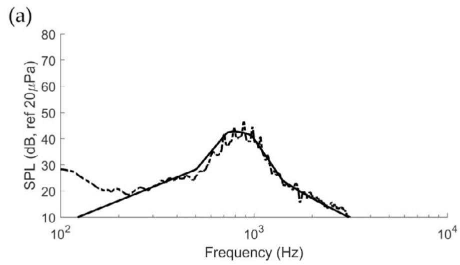


**Fig. 9.** Comparison of measured (dash lines) and BPM-predicted (solid lines) Sound Pressure Level Spectra for an untripped NACA 0012 airfoil at (a) 20 ms$^{-1}$ flow speed at 0° effective AoA [64], and (b) 80 ms$^{-1}$ flow speed at 2.8° effective AoA [65].

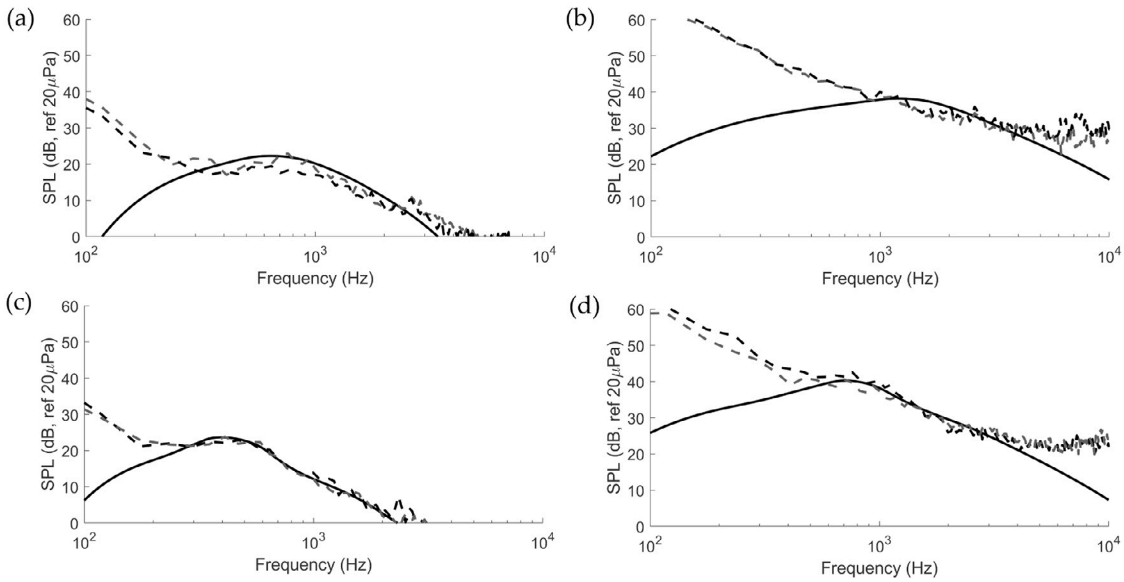


**Fig. 10.** Comparison of measured (dash lines) and BPM-predicted (solid lines) Sound Pressure Level Spectra for a tripped NACA 0012 airfoil at (a) 16.5 ms$^{-1}$ flow speed at 1.4° effective AoA, (b) 47.0 ms$^{-1}$ flow speed at 1.4° effective AoA, (c) 13.3 ms$^{-1}$ flow speed at 4.2° effective AoA, and (d) 36.5 ms$^{-1}$ flow speed at 4.2° effective AoA.
*Source:* All the spectra are taken from Chong et al. [66].

noise spectra for the tripped boundary layer case compares less well since oscillations in the spectrum arising from interference between coherent sources along the chord cannot be captured by the 1/3 octave prediction. The increase in noise at frequencies above 10 kHz at the flow speed of 35.1 m/s was due to an issue with side plates, which has since been resolved.

It is clear that the present BPM model relies on a number of assumptions that do restrict its validity. In particular, the tuning procedure is based on measurements of the NACA0012 airfoil shape only. It is implicitly assumed that the trailing-edge noise is solely driven by the measured boundary layer displacement thickness and the angle of attack dependency for that specific airfoil. Consequently, using different airfoil shapes may compromise its accuracy, e.g. if the airfoil shape has important effects on both attributes at the same time that do not resemble what is observed for the NACA0012 airfoil. Nevertheless, as mentioned earlier, this model has been a reference for a long period of time for predicting trailing-edge noise in many applications, which will be discussed in more detail in Section 5.

### 3.1.2. TNO model

The methodology described in the previous section relates directly, through scaling laws, some global flow and boundary layer characteristics to the far-field noise as a result of the turbulence scattering process occurring at the trailing-edge. It is expected that more accurate models can be obtained if, instead of using scaling laws and empirical tuning, the model is built upon a more detailed description of the physical processes involved. The proposed strategy consists in modeling separately the turbulent fluctuations within the boundary layer and their effects on the wall-pressure near the trailing-edge on one side, and their scattering by the trailing-edge into sound waves on the other.

Theoretical aspects of the trailing-edge scattering mechanism have been discussed in detail in Section 2 and analytical solutions have been established in Eqs. (30) and (32) as the so-called Amiet's and Howe's model, respectively. The remaining step consists in defining the wall-pressure turbulent fluctuations, or more precisely their frequency–wavenumber power spectrum denoted as $\Phi$ in these equations, in the vicinity of the trailing-edge. Preliminary discussions about its specificities and some theoretical aspects for its derivation are provided in Section 2.3. However, the closure of the wall-pressure spectral model is not completed yet. For instance, the flow and turbulence physical quantities in Eq. (67) remain to be defined in order to obtain its numerical evaluation. There exists a large variety of options for obtaining a self-contained model for the wall-pressure spectrum, but these can be divided into two main categories:

- Models based on quantitative information about the turbulence characteristics within the boundary layer flow combined with a theoretical analysis providing an estimation of the wall-pressure spectrum,
- Empirical models for the wall-pressure spectrum tuned to fit experimental data.

The present section is only concerned with the former approach, while the latter is dealt with in the following Section 3.1.3. Note that boundary layer turbulence is a whole area of research in itself and the derivations detailed below for obtaining a wall-pressure spectral model following the former approach also contain a certain degree of empiricism. Therefore, this type of approach is denoted as 'semi-empirical'.

The first functional model combining scattering theory with a semi-empirical definition of the wall-pressure spectrum is introduced by Parchen et al. [67]. It is commonly referred to as the TNO model because the authors worked at that time at the Dutch research institute of the same name. A RANS-CFD solver is used to calculate relevant quantities of the turbulent boundary layer, which are used as inputs to the wall-pressure model derived by Blake [54] introduced earlier in Eq. (67). Howe's trailing-edge diffraction theory [3] is used for the scattering part, although a simplified version of the analytical solution in Eq. (32) proposed by Brooks and Hodgson [68] is used instead. In its original version, this model has a tendency to underestimate trailing-edge noise [69] and these discrepancies can be mainly attributed to the assumptions made to evaluate the different turbulent quantities in Blake's Eq. (67) [70].

Subsequently, the TNO model has been derived into a variety of flavors depending on the choice of the flow solver (XFOIL or CFD, see discussion below) used to compute the boundary layer flow at the trailing edge. Various assumptions and derivations are also proposed in the literature for evaluating the different turbulent quantities that appear in the wall-pressure model in order to close it and remedy the above-mentioned discrepancies. Finally, the choice of the scattering theory (i.e. Amiet or Howe, see Section 2) also varies depending on the different contributions in this field. These different options are discussed below.

To begin with, the choice of the flow solver is discussed. The XFOIL flow solver has been used for decades to predict low-Mach airfoil flows in free field with success [63]. It is limited to subsonic flows, but can handle low to high Reynolds numbers. As output, this code provides global quantities such as displacement and momentum thicknesses around the airfoil profile, from which the boundary layer thickness at the trailing edge can be derived. Furthermore, the boundary layer average velocity profile $U_1(x_2)$ can be calculated using a standard turbulent boundary layer theory such as Cole's law [71] or improved versions of it [72]. Note here that there also exist improved versions of XFOIL, such as RFOIL [73] and XFLR5/QBlade [74], that increase its range of validity. If using a CFD solver, all the above quantities are readily available, although a precise evaluation of the boundary layer thickness can be tricky. Nevertheless, this does not significantly affect the results since the turbulent energy content in the outer part of the boundary layer is small and its contribution to the noise emission is minor.

Once the average flow quantities have been determined, the more sensitive turbulence characteristics, namely $\overline{u_2^2}$, $L_2$ and $\Phi_{22}$ in Eq. (67), must be evaluated. Concerning the turbulent shear stress perpendicular to the airfoil, it can be directly related to the turbulent kinetic energy as $\overline{u_2^2} = \alpha\, k_t$ where the factor $\alpha$ is usually assumed constant and equal to 0.45 and 0.3 on the suction and pressure sides, respectively [67]. Using the CFD-RANS code, $k_t$ is readily available across the boundary layer. Using XFOIL, it must be derived using approximations from a turbulent boundary layer theory. The turbulent kinematic viscosity as used in RANS models is defined by:

$$\nu_t = C_\mu \frac{k_t^2}{\epsilon}$$

where $\epsilon$ is the turbulent energy dissipation rate, and the constant $C_\mu$ is estimated equal to 0.09. Assuming turbulent energy equilibrium in an isotropic homogeneous turbulent flow yields:

$$\epsilon = -\overline{u_1' u_2'}\,\frac{\partial U_1}{\partial x_2}$$

where $\overline{u_1' u_2'}$ is the cross-velocity Reynolds turbulent shear stress. Combining the Boussinesq hypothesis:

$$\overline{u_1' u_2'} = -\nu_t \frac{\partial U_1}{\partial x_2}$$

with the two previous equations provides the following approximation for the turbulent kinetic energy:

$$k_t = \sqrt{\left(\nu_t \frac{\partial U_1}{\partial x_2}\right)^2 / C_\mu} \tag{71}$$

as proposed by Parchen [67]. Independently, combining the Boussinesq hypothesis for the Reynolds turbulent stresses and Prandtl's hypothesis yields:

$$\nu_t = l_m^2 \left| \frac{\partial U_1}{\partial x_2} \right| \tag{72}$$

Finally, the mixing length scale in Eq. (72) is estimated across the boundary layer using Schlichting's expression:

$$l_m(x_2) = 0.085\,\delta \tanh\left(\frac{\kappa\, x_2}{0.085\,\delta}\right)$$

with $\kappa = 0.41$, which can in turn be used to evaluate Eq. (71).

The turbulence correlation length $L_2$ can be approximated from the mixing length scale as:

$$L_2 = l_m/\kappa \tag{73}$$

which is an obvious choice if using XFOIL. This expression was also used in the original TNO model. However, a RANS solver also provides the turbulence dissipation rate $\epsilon$ across the boundary layer. This can be related to a time scale of the turbulence and subsequently to a length scale. Accordingly, Lutz et al. [69] proposed a more elaborate derivation assuming isotropy and using the characteristics of Kolmogorov turbulence spectrum in the inertial range, yielding the following approximation:

$$L_2 \approx 0.387\,\frac{k_t^{3/2}}{\epsilon}$$

which appears to improve the model predictions compared to the simpler formula in Eq. (73) [70]. Moreover, Grasso et al. [51] also noted that the Prandtl theory underestimates the correlation length $L_2$ when comparing to DNS data on airfoils as described in Section 3.3 (Fig. 13 (a) in [51]). In Fischer et al. [75], the cross-correlation $R_{22}$ between various boundary layer vortex sheets is not merged into a single quantity $L_2$, but a correlation function is introduced yielding to a double integral over $y$ as in Eq. (64) as originally proposed by Panton and Linebarger [52], which improves the results at low frequencies.

Finally, the spectral tensor diagonal component for the turbulent velocity fluctuations perpendicular to the wall $\Phi_{22}$ stems from a classical turbulence spectral theory. Assuming isotropy and using the Von Kármán energy spectrum yields the following turbulent stress tensor component:

$$\Phi_{22}(k_1, k_3) = \frac{4}{9\pi k_e^2} \cdot \frac{(k_1/k_e)^2 + (k_3/k_e)^2}{[1 + (k_1/k_e)^2 + (k_3/k_e)^2]^{7/3}}$$

where $k_1$ and $k_3$ are the wavenumbers along the airfoil chord and span, respectively, and $k_e$ is the wavenumber of the energy-containing eddies which is the inverse of the outer integral length scale $L$. The latter may be related to the correlation length $L_2$ along the perpendicular to the wall as:

$$k_e = 1/L = 0.7468/L_2$$

from an analysis of the Von Kármán spectrum in the energy-containing and inertial ranges for isotropic turbulence [76]. Note that the comparison with DNS on airfoils performed by Grasso et al. [51] suggested that the Rapid Distortion Theory (RDT) spectrum might even be a better choice (Fig. 12 in [51]).

However, turbulence anisotropy appears to play a significant role in the correct evaluation of the wall-pressure spectra. Following the approach of Panton and Linebarger [52], it is assumed that the effect of anisotropy can be accounted for by distorting the previous spectral tensor component independently in the 2 wavenumber directions, yielding the following stretched tensor:

$$\Phi_{22}(k_1, k_3, \beta_1, \beta_3) = \frac{4\,\beta_1\beta_3}{9\pi k_e^2} \cdot \frac{(\beta_1 k_1/k_e)^2 + (\beta_3\, k_3/k_e)^2}{[1 + (\beta_1 k_1/k_e)^2 + (\beta_3\, k_3/k_e)^2]^{7/3}}$$

Several models have been proposed for defining the stretching parameters $\beta_1$ and $\beta_3$ [53,77–79]. From DNS data in the adverse pressure gradient zone near the trailing edge, Grasso et al. [51] has recently deduced the ratio of the streamwise to transverse integral length scales (Fig. 13 (b) in [51]).

In more recent works, the influence of the turbulence–turbulence interaction is investigated [51,80], the latter being always neglected compared to the contribution of the mean shear–turbulence interaction in earlier works.

Attempts have been made to assess the accuracy of the TNO modeling approach relatively to simpler (e.g. BPM) or more advanced (e.g. LES or CAA related) methods. Two of these attempts are reported here. The first case was conducted in the context of wind turbine airfoils [81]. Two different (although relatively close to each other) airfoil designs were measured successively in the same acoustic wind tunnel. Thus, in addition to absolute noise levels, the trends between the two airfoil noise levels were also investigated in order to evaluate the sensitivity of the models to these relatively small changes in the geometric parameters. Two TNO-type approaches were compared with the BPM model and a more advanced model. The main conclusions from this study are that none of the modeling approaches can reach the level of accuracy required for wind turbine design, although there are also uncertainties in the measured data themselves. Consequently, wind tunnel noise measurements in combination with modeling are still both required for the purpose of wind turbine design. The second case is a longer term effort conducted as part of the BANC project [82–84]. Here, a number of experimental data sets acquired in two different wind tunnels with three measurement techniques are considered. This provides an error estimate for the acoustic measurements themselves, as illustrated by the error bars in Fig. 11. In addition, the study also focused on the turbulent boundary layer parameters, which are critical for trailing-edge noise emissions as discussed earlier. TNO-type models were compared with more advanced modeling approaches (hybrid-CAA and Lattice-Boltzmann) during the successive benchmark exercises. It appears that advanced methods perform better in most cases, showing that the TNO-type models should be further improved to reach the level accuracy required for engineering applications.

To conclude this section, it is noted that, so far, TNO model implementations have used either a simplified flow solver, such as XFOIL, or more advanced RANS codes in order to evaluate the turbulent boundary layer quantities above the trailing-edge. Nevertheless, more advanced simulation tools, e.g. LES or DNS (see Sections 3.2 and 3.3), could be applied here to collect the necessary information about the boundary layer turbulence to close the TNO model formulation or its generalized version based on Panton and Linebarger's formulation.

### 3.1.3. Wall pressure spectrum model

The wall pressure spectrum near the trailing edge is an important input to Howe's model [91] and Amiet's model [19] (see Section 2). This wall pressure spectrum can be computationally obtained using empirical or semi-empirical models. In fact, Amiet used an empirical wall pressure spectrum model, which was developed based on the measurement of Willmarth and Roos [92]. In a scientific community, an empirical model refers to functional forms, which do not necessarily have physical grounds, with several coefficients that are determined through the match with experimental data while a semi-empirical model refers to functional forms that are derived based on embedded relevant physics along with empirically determined coefficients. Even though there is a subtle difference in the definition between an empirical model and a semi-empirical model, we do not distinguish the difference between the two when it comes to wall pressure spectrum models in the current paper. In fact, some researchers named empirical models and others named semi-empirical models although the functional forms are essentially the same. It is important to note, when this wall pressure spectrum model is used in conjunction with Howe's model or Amiet's model, it represents an incident wall pressure spectrum, which is not affected by a trailing edge. In other words, the acoustic models solve the scattering of this wall pressure spectrum by a trailing edge so that this wall pressure spectrum should not include the scattered part. However, it would be challenging in the measurement and compressible high-fidelity LES or DNS simulations to distinguish the incident wall pressure spectrum from the scattered wall pressure spectrum near the trailing edge. A filtering approach in the wavenumber domain [44,93,94] is one way to separate the wall pressure fluctuations from scattered acoustic pressure fluctuations.

Fig. 12 shows typical measurements on the suction side surface pressure spectra normalized by the square of the dynamic pressure $q_0 = \frac{1}{2}\rho U^2$ for a NACA 65(12)-10 airfoil at 5% chord upstream of the trailing edge at flow speeds of 20 and 40 m/s at the four geometric angles of attack of 0°, 5°, 10° and 15° [41]. The frequency is normalized by the outer scale $\omega\delta^*/U$ and inner scales $\omega\nu/u_\tau$ respectively, where $\delta^*$ is the boundary layer displacement thickness, $\nu$ is the kinematic viscosity and $u_\tau$ is the friction velocity. All boundary layer parameters were estimated using the airfoil panel code XFOIL.

In the low frequency range, $\omega\delta^*/U < 1$, the spectra obtained at the different flow speeds and AoA's collapse when plotted against frequency normalized on the outer scale $\delta^*$, suggesting that low frequency hydrodynamic pressure fluctuations are generated by the larger scales of boundary layer turbulence. In the high frequency range, $\omega\nu/u_\tau > 2$, the spectra collapse to within 5 dB when normalized on inner scales, which is consistent with similar studies on airfoil boundary layers, such as by Garcia-Sagrado and Hynes [95], suggesting that the small-scale of turbulence is the cause of high frequency hydrodynamic pressure fluctuations and high frequency noise. This characteristics of the boundary layer pressure will be shown further in Section 4.2 of the "trailing-edge noise reduction" to have significance in the understanding of the use of surfaces (canopies) within the boundary layer aimed at reducing airfoil self-noise.

We note in Fig. 12 that different parts of the spectra follow the different frequency power laws, $f^1, f^{-1}, f^{-2.5}$ and $f^{-5}$. Similar variations with frequency have also been found on the CD airfoil [26]. They are exploited below to derive empirical expressions for the surface pressure boundary layer spectrum for use in trailing-edge noise prediction models. This frequency scaling will be applied again in Section 4.2 to understand the effect of surface treatments on the boundary layer characteristics, which act differently on the inner and outer portions of the boundary layer.

Earlier empirical wall pressure spectrum models include Maestrello's model [96] and Cockburn and Roberston's model [97]. Howe [91] proposed a new model for the wall pressure spectrum based on Chase's theoretical work [98]. A significant breakthrough on the empirical model was made by Goody [85], who presented a functional form that fits the measured pressure spectrum for zero pressure gradient flows. His model is an updated version of the Chase–Howe model [91,98]. The Goody model involves exponents in the denominator that correctly scale with the middle and high frequencies. In his model the Reynolds number trends are accurately reflected. Hwang et al. [99] compared different empirical models that were published before 2009, and they found that the Goody model is the most accurate for zero pressure gradient flows.

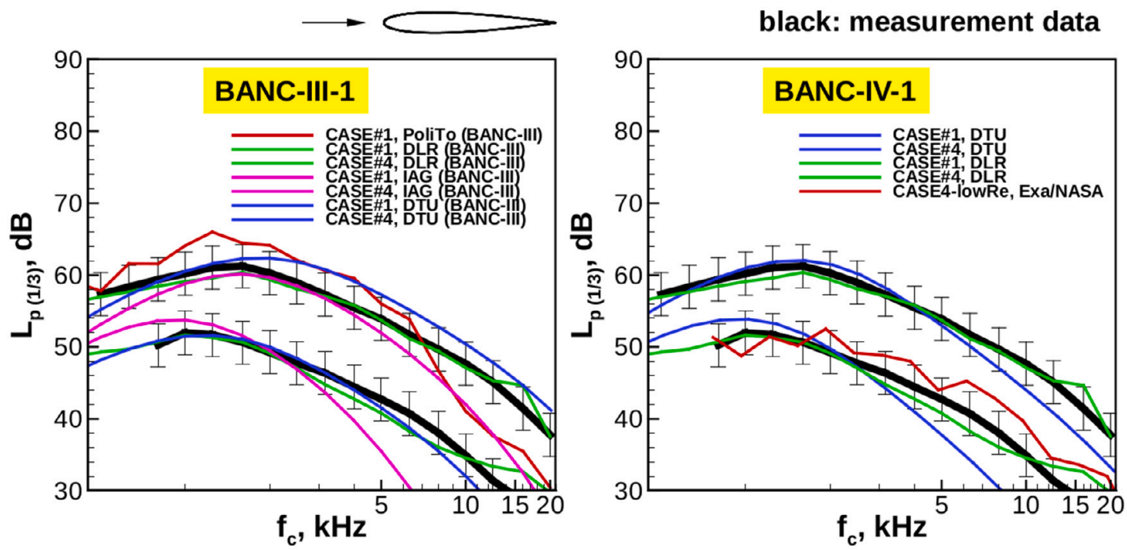


(a)

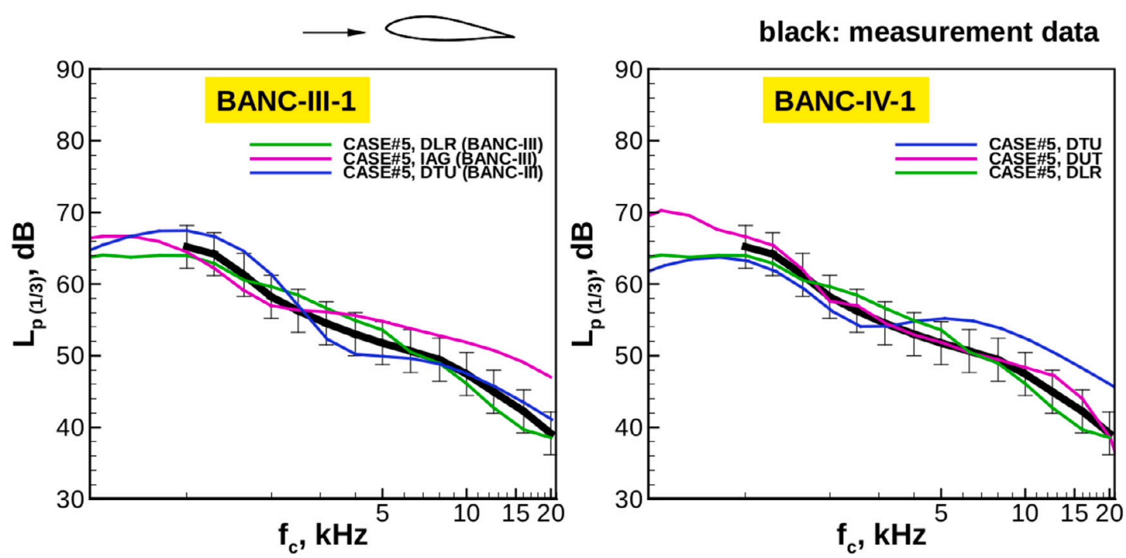


(b)

**Fig. 11.** Comparison of three BANC trailing-edge noise cases for predictions using various trailing-edge noise models and measurement data in different wind tunnels: (a) Cases #1 and #4: NACA0012 at 0° angle of attack for two different wind speeds, (b) Case #5: DU96-W180 airfoil at 4° angle of attack [83,84] (Methods: PoliTo: hybrid RANS/LES coupled with synthetic turbulence and Ffowcs Williams–Hawkings far-field propagation; DLR: CAA solver PIANO, coupled with stochastic source model based on RANS statistics; IAG: TNO-type model using RANS for boundary layer calculation and Howe's model for acoustic field; DTU: TNO-type model using RANS for boundary layer calculations and Howe's model for acoustic field; Exa/NASA: Lattice-Boltzmann PowerFLOW flow solver coupled with the Ffowcs Williams–Hawkings acoustic analogy; DUT: Lattice-Boltzmann flow solver coupled with the Ffowcs Williams–Hawkings acoustic analogy).

**Table 1**
Parameters (a–d) for the empirical wall pressure spectrum models.

| Model | a | b | c | d |
|---|---|---|---|---|
| Goody [85] | 3.0 | 2.0 | 0.75 | 0.5 |
| Rozenberg [86] | $[2.82\,\Delta^2\,(6.13\,\Delta^{-0.75}+d)^e][4.2(\Pi/\Delta)+1]$ | 2.0 | 0.75 | $4.76(1.4/\Delta)^{0.75}[0.375e-1]$ |
| Kamruzzaman [87] | $0.45[1.75(\Pi_c^2\beta_c^2)^m+15], m=0.5(H_{12}/1.31)^{0.3}$ | 2.0 | 1.637 | 0.27 |
| Catlett [88] | $3.0 + e^{7.98(\beta_{\Delta^*} Re_{\Delta^*}^{0.35})^{0.131}} - 10.7$ | 2.0 | $0.912+20.9(\beta_\delta Re_\delta^{0.05})^{2.76}$ | $0.397+0.328(\beta_\delta Re_{\Delta^*}^{0.35})^{0.310}$ |
| Hu [89] | $[81.004(10^{-5.8\cdot 10^{-5} Re_\theta H-0.35})+2.154]10^{-7}$ | 1.0 | $1.5(1.169\ln(H)+0.642)^{1.6}$ | 0.07 |
| Lee [90] | $\max(a_{Roz},(0.25\beta_c-0.52)a_{Roz})$ | 2.0 | 0.75 | $\max(1.0,1.5d_{Roz})(\beta_c<0.5)$ or $d_{Roz}(\beta_c >= 0.5)$ |

All these earlier models, however, were developed for zero pressure gradient flows such as a flow over a flat plate. Therefore, these models are not adequate for solving airfoil trailing-edge noise, which involve moderate or large adverse or favorable pressure gradients. Since the adverse pressure gradient on the suction side of an airfoil generates the dominant trailing-edge noise in a wide range of frequencies, a

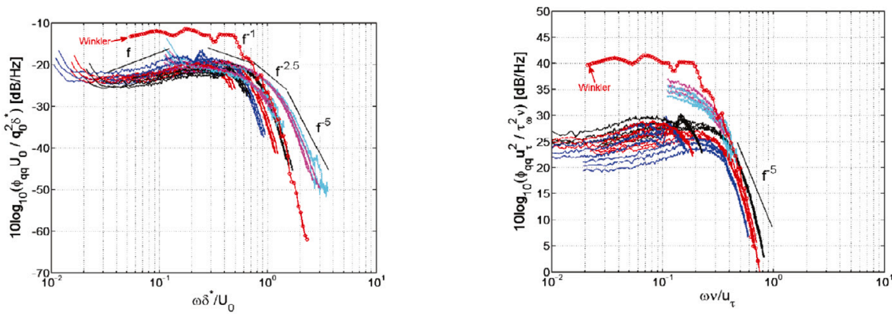


(a) (b)

**Fig. 12.** Surface pressure spectra at 20 and 40 m/s at AoA = 0°, 5°, 10° and 15° and different heights through the tripped boundary layer on a NACA 65(12)-10 airfoil plotted against non-dimensional frequency scaled with (a) outer layer properties, and (b) inner layer properties [41].

**Table 2**
Parameters (e–h) for the empirical wall pressure spectrum models.

| Model | e | f | g | h |
|---|---|---|---|---|
| Goody [85] | 3.7 | 1.1 | −0.57 | 7.0 |
| Rozenberg [86] | $3.7 + 1.5\beta_c$ | 8.8 | −0.57 | $\min(3.0, 19/\sqrt{R_T}) + 4.0$ |
| Kamruzzaman [87] | 2.47 | $1.15^{-2/7}$ | −2/7 | 7.0 |
| Catlett [88] | $3.872 - 1.93(\beta_\delta Re_\delta^{0.05})^{0.628}$ | $2.19 - 2.57(\beta_\delta Re_\delta^{0.05})^{0.224}$ | $-0.5424 + 38.1(\beta_\delta H^{-0.5})^{2.11}$ | $7.31 + 0.797(\beta_\delta Re_\delta^{0.35})^{0.0724}$ |
| Hu [89] | $1.13/(1.169\ln(H) + 0.642)^{0.6}$ | 7.645 | −0.411 | 6.0 |
| Lee [90] | $3.7 + 1.5\beta_c$ | 8.8 | −0.57 | $\min(3.0, (0.139 + 3.1043\beta_c)) + 7.0$ |

significant attention was paid to the development of an empirical model for adverse pressure gradient flows. Rozenberg et al. [86] extended the Goody model to account for the adverse pressure gradient effects by using six adverse pressure gradient flow measurement data. They used the wake strength parameter, Clauser's parameter [100], and the ratio of the boundary layer thickness to displacement thickness to derive empirical constants. This model cannot be used for favorable pressure gradient flows. Kamruzzaman et al. [87] developed a new empirical model for adverse pressure gradient flows. They used several airfoil measurement data for a range of Reynolds numbers and angles of attack to find their empirical model constants. Their model accounts for highly loaded boundary layer effects. Catlett et al. [88] developed a new empirical model for adverse pressure gradient flows by extending the Goody model. Suryadi and Herr [101] found that both the Rozenberg and Catlett models showed large discrepancies compared to measurement data for a DU96-W-180 airfoil. A typo in the exponent $A_2$ in Rozenberg et al. [86] is most likely at the origin of these differences and using the corrected coefficient $h$ in Table 1 recovers the proper high-frequency behavior, the −5 slope of Goody's model as found experimentally [26] and numerically [93,102]. Hu [89,103] developed a new empirical model for adverse and favorable pressure gradient flows. They claimed that the Clauser's equilibrium parameter is not suitable to define the shape of the spectrum. Instead, they used the boundary layer shape factor to derive empirical constants. Lee [90] provided a review of these empirical wall pressure spectrum models including Goody's model, Catlett's model, Rozenberg's model, Kamruzzaman's model, and Hu's model for zero and adverse pressure gradient flows. He found that none of these models provide consistently satisfactory results for different geometries and flow conditions. Based on the limitations and observed trends, he developed a new empirical model that works for zero and adverse pressure gradient flows as well as minor favorable pressure gradient flows. His model is an extension of Rozenberg's model, and it was found that Lee's model yields more accurate results at high adverse pressure gradient flows and near-zero pressure gradient flows than Rozenberg's model.

Lee [90] expressed all those empirical models in the universal wall pressure spectrum shape, which is given as

$$\Phi_{pp}(\omega)SS = \frac{a(\omega FS)^b}{[i(\omega FS)^c + d]^e + [(f R_T^g)(\omega FS)]^h} \tag{74}$$

where $a - i$ are parameters that depend on the model and $R_T$ is ratio of timescales, $(\delta/U_e)/(\nu/u_\tau^2) = (u_\tau \delta/\nu)\sqrt{C_f/2}$, that characterizes the Reynolds number effect. Note that Kamruzzaman et al. [87] used a slightly modified $R_T$, $(\delta^*/U_e)/(\nu/u_\tau^2)$. The parameter $\delta$ denotes the boundary layer thickness, $\delta^*$ the boundary layer displacement thickness, $U_e$ the boundary layer edge velocity, $\nu$ the kinematic viscosity, $u_\tau$ the friction velocity, and $C_f$ the skin friction coefficient. The variables $SS$ and $FS$ are the spectrum scale factor and frequency scale factor respectively.

The parameters used in Eq. (74) define the shape of the wall pressure spectrum. Parameter $a$ determines the overall amplitude of the spectrum. Variables $b, c, e$, and $h$ control the slope of the spectrum at different frequencies. The low frequency slope is determined by parameter $b$ and the roll-off rate at middle frequencies, or an overlap region is determined by parameters $b$, $c$, and $e$, and the high frequency slope is determined by parameters $b$ and $h$. Parameters $f$ and $g$ affect the onset of the transition between the overlap and high frequency. Parameter $d$ affects the location of the low frequency maxima. Parameter $i$ is 1.0 for all models, except in the Rozenberg's model and Lee's model where a constant of 4.76 is used due to the replacement of the boundary layer thickness in the Goody model with the boundary layer displacement thickness, assuming $\Delta = \delta/\delta^* = 8$.

Tables 1–3 show the parameters $(a-i)$ and scale factors for six models: Goody, Rozenberg,[7] Kamruzzaman, Catlett, Hu, and Lee. In Lee's model, $a_{\mathrm{Roz}}$ and $d_{\mathrm{Roz}}$ indicate $a$ and $d$ of Rozenberg's model. It should be noted that Kamruzzaman et al. [87] used an empirical equation for the Clauser's parameter ($\beta_c$) while both Rozenberg et al. [86] and Lee [90] used a modified Clauser's parameter using the boundary layer momentum thickness. Lee used an absolute value of this parameter for a favorable pressure gradient flow.

As discussed in the previous paragraphs, empirical or semi-empirical wall-pressure spectrum models require boundary layer parameters including the boundary layer thickness, displacement thickness, momentum thickness, edge velocity, pressure gradient, and skin friction coefficient near a trailing edge. Typically, $x/c = 0.99$ is used for extracting these parameters where $x$ and $c$ are the streamwise location

[7] Original Rozenberg paper used $\min(3.0, 19/\sqrt{R_T}) + 7.0$ for h value.

**Table 3**
Parameters (i, SS, FS) for the empirical wall pressure spectrum models.

| Model | i | SS | FS |
|---|---|---|---|
| Goody [85] | 1.0 | $U_e/\tau_w^2\delta$ | $\delta/U_e$ |
| Rozenberg [86] | 4.76 | $U_e/\tau_{\max}^2\delta^*$ | $\delta^*/U_e$ |
| Kamruzzaman [87] | 1.0 | $U_e/\tau_w^2\delta^*$ | $\delta^*/U_e$ |
| Catlett [88] | 1.0 | $U_e/\tau_w^2\delta$ | $\delta/U_e$ |
| Hu [89] | 1.0 | $u_\tau/Q^2\theta$ | $\theta/U_0$ |
| Lee [90] | 4.76 | $U_e/\tau_w^2\delta^*$ | $\delta^*/U_e$ |

and the chord length of an airfoil. These parameters can be obtained through viscous panel methods such as XFOIL [104] or steady RANS solvers. It should be noted that these semi-empirical wall-pressure spectrum models do not require the detailed boundary layer profiles such as a velocity profile or a turbulent kinetic energy profile, which are typically inputs to TNO-type models. Hence, it is less sensitive to aerodynamic solvers. Since XFOIL does not provide the boundary layer thickness, it can be computed using the following empirical model.

$$\delta = \theta\left(3.15 + \frac{1.72}{H_k - 1} + \delta^*\right) \tag{75}$$

where $H_k$ is the shape factor or $\delta^*/\theta$, and $\theta$ is the boundary layer momentum thickness. When CFD is used, the boundary layer thickness can be determined from the velocity profile. However, the velocity profile does not reach a constant value for an airfoil flow unlike a flat plate flow so that it is not easy to determine the exact location of the boundary layer thickness. In this case, a total pressure profile or a turbulent kinetic energy can be used instead as they are constant outside of the boundary layer. Readers can find this process in the Refs. [105,106].

Fig. 13 shows trailing-edge noise predictions for Benchmark Problems for Air frame Noise Computations (BANC) cases [82] using Goody's model, Rozenberg's model, Hu's model, Kamruzzaman's model, and Lee's model, which were presented by Lee and Shum [107]. The test conditions are shown in Table 4. Trailing-edge noise was predicted by Howe's model [91] or Eq. (33) for a low Mach number and an observer perpendicular from the trailing edge.

The wall-pressure spectrum $\Phi_{pp}$ obtained at 99% of the chordwise distance from the leading edge was used to predict acoustics. The convection velocity was assumed to be [54]

$$U_c = 0.7\,U_\infty \tag{76}$$

The spanwise coherence length scale $l_3$ uses Corcos's model [108].

$$l_3 = \frac{U_c}{b\omega}, \quad b = 1.0 \tag{77}$$

Note alternative constants for both convection velocity and spanwise coherence length can be found in [26,109,110]. Sound pressure level is computed as follows:

$$SPL(f) = 10\log_{10}\left[\frac{2\pi S(\omega)\Delta f}{P_{ref}^2}\right] \tag{78}$$

where $P_{ref} = 2\times10^{-5}Pa$ and $\Delta f$ is the spectral resolution.

For comparisons with measurement data, the narrow band sound pressure level was converted to the 1/3rd octave band spectrum. In the measurement, $\pm$ 3 dB was added since different measurement facilities showed $\pm$ 3 dB uncertainties in the BANC paper. It is shown that, overall, Lee's model provides the closest match with measurement data among all models.

These wall pressure spectrum models have been extensively used in predicting trailing-edge noise. Several papers are summarized below.

Karimi et al. [111] used a hybrid uncorrelated wall plane waves-boundary element method technique. RANS CFD was used to estimate the turbulent boundary layer parameters. Goody's model [85] was used to obtain the wall pressure spectrum. Chase [112], Corcos [113], and generalized Corcos model [114] were used to compute the cross-spectrum function. From the wall pressure spectrum, the incident pressure was realized using the assumption of uncorrelated wall plane waves. Once the incident pressure was found, boundary element method was used to compute the scattered waves.

Küçükosman et al. [105] used the above semi-empirical wall pressure spectrum models in Amiet's model for a NACA0012 airfoil, with a specific emphasis on the sensitivity to the various methods calculating the inputs parameters to the models. They also found that Lee's model provides the most accurate results for wall pressure spectrum among other models, but it was found that trailing-edge noise was slightly over-predicted with Lee's model. It is not clear how the over-prediction occurred in the noise comparison when the wall pressure spectrum is well matched.

Due to the fast turnaround time, the empirical wall pressure spectrum models were used in low-noise airfoil optimization or parameter sensitivity study. Volkmer and Carolus [115] used XFOIL, Kamruzzman's wall pressure spectrum model, and a genetic algorithm to find low-noise airfoils. They cautioned the potential inaccuracy of the predictions with the optimal airfoil shape against the measurement data. In order to improve the accuracy for airfoil optimization problems, Ricks et al. [116] used RANS CFD, Lee's wall pressure spectrum model, Amiet's model, and a genetic algorithm to find low-noise airfoils. They showed a noise reduction by around 2 dB, but they pointed out that noise reduction resulted in a reduction in lift–drag ratio. Chen and Lee [117] used Lee's wall pressure spectrum model and Howe's model to investigate the effect of seven physical airfoil design parameters on trailing-edge noise. They found that the reduction in a trailing boat-tail angle, which is related to the trailing edge thickness, yields a reduction in noise as well as an increase in lift–drag ratio. Chen and Lee [118] optimized the boat-tail angle or a concave shape of a trailing edge using the Kriging surrogate model and GA optimization tool. The Kriging surrogate model was constructed with Lee's wall pressure spectrum model and Howe's acoustic model. They achieved 4 dB noise reduction with the optimized airfoil shape while increasing the lift-to-drag ratio.

Tian et al. [119] used Goody's model [85] and Rozenberg et al.'s model [86] for the wall pressure spectrum to predict wind turbine noise in the presence of wind shear and atmospheric turbulence. General descriptions about wind turbine trailing-edge noise will be given in Section 5.

Rozenberg [120] and Christophe [121] first recognized the possible sensitivity of the noise prediction to the various models used to reconstruct wall-pressure fluctuations and how the parameters were extracted from the RANS simulations. This led to the uncertainty quantification (UQ) performed with the Stochastic Collocation expansion on the trailing-edge noise of a controlled-diffusion airfoil by Christophe et al. [122]. Note that a tensor grid of 81 RANS computations was used. They have also compared with direct unsteady LES predictions of the trailing-edge noise for this airfoil case as explained in Section 3.2. The full UQ methodology is summarized in Fig. 1 in Ref. [123]. It showed that Rozenberg's model was mostly sensitive at high frequencies due to the uncertainty of the wall shear stress $\tau_w$, whereas Panton and Linebarger's model as implemented by Remmler et al. [53], was more sensitive at low frequencies because of the slower convergence of the Monte Carlo method used to calculate the quintuple integral in Eqs. (64), (65) and (66). This led to rather choosing the maximum shear stress in the boundary layer that is less sensitive to the quality of the RANS simulation than $\tau_w$ in Rozenberg's model, and to improve the Monte Carlo convergence in Panton and Linebarger's model [51].

### 3.1.4. RANS-based statistical noise model

The semi-empirical models that mentioned in the previous subsections, including BPM model, TNO model, wall pressure spectrum model, need turbulent boundary layer parameters. These models can

**Table 4**
Test conditions for BANC experiments. [82].

| Case # | Airfoil | Chord length [m] | Fixed transition position ($x/c$) | $U_\infty$ [m/s] | AoA (deg) |
|---|---|---|---|---|---|
| 1 | NACA0012 | 0.4 | SS: 0.065, PS:0.065 | 56.0 | 0 |
| 2 | NACA0012 | 0.4 | SS: 0.065, PS:0.065 | 54.8 | 4 |
| 3 | NACA0012 | 0.4 | SS: 0.060, PS:0.070 | 53.0 | 6 |
| 4 | NACA0012 | 0.4 | SS: 0.065, PS:0.065 | 37.7 | 0 |
| 5 | DU96-W-180 | 0.3 | SS: 0.12, PS:0.15 | 60.0 | 4 |
| 6 | NACA64–618 | 0.6 | Natural transition | 45.03 | −0.88 |
| 7 | NACA64–618 | 0.6 | Natural transition | 44.98 | 4.62 |

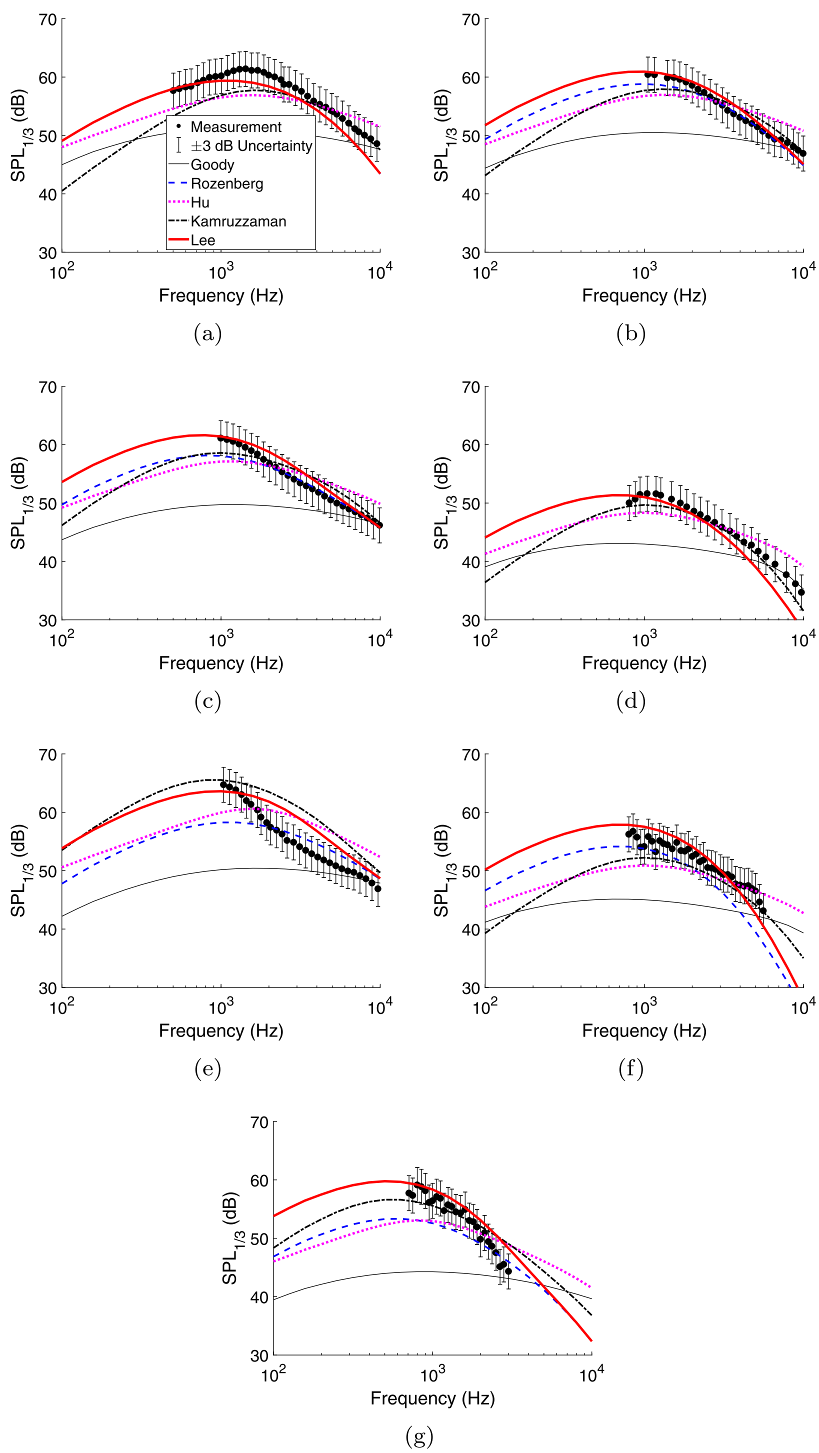


**Fig. 13.** Comparison of seven BANC trailing-edge noise cases for predictions using the five empirical wall pressure spectrum models and measurement data: (a) case 1, (b) case 2, (c) case 3, (d) case 4, (e) case 5, (f) case 6, (g) case 7 [107].

be used in conjunction with steady RANS CFD simulations that provide turbulent boundary layer parameters. Steady RANS solutions can also be used to find statistical representations of turbulent velocity fluctuations or acoustic source terms, such as a turbulent velocity cross correlation function or a cross spectrum, which are used to predict trailing-edge noise. This subsection is devoted to the latter approach. In general, there are three ways to use the turbulent velocity fluctuations for trailing-edge noise predictions: (1) compute the wall pressure spectrum through Poisson's equation, (2) use the turbulent velocities as the source term in an acoustic propagation solver, and (3) construct a two-point turbulent velocity correlation function or a cross-spectrum function as the source to the Green's function approach.

First, Glegg et al. [124] inverted a turbulent kinetic energy (TKE) profile, which is obtained from RANS results, to the vortex sheet strength to obtain the turbulent velocity fluctuations. Then, the linearized form of Poisson's equation along with the velocity fluctuations provides the wall pressure spectrum and Howe's model yields trailing-edge noise spectrum. The choice of the length scale is an important factor, which impacts the turbulence model. The inversion process of the turbulent kinetic energy involves additional numerical calculations. Chen and MacGillivray [125] obtained the squared vertical velocity fluctuation using the turbulent kinetic energy and anisotropic turbulence model. The turbulent kinetic energy and anisotropic turbulence model were obtained from the Reynolds stress RANS model. They included both the mean shear–turbulence interaction and the turbulence–turbulence interaction in the solution of the Poisson equation. They claimed that the turbulence–turbulence interactions are responsible for the generation of high-frequency pressure fluctuations and noise. Grasso et al. [126] also obtained the wall pressure spectrum by solving the Poisson equation (Panton and Linebarger's model) in conjunction with Amiet's model for the far-field sound as shown in Section 3.1.2. Their wall pressure spectrum model only included the mean shear–turbulence interaction [52,53]. RANS simulations provided the mean velocity, averaged vertical velocity fluctuation squared or turbulent kinetic energy, and turbulent length scale needed in the model. They also used the scale adaptive simulation (SAS), which is a hybrid RANS/LES model and an intermediate approach to full LES predictions as shown in Section 3.2, to extract the necessary input data. Their results showed that SAS-based model improved the predictions compared to RANS-based model.

Second, the turbulent velocity fluctuations can be used in conjunction with an acoustic propagation solver. Ewert et al. [127] used Random Particle Mesh (RPM) approach to generate the statistical turbulence velocities. The RPM method generates a fluctuating vector potential by spatial convolution of spatio-temporal white noise with a filter. They used Reynolds stress model RANS. RANS solutions provided the turbulent kinetic energy and length scale. The Acoustic Perturbation Equations was then used to propagate the sound. Similarly, Cozza et al. [128] used Eulerian Solenoidal Digital Filter (ESDF) to reproduce a solenoidal fluctuating turbulent velocity using RANS simulations. The mean velocity, turbulent kinetic energy, and specific rate of dissipation, which are obtained from RANS simulations, are the main inputs to their model. The stochastic source model was coupled with a frequency-domain Galerkin finite element solver of the Acoustic Perturbation Equations for the solution in the near field region. Then, Ffowcs Williams and Hawkings equation was used to predict far-field noise.

Third, the two-point space–time velocity correlation function or the cross-spectrum function between two points in the boundary layer are constructed from RANS. These correlation function or cross-spectrum function are then used in the solution of Green's function. Bai and Li [129] modeled the two-point space–time velocity correlation function using both the isotropic turbulence assumption and the anisotropic turbulence assumption. Their approach is an extension of the adjoint Green's function of the linearized Navier–Stokes equation, which was originally used in jet noise predictions [130]. The turbulent kinetic energy and dissipation rate, which are the inputs to the correlation functions, were obtained by RANS simulations. The linear and nonlinear Reynolds stress models, which are also inputs to the correlation functions, were used based on the mean flow quantities. The adjoint Green function was reduced to the solution of the Helmholtz equation assuming a uniform flow. The sound pressure spectral density calculation requires the volume integral of the source. They investigated the effect of the turbulence anisotropy and different Reynolds stress components. For example, the streamwise Reynolds normal stress contribute mostly to far-field noise and the other two components are nearly the same. Albarracin et al. [131] used a statistical model of the turbulent velocity cross-spectrum between two points in the boundary layer and the use of this information as an input to Green's function solution for airfoil trailing-edge noise. Ffowcs Williams and Hall's approximation of the turbulent velocity squared were used. The Green's function for a rigid half plane was used [11]. For the turbulent velocity cross-spectrum, they used Morris and Farassat's model [132], which was originally developed for jet noise predictions. RANS CFD was used to extract the turbulent kinetic energy and dissipation, which are needed in the turbulent velocity cross-spectrum. This model requires a volume integration near the source region. Although this method provided good agreement against measurement data for a NACA0012 airfoil at zero angle of attack, it showed a large deviation at low frequencies at non-zero angles of attack. For a DU96 airfoil, the high-frequency was significantly over-predicted. A further refinement of the model is needed. This method was also used by Rumpfkeil [133] to compare noise predictions with other methods including Remmler's wall pressure spectrum model [53].

### 3.2. LES predictions

Even though the analytical and semi-empirical models described above provide simple and easy-to-run prediction tools, which could be integrated in a design cycle for instance, they still rely on some drastic simplifications of both the geometry (mostly infinitesimally thin flat plates in analytical models) and the flow physics (uniform flow with frozen turbulence at the trailing edge). To make sure that a minimum degree of relevancy is achieved with these analytical and semi-empirical models, some numerical validation can be sought. As mentioned above, airfoil self-noise results from the scattering of a boundary layer turbulent flow at the trailing edge. It can be related to either the vortical and aerodynamic unsteady velocity field around the trailing edge (Ffowcs Williams and Hall's approach) or to the induced aerodynamic unsteady pressure field on the airfoil surface (Howe's and Amiet's approaches). Therefore, to achieve the validation goal, all the relevant turbulent scales developing in the turbulent boundary layer over the airfoil and its near wake must be captured in the simulation. The RANS simulations previously described in Section 3.1.4 cannot provide such information as all turbulent scales are modeled, and we must resort to at least a Large Eddy Simulation (LES) or an unsteady method that captures some relevant turbulent structures such as the Scale Adaptive Simulation [134], used for instance by Grasso et al. [126] as shown in Section 3.1.4. Moreover, as shown below, because trailing-edge noise is measured in the far field at a distance much larger than the mock-up scale (airfoil chord length), it will be very expensive to directly compute the sound at the microphone positions with LES. Therefore, almost all numerical noise predictions will use a hybrid method, which combines a near-field LES around the airfoil to capture the unsteady turbulent flow field and an acoustic analogy that considers these flow statistics as equivalent noise sources and propagates them to the far field to yield the acoustic pressure at the measurement locations.

Note that trailing-edge noise has also been recognized early on, as a test case for numerical methods in Computational Aero-Acoustics (CAA) [135,136]. Yet, Singer et al. [136] only considered the vortex shedding mechanism as they only used an unsteady compressible RANS simulation to capture the sources around a thin airfoil with a vortex generator and computed the far-field noise with Farassat's formulation 1A of Ffowcs Williams and Hawkings' analogy. Later, a new simpler time-domain formulation termed 1B was proposed by Casper and Farassat [137]. All the other early approaches tried to resolve the turbulent flow field and opted for incompressible LES coupled with different acoustic analogies that account for the scattering effect, such as Ffowcs Williams and Hall's analogy or Amiet's model. As all experiments involved low Mach numbers (below 0.3) and moderate Reynolds number based on the chord, $Re_c \leq 10^6$, it was natural and more cost effective to resort to incompressible solvers. For instance, Manoha et al. [135] coupled their incompressible results on the blunt NACA0012 tested at NASA with Curle's analogy using the wall-pressure statistics on the airfoil and Ffowcs Williams and Hall's analogy using the near-wake velocity statistics. Their limited domain size and grid resolution could only yield a fair agreement over a limited frequency range with Brooks and Hodgson's experimental data on the NACA0012 airfoil [68]. A more extensive comparison was then achieved by Wang et al. [138] on a slanted flat plate, which had been tested at the university of Notre Dame by Blake [139]. They coupled their LES results with Ffowcs Williams and Hall's analogy using the computed near-wake velocity field. Detailed comparisons with experiment were provided not only for the far-field noise but also for both the mean flow field and the wall-pressure fluctuations along the airfoil for the first time. Fair agreement was obtained for both the noise sources (wall-pressure spectra) and the far-field sound (noise spectra). To yield the latter, Wang et al. [138] also provided a computationally efficient way of estimating the integral over the noise source volume near the trailing edge, which is valid if the spanwise extent of the source field is acoustically compact (see below). Finally, a further refinement on the acoustic side was provided by Oberai et al. [140]. They performed a two-dimensional computation of the Green's function tailored to a slightly cambered Eppler airfoil to yield the slight asymmetry on the noise directivity induced by the actual airfoil camber.

In all the above simulations two main limitations prevent achieving a close agreement with experimental data obtained in anechoic open-jet wind tunnels. On the one hand, all simulations were performed in free field to simplify the far-field boundary conditions. On the other hand, limited or no span was considered because of the limited computational capabilities of the time. The former prevents having the proper aerodynamic loading on the airfoil and the latter constraints the proper stretching of the turbulent eddies in the spanwise direction. In both cases, the turbulent statistics needed to correctly predict trailing-edge noise are altered. To address the installation effects on the NACA0012 airfoil, Brooks, Pope and Marcolini proposed an empirical correction on the angle of attack [141]. Yet, such a correction is only rigorously valid for such an airfoil over the limited incidence range over which the tests were performed. Installation effects in an anechoic open-jet wind tunnel were first systematically and numerically studied by Moreau et al. [142]. They showed that this could have some significant effects on the flow field and that an empirical correction may indeed not be suited for all airfoils. Accounting for the jet deflection and the equivalent solidity effect imposed by the jet shear layers recovered the loading on the cambered Controlled Diffusion (CD) airfoil tested by Moreau et al. [26,109] in the two open-jet wind tunnels at Ecole Centrale de Lyon. Note that such an effect could already be clearly seen on the slanted plate computed by Wang et al. in the mean pressure distribution shown in Fig. 5 in [138]. Significant effort was then put on mimicking the experimental set-up and properly setting the boundary conditions in the LES around the airfoil as explained below. For the spanwise extent of the computational domain, Wang et al. [138] already discussed this issue as their spanwise width of the computational domain $L_z$ was only a small fraction of the actual mock-up span $L$. Following Kato's analysis on the cylinder [143], they showed that a necessary condition

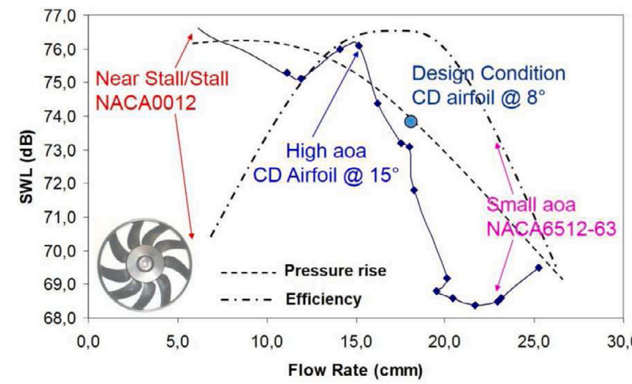


**Fig. 14.** Sketch of aeroacoustic performances of an automotive engine cooling fan (pressure rise, efficiency and sound power level) and corresponding incompressible LES on various airfoils.

was that the spanwise coherence of the wall-pressure fluctuations was smaller than the computational domain span. The source regions in the computational domain then radiate in a statistically independent manner, and the total noise spectrum is the sum of contributions from $L/L_z$ independent source regions along the span.

To tackle the loading issue on the airfoil, and keep simulations affordable, the following two-step simulation strategy has been devised. A couple of preliminary incompressible RANS computations are initially performed. First, a two-dimensional RANS computation of the flow around the airfoil is conducted considering the wind tunnel nozzle shape and geometrical configuration used in the experiments. The domain size is selected to include most of the wind tunnel size and large enough to have a negligible effect on the jet deflection. The nozzle outlet velocity profile known from hot-wire measurements is set as a steady inflow condition to the computational domain. A truncated airfoil domain is then extracted from this simulation in the potential core of the jet to prevent any jet shear-layer interference. Inflow boundary conditions for the restricted domain is extracted from the initial full RANS simulation. A much finer and regular grid meeting LES specifications is then generated on the restricted domain [144,145], and a new RANS computation is achieved to yield the initial condition for the consequent LES. The two-dimensional grid is then extruded to provide a sufficient spanwise extent to include the spanwise coherence of the wall-pressure fluctuations. The RANS results and steady inlet boundary condition are then copied in the spanwise direction to provide a proper initial condition to the consequent LES.

The first incompressible LES that followed such a methodology was achieved in 2003 by Wang et al. [146] on the CD airfoil with its proper loading and a significant span (10% of the airfoil chord). Note that such a simulation took over a year to converge the flow statistics properly, and several more to consolidate the methodology and the turbulent flow as well as acoustic results [24]. Such a simulation corresponded to a geometrical angle of attack of 8° and a Reynolds number $Re_c \simeq 1.5 \times 10^5$. It was driven by a practical engineering problem as it corresponded to the design flow condition of a Valeo automotive engine cooling fan at midspan (see Section 5.2). Yet, many more flow conditions are encountered by such fan systems depending on the car operating condition as shown in Fig. 14. Thus, in 2008–2009, several different LES were performed on different airfoils (CD airfoil, NACA0012 and NACA 6512–63 airfoils) at various flow conditions (at similar $Re_c$) to cover most of the performance curves shown in Fig. 14 and to test the methodology broadly [147–149]. Each case was selected because it had a corresponding experimental data base in open-jet anechoic wind tunnels as described below in Section 4 [25,26,149]. Fig. 15 shows, for instance, the instantaneous flow fields on the CD airfoils for the two geometrical angles of attacks of 8° and 15° respectively [147]. The

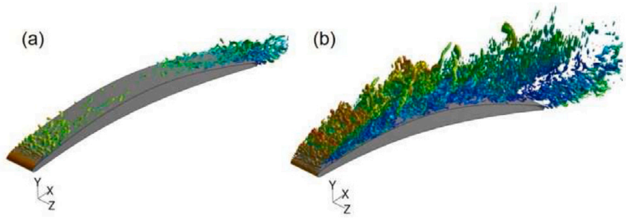


**Fig. 15.** LES results on the CD airfoil with Fluent [147]: iso $Q$-criterion contours colored by the velocity magnitude at a geometrical angle of attack: (a) 8° and (b) 15°. (For interpretation of the references to color in this figure legend, the reader is referred to the web version of this article.)

iso-contours of the $Q$-criterion colored by the velocity magnitude stress the very different flow topology and turbulent scales involved in both flow conditions. Noteworthy, even though the high angle of attack is fully separated at the leading edge and involves much larger eddies shed over the airfoil suction side, small eddies are still grazing along the walls providing some positive convection velocity near the trailing edge, partially fulfilling Amiet's model assumptions. For all cases, a good agreement with experiment on the mean loading was found, validating the two-step approach. Most of them were able to reproduce the wall-pressure fluctuations near the trailing edge correctly. For the attached cases, the turbulent statistics required about 5 to 6 flow-through times to converge. The most challenging simulations being the high incidence cases, as the domain spanwise extent was still too limited to properly include the spanwise coherence of the wall-pressure fluctuations over a large frequency range, at least twice the number of flow-through times was required to converge the statistics. Moreover, near stall, some strong interaction with the jet shear layer was evidenced. Nevertheless, the consequent noise predictions by coupling the LES results with various acoustic analogies, namely Ffowcs Williams and Hall's analogy or Amiet's model, provided some reasonable agreement with far-field noise measurements in all cases. Both Christophe et al. [147] and Winkler et al. [148,150] also noted that Curle's analogy previously used by Manoha et al. for instance [135], was failing beyond the airfoil compactness limit, as expected as it does not account for the airfoil scattering. This has also been confirmed more recently by Martinez-Lera et al. [151] that used a finite-element method to numerically compute the actual or tailored Green's function in equation (9) (as previously Oberai et al. [140] and Moreau et al. [27]). Note that incompressible LES does not include the acoustic scattering effect in the flow field, which is a part of the compressiblity effect, so that a separate scattering process, such as Ffowcs Williams and Hall's analogy, Amiet model's, or Howe's model, should be accounted for in noise predictions. Curle's analogy or Ffowcs Williams and Hawking equation with the free-space Green's function are not compatible with incompressible LES since those equations require the complete noise source terms in the flow field, that are the incident and scattered pressure fluctuations, without a separate scattering process involved. Alternatively, a tailored Green's function (see Section 2) can be used in incompressible LES along with Curle's analogy or Ffowcs Williams and Hawking equation to account for the sacttering effect. It is adequate to couple Curle's analogy or Ffowcs Williams and Hawking equation (impermeable or permeable) along with the free-space Green's function with compressible LES, which will be discussed later. Similarily, it would be erroneous to couple compressible LES with Ffowcs Williams and Hall's analogy, Amiet model's, or Howe's model since the scattering effect is double counted in the source term (flow field) and the scattering process.

More recently, additional simulations were performed on the CD airfoil around the nominal incidence of 8° with the LES code CDP developed at Stanford to perform an uncertainty quantification on the noise prediction by the hybrid method combining incompressible LES with Amiet's model [122]. The angle of attack was varied by ±2°. Interestingly, at the smallest angles of attack a flow bifurcation was observed and the laminar separation bubble (LSB) moved from the leading edge to the trailing edge. Amiet's model was used with two different methods to reconstruct the pressure fluctuations (see Section 3.1.3): Rozenberg's semi-empirical model [86] and Panton and Linebarger's model [52,53]. As with RANS simulations (see Section 3.1.3), the former showed more sensitivity at high frequencies driven by the uncertainty on the friction velocity, whereas the latter was more sensitive to the lowest frequencies mostly because of the convergence of the Monte Carlo method used to compute the quintuple integrals. Overall, on the CD airfoil, several incompressible LES have been run with both commercial (Star-CD [153], Fluent [147], CCM+ and openFOAM [151,154,155]) and research codes (Wang's LES code [24], Turb'flow [156], Saturne [157], CDP [27] and SFELES [154]). At the reference design condition, a similar degree of accuracy can be reached at the trailing edge provided enough grid points are used. More sensitivity is found at the leading edge in the prediction of the LSB, as can be seen from the mean pressure distribution in the length of the plateau varying between 3 and 12% of chord [154]. Christophe et al. [147] also compared different boundary conditions in the spanwise direction, and showed that periodic boundary conditions are the most suited. Similar results were also found by Winkler et al. [148] on the NACA 6512–63 airfoil. Finally, Moreau et al. [27] showed that, given some optimization of the grid topology, trailing-edge noise for an airfoil at a similar Reynolds number $Re_c$ of about $1.5 \times 10^5$ could be achieved with about 1 million grid points on a 10% span, which makes it quite affordable by current computational standards. Moreover, for attached flow conditions, given the above limited number of flow-through times required to converge the flow statistics near the trailing edge, reliable pressure or velocity fluctuations can be obtained for the consequent acoustic prediction with acoustic analogies in a matter of couple of days (compared to a year for the above first full simulation). This methodology has then been successfully applied to more complex flow configurations: airfoils with a blowing slot on the suction side [158], airfoils with different tripping devices on the suction side [25,148,150] and airfoils with a plate and the nozzle scattering [159]. For the blowing case, an additional source at the airfoil slot was shown to contribute at high frequencies. For the tripping cases at low angle of attack, the extra broadband hump caused by laminar boundary layer instability was properly captured in a similar way as found by Moreau and Roger from experimental data (figure 15 (a) in [21]). In the scattering by close objects, Christophe et al. [160] validated a near-field extension of Amiet's model originally proposed by Kocukcoskun.

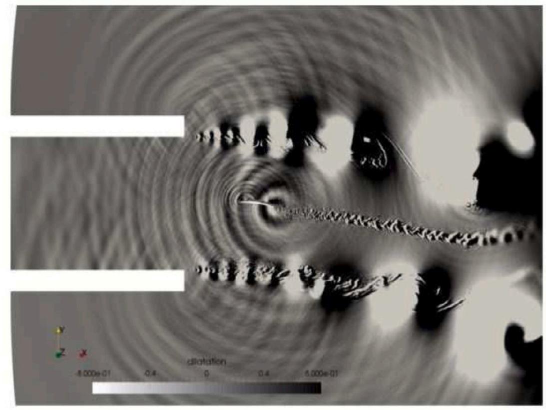

**Fig. 16.** Dilatation field in the midspan plane of the CD airfoil at 8° with AVBP [152].

Finally, some other hybrid methods have also been proposed. Instead of resorting to some acoustic analogy, Shen et al. [161,162]

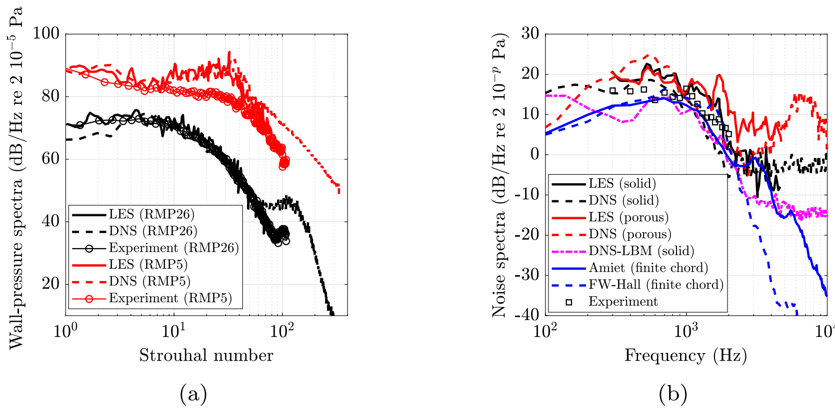


**Fig. 17.** (a) Power spectral densities of the near-field wall-pressure fluctuations and (b) the far-field acoustic pressure at 90° of the CD airfoil at 8°. Experiment: ECL [26] and UdeS [152]; LES: AVBP [152]; DNS: HipSTAR [165] and PowerFLOW [166].

coupled flow results from unsteady incompressible simulations on a NACA 0015 airfoil at a Reynolds number $Re_c = 1.6{\times}10^5$ with some form of the linearized Euler equations, termed the acoustic/compressible perturbation equations. A similar flow-acoustic splitting technique termed Perturbed Compressible Equations was used by Moon and co-workers [163] and applied to the trailing-edge noise of a thick flat plate, an approach they had first validated on the unsteady flow around a cylinder [164]. Overall, all these hybrid methods that combine acoustic analogies accounting for edge scattering or Linearized Euler propagators with incompressible LES results confirm that, at low speeds, the dominant airfoil noise source in clean inflow and fully turbulent flow at the trailing edge is the diffraction of pressure fluctuations at the trailing edge. More precisely, the inertia of the turbulent eddies born in the airfoil turbulent boundary layer is strongly modified at the trailing edge, yielding acoustic waves that are diffracted by this edge. Note, however, that Martinez-Lera et al. [151] already pointed out that additional quadrupole noise sources may contribute significantly at high frequencies in the reference CD airfoil case. With such a hybrid method based on incompressible flow solutions, the acoustic information is restricted to the airfoil surface (dipole sources) and no additional sources (quadrupole sources) in the flow field can be captured. One of the first compressible LES to tackle such a problem in free field was performed by Wolf and Lele [167] on a tripped NACA 0012 airfoil with a blunt trailing edge at a fixed Reynolds number $Re_c = 4.08 \times 10^5$ for an angle of incidence of 5°. Two different Mach numbers 0.115 and 0.4 were considered. They coupled their LES results with a Ffowcs Williams and Hawkings' acoustic analogy, and included both dipole and quadrupole source terms. Note that they used a three-dimensional wideband multilevel adaptive fast multipole method to accelerate the calculations of aeroacoustic integrals. Their acoustic prediction showed reasonable agreement with Brooks et al.'s measurements [141], and they noted that nonlinear quadrupole noise sources played an important role in far-field sound radiation at a high Mach number. Furthermore, they confirmed that convection effects are relevant for all frequencies as shown by Amiet's model, for instance, and that the additional quadrupole sources at a high Mach number have a more pronounced effect for medium and high frequencies [168]. Additional free-stream compressible LES have been achieved on the CD airfoil for a wider range of Reynolds numbers, $Re_c$, and Mach numbers [169–171]. Deuse and Sandberg [169,171] considered four Mach numbers 0.2, 0.3, 0.4 and 0.5 at an angle of attack of 8° at the same Reynolds number $Re_c = 10^5$, whereas Boukharfane et al. [170] computed three Mach numbers 0.3, 0.5 and 0.7 and varied the Reynolds number $Re_c$ from $8.3 \times 10^5$ to $2.4 \times 10^6$ (same chord length as in the parallel experiment performed within the EU-project CRORTET) and the angle of attack from 1 to 7°, to cover the regimes typically encountered in Contra-Rotating Open Rotors or Ultra High By-pass Ratio engines. The former showed, using a high-order finite difference solver HiPSTAR within a flexible overset grid framework, that two or three noise sources are actually present on the airfoil: the above trailing-edge scattering but also an additional noise source at the leading edge (the reattachment point of the LSB) and another weak one in the wake (see for instance the three wave fronts evidenced in Fig. 17 in [171]). The transition/reattachment source actually becomes more relevant with increasing Mach number as the LSB size is growing and becoming more unstable. Noteworthy, Boukharfane et al. [170] observed increasing LSB sizes with increasing angle of attack but slightly reduced ones with increasing Reynolds numbers (and consequently Mach numbers). They only computed the mean loading and the noise sources (the wall-pressure fluctuations) so far. They found good agreement with experiment even in the higher Mach number case that had a normal shock on the suction side.

However, all these compressible LES only compute the near field in free field and do not propagate to the far field accounting for the above installation effects in anechoic wind tunnels, which preclude some direct comparison with experiment. A first attempt to take into account the installation effects in a compressible LES with the code AVBP developed by Cerfacs, was made by Salas et al. [13,172] on a simplified two-element high-lift device, which included a limited extruded span of the two-dimensional mock-up embedded in the wind-tunnel jet and the nozzle exit (basically the same set-up as used above to provide realistic boundary conditions to incompressible LES). The dilatation field in the midspan plane clearly showed the wave fronts of the trailing-edge noise from both elements, the diffraction of the flap noise by the main element, and the scattering by the nozzle lips. Some additional laminar boundary layer instability noise was also evidenced for the first time on the flap suction side. The same procedure was then applied to the CD airfoil at the reference condition [165]. Fig. 16 shows the corresponding dilatation field in the midspan plane. On top of the phenomena found by Salas and Moreau (yielding the fringes observed in radiation maps), the additional noise at the leading edge from the transition/reattachment noise source is also observed. Yet, this noise source is partially shielded by the scattering at the nozzle lips. Wall-pressure spectra close to the trailing edge and far-field acoustic spectra at 90° from the airfoil are shown in Fig. 17. Excellent agreement is found for all simulations with experiments run in the open-jet anechoic wind tunnels at ECL and Université de Sherbrooke (UdeS). All the above compressible simulations resort to a coupling with Ffowcs Williams and Hawkings' analogy to yield the far-field noise. Recently a new numerical approach had emerged that can both capture the near-field noise generation and the propagation to the far-field accurately: the Lattice Boltzmann Method (LBM) that solves the Boltzmann equation on a cubic lattice (voxels), instead of the compressible Navier–Stokes equations [173,174]. The ability of the hybrid LBM-Very Large Eddy

Simulation to directly compute the far-field noise on the complete experimental set-up was first demonstrated by Brès et al. [175] on the tandem cylinder aeroacoustic benchmark with the PowerFLOW code. The same method was then successfully applied to the NACA 5510 airfoil with a tip gap at a Reynolds number $Re_c = 9.6 \times 10^5$, which had been experimentally characterized at Ecole Centrale de Lyon [176,177]. A similar but wall-resolved study was also achieved on the NACA 0018 airfoil at a Reynolds number $Re_c = 2.8 \times 10^5$ and an angle of attack of 0° by Avallone et al. [178]. The flexibility of the method also allowed investigations of noise reduction mechanisms of sawtooth and combed-sawtooth trailing-edge serrations as shown in Section 3.4.

### 3.3. DNS predictions

In Section 3.2, LES on airfoils were shown to provide accurate and reliable flow statistics to predict trailing-edge noise provided a large enough spanwise extent and some installation effect were accounted for. However, only the largest turbulent scales are resolved and, depending on the grid and the numerical scheme accuracy, the frequency range of the prediction might be limited and additional unsteady sources may be missed. Moreover, most of the current experimental data and consequent simulations are only available at low speeds corresponding to transitional Reynolds numbers $Re_c$. The question then arises about the proper modeling of the transition to turbulence by LES, which may modify the development of the turbulent boundary layers along the airfoil and, therefore, the flow statistics close to the trailing edge. Only direct numerical simulations (DNS) can resolve all the relevant turbulent scales and alleviate such uncertainties. Moreover, the continued growth of available computing power has made DNS of compressible flows around an airfoil to predict trailing-edge noise possible and more affordable at transitional $Re_c$.

As in the LES case, the first DNS have been achieved in free field over a limited computational domain to limit the grid size. Indeed, to achieve proper grid resolution down to the Kolmogorov scale for the range of Reynolds numbers around $10^5$, the mesh size is around 200–400 million cells, an order of magnitude larger than for the above LES that ranged from 1 to 40 millions (dimensionless grid sizes $\Delta x^+ < 10$, $\Delta y^+ < 1$ and $\Delta z^+ < 10$ for the DNS versus $\Delta x^+ < 30-40$, $\Delta y^+ \simeq 1$ and $\Delta z^+ < 20-30$ in the above wall-resolved LES). Very few incompressible DNS have been performed with the goal of predicting airfoil noise. Noteworthy, within the framework of the French research program STURM4, Benhamadouche et al. [157] compared various LES with different subgrid-scale models to a DNS on the CD airfoil at the reference flow condition with the Saturne code. As shown in Fig. 18, the mean pressure coefficient remains similar to the LES results (represented here by the results of Wang et al. [24]), except close to the reattachment point of the LSB where the DNS now captures the positive pressure gradient zone after the transition to turbulence [157]. Similar results are found for all the other compressible DNS described below, stressing the clear different behavior between the LES and DNS in the transition zone. Yet, downstream close to the trailing edge similar turbulent boundary layers are found and the wall-pressure spectra and spanwise coherence are quasi identical. The consequent far-field noise prediction with Amiet's model for instance is then similar.

In 2007, Sandberg et al. [179] performed some first compressible 2-D DNS on an semi-infinitely thin flat plate at two Mach numbers (0.4 and 0.6) with an early version of the high-order compressible code HipSTAR. They showed that Amiet's surface pressure jump transfer function predicted the scattered pressure field accurately, and found good overall sound directivity even though viscous effects tended to smear the model lobes at high frequencies. They also found an additional wake source at a higher Mach number responsible for a downstream pointing lobe. Most of these initial findings were then confirmed by a full 3-D DNS [180]. Several consequent DNS were achieved on two symmetric NACA airfoils (NACA-0006, NACA-0012) at two angles-of-attack (5°, 7°) at a Reynolds number $Re_c = 5 \times 10^4$ and a Mach number

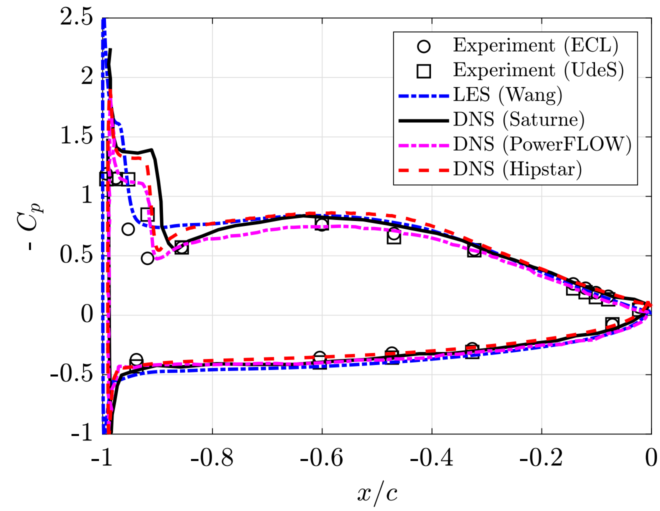


**Fig. 18.** Mean wall pressure coefficient on the CD airfoil at 8°. Experiments from ECL [26] and UdeS [152]; DNS results with Saturne [157], PowerFLOW [166] and HipSTAR [165].

of 0.4 [181]. Note that the Mach number cannot be lowered below 0.25 without any significant time-step penalty. Even at this low Reynolds number, multiple noise sources were found on the airfoil suction side. For instance, LSB reattachment points were identified to be the location of noise production that were highly unsteady (variations in the streamwise and spanwise directions), unlike the noise production at the airfoil trailing edge that is fixed in space. A good summary of those early DNS with the necessary numerical parameters to achieve a proper accuracy can be found in [182].

However, as shown in Section 3.2, installation effects in a anechoic open-jet wind tunnel can have some significant effects on the flow field and consequently on the noise radiated by the airfoil trailing edge. Therefore, to achieve a proper comparison with experiment (a missing element in the early DNS), two different strategies have be devised to include the jet effect. On the one hand, with the LBM, the whole acoustic wind tunnel environment over a limited spanwise extent is accounted for. In 2011, Sanjose et al. [166] performed the first full DNS simulation of the CD airfoil embedded in the jet of the large open-jet anechoic wind tunnel at Ecole Centrale de Lyon, France. Excellent agreement with experiment is found on the airfoil loading in Fig. 18. The shear layer of the thin LSB undergoes some Kelvin–Helmholtz instability with rollers that break down near the reattachment point and trigger transition to turbulence, as shown by the iso-contours of the $Q$-criterion in Fig. 19(a). A forest of hairpins then develops downstream with the thickening of the turbulent boundary layer: as expected, much more turbulent structures can be seen compared to the early LES results in Fig. 15. The noise sources at the trailing edge are also properly captured as seen in the wall-pressure spectra in Fig. 17 for two Remote Microphone Probes (RMP), one at the leading edge close to the reattachment point of the LSB (RMP5) and the other close to the trailing edge where the pressure statistics are collected for Amiet's model (RMP26). The radiated acoustic field is represented by iso-contours of the dilatation field in Fig. 20(a). The dominant noise source at the trailing edge is clearly identified with wave fronts that are directed more upstream with a Cardioid shape, which is typical of a non-compact dipole. The diffraction by the nozzle lips is also clearly seen, which modifies the sound directivity [21]. Finally, an additional weak high-frequency noise source is also observed close to the LSB reattachment point as found in the free stream cases. On the other hand, the two-step strategy presented above for the incompressible LES can also be applied to the compressible DNS. Yet, an additional numerical problem in such compressible simulations arises from the inlet and

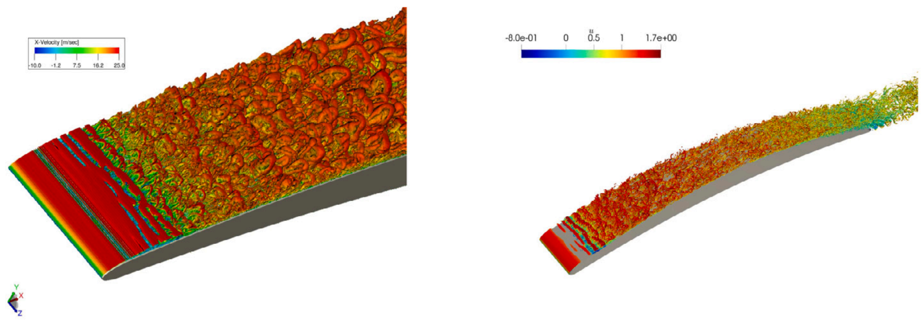


(a) (b)

**Fig. 19.** DNS results of iso $Q$-criterion contours colored by the velocity magnitude at a geometrical angle of attack of 8° on the CD airfoil: (a) PowerFLOW [166] and (b) HipSTAR [165]. (For interpretation of the references to color in this figure legend, the reader is referred to the web version of this article.)

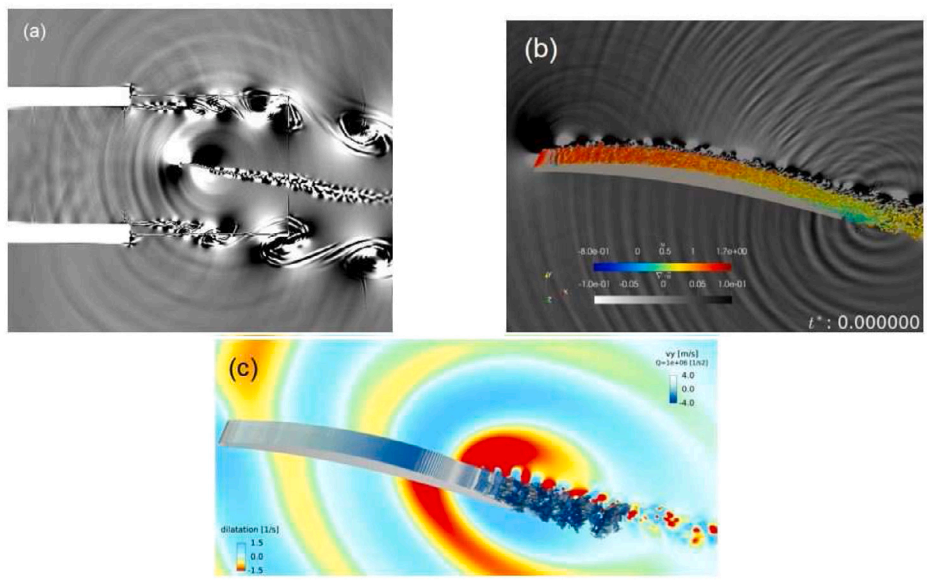


**Fig. 20.** Dilatation field in the midspan plane of the CD airfoil with (a) PowerFLOW at 8° [166], (b) HipSTAR at 8° [165], and (c) PowerFLOW at 5° [166].

outlet boundary conditions that are set close to the airfoil. Specific non-reflecting boundary conditions or radiation boundary conditions possibly combined with sponge layers need to be implemented [183–185]. In the LBM case, only the latter are used in several voxel regions with increasing viscosity. An example of such an approach is presented in Fig. 20(b), which also corresponds to the CD airfoil at the reference flow condition. The corresponding mean loading is also shown in Fig. 18. The latter validates the method as it is very close to the other two DNS with a favorable pressure gradient zone but with a slightly longer LSB length. The iso-contours of $Q$ criterion in Figs. 19 (b) and 20(b) stress a similar transition process in the LSB and a consequent development of a hairpin forest on the airfoil suction side as in the LBM DNS. The dilatation field in Fig. 20(b) also confirms the two noise sources already seen in the AVBP LES (Fig. 16) and in the LBM DNS (Fig. 20(a)). Yet, the finer mesh in the wake triggers a third noise source in the wake, which is responsible for the additional high-frequency hump seen both in the wall-pressure spectra close to the trailing edge (Fig. 17(a), RMP26) and in the far-field acoustic spectra (Fig. 17(b)). Note that the latter is clearly evidenced by comparing two acoustic analogies, one including the airfoil surface only (termed "solid") and the other including the wake (termed "porous"). This additional noise source is also stronger in the Navier–Stokes DNS than in the LBM DNS, which is attributed to a slightly thicker and more energetic boundary layer in the former. Finally, this extra noise source also explains the difference between Amiet's and Ffowcs Williams and Hall's results as it is included in the former (measured wall-pressure fluctuations including this acoustic contribution at RMP26) and not in the latter (the CDP incompressible velocity field having no acoustic information).

Finally the full LBM model of the anechoic experimental set-up has also been extended recently to a lower angle of attack of 5° [48], for which there is a flow bifurcation and a complete change of flow topology and noise signature: additional intermittent tones are now found on top of a broadband hump, corresponding to laminar boundary layer instability noise, as pointed out experimentally by Padois et al. [186]. To capture and understand the intermittent tonal noise, this simulation required much longer simulation times to be able to capture the intermittency observed in both the flow field and the acoustic far field: 50 flow-through times were needed to fully capture the breathing of the LSB that had moved close to the trailing edge, and was alternatively shedding strong and short energetic rollers (intense events) and soft and thin ones (quiet events) as shown by the iso-contours of $Q$ criterion in Fig. 20(c). These rollers are seen to break down and to trigger transition to turbulence close to the trailing edge, and to provoke the consequent intense modulated tonal noise seen in the dilation field (characterized by a much larger wavelength corresponding to about 1 kHz than the wavefronts seen in the reference case in Figs. 20 (a) and (b)). Very good agreement with experiment was again observed by Sanjose et al. [48], and several modal analysis showed that the tonal noise is not seen to come from Tollmien–Schlichting waves forming in the laminar boundary layer as previously conjectured, but rather from a Kelvin–Helmholtz instability generating these rollers that break down near the trailing edge and causing another form of trailing-edge noise. A linear stability analysis also showed that Kelvin–Helmholtz waves are only convectively unstable and that only the intense events could sustain the instability, explaining the observed intermittency of the tonal noise in this particular configuration. Similar results and flow features have also been reported recently by Winkler et al. [25] on a NACA 6512–63 airfoil. Two different compressible DNS with a tripped and an untripped airfoil were run: the latter showed similar flow features (unstable LSB on the aft of the airfoil shedding rollers that break down close to the trailing edge) and much more complex dilatation field patterns also suggesting strong tonal noise on top of a broadband hump. More details can be found in [165]. The number of flow-through times was limited to 5, too short to observe any intermittency or noise modulation that could have been deciphered with the same modal analysis as on the CD airfoil.

Overall the compressible DNS have already shed a lot of light on the different airfoil noise mechanisms at transitional Reynolds numbers, and highlighted several additional noise sources and much more complex noise generation mechanisms than the previous hybrid method combining incompressible LES and acoustic analogies. They have confirmed that, for the often dominant trailing-edge noise scattering, most of the assumptions underlying the above analytical models can be justified and used as first approximations for self-noise predictions of more complex systems such as rotating machines (see Section 6). Finally, current DNS capabilities correspond to Reynolds number slightly above $10^5$, but the next decade will reach $10^6$. Moreover, some recent DNS results in free space have been presented on airfoil noise during flow separation and stall at high angles of attack [187]. As pointed out above for the CD airfoil at high angle of attack, the issue in this case is the effect of the spanwise domain size. Consequently, those simulations are still limited to low Reynolds numbers ($Re_c = 5 \times 10^4$).

### 3.4. Noise control

High-fidelity numerical simulations such as LES or DNS provide a detailed insight into flow turbulence physics that is related to trailing-edge noise reduction. Low-fidelity numerical simulations offer an opportunity to explore a wide range of design parameter spaces, or an optimization of shapes or flow control inputs.

Several passive trailing-edge noise control devices, namely serrations and porous appendices, have been simulated by LES or DNS using the different approaches described in Sections 3.2 and 3.3. For instance, incompressible LES of serrated airfoils were first tackled by Winkler [188] on a NACA 6512–63 airfoil at 0° angle of attack in the Siegen experimental set-up as described above. Several serrated configurations combined with the slotted configuration [158] were simulated showing the correct experimental trend. The serrations were found to reduce the wall-pressure fluctuations on the edges and also the spanwise correlation length on the serrations (Figs. 6.16 and 6.17 in [188]). Arina et al. [189] then combined a compressible LES with Ffowcs Williams and Hawkings's analogy to simulate a NACA 65–1210 airfoil in free field at a small 5° incidence. Note that slightly blunt serration tips and roots were introduced to ease the grid generation and to limit the computational effort. They reproduced the Overall Sound Pressure Level (OASPL) directivity measured at the University of Southampton quite satisfactory, and showed that the noise reduction is mostly achieved at low and mid-frequencies, which could be traced to the modification of the flow separation at the trailing edge seen in the clean airfoil. However, there was no assessment of the possible aerodynamic impact. A similar methodology was later used on serrated cambered SD2030 airfoils (either isolated or in cascade) by Ji et al. [190]. They showed marginal agreement with parallel experiments. They also found an overall 3–4 dB noise reduction with serrations, but also a significant undesired reduction of aerodynamic performances (60% lift reduction). They attributed the noise reduction to a funneling motion, caused by the generation of streamwise-oriented vortices at the root of the trailing-edge serrations. Taking advantage of the flexibility of the LBM/VLES framework, Avallone et al. [178] studied the noise-reduction mechanisms of sawtooth and combed-sawtooth trailing-edge serrations on a NACA 0018 airfoil, and confirmed Ji's findings on the streamwise-oriented vortices. The main findings are summarized in Section 4.

On the DNS side, Sandberg and Jones [191,192] were the first to look at the effect of trailing-edge serrations on a NACA 0012 in free-field at a low Reynolds number of $5 \times 10^4$ at a 5° incidence. They used flat-plate trailing-edge extensions. They found that the overall hydrodynamic field on the airfoil was not significantly affected upstream of the serrations and that the noise reduction was mostly achieved in the high frequency range caused by the effect of the serrations upon the diffraction process, consistently with the analytical model predictions in Section 2. Moreover, the secondary noise source in the reattachment region of the LSB was not modified. Sanjose et al. [193] were then the only ones to actually simulate the open-jet wind tunnel environment and demonstrated similar noise gains as in experiments on the CD airfoil at 8° incidence and a Reynolds number of $1.5 \times 10^5$ [44]. They considered fully three-dimensional serrations that preserved the airfoil shape and demonstrated that the serrations hardly modified the clean airfoil loading shown in Fig. 18. Similarly to Sandberg and Jones, they found that the noise reduction was achieved at high frequencies by a modification of the diffraction process and that the flow statistics were hardly modified before the serrations [44]. The latter result has also been confirmed experimentally by Avallone et al. [194] on a NACA 0018 airfoil. Besides generalizing the previous DNS results to a 3D serration configuration on an industrial cambered airfoil, Sanjose et al. [193] also showed that one of the noise reduction mechanisms was actually to alleviate the small vortex shedding that occurred on the straight airfoil pressure side as shown in Fig. 21 (zoomed view at the trailing edge on the pressure side). Finally, as shown in Section 2 (Figs. 8 (b) to (d)), the prediction of Ayton's analytical model compares very well with this DNS data.

Consequently, the latter has been selected for low-fidelity numerical simulations of the noise mitigation by serrations by Kholodov and Moreau [57–59]. They performed an optimization of the serration shape including slits based on the CD airfoil flow characteristics, and showed that the sharper serrations achieve the more noise reduction [57], and that for increasing serration wavelengths, the serration shape for optimal noise reduction smoothly changes from ogee to sawtooth, and from sawtooth to sinusoidal or iron shape [58]. They also showed that the effect of slits distributed on the main serration shape appears at high frequencies and noise reduction up to 20–30 dB can be achieved [58]. When adding additional aerodynamic constraints on the lift-to-drag ratio and the moment coefficient respectively, the maximum noise reduction achieved at high frequencies is significantly reduced to about 4 dB, and this gain is primarily limited by the decrease in the moment coefficient of the serrated airfoil [59].

Simulations on porous or compliant trailing edges are much more limited. Bae and Moon [195] were probably the first to apply LES on a thick flat plate at 0° and 5° incidences and a Reynolds number of $1.3 \times 10^5$, to study the effect of a passive porous surface on trailing-edge noise. They used a continuum approach and a volume-averaging method that considers an incompressible flow in a rigid homogeneous porous medium. The closure model for the drag force is given by Ergun's equation, which includes the linear Darcy's law corrected by a non-linear term [196]. This intrinsic pressure can be reformulated into a superficial average pressure with the non-linear Dupuit–Forchheimer relationship [197]. Bae and Moon showed a significant tonal noise reduction of 13 dB at 0° incidence, which is caused by the reduction of the spatial correlation length of the wall pressure fluctuations in both streamwise and spanwise directions. 3–10 dB noise reduction was

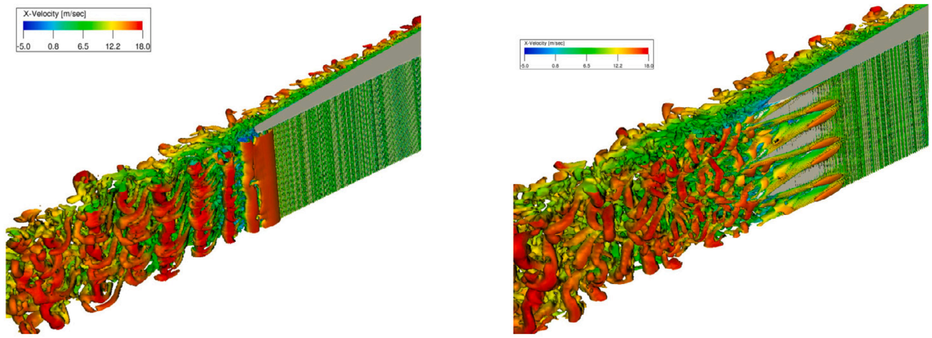


(a) (b)

**Fig. 21.** PowerFLOW DNS results [166] of iso $Q$-criterion contours colored by the velocity magnitude at a geometrical angle of attack of 8° on a CD airfoil: (a) the straight edge [165] and (b) the serrated edge. (For interpretation of the references to color in this figure legend, the reader is referred to the web version of this article.)

also obtained over a broad frequency range at 5° incidence. Similar numerical approaches have been recently applied by Koh et al. [198] and Ananthan et al. [199]. Koh et al. [198] again considered thick flat plates at 0° incidence and a similar Reynolds number of $1.35 \times 10^5$, but with different trailing-edge shapes. The noise reduction by the porous medium reached 11 dB for a sharp corner, and only 4 dB for a semi-circular trailing edge. It was again coming from a massive reduction of the vortex-shedding tone, and the directivity was modified by the porous trailing edge in the high frequency range. On the other hand, Ananthan et al. [199] considered a 3D cambered DLRF16 airfoil at −0.5° incidence and a higher Reynolds number of $10^6$. Note, however, that only the trailing-edge region is resolved in a LES mode. They also observed a significant noise reduction of up to 12 dB in the low to mid frequency regime. However, a noise increase at the mid to high frequencies was attributed to the friction between the flow and the surface (roughness noise). A similar method has also been recently applied to the airfoil leading-edge problem and successfully compared to some analytical RDT results on an equivalent cylinder by Zamponi et al. [200]. Yet, a similar comparison with the analytical models described in Section 2 is still needed for the trailing-edge noise mechanism. Within the hybrid LBM/VLES method, a similar model using an equivalent fluid region for a homogeneous porous medium has been implemented [201]. Teruna et al. [202] studied the noise generation from a NACA 0018 airfoil at 0° incidence and a Reynolds number of $2.8{\times}10^5$, with and without a porous trailing edge. They found the same noise abatement by up to 9 dB in the low frequency range as in the parallel experiment by Rubio Carpio et al. [203]. They showed that the porous surface behaves as continuous trailing edges with acoustic scattering at multiple locations. They also noted that the flow statistics were hardly changed upstream of the treated area, similarly to the above findings with serrations.

In all the above simulations the airfoil trailing edge cannot deform, which is not the case, for instance, in the silent flight of owls [204]. Recently, Nardini et al. [205] performed a DNS on an elastic trailing-edge and studied the effect of its structural compliance. By performing an acoustic decomposition to separate the contribution of the motion-induced noise from the scattering due to the interaction of the incident fluctuations with the trailing edge, they showed that the noise reduction is mostly achieved when the relative phase and amplitude of these two acoustic contribution ensure their mutual cancellation. This could yield interesting noise mitigation strategies in the future.

Finally, Bodling and Sharma [206,207] used LES to investigate the trailing-edge noise reduction with finlet, a passive noise control device inspired by owl wings developed by Clark et al. [208] (see Section 4.2.5). They found that finlets lift up turbulent eddies in the boundary layer so that the associated noise is reduced. Shi and Lee [209] used RANS CFD to efficiently predict noise reduction with finlets. They found similar results with LES outcomes. They addressed that the velocity deficit in the boundary layer plays a role in noise reduction. Shi and Lee [210] also studied a 2-D bump for noise reduction. The bump retards the velocity and reduces the turbulent kinetic energy in the boundary layer so that the trailing-edge noise is reduced. However, this bump may increase the bluntness noise so that it should be carefully used. Chen and Lee [118] proposed a concave shape of a trailing edge by controlling a boat-tail angle using a high-order polynomial function. The concave shape effectively reduces the thickness of a trailing edge and the pressure gradient values, hence resulting in noise reduction. The optimized concave shape was found to decrease the noise levels by 4 dB while slightly increasing the lift-to-drag ratio.

### 3.5. Outlook

Empirical and semi-empirical models have many advantages in terms of the computational cost and data processing. These methods are typically used in industrial design practices. The importance of these methods will be continued.

A fully parametric model such as the BPM model provides a very rapid evaluation tool of trailing-edge noise. In this context, it is attractive during the early design phase of, e.g. a wind turbine rotor. However, the simplified physics on which it is based upon limits its accuracy and range of applicability. Better tunings may be achieved, but the method is intrinsically limited by these hypotheses.

More advanced engineering models involving a more detailed description of the physics involved have subsequently emerged. TNO-type models attempt to address the above limitations by distinguishing and solving separately the boundary layer turbulence and the acoustic scattering occurring at the trailing edge. Nevertheless, these models are still based on a number of assumptions that also restrict their accuracy. In particular, boundary layer turbulence is dealt with simplified and generic spectral models that do not fully account for a number of phenomena, such as intermittency or the spatially varying characteristics (e.g anisotropy) of turbulence across the boundary layer. It is expected that improvements may be achieved for this part of the model by resorting to more advanced either theoretical or modeling approaches. Indeed, so far, TNO-type models rely on flow solvers, such as integral boundary layer solvers (e.g. XFOIL) or CFD-RANS flow solvers. The associated assumptions about the boundary layer flow may be relaxed by resorting to more exhaustive experimental data, and more advanced models such as LES or DNS. The former should already be available at transitional Reynolds numbers and applied to more flow conditions (the complete polar range for instance). The latter should provide further insights into possible additional noise sources (LSB, wake sources) and some insights on how to model them. With increasing computational resources, higher Mach numbers and consequently higher Reynolds numbers could also be tackled.

Recently, several empirical wall pressure spectrum models were developed for adverse pressure gradient flows. Some of these models demonstrated the success of predicting airfoil trailing-edge noise. It is expected that these models will be continually used for airfoil trailing-edge noise predictions or other application problems due to an easy and fast calculation. However, the accuracy of these models is questionable for large favorable pressure gradient flows. Although the suction side with adverse pressure gradient flows dominates the noise spectrum, empirical models need to be further refined for large favorable pressure gradient flows to accurately predict high-frequency noise generated from the pressure side. All the empirical models have inherently a valid range corresponding to the calibrated experimental data. Outside this calibrated range, the accuracy is not guaranteed. For example, there are no accurate empirical models that predict noise in a separated flow region, mainly due to a lack of experimental data. Empirical wall pressure spectrum models for separated flows can be developed in conjunction with experimental activities. However, it is hard to justify the need to develop an empirical wall pressure spectrum model for highly separated flows since the low- or medium-fidelity aerodynamic solvers, such as steady RANS, would not provide accurate boundary layer flows for highly separated flows, which are inputs to the wall pressure spectrum models. If LES or DNS is used for separated flows, more accurate wall-pressure spectrum can be directly obtained from the CFD outputs, so that empirical models are no longer needed. Physics-based reduced order models could then be built from such numerical data bases.

Several RANS-based statistical turbulence models were developed in the past decade. The prediction accuracy of these models still depend on many semi-empirical parameters to characterize the turbulent velocity or cross-spectrum. A comparison with more experimental and LES/DNS data will assist the further refinement of these parameters and models.

Finally, it is expected that LES/DNS will be more used in various noise control concepts, as described in Section 4, to provide detailed flow physics that may be elusive in experiments. These high-fidelity simulations will further guide and fine-tune RANS-based semi-empirical models for various designs.

## 4. Experimental approach

Before surveying the important milestones in the measurement of airfoil trailing-edge noise, we first present a brief overview of the characteristics of airfoil trailing-edge noise obtained experimentally in the open jet wind tunnel at the University of Southampton. Measurements of the spectrum of radiated acoustic pressure were made by Gruber [41], a PhD thesis, due to a NACA 65(12)-10 airfoil at a single microphone located at 1.2 m and 90 degree from mid-span of the trailing edge with 0.15 m chord and 0.45 m span at 0 geometric angle of attack at a flow speed of 40 m/s. A trip was located at 10% of the chord to force the boundary layer to turbulence. The pressure spectrum is shown in Fig. 22(a) as a blue curve. For comparison is the corresponding spectrum, shown as a red curve, obtained when a turbulence grid is located within the jet nozzle and the in-flow turbulence intensity increases from about 0.45%, without the grid, to approximately 2% when the grid is added. The background noise spectrum due to the jet shear layers and due to the grid are also shown, which is only a few decibels below the trailing-edge noise at high frequencies, indicating the difficulty with using single microphones for airfoil self-noise measurements.

In this example, the noise due to the interaction of this turbulent flow with the leading edge is significantly greater than that due to the tripped boundary layer interacting with the trailing edge at all frequencies up to about 5 kHz. At frequencies greater than about 10 kHz trailing-edge noise becomes the dominant noise source. Clearly, therefore, in flows with much lower, more realistic levels of turbulence intensity (< 0.5%), such as that encountered by wind turbine blades, trailing-edge noise is the dominant airfoil noise source over most of the frequency range.

Both the leading edge and trailing edge acoustic pressure spectra can be seen to oscillate with frequency. This feature of airfoil spectra provides direct evidence that the equivalent radiating source distribution is the result of edge scattering of the turbulent flow, which is in the form of a highly coherent (dipole) source distribution along the airfoil chord, that interferes in the far field leading to the oscillations in the spectra and single-frequency directivity, shown in Fig. 22(b). This behavior is accurately reproduced from the flat plate theories discussed in Section 2.

Fig. 22(b) also shows a comparison between the measured and predicted directivity of the NACA 65(12)-10 airfoil at the non-dimensional frequency of $fc/U = 15$, where $c$ is the chord and $U$ is the flow speed. It is characterized by a main radiation lobe pointing upstream of the flow direction, suggesting that the boundary layer is back-scattered at the trailing edge, with a number of minor side lobes. The measured data is indicated by * where good qualitative agreement with predictions are obtained. Note the absence of microphone data well downstream due to the presence of the jet, and well upstream due to the presence of the nozzle. Similar results have also found on the CD airfoil provided the diffraction at the nozzle lips is accounted for (see Fig. 9 in [21]).

Also shown in this figure as a red curve is the corresponding directivity with the introduction of a serration at the trailing edge, which will be discussed later. As shown explicitly by the theoretical analysis of trailing-edge noise by Amiet [19] and its extension [20] in Section 2, the far-field noise pressure PSD (Power Spectral Density) may be expressed directly in terms of the boundary layer pressure spectrum evaluated sufficiently close to the trailing edge such that it is representative of the impinging flow on the trailing edge and is not influenced by the scattered wave. For accurate trailing-edge noise predictions, therefore, it is essential that the characteristics of the turbulent boundary are known just upstream of the trailing edge where scattering into acoustic radiation occurs.

### 4.1. *Trailing-edge noise measurements and mechanisms*

#### 4.1.1. *Early trailing-edge noise measurements (1970's - early 1980's)*

Experimental investigations into the characteristics of airfoil trailing-edge noise began in the early 1970's, roughly at the same time as the mechanisms of trailing edge radiation were being mathematically formulated in terms of the amplification of weakly radiating convected hydrodynamic pressure fluctuations near the trailing edge [6,211,212]. One of the main barriers to making accurate airfoil trailing-edge noise measurements in aeroacoustic wind tunnel facilities was their high levels of background noise due to, for example, the tunnel nozzle lips, the open jet turbulent shear layer and the downstream collector, which tended to mask the airfoil noise, particularly at high flow speeds. Much of the early work on trailing-edge noise measurements have therefore focused on the use of measurement and signal processing techniques that provide reductions in facility noise. This issue remains a problem today, particularly in large facilities at high flow speeds. This section provides a review of some of the seminal experimental work on TE noise measurement and its radiation mechanism. Note that this review is not exhaustive but is meant to convey the important issues in the measurement of airfoil trailing-edge noise.

One of the first published accounts of airfoil trailing-edge noise measurement was by Paterson et al. [213] at the United Aircraft Research Laboratories (UARL) and Sikorsky Aircraft Division. This early work encapsulates most of the important issues in measuring airfoil trailing-edge noise and the characteristics of its far-field radiation. Trailing-edge noise measurements were made on NACA 0012 and NACA 0018 airfoils with 0.24 m chord at a range of Reynolds number of $8\times10^5$ to $2.2\times10^6$ at various angles of attack in an open-jet facility within an anechoic chamber. Side plates were used to maintain a 2D mean flow over the span of the airfoil. A number of $1/4''$ flush-mounted microphones

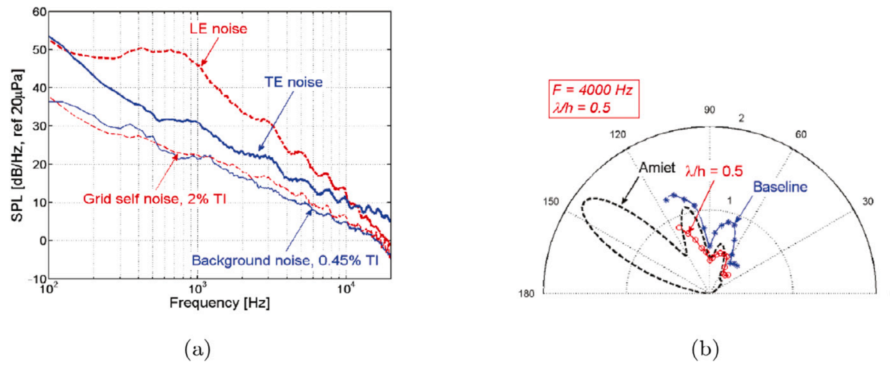


**Fig. 22.** (a) Sound Pressure Level Spectral Density due to a NACA 65(12)-10 airfoil with and without grid turbulence (Source: Gruber [41]) and (b) a comparison between the measured and predicted directivity of a NACA65(12)-10 airfoil noise at the non-dimensional frequency of $fc/U = 15$. (For interpretation of the references to color in this figure legend, the reader is referred to the web version of this article.)

were embedded into the airfoil to measure pressure fluctuations at various chordwise and spanwise locations along the airfoil surface due to the turbulent boundary layer. A single microphone 2 m above the airfoil trailing edge in the mid-span plane was used to measure the far-field noise. This measurement configuration and sensing arrangement remains today the standard procedure for measuring airfoil trailing-edge noise. Processing was limited to single-channel data and spectra limited to 1/3 octave and 10 Hz bandwidths.

At the lower Reynolds numbers the spectra were found to contain numerous tones arising from laminar instability waves, but which disappeared once the Reynolds number was increased and the boundary layer transitioned to turbulence. The use of trips on the airfoil suction side had little effect on the presence of tones but suppressed the tones when located more than 80% chord on the pressure side. At the highest Reynolds numbers, airfoil noise was completely masked by the background facility noise.

Another important early experimental study into the measurement of trailing-edge noise was by Yu and Joshi [214], who presented an experimental study of the trailing-edge noise from an uncambered NACA 63–012 with 0.61 m chord made in an open-jet aeroacoustic facility. Surface pressure transducers were used to monitor the pressure fluctuations beneath the boundary layer. Measurements were made at Reynolds numbers of $1.22 \times 10^6$ and $2.21 \times 10^6$. One of the innovations of this study was that surface pressure fluctuations on the upper and lower surfaces were made simultaneously with a single far-field noise measurement, allowing the causal relationship to be examined between hydrodynamic pressure fluctuations near the trailing edge and its subsequent radiation to the far field through measurements of their space–time correlation. However, the surface pressure probes were later shown to be insufficiently close to the trailing edge to provide a sufficiently accurate assessment of the boundary layer flow arriving at the trailing edge. The spectra measured simultaneously near the trailing edge on the pressure and suction sides were found to differ by nearly 180°, thereby providing an evidence, for the first time, of the existence of the Kutta condition.

A milestone in the understanding of airfoil trailing-edge noise obtained through measurement was made in 1981 by Brooks and Hodgson [68]. They provided the first detailed survey of the two-point surface pressure statistics near the airfoil trailing edge, comprising both the impinging hydrodynamic boundary layer pressure field and the subsequent near field scattered contribution responsible for the far-field radiation. Noise and aerodynamic noise measurements were made on a symmetric NACA 0012 airfoil with 0.61 m chord in the Quiet Flow Facility (QFF) at NASA Langley Research Center. Various hardwood extensions were introduced to the main airfoil body to study the effect on trailing-edge noise of edge thickness, ranging from a 'sharp' edge to 2.5 mm. Surface pressure sensors were embedded flush to both upper and lower surfaces along the airfoil chord and span of the airfoil. The furthest downstream sensor was 2.54 mm, or 0.42% chord, from the trailing edge. Far-field pressure measurements were made using an arc of sensors at mid-span and the results were corrected for shear layer refraction [215]. Measurements were made at a range of flow speeds and angles of attack, with and without boundary layer tripping. Pitot tubes were used to determine the boundary layer profile.

Power Spectral Density measurements of the boundary layer pressure spectrum indicated evidence of a characteristic frequency $f \sim \delta^{-1}$ linked to the boundary layer thickness $\delta$, which determines the largest eddy size in the boundary layer. Chordwise coherence measurements of the surface pressure indicated the extent to which the boundary layer deviated from the 'frozen' behavior, assumption universally made in airfoil broadband noise prediction models, whereas the spanwise coherence $\gamma$ was found to decay faster with frequency and spanwise separation distance $y_3$ (see Fig. 3) and roughly follow $\gamma = \exp(-\zeta\omega y_3/U_c)$, where $\zeta$ is an empirical constant of 0.62. The spatial integral of $\gamma^2$ with respect to $y_3$ determines the frequency-dependent coherence length, which appears explicitly as a multiplicative factor in the expression of the far-field pressure PSD due to trailing-edge noise from a flat plate [19]. A frequency-dependent phase speed of the surface pressure was determined from the phase spectrum between two chordwise sensors and found to slow as frequency is increased. The two-points statistics of the surface pressure fluctuations were used to determine the empirical constants of a frequency–wavenumber spectral density proposed by Chase [211] and Chandiramani [212] of the incident boundary layer field for use in the model of the unsteady surface pressure distribution, including near field scattering from the trailing edge, proposed by Howe [3], following the work of Chase [211]. This formulation was used to predict the cross spectrum of surface pressures between any two points on the same surface and between two points on opposite surfaces. The magnitude and phase of measured chordwise surface pressure cross spectrum was shown to be in close agreement with the theoretical predictions, thereby providing a direct confirmation of the existence of the scattered field due to the trailing edge.

Another innovation in this study is that the far field trailing-edge noise was determined from the coherent part of the signal between two microphones equally spaced on opposite sides of the airfoil trailing edge, by exploiting the anti-symmetry of the radiated field, and that background noise is mutually incoherent with the airfoil noise.

#### 4.1.2. Brooks, Pope and Marcolini (1989)

Even today, the prediction of airfoil trailing-edge noise due to an airfoil of an arbitrary geometry remains highly challenging. The problem is not with predicting the effect of the trailing edge on the convecting boundary layer flow but with the prediction of the characteristics of the turbulent boundary layer itself under the influence of a pressure gradient as it convects toward the trailing edge.

Brooks et al. [46] placed a series of two-dimensional NACA 0012 airfoil, of chord lengths varying from 2.54 cm to 30.48 cm, and angle of attack (AoA) between 0° and 25.2° in the test section of the Quiet Flow Facility at NASA Langley at flow speeds of up to 70 m/s, corresponding to a maximum chord-based Reynolds numbers of 1.5 million. Airfoil trailing-edge noise measurements were made in 1/3 octave bands using the two-microphone technique described in Brooks and Hodgson [68] located at 90° to the trailing edge. Measurements were made without and with a boundary layer trip to ensure transition to turbulence. Flow measurements were conducted using hot wire anemometry in NASA Langley's QFF. Boundary layer displacement and momentum thickness were calculated using a three-dimensional traverse of a single-wire and cross-wire. The prediction methods based on these experiments, so called the BPM model, were described in Section 3.1.1.

#### 4.1.3. Modern trailing-edge noise measurements

Since these early studies, there have been a number of detailed experimental investigations into the measurement of airfoil trailing-edge noise, aimed mostly at understanding the relationship between airfoil geometry, angle of attack and Reynolds number and radiated self-noise. It is noteworthy that while measurement techniques have been considerably improved, the basic measurement principles remain the same as in 1973 with the pioneering work of Paterson et al. [213]. One particular innovation used in modern measurements is the use of large multi-channel phased array systems for generating source maps and suppressing background noise. Usually, however, their spatial resolution is constrained by the acoustic wavelength. These techniques are particularly useful in highly reverberant environments, such as in closed tunnels or when excessive levels of facility noise are present. We now present a brief survey of some recent airfoil self-noise measurements.

A significant research effort into the understanding of airfoil trailing-edge noise was undertaken in the open jet wind tunnel at the Laboratoire de Mécanique des Fluides et Acoustique of ECL. This work involved many different airfoils at lower and transitional Reynolds numbers, including flat plates, NACA0012 and several low-speed fan profiles. The largest body of experimental data is however on the industrial cambered CD airfoil [21,26,109,142,216]. The latter has been intensively used in propulsion systems (compressor and turbofan blades) and ventilation systems (automotive and aerospace applications).

An illustration of this work is found in Moreau and Roger [26], in which the effect of trailing-edge noise due to variations in mean loading were investigated for the CD airfoil. The airfoil was placed at the exit of the wind-tunnel nozzle and was instrumented with several remote microphone probes clustered at both the airfoil leading and trailing edges. The surface pressure statistics were collected at a chord-based Reynolds number $Re_c$ up to $2.9 \times 10^5$ at various geometrical angles of attack ranging from −5° to 27°. Yet, the most studied case used in Sections 2 and 3 is $Re_c \simeq 1.5 \times 10^5$ at 8°. A particular novelty of this work is that the airfoil was placed in two different open jet facilities with jet widths of 0.13 m and 0.5 m, which was recently complemented by an additional jet width of 0.3 m in the recent UdeS anechoic wind tunnel [217]. Note that the latter experiments involve very low background noise (down to −20 dB) and have extended the experimental frequency range for the lowest speeds significantly (covering the whole range of interest up to 10 kHz). The radiated sound was measured simultaneously with the wall-pressure fluctuations close to the trailing edge. In the ECL experiments, two different flow regimes at two different incidences were investigated in detail. On the airfoil suction side they correspond to an attached turbulent boundary layer triggered by a thin LSB at the leading edge (8°), and to a large flow separation from the leading edge (15°) respectively, as later evidenced by the LES results shown in Section 3.2 (see Fig. 15). The two jet width configurations provide some insight into the "cascade" loading effect. Measurements at the larger jet width were found to trigger an earlier onset of leading edge flow separation and larger LSB than at the smaller jet width because of the reduced flow guidance by the jet shear layers [142]. The transition to turbulence then occurs earlier in the larger nozzle, resulting in higher levels of pressure fluctuations near the trailing edge. Both jet widths still trigger the same overall wall-pressure spectra for the same flow regime, but no equivalent angles of attack can be defined for this airfoil. Two different speeds were also investigated, which provided some insights into the Reynolds-number effect on the trailing-edge noise. No significant change of flow regime was observed for the same incidence, and only larger spectra levels were obtained for the higher speed, confirming the dipolar nature of trailing-edge noise. Surface pressure measurements on the suction and pressure sides were found to exhibit two distinct behaviors. Pressure fluctuations were hydrodynamic in nature on the suction side (turbulent boundary layer), while they were acoustic in nature on the pressure side (laminar boundary layer). High levels of intermittent fluctuations were observed at the leading edge typical of a transitional boundary layer with a LSB, whereas the statistics of the surface pressure were found to be highly stable at the trailing edge. All wall-pressure spectra measured from the mid-chord up to the trailing edge, were observed to follow a clear $f^{-5}$ frequency power-law above a threshold frequency, which scales with a Strouhal number based on the local suction side boundary layer thickness (see Fig. 12).

Another notable study on trailing-edge noise measurement was by Shannon and Morris [218], in which the radiated sound spectra produced by a trailing edge model with 0.91 m chord was measured using a large aperture 40 microphone phased acoustic array at flow speeds between 15 m/s and 30 m/s. Their signals were processed using the three beamforming algorithms, delay–sum, weighted Cross Spectral Matrix (CSM), and the deconvolution-based method DAMAS for localizing the "sources" on the airfoil and suppressing the background facility noise. Each method was found to have their own pros and cons depending on the frequency range of interest and the relative magnitude between the parasitic source and the source of interest. In general, DAMAS was found to provide the best rejection of parasitic noise for frequencies greater than 500 Hz, below which the DAMAS results failed to converge. The CSM results were found to be superior to the delay–sum method in the frequency range $250 < f < 500$ Hz, while the delay–sum algorithm provided the least overall rejection of parasitic noise, but was still effective at the very low frequencies ($f < 250$ Hz) where the CSM was not well defined. For both the CSM and DAMAS methods, the importance of appropriately defining the integration region was demonstrated. A composite spectrum was generated at each flow speed by selecting the algorithm that was found to produce the least bias error for a given frequency range.

At roughly the same time, noise measurements were conducted at Notre Dame involving an airfoil trailing edge similar to that previously used by Blake and Gershfeld [219]. A flat strut with a 0.91 m chord, was placed in Notre Dame's Anechoic Wind Tunnel (AWT) [220]. A boundary layer trip was applied to the airfoil, which was tested at Reynolds numbers from $1.2 \times 10^6$ to $1.9 \times 10^6$. Surface pressure fluctuations were measured near the trailing edge, and far-field noise was simultaneously collected with a large aperture microphone array. In a separate closed-walled facility, Particle Image Velocimetry (PIV) was used to characterize the flow field near the trailing edge. Flow measurements from the phase-locked PIV compared against the computed acoustic spectra were qualitatively compared.

Extensive measurements on airfoil trailing-edge noise was also made at NLR in the Netherlands, which also focuses on the development of phased array measurements and the effect of the sideplates on the noise measurements [221]. It was shown that significant measurement errors can occur by the use of rigid sideplates, which can be reduced by the use of sound absorbing plates.

### 4.2. Noise control

#### 4.2.1. Conventional sawtooth trailing edge serrations

The early pioneering work on trailing-edge noise in the 1970's established conclusively that the airfoil trailing edge plays an essential role in trailing-edge noise generation by converting the kinetic energy of the boundary layer vorticity passing over it into acoustic wave motion. It is, therefore, somewhat surprising that the notion of modifying the trailing edge geometry to weaken its scattering efficiency, and hence reduce noise, was not properly investigated until the 1990's. Possibly inspired by the structure of the wings of owls [204], which are well known for their quiet flight, researchers began considering the use of serrations, or undulations, onto airfoil trailing edges for reducing noise. Trailing edge serrations were shown theoretically by Howe [39] to produce reductions in radiated trailing-edge noise by a mechanism associated with cancellation effects along the oblique trailing edge of individual Fourier components of boundary layer pressure (see Section 2.2.2).

In this section, we review some of the experimental studies on the use of simple "sawtooth" trailing edge geometries for the reduction of trailing edge self-noise, the geometry of which is characterized by a peak-to-height distance of $2h$ and a wavelength $\lambda$ as shown in Fig. 7. We emphasize that this review is not exhaustive but is intended only to illustrate our current understanding of noise reductions obtained through trailing edge serrations. The performance of more recent innovative serration geometries will be discussed below in the next subsection. One of the first documented measurements of trailing-edge noise reductions through serrations was by Dassen et al. [222]. Trailing edge serrations with an amplitude of 25 mm and wavelength of 5 mm was attached to six flat plates and eight 2D NACA airfoils of 0.25 m chord length at the chord-based Reynolds numbers $Re_c$ of $7\times10^5 < Re_c < 1.4\times10^6$. Noise reductions of up to 10 dB in the frequency range of 1 kHz to 6 kHz for the serrated flat plates were reported. Noise reductions were found to be only weakly dependent on the inclination angle of the trailing edge, but was found to be significantly influenced by misalignment of the serrations with respect to the flow direction and chord plane. Deviations by 15° were found to increase the radiated noise by up to 10 dB. Furthermore, measured noise reductions were found to be significantly smaller than that predicted by the theoretical model of Howe [39]. Largest noise reductions were achieved at low to mid frequencies, while noise increases were observed at high frequencies. Whilst no spectra were provided in their paper, this early measurement encapsulates the general characteristics of the noise reduction spectra due to trailing edge serrations on airfoils.

The application of serrations to the airfoils used on wind turbines was undertaken by Oerlemans et al. [223], who measured the noise reductions in model-scale wind turbine blades. Serration plates with a relatively thin thickness of 2 mm were mounted to the pressure side of the outer 12.5 m of the wind turbine blade with a rotor diameter of 94 m. The length of the serration plates was maintained at about 20% of the local chord, resulting in the serration length to becoming a function of the rotor radius. To give some perspectives, the smallest and largest serration length is 10 cm and 30 cm at the tip and the most inboard position, respectively. The authors also took care to align the plane of the serration with the flow direction to prevent high frequency noise increase due to the cross-flow through the sawtooth gaps, as well as to minimize the impact on the aerodynamic loading. After appropriately optimized with the serrations, overall reductions of 6–7 dB in turbulent boundary layer trailing-edge noise were recorded over a variety of flow conditions, with insignificant changes in aerodynamic performance. Oerlemans et al. [223] and Hurault et al. [224] applied these optimized serrations to full-scale wind turbines. Noise reductions were found to be lower than that obtained under laboratory conditions but still worthwhile at frequencies below 1 kHz where average overall sound power level reductions of 3.2 dB were reported for the upwind measurements on the clean rotor, and 1.2 dB and 1.6 dB reductions for the downwind measurements on the clean and tripped rotor, respectively. More in-depth discussion on the application of serrations for the reduction of wind turbine noise can be found in Section 5.1.

Later, Gruber et al. [225] and Moreau and Doolan [226] investigated experimentally the influence of different parameters on the noise reduction performance of flat plate serrations inserted into a cambered airfoil and flat plate, respectively. Moreau and Doolan [226] have investigated experimentally the acoustic and aerodynamic effects of trailing-edge serrations on a flat plate at low-to-moderate Reynolds numbers ($1.6\times10^5 < Re_c < 4.2\times10^5$). The main body of the flat plate has a span of 450 mm and a thickness of 6 mm with an elliptical leading edge. Two different serration geometries were compared, with a fixed root-to-tip amplitude of 2h = 30 mm and two different wavelengths of $\lambda$ = 3 mm ($\lambda/h$ = 0.2) and with $\lambda$ = 9 mm ($\lambda/h$ = 0.6). The serrated and reference plate models have the same mean chord of 165 mm. Reductions in overall SPL by up to 3 dB were observed in broadband trailing-edge noise. Noise reduction were found to depend on Strouhal number $St_\delta = f\delta/U$ and the serration wavelength. Theoretical predictions of the noise reductions due to Howe were in poor agreement with experimental data. Contrary to predictions, however, the wider serrations with larger wavelength-to-amplitude ratio $\lambda/h$ were found to provide superior noise reductions to narrower serrations by achieving higher attenuation levels and no noise increase in the mid-frequency region. Unsteady velocity data in the very near wake of the straight and serrated trailing edges suggested that, for this particular configuration, the noise-reduction capability of trailing-edge serrations is related to their influence on the hydrodynamic field at the source location rather than on a reduction in sound radiation efficiency at the trailing edge. Moreau and Doolan [226] therefore concluded that the main reason for the discrepancy between measured and predicted reductions is the effect of the serrations on the impinging boundary layer turbulence, which are not included in Howe's theoretical predictions. Note, however, that this is somewhat in contradiction with all the current DNS results reported in Section 3.4, which did not show any significant modification of the incoming turbulent flow statistics by the serrations [44,191–193]. This will also be corroborated by several more recent experiments described below.

Gruber et al. [227] have investigated the noise reductions from over 30 serrated trailing edges with different sawtooth geometries on a cambered NACA 65(12)-10 airfoil with 450 mm span and 150 mm chord. Their measurements of the effect on noise reductions due to varying serration wavelengths are illustrated in Fig. 23, which presents the sound power level spectra for different serration wavelengths at a fixed value of serration height $h$ at a flow speed of 40 m/s over a frequency range between 0.3 kHz and 7 kHz, and between 7 kHz and 20 kHz, respectively. The results in Fig. 23 are consistent with the predictions with Howe, which suggests that noise reduction performance improves with increasing obliqueness but is contrary to the flat plate measurements of [226]. However, reducing the serration wavelength can be seen to have the opposite effect on noise spectrum at higher frequencies above about 7 kHz in Fig. 23, which increases as the serration is made narrower.

The sensitivity of the noise reductions to the serration height and flow speed may be summarized in two figures. Fig. 24(a) shows contours of the difference in sound power level in dB between the serrated airfoil and baseline airfoil versus flow speed and frequency for a serration width of $2h$ = 10 mm and $\lambda$ = 3 mm. Results are shown on a restricted scale between −2 dB to 2 dB to delineate more clearly the transition between noise reductions (blue) and increases (red). Fig. 24(b) shows contours of noise reductions with the serration amplitude, normalized with respect to both boundary layer thickness (left scale) and serration wavelength (right scale).

The experimental results from Gruber et al. [227] may be summarized as follows:

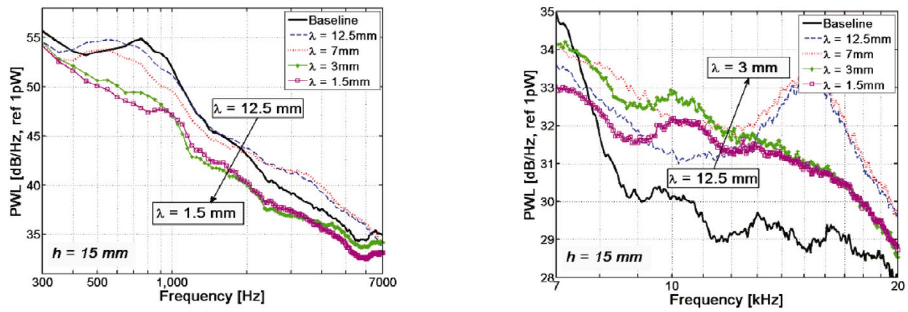


(a) (b)

**Fig. 23.** Comparison of the Sound Power Level (dB) spectra for the baseline airfoil and with different serration wavelengths plotted between (a) 300 Hz and 7 kHz and (b) 7 kHz and 20 kHZ, with $h$ = 15 mm and $U$ = 40 m/s (Gruber et al. [227]).

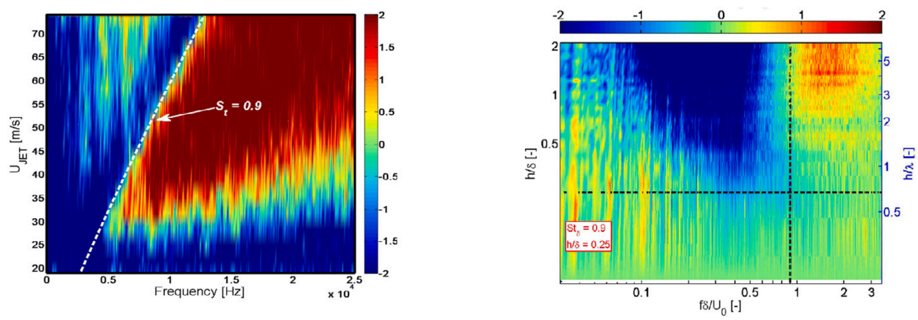


(a) (b)

**Fig. 24.** (a) Contours of the change in Sound Power Level (dB) versus frequency and flow speed and (b) Contours of the change in Sound Power Level (dB) versus non-dimensional frequency and non-dimensional serration height normalized on boundary layer thickness (left y-axis) and serration wavelength (right y-axis). (For interpretation of the references to color in this figure legend, the reader is referred to the web version of this article.)

1. At low frequencies (300 Hz to 400 Hz), the level of noise reductions were less than 1 dB but were difficult to quantify accurately as the airfoil noise was masked by the presence of jet noise. The use of coherent power method described in Brooks and Hodgson [68] or the use of phase arrays could remove this issue in this frequency range.
2. Fig. 24(a) suggests that at every velocity, there exists a frequency below which the noise has been reduced by up to 7 dB, while above it the noise has been increased. This frequency can be clearly seen to increase linearly with flow speed, leading Gruber to speculate that this 'transition' frequency $f_0$, follows a Strouhal number dependence $f_0\delta/U \sim 1$. Note that there is no evidence to suggest that the boundary layer thickness is the appropriate length-scale in this problem except that it provides a Strouhal number of order 1. A similar behavior was observed by Qiao et al. [228] for a cambered SD 2030 airfoil.
3. The increase in noise at these high frequencies was attributed to cross-flow through the roots between adjacent teeth driven by the mean pressure difference between pressure and suction sides.
4. Spectral shape and dependency on the angle of attack appeared to be small, compared to other parameters.
5. There exists a value of serration amplitude, $h/\delta > 0.5$, below which sawtooth serrations are inefficient at attenuating noise radiation. Again, Gruber et al. [227] were not certain that $\delta$ is the correct length-scale for normalizing $h$ but argue that it is highly plausible since, for $h/\delta < 0.5$, the serration height is smaller than the largest eddy size, and hence, cannot be scattered effectively at the trailing edge.
6. The convection phase speed and the coherence between surface pressure measurements near the sawtooth edges were found to be smaller than for the baseline straight edge, which was proposed as the main noise reduction mechanism.

More recent experimental studies on the use of trailing edge serrations for reducing airfoil noise have focused on more aerodynamically optimized shapes and the understanding of the complex 3D flow around the serrations, which may explain the difference of serration performances between a non-lifting flat plate and an airfoil at incidence. Moreau et al. [229] have for instance modified the cambered CD profile to embed a truly three-dimensional serration that preserves the airfoil shape (same pressure and suction surfaces with same mean chord length), and that consequently hardly modifies the aerodynamic loading as confirmed by the parallel DNS of Sanjose et al. [193] described in Section 3.4. Similarly to Gruber et al. [227] they covered a large range of flow velocities and angles of attack and obtained radiation maps similar to Fig. 24, but had the largest gain along a Strouhal number based on the boundary layer thickness at the trailing edge $\delta$ of 0.12. High gains (more than 10 dB) are seen at discrete frequencies corresponding to the tonal noise. An overall gain of 1–2 dB on the broadband noise is mostly found at high frequencies as in all previous experiments. Note that the slight vortex shedding on the pressure side signing at 1 kHz is also alleviated as evidenced in Section 3.4 (Fig. 21). Hot-wire measurements were also conducted around the serrations that stress an enhanced mixing by the serrations. Two symmetric maxima of turbulent kinetic energy around the maximum of the velocity profile at the tooth tip were the traces of the two side-edge vortices developing on each side of the serration tooth as seen in the DNS of Sanjose et al. [193] (Fig. 21(b)).

Two noteworthy studies on the visualization of the 3D flow in the vicinity of the trailing edge serrations were also performed by Chong and Vathylakis [17] on flat plate, and by Avallone et al. [194] on a NACA 0018 airfoil. Chong and Vathylakis [17] visualized the flow on the surface of a flat plate serration attached to a flat plate by the use of active liquid crystals distributed over the surface of a single serration, which are highly sensitive to temperature changes resulting from turbulence activity and 34 surface pressure sensors. Measurements were made with the flow passing over just one side in a wake-jet arrangement. The results from the liquid crystal experiments for both wide-angle and narrow-angle sawtooth demonstrated lower temperatures associated with higher levels of turbulence for the sawtooth's oblique side edges and tips compared to the straight trailing edge. The temperature difference in the other locations remained unchanged.

The wall pressure PSD at the surface near the serration tips and oblique edges of a serrated trailing edge showed high levels of pressure spectra in the same frequency range where far-field noise reductions were found to occur. Streamwise and spanwise coherence measurements between the surface pressure measurements were also performed. The spanwise coherence close to the sawtooth oblique side edge and tip were found to be slightly higher than the straight edge counterpart. In general, however, spectral levels were found to be higher than for the corresponding straight baseline trailing edge. This important result, which is also consistent with the surface pressure measurements of Gruber [41] and Moreau et al. [229], suggests that the noise reduction mechanism arises from reductions in the scattering efficiency associated with the oblique edges and not a reduction in source strength. This also confirms all present DNS results.

An innovation in Chong and Vathylakis [17] is that the boundary layer velocity measured using a hot wire probe and the wall pressure signals were also analyzed using a conditional-averaging technique to investigate the temporal variations of the coherent structures in the straight and serrated sawtooth trailing edges. Near the sawtooth oblique side edge, the turbulence substructures exhibit simultaneously weakened sweeping and ejection motions. Despite the shifting dynamics of the local turbulence transport, the mean turbulence level remains about the same across the boundary layer. However, near the sawtooth tip, an extensive flow mixing between the turbulent boundary layer and the pressure-driven vortical structure is clearly demonstrated, as also evidenced by Moreau et al. [229].

A further insight into the mechanisms of noise reductions through trailing edge serrations was obtained by Avallone et al. [194] through a direct visualization of the three-dimensional flow field over the suction side and near-wake of a NACA 0018 airfoil with trailing-edge serrations by means of planar and time-resolved tomographic particle image velocimetry. Consistently with Chong and Vathylakis [17] and all DNS results, the incoming flow was found to be only mildly affected by the presence of the serrations while, further downstream, the flow pattern is more complex when compared to a straight trailing edge. The flow was found to be characterized by pairs of counter-rotating streamwise-oriented vortical structures in the space in between the serrations driven by mean pressure difference between the suction and the pressure sides of the airfoil, as shown in Fig. 25, similarly to the DNS results in Fig. 21(b).

These structures cause a funneling effect that acts to distort the mean flow which, according to Chong and Vathylakis [17], causes a local variation of the effective angle seen by the turbulent flow approaching the serration edges, resulting in higher surface pressure fluctuations at the root compared with the tip. A further evidence of this experimental finding is presented by Woodhead et al. [230] in which two adjacent root sources (Double Root Serration) separated in the streamwise direction led to a destructive interference between the two partially coherent sources that are delayed in time. This serration is discussed in greater detail in Section 4.3 later.

As a closing remark for this subsection, it is clear from the work surveyed above that the main difficulty with designing and predicting the performance of effective trailing edge serrations for loaded airfoils is related to the complex flow physics around individual serration

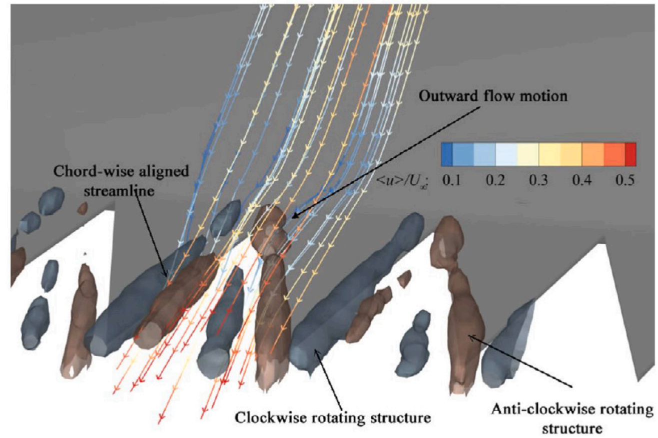


**Fig. 25.** Iso-surface of streamwise vorticity along the serration surface. Streamlines are color-contoured with streamwise velocity component. Free-stream velocity is $U_\infty = 10$ m/s. (For interpretation of the references to color in this figure legend, the reader is referred to the web version of this article.)
*Source:* (From Avallone et al. [194]).

teeth. The flow field appears to be dominated by a system of contra-rotating vortices, which generate high levels of pressure fluctuations along the oblique edges and on the tip. The convection speed of these flow disturbances normal to the oblique edge are considerably slower compared to the straight edge [17,194,227], leading to less efficient radiation to the far field. Under mean loading conditions, however, flow passing through the serration roots appear to be a source of high frequency noise at frequencies $f > U/\delta$, which may mask the reductions in noise by the oblique edges. We now describe alternative edge geometries aimed at attempting to mitigate this effect.

#### 4.2.2. Non-conventional serrations

So far, a review on the trailing edge serration for airfoil self-noise reduction has been focused on a relatively simple geometry — sawtooth shape, which can normally be described sufficiently by the serration amplitude and serration wavelength. The previous section has established that an optimal configuration entails a serration with large amplitude and small wavelength. However, a narrow focus on these geometrical variables is no longer adequate and is unlikely to yield a further reduction beyond the current level of 6–7 dB achieved in the laboratory test. Improved understanding on the mechanisms of serration and a pool of technological information have been created after several decades of worldwide research efforts. This encourages some innovative thinking for further development of novel serration configurations based on the following principles:

1. Can an effective shielding or shape optimization be designed to degrade the main scattering source of a serration, e.g. at the root region, or refraining from stationary points on the serration profile?
2. Adopting a long, sharp and thin serration at the rear of an airfoil as an add-on device could be flimsy, thus presenting some complex stiffness and flexibility issues, but most importantly, a flow misalignment issue. Whilst this will certainly affect the noise performance of the serration, can this actually be exploited in a positive way?
3. Introducing the "cut-in" serration concept — an alternative to the add-on type.

4. The empty space/gap between the serration — can the prevention of the local three-dimensional flow and distortion of the near wall streamline be useful to improve noise reduction?

An interesting and new design based on principle (1) is introduced by the TU Delft group, Netherlands, on the "iron-shaped" serration [56] first mentioned in Section 2.4. Fig. 26 shows the iron-shaped serration alongside a conventional sawtooth serration, as well as the distributions of noise sources at low frequency (upper) and high frequency (lower) between them. The iron-shaped serration has a reduced free space due to the tangent constraint on the side edges. This exact feature helps to inhibit the three-dimensional flow at the root region and the gap between the serration, a phenomenon the authors attribute to the reduction in effectiveness of the serrations in mitigating the self-noise radiation. The reduced noise source levels at the root of the iron-shaped serration, and a more gradual interaction between the flows coming from the now almost parallel two side edges, enable this new design to achieve approximately 2 dB higher level of noise reduction than the conventional sawtooth serration. The principle of shape optimization of the serration is also reported by Lyu et al. [55,231], on what is called the "ogee-shaped" serration that is governed by a shape function to result in a variation of the sharpness for the serration root and tip. To some extents, the iron-shaped serration may be considered as a derivative of the ogee. Although in the paper the ogee-serration is only implemented at the leading edge, with an elevated inflow turbulence (thus a bypass transition on the airfoil surface), an evidence of self-noise reduction is presented at a high frequency. It is also worth mentioning that self-noise reduction by the leading edge serration (conventional sawtooth type) has also been observed by Chong et al. [232] and Biedermann [233], the latter whose beamforming map can show a clear reduction of noise levels at the trailing edge at some characteristic frequencies.

As a closing remark for the non-conventional serrated trailing edge based on the principle (1), an emerging area is the manipulation of the serration shape function to alter the effective distance between the root and tip. Recent works from Kholodov and Moreau [57–59] provide some parametric studies on the serration shape optimization, including multiple slits distributed on the serration edge. An important design principle proposed by the authors is that when the serration wavelength increases with respect to the turbulence spanwise correlation length, the optimal serration shape should change from ogee to sawtooth, and from sawtooth to sinusoidal or iron shape. Readers can refer to Section 3.4 for more detailed discussion.

For the principle (2), various aeroelasticity/stiffness characteristics of a thin, long and narrow serrated trailing edge add-on (a supposedly optimal configuration), under a particular loading condition, external excitation, and dependency on the different materials and attachment methods to the main airfoil body, could inadvertently be deflected upward or downward resulting in a deviation of the alignment to the incoming flow. Much like a trailing edge flap of an aircraft wing, this could well result in a shift of the global flow circulation around the airfoil body, and understandably affect the noise performance of the serration. Arce Leòn et al. [234] studied a combined effect of airfoil angles of attack and the serration flap angles (flap-down only, toward the pressure side). Across all the angles of attack investigated, the flap-down serration is found to degrade the noise performance, and in some cases, a significant noise increase can be observed at a high frequency region. Various results presented in the paper on the boundary layer and near wake development all pointed to the fact that a flap-down serration can increase the statistical turbulence level in the near field and promote the edge-oriented streamwise vortices, suggesting these to be the reason to impede the serration performance. This is an interesting aeroacoustics observation in what supposedly to be a lift-generating friendly configuration (flap-down). One might then ask whether an opposite trend can be realized in a serration flap-up position. Although a different airfoil is used, Vathylakis et al. [235] also observed the same aeroacoustics trend in the flap-down configuration,[8] but interestingly, a gently flap-up serration can actually produce a better noise reduction performance at high frequencies by a further 2 dB, although a slight degradation in the noise performance at low frequencies was also noted. In addition, a noise increase at very high frequencies (> 10 kHz) can be avoided. Recent works from Woodhead et al. [236] concluded that the direction of the serration flap angle can exert the following effects:

- In the flap-down configuration, the blade-loading will become a negative factor that causes a deterioration of the noise reduction performance across the entire frequency range,
- In the flap-up configuration, three spectral frequencies zones can be defined. At the low frequency zone, the diminished cross flow at the sawtooth gaps will impede the noise reduction capability. At the middle frequency zone, the re-distribution of the turbulence sources and reduction of the turbulence spanwise length scales will enhance the noise reduction performance. Improvement of the noise performance can also be achieved at the high frequency zone owing to the lack of interaction between the cross flow and sawtooth structure.

Therefore, the flap angle could indeed represent another optimization parameter for the self-noise reduction by serration (in addition to the serration amplitude and wavelength). Woodhead et al. [237] exploited this property to design their serrations with the flap angle as a periodic function in the spanwise direction, which is illustrated as $\eta$ in Fig. 27 pertaining to the *spanwise wavy serration*. This configuration would entail the spanwise wavy serration to containing flap angles in both the positive and negative directions periodically. In the figure, the spanwise wavy serration has $\eta$ = 15 mm, and its serration amplitude and serration wavelength are the same as the straight serration. Interestingly, Woodhead et al. [237] found that a more rapid spanwise waviness of the serration can outperform the noise reduction performance at the middle to high frequency ranges, while remains the same level at low frequencies, when compared to the straight serration.

In some high pressure loading configurations, one could consider cutting the serration "inward" to the airfoil body to avoid uncontrollable deflection of the thin add-on serration. Other reasons that favor the application of the principle (3) into the serration design include the desires to retain the airfoil's original shape, not artificially lengthening the chord, so that low maintenance, better structural integrity and weight saving are achieved. Perhaps, one could argue that a "cut-in" type serrated trailing edge represents the first intuition. Earlier works from Dassen et al. [222] employed a number of "cut-in" type serrated trailing edges where significant self-noise reduction has been reported, but no acoustic spectra were presented in the paper. Interestingly, the authors commented that "... *the spectra were corrected for whistling tones, which were sometimes found to occur even after a roughness strip was attached to the model*". It would later become clear that such "whistling tones" is the by-product of the bluntness-induced vortex shedding in the wake, an inevitable feature for a cut-in serrated trailing edge, instead of the laminar instability in the boundary layer [238]. This presents a dilemma. The desire to have a large serration amplitude to achieve a higher level of self-noise reduction would entail a deeper cut-in, resulting in a larger blunt-thickness and radiation of a high amplitude tone at a lower frequency. So, is the cut-in type serrated trailing edge a complete obsolete concept? Whilst it is undoubtedly not the first choice for many, there are some efforts to mitigate the impact of the bluntness-induced vortex shedding tone noise whilst preserving the serration effect in the broadband self-noise reduction. For example, Chong et al. [239] has limited success in suppressing

[8] Note that there is a mistake in Fig. 8a of that paper where the SPL for the −5° and −15° are accidentally switched and wrongly labeled.

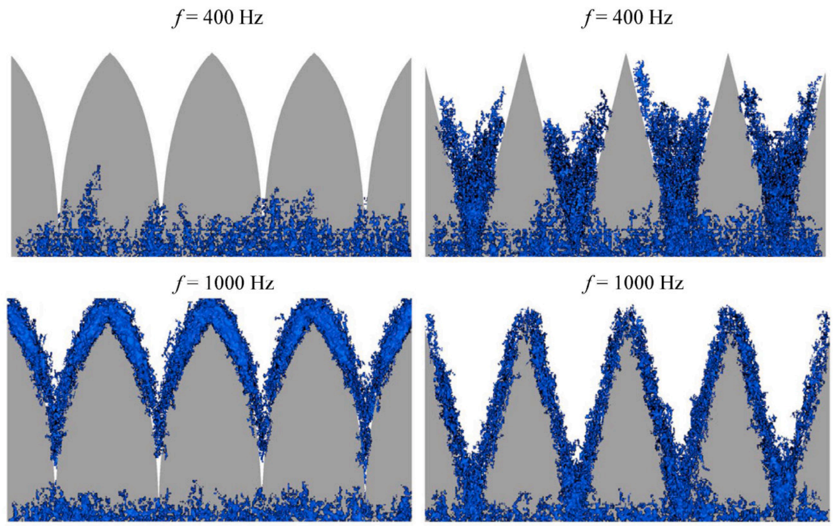


**Fig. 26.** Iron-shaped curved serrated trailing edges (left) in comparison with conventional serrated trailing edges (right).
*Source:* From Avallone et al. [56].

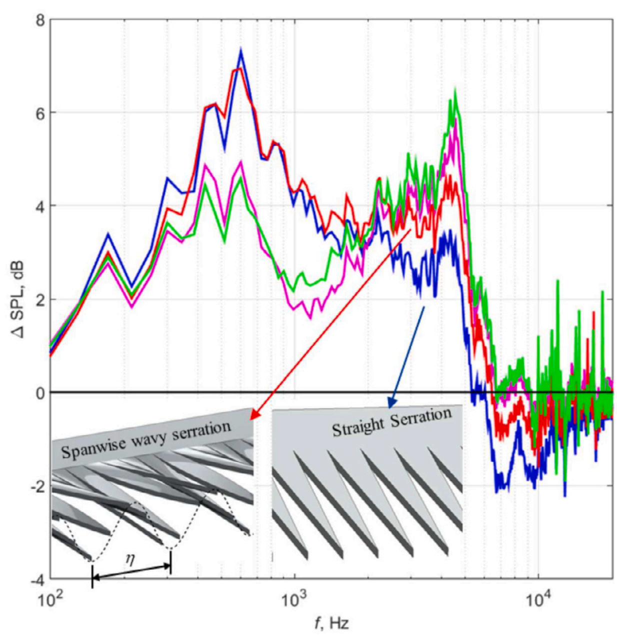


**Fig. 27.** Comparison of the ΔSPL, dB produced by the spanwise wavy serrated trailing edge (red line) and straight serrated trailing edge (blue line), both of which share the same serration amplitude and serration wavelength. Positive value of ΔSPL denotes noise reduction compared to the baseline trailing edge, while negative value of ΔSPL represents noise increase. The green line and purple line represent other serration configurations not discussed here. (For interpretation of the references to color in this figure legend, the reader is referred to the web version of this article.)
*Source:* (From Woodhead et al. [237]).

the bluntness-induced tone when they apply the woven-wire mesh screen over the cut-in serrated trailing edge to impose flow-resistivity in the gap between the serration. Although not measured directly, the pressure drop coefficient (ratio between the static pressure drop across the screen and the dynamic pressure) of the woven-wire mesh screen is estimated to be about 1.5. The mitigation can also be in the form of imposing multi-scale/fractal in the oblique edges [240–242]. All these studies report loss of spanwise coherence and turbulence energy for the otherwise bluntness-induced vortex shedding through the phase-dependent interaction with the secondary flow structures generated by the corrugated edges. In particular, the noise measurement by Hasheminejad et al. [242] confirmed that the bluntness-induced vortex shedding tone can be reduced significantly by a multi-scale/fractal cut-in serrated trailing edge. Interestingly, they also observed a better performance in the broadband self-noise reduction at higher frequencies. The combination of effective mitigation of the bluntness-induced tone and improved level of turbulent-broadband noise reduction could be a realistic prospect for the cut-in type serrated trailing edge in the near future.

The three-dimensional flow that is dominant across the serration surface results in a higher local contribution to the far-field radiation at the serration root with respect to the tip [194]. Therefore, one avenue to further improve the effectiveness of the serration is to reduce the tendency of flow distortion, especially near the root region. In other words, "straightening" the flow, which is related to the Principle (4) for the exploitation of the empty space/gap between the serration, represents the key. An earlier work by Vathylakis et al. [243] utilized the so-called "poro-serrated" trailing edges and used several types of porous materials to completely fill the gap of the otherwise cut-in type serration, which demonstrated an improved broadband self-noise reduction performance in addition to the complete suppression of the bluntness-induced vortex shedding tone. Some examples of the poro-serrated trailing edges used in that paper are shown in Figs. 28(a–b). Follow-up works by Chong and Dubois [245] demonstrated that the flow-resistivity in the space/gap between the serration could become a 4th optimization parameter for the serration, in addition to the serration amplitude, wavelength and flap angle. A zero flow-resistivity at the serration space/gap refers to the original cut-in type serrated trailing edge, whereas an optimized value of the flow-resistivity can be manipulated until the poro-serration outperforms the cut-in serrated trailing edge at the frequency range of interest. If the flow-resistivity is too high in the serration space/gap, the trailing edge is reverting back to a baseline configuration and the noise reduction performance will drop. The poro-serration concept has also been applied to the add-on by Jiang et al. [246] and Liu et al. [247]. In parallel, Oerlemans [244] invented the Dinotails®, a comb-serration add-on (see Fig. 28(c)) that is a much improved version of serration where an additional level of noise reduction has been demonstrated. This configuration has been realistically implemented in industrial wind turbines. The space between the serration is filled by comb-filament, which, in a detailed numerical study later by Avallone et al. [178], was found to attribute them for the straightening of the outward/inward flow in the space between

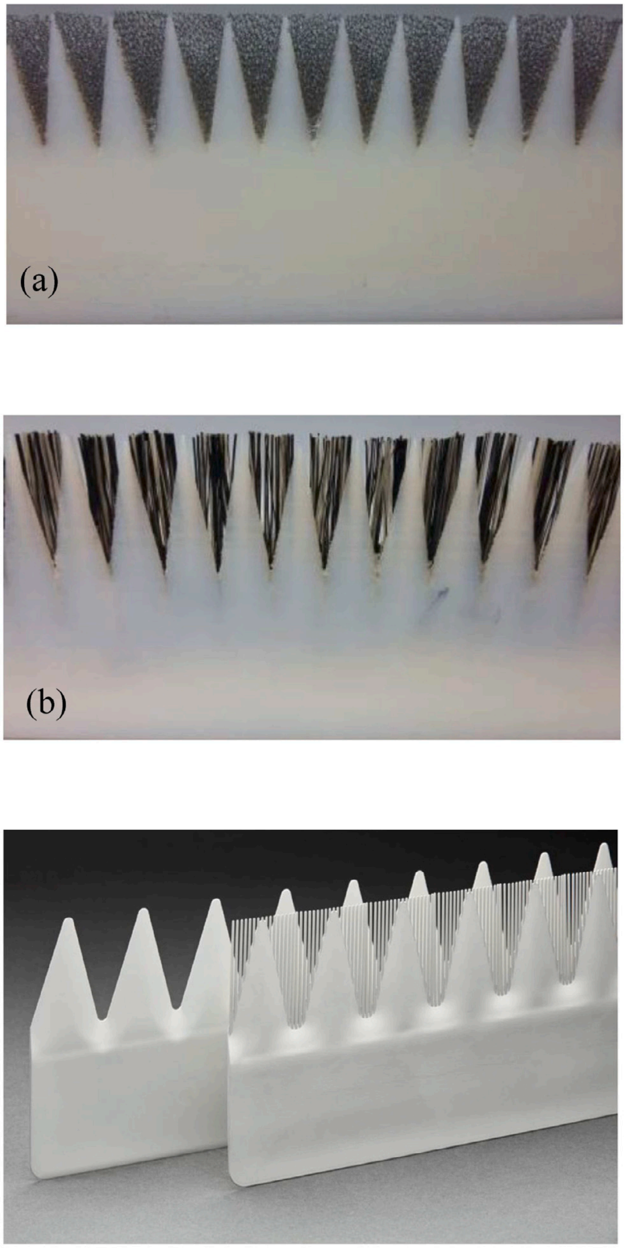


(c)

**Fig. 28.** (a,b) Poro-serrated trailing edges (from Vathylakis et al. [243]) and (c) comb-serrated trailing edge (from Oerlemans [244]).

the serration and spreading the noise sources more uniformly from the pre-dominant serration root to the edges of the entire serration.

There were some attempts to introduce flow permeability directly into the serration surface. Gruber et al. [41,248] patented a geometry of the "slitted-serrated" trailing edge, shown in Fig. 29. This configuration primarily aims to reduce the phase speed and spanwise correlation length of the turbulent eddies passing the serration. A secondary consideration of the slitted-serrated geometry is to avert the high frequency noise increase by distributing the cross flow through the slitted gaps within the sawtooth, instead of creating a large funneling effect in the serration gap in the case of solid sawtooth surface. This has been successfully demonstrated in their results where high frequency noise radiation by the slitted-serrated trailing edge is consistently below as compared to both the baseline and conventional serrated trailing edges. The outcome is a bit mixed with regard to the broadband noise reduction by the slitted-serrated trailing edge. While a better broadband noise reduction level than that of the conventional serration has been demonstrated by the slitted-serrated trailing edge with a large slit height at the mid frequency region, the performance at the low-to-mid frequency region is slightly worse. A similar slitted-serrated principle was also investigated by Arce Leòn et al. [249]. Their reasoning of the slitted-serrated configuration is the relaxation of the impedance discontinuity in what would otherwise be dominant for a conventional sawtooth configuration. To execute this mechanism effectively, they argued that a further modification of the slitted-serrated trailing edge to the so-called hybrid configuration (see Fig. 29(b)) is necessary. By having a less serration root exposed to the slitted treatment, thus allowing a certain level of tune-ability for the impedance distribution across the sawtooth surface, the level of broadband noise reduction is higher than that of the conventional serration at the low-to-mid frequency range.

Before closing this subsection on the non-conventional serrated trailing edges, readers could refer to a recent paper by Jiang et al. [246], who compared the noise reduction performance by most of the configurations discussed here. The Reynolds number is relatively modest but three major airfoil noise sources were investigated: the laminar instability tonal noise, the turbulent boundary layer broadband noise (which is relevant to the current topic), and the bluntness-induced vortex shedding tonal noise.

#### 4.2.3. *Brushes, compliant/elastic edges, and slits*

Turbulent boundary layer on surfaces is not itself an efficient source for radiating noise into the far field. However, when it meets a geometrical discontinuity, such as the trailing edge of an airfoil, the enforced unsteady Kutta condition at the trailing edge would facilitate some of the turbulent energy to be scattered into far-field noise in a dipolar pattern. Therefore, if one can relax the abrupt geometrical discontinuity, the efficiency of noise scattering could be reduced. Based on this principle, Herr and Dobrzynski [250] applied an edge extension in the form of brushes/fringes to the rear of a large airfoil model. This configuration is proven effective for the reduction of the turbulent-broadband self-noise across a relatively large range of frequency. At that time, a speculation was made that these brush filaments would collectively realign the main flow and break down the otherwise dominant spanwise roller into many streamwise oriented vortices to dampen the hydrodynamic pressure fluctuation. This hypothesis would later be verified by Avallone et al. [178] albeit in a comb-serration study. Another investigation by Finez et al. [251] on the use of trailing edge brushes also observed a reduction of the turbulent-broadband self-noise. They attributed this to the significant reduction of the spanwise correlation length scale of the turbulent eddies, which is part of the turbulence statistical properties contributing to the far-field radiation [19]. It is worth mentioning that Herr and Dobrzynski [250] attributed the lack of high frequency noise increase to the ability to attenuate the crossflow by their brush bundles of flexible fibers, perhaps under the same mechanism as the Gruber's slitted-serrated trailing edge discussed earlier. Such advantage of flexible fibers could also be exploited to target other noise mechanisms, including the turbulent-broadband self-noise.

According to Amiet [19], another major turbulence statistical property that governs the far-field radiation is the wall pressure fluctuation spectra near the trailing edge. The level of the radiated noise is dictated by the net wall pressure contribution from both sides of the airfoil edge surfaces, $\triangle\overline{P'^2}(f)$. When the edge becomes flexible and compliant, i.e. possession of a good adaptability to the turbulent flow disturbances, it has a potential to reduce the level of the $\triangle\overline{P'^2}(f)$. Jaworski and Peake [33] observed that an elastic edge would change the scaling behavior of the far-field sound with velocity from the 5th to the 7th power over a finite low frequency range, thus indicating a fundamental change in the self-noise mechanism (see Section 2.2.1). As mentioned

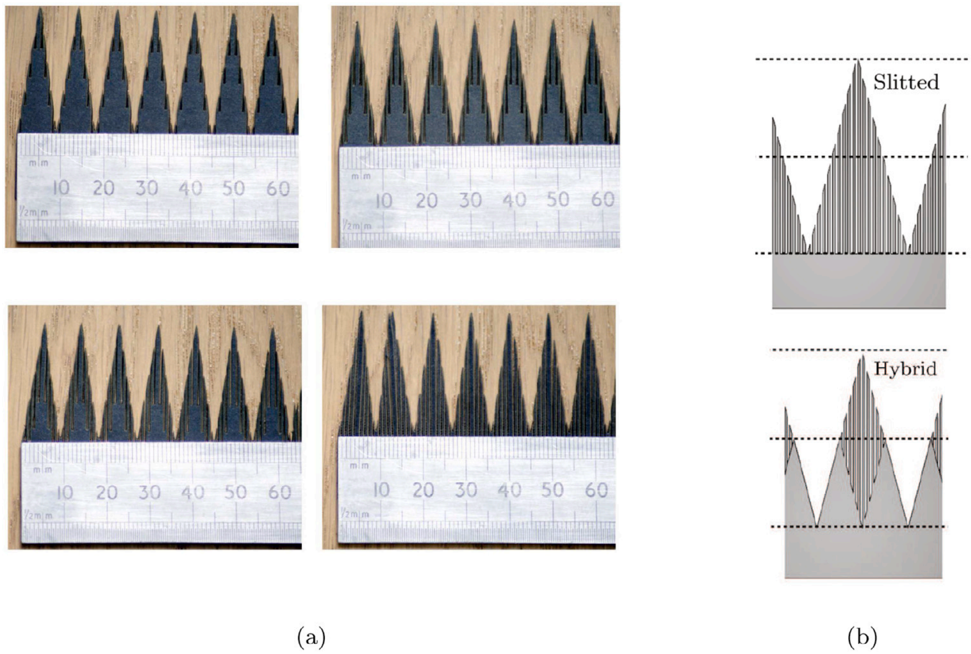


**Fig. 29.** (a) Slitted-serrated trailing edges (Gruber [41]) and (b) hybrid-serrated trailing edge (Arce León et al. [249]).

in Section 3.4, Nardini et al. [205] also observed noise reduction using an elastic edge at low frequency, but they pointed out that the radiated spectra would also be contaminated by narrowband components corresponding to the natural oscillation frequency and harmonics of the elastic edges. These extraneous narrowband peaks are difficult to be mitigated, and would severely negate the benefits achieved by the elastic trailing edge in the overall noise performance. Experimentally, there has not been many published works on the compliant/elastic trailing edge to treat the turbulent-broadband self-noise. Interestingly, the compliant/elastic trailing edge has more success in the case of laminar instability tonal noise, which is demonstrated by Das et al. [252] and Talboys et al. [253]. The self-oscillating "flaplets" developed by Talboys et al. [253] are capable of disrupting the laminar separation bubble, and possibly even the growth mechanism of the Tollmien–Schlichting waves, to mitigate the instability noise radiation. The lack of footprints for the oscillation-induced peaks in their acoustic spectra might be due to the masking effect of the significantly larger level of the instability noise in the form of broadband-hump embedded with multiple discrete tones.

In their efforts to investigate the mechanisms of the turbulent-broadband noise reduction by the brushes/filament, as well as the compliant/flexible/elastic edges, the various authors mentioned in the previous paragraph mostly the source areas in the flow field. It is worth reminding that one of the main reduction mechanisms for a conventional serrated trailing edge is due to the acoustical interference between the scattered pressure waves along the oblique edges [254]. However, acoustical interference achieved by a conventional serrated trailing edge is random, and no optimal phase angle between the scattered waves could be established. In other words, there is no frequency-tuning capability. Therefore, if one considers a straight trailing edge orthogonal to the flow direction to be the least efficient configuration for destructive interference due to the zero phase angle imposed on the scattered pressure waves, or rather the most effective configuration for the constructive interference, a slit trailing edge like the one depicted in Fig. 30 that configures the edges to be parallel to the main flow direction could exert the opposite effect. This hypothesis is put forward by Woodhead et al. [230], a joint venture between Brunel and Southampton. As a generic term, the phase angle can be related to the angular frequency and the turbulent eddies convection speed ($U_c$) by $\hat{\omega} \equiv \omega l / U_c$ with $l$ is the longitudinal displacement between the two sources. A perfect destructive interference should occur when the acoustic radiation from two coherent sources, S1 and S2 in Fig. 30(a), are 180° out-of-phase. The relevant phase angle can be expressed as $n\pi$, where $n = 1, 3, 5$, and so on for destructive interference. This results in the cancellation of the acoustic radiation. In contrast, a perfect constructive interference occurs when the acoustic radiation is in-phase between the two coherent sources (i.e. when $n = 2, 4, 6$, and so on), which results in the amplification of the acoustic radiation to the far field. To summarize $\hat{\omega} = n\pi$ or in terms of Strouhal number

$$St = \frac{fl}{U_c} = \frac{1}{2} n \begin{cases} \text{for destructive interference,} & n = 1, 3, 5, \dots \\ \text{for constructive interference,} & n = 2, 4, 6, \dots \end{cases} \tag{79}$$

A strong feature in Eq. (79) is that, under a particular inflow velocity, the value of $l$ can dictate the frequency characterized by the destructive interference (as well as the constructive interference). In other words, it is possible to fine-tune a desired frequency to achieve the maximum level of noise reduction by trailing edge geometrical modifications in a slit configuration. This hypothesis has been positively demonstrated [230,255]. Some of the results are presented in Fig. 30(b), which shows the contour of $\triangle$PWL (different in the sound power level) at various slit amplitudes, $H$, against $f$ at different $U_\infty$ (freestream velocity). A positive $\triangle$PWL denotes noise reduction, whilst a negative $\triangle$PWL means the opposite. The results clearly demonstrate the co-existence of the destructive and constructive acoustical interferences imposed by the slit trailing edge. Significant noise reduction fits very well to the curve pertaining to $St = 0.5$ and 1.5, which according to Eq. (79) corresponds to the destructive interference mechanism between the roots and tips of the slits. Similarly, constructive interference at $St = 1$ is confirmed by the measured noise increase.

### 4.2.4. Porous airfoil

Applying porous treatment to either the entire airfoil or the trailing-edge region for the reduction of self-noise radiation has gained traction in the last decade. Some attribute the porous treatment to be analogous to the coating of soft and downy surfaces of owl's wing [204].

Geyer et al. [256] procured 16 different porous materials that provide a range of flow resistivity, and they used each porous material to manufacture the entire SD7003 2D airfoil including one of solid non-permeable airfoil as the reference. Some examples of the porous airfoils

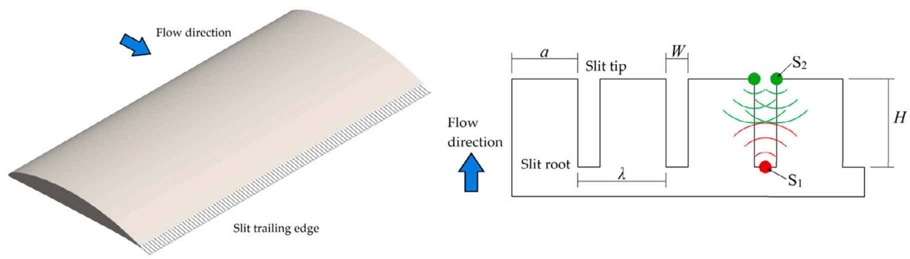


(a)

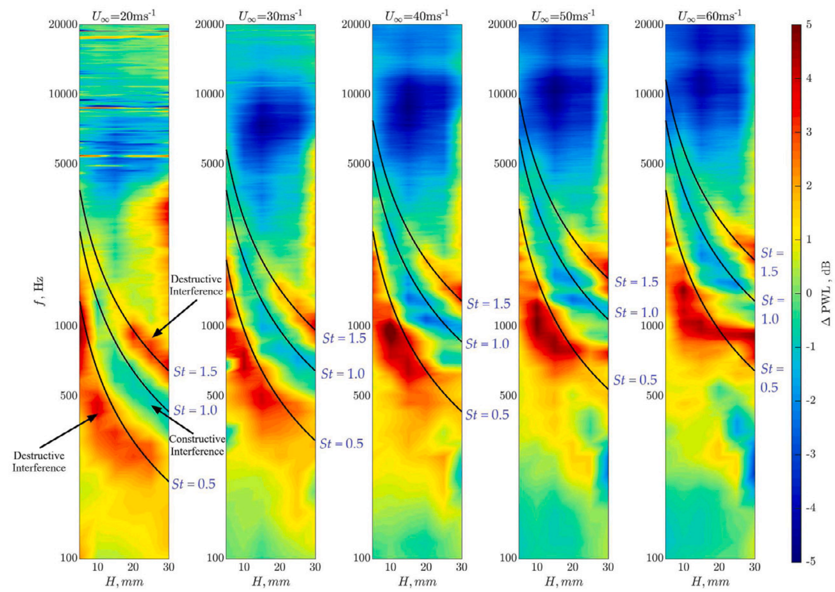


(b)

**Fig. 30.** (a) Topology applicable to the slit trailing edge where the scattering sources are defined as: (red) $S_1$ - root source and (green) $S_2$ - tip source and (b) Difference in Sound Power Level (dB) in contour maps of frequency versus slit amplitude, $H$, at $20 \leq U_\infty \leq 60\,\mathrm{m/s}$ (Woodhead et al. [230]). (For interpretation of the references to color in this figure legend, the reader is referred to the web version of this article.)

are shown in Fig. 31. The flow resistivity is defined by a porous sample subjected to through flow, which relates to the ratio of the steady pressure difference on either side of the sample in question, and the product of the thickness of the sample and the flow velocity. They found that the sound pressure level generated at the trailing edge of these porous airfoils can be up to 15 dB lower than that generated by the solid (reference) airfoil, over a large range of mid frequencies. Increases in noise were observed at high frequencies due to the generally rougher surface texture of the porous material. They stated that the material flow resistivity is an appropriate physical metric to represent the loss mechanism of unsteady flow through the pores. They observed an increase in the turbulent boundary layer thickness and boundary layer displacement thickness, although the details of the boundary layer profile and its energy spectra were not reported. The dependence of flow resistivity by a porous trailing edge on the reduction of turbulent-broadband noise was corroborated by Herr et al. [257], who reported noise reductions at low to mid frequencies. They ascertained that porosity is not the main parameter that yields the broadband noise reduction. This is because by merely taping the airfoil surface to achieve the porosity, but, without facilitating through flow across the trailing edge surfaces, the noise reduction benefits will not be achieved. The underpinning mechanism is owing to the creation of a permeable medium that allows communication between flows on the upper and lower sides of the airfoil, thus reducing the acoustical dipole strength at the trailing edge. In other words, the porous treatment is a source (turbulent boundary layer) targeting approach.

It appears that, to satisfy the condition of a low noise airfoil, the porous materials need to be of low flow resistivity, but the resulting low level of steady pressure differences due to the permeable flow will cause a significant loss of the aerodynamic lift. An increase in drag is also reported. A partially porous airfoil (targeting only the trailing edge part) represents an alternative design that can minimize the aerodynamics penalty, while still preserving the aeroacoustic benefits. Geyer and Sarradj [258] limited the porous coatings to the last 5% of the chord length from the trailing edge. They observed a reduction in far-field noise up to 8 dB and a negligible decrease in lift. A further study on the porous treatment at the trailing edge only (last 20% of the chord) has been conducted by Rubio Carpio et al. [203]. Focusing on the flow permeability, a relevant but anti-correlated metric to the flow resistivity, they observed that the permeability of the porous insert is linked to the increase of the anisotropy of highly energetic turbulent motions, with up to 11 dB noise reduction at Strouhal number = 0.09 achieved by porous material with high permeability. Note that the Strouhal number is based on the displacement thickness. It is a fair assumption that the best recovery of the aerodynamic performances should be underpinned by the lowest porous coverage to the trailing edge. Recent studies by Zhang and Chong [259,260] continued to observe a significant broadband noise reduction after a further reduction of the porous coverage on the trailing edge down to as low as 3.7% of

**Fig. 31.** Some of the porous airfoils used in Geyer et al. [256].

the chord. Not only this emphasizes the point that the main trailing-edge noise source is situated very near to the edge, but it also implies that the response of the turbulent boundary layer to the perturbation by the permeable flow is quite spontaneous.

Due to the complexity involved in the manufacturing process, most of the porous materials investigated previously in the research community were procured commercially. However, the porosity, flow resistivity and permeability levels of the commercial porous materials are usually pre-determined. This makes a systematic study in the research community quite a challenging task. In addition, even the same grade and type of porous materials can have inhomogeneous internal pore structures and permeability tensors between samples. This inconsistency can complicate any attempts to generalize the porous airfoils in their noise reduction performance. Recently, the rapid advances of the additive manufacturing technique (e.g. 3D-printing), could provide an alternative for the manufacture of permeable trailing-edge inserts with high accuracy. The easiest way is to connect the suction and pressure sides of the airfoil with straight channels, without tortuosity, through 3D-printing, such as the propeller blades adopted in Jiang et al. [261]. Rubio Carpio et al. [203] measured the far-field noise radiated by a NACA0018 airfoil retrofitted with solid and 3D-printed permeable trailing edge inserts. It was observed that the 3D-printed inserts (which have straight internal channels) must be at least 3 times as permeable as the metal foam (unstructured internal channels) in order to obtain similar broadband noise attenuation levels. This means that the bulk permeability tensor could also be an important parameter. The challenge to encourage a wide proliferation of 3D-printed low noise airfoil is further exacerbated by its tendency to radiate the significant bluntness-induced vortex shedding tonal noise, as reported by Zhang and Chong [259,260] in their investigation on the porous trailing edges with straight through holes arranging in a rectilinear fashion. They suggested that the ratio between the critical geometrical thickness (pertaining to the trailing edge location that coincides with the first porous row) and the local turbulent boundary layer displacement thickness should be less than 2 to avoid the generation of the extraneous tone noise.

Finally, Moreau et al. [229] modified the trailing-edge of the CD airfoil to embed a liner-type porous treatment consisting of regular grooves covered by wire-meshes of different flow resistivity. Note that no connection was made between the two airfoil sides and grooves are put on each side of a splitting plate below the wire-mesh to mimic the efficiency of a liner, and to provide good structural strength. Consequently, no significant change of loading (mean wall-pressure coefficient) was observed. Hot-wire measurements in the near wake showed no change of the wake thickness and flow deviation but a significant decrease of the turbulent kinetic energy downstream of the trailing edge suggesting some viscous damping by the porous medium, and smaller wake deficits suggesting reduced drag. This was further confirmed by boundary-layer profiles near the trailing edge that showed similar boundary layer thickness but some significant reduction of the wall-shear stress and thus the wall friction. Significant noise gains were obtained with all porous treatments, with the highest reduction for the least resistive mesh. Tonal noise was completely alleviated in all cases and some significant broadband noise reduction was only achieved with the least resistive mesh. Moreau et al. [229] also suggested that not only the porous medium damps the pressure fluctuations near the trailing-edge but also modifies the whole transition process on the suction side. Additional PIV measurements near the trailing edge by Yakhina et al. [262] showed that the porous trailing edge yields a significant reduction in velocity fluctuations, which are the principal contributor to the surface pressure fluctuations as shown in Section 3.1.2. These results have also been confirmed on a recent flat plate experiment on scaled porous treatments at the trailing edge [263,264], providing the additional information that some significant flow penetration exists on the least resistive mesh which triggers not only a modification of the local impedance but also of the no-slip boundary condition and of the turbulent flow statistics.

Indeed, it is known that turbulent boundary layers on permeable surfaces can be modified via interactions originating from various mechanisms. The nature of these modifications not only depends on the ratio between the length scales of the flow field and of the porous matrix, but also on the preferred directionalities of the porous material and of the flow. In particular, Jimenez et al. [265] showed that the interaction between the turbulent boundary layer and a porous surface with a strong wall-normal permeability tensor can generate large-scale secondary structures that lift the near wall low-speed streaks away from the surface. Rosti et al. [266] showed that making the permeability tensor to become anisotropic, such as enhancing the in-plane permeability while reducing the wall-normal permeability, can lead to the increase of the near wall slip velocity. The reduced near wall velocity gradient thus leads to a viscous drag reduction, which might also have implication to the wall pressure fluctuations. This emphasizes the importance of the correct tuning of the bulk permeability tensor of the porous medium used in the turbulent-broadband noise reduction.

The literatures thus far suggested that the trailing-edge self-noise reduction by porous treatment is based on the source-targeting mechanism. Another effective method that also targets the source, namely the “finlet", will be discussed next.

#### 4.2.5. Canopies, fences, and finlets

More recently, attention has turned to the reduction of airfoil trailing-edge self-noise by the manipulation of the turbulent boundary layer itself just upstream of the trailing edge where it is then scattered into sound. This approach is fundamentally different from the use of serrations that target the scattering efficiency of the trailing edge rather than the source of turbulence. This work began by the team at Virginia Tech who have demonstrated that introducing ‘canopies’ into the turbulent boundary layer, which may be constructed from fabric, wires, or rods, produced significant reductions in the surface pressure spectrum near the trailing edge, and hence significant reductions in the far-field noise radiation. These treatments were chosen to reproduce the downy canopy that covers the surface of exposed flight feathers of many owl species [204].

The first attempt at using canopies to reduce boundary layer noise was by Clark et al. [267], who investigated the use of canopies to reduce the aerodynamic noise from a rough surface. Four mesh-like polyester fabrics were used to mimic the effect of the canopy portion of the owl downy, chosen to qualitatively similar to the structure of the owl's downy coating (high open area ratio and interlocking fibers). The fabrics were structured as meshes with a 2.5:1 ratio of pore sizes, a 5:1 ratio of thread diameters, and open area ratios from 38% to 76%. However, even the finest fabric investigated had a thread diameter about three times the estimated diameter of the owl's hairs. The fabric canopies were suspended above the surface by the use of two tapered half-round dowels mounted on either side of the test area. All canopies tested were observed to have a strong influence on the wall surface pressure spectrum, and an attenuation of up to 30 dB were observed.

In a subsequent investigation, a form of canopy was used to reduce the trailing-edge noise due to a tripped DU96-W180 airfoil in the form of finlet fences and finlet rails located directly upstream of the trailing edge [267]. Schematics of each are shown in Fig. 32 and are characterized by a height, spacing, thickness and extension distance beyond the trailing edge. The height of the finlet was varied between 10% and 100% of the boundary layer thickness and therefore mostly act on the outer scales of the turbulent boundary layer.

A total of 20 variants of designs were fabricated using rapid prototyping. All design variants involved either the rail, or the fence treatment, beginning 87.3% chord upstream. In all cases, the treatment was supported on a thin sheet of material (the substrate) glued to the airfoil. Reductions in broadband trailing-edge noise of up to 10 dB were reported with a negligible impact on aerodynamic performance. However, their investigation was limited to far-field noise and surface pressure data and, hence, the precise noise reduction mechanism was not clearly established. Treatments were found to be effective over an angle of attack range that extends to over 9 degrees from the zero-lift condition. Airfoil treatments were observed to have no detrimental effect on the lift performance of the airfoil, although the slight increase in drag was commensurate with the increase in wetted surface area associated with the treatment. In a subsequent study by Gonzalez et al. [268], the fabric canopy was replaced by rods. The Sound Pressure Level reduction spectra were found to occur in two distinct frequency regions. At low frequencies (convective scales much greater than the canopy height) reductions were found to collapse reasonably well on non-dimensional frequency $fh/U_m$ defined with respect to the canopy height $h$ and the boundary layer edge velocity $U_m$ (see Fig. 33(a)).

Noise reductions at low frequencies are believed to be due to the introduction of an additional shear layer that displaces the large-scale structures in the boundary layer away from the airfoil surface. At high frequencies the dissipation-type frequency scaling $f\nu/U_h^2$ is more appropriate, where $U_h$ denotes the local velocity at canopy height and $\nu$ the kinematic viscosity, as plotted in Fig. 33(b). In this frequency range, surface pressure spectral level reductions were observed to increase exponentially, strongly suggesting an enhancement of dissipation by the surface treatments due to the transfer of energy from large to small scales. Independently, numerical simulations using LES [206,207] or RANS [209,210] revealed the shift of the near-wall turbulent kinetic energy upward, which could explain the noise reduction at high frequencies. This is related to change in the mean flow velocity profile by a finlet and its effect on the wall pressure spectrum, which is referred as "shear sheltering" [269]. However, as recognized by Gonzalez et al. [268]: *"These studies show a consistent, but not entirely clear, picture"*, the fundamental noise reduction mechanisms and the limitations of this technology, therefore, need to be further investigated.

*4.2.6. Active methods*

So far, discussion on the mitigation of trailing-edge self-noise only focused on devices that require no energy input or active control mechanisms. The control strategies discussed thus far, which can be exclusively categorized as "passive", are likely to incur negative effects on the aerodynamic performances due to the integration of non-compatible shape onto the otherwise streamlined airfoil, as well as the introductions of surface roughness, porous lifting surfaces, and structural-aeroelasticity coupled instability. A good example is the trailing-edge serration. Although the capability of this bio-inspired device for the reduction of the broadband self-noise has already been well-known since many decades ago, only a few industrial sectors such as the automotive engine cooling fan suppliers, the industrial ventilation sector (the "Owlet" trademark) and the wind turbine business have meaningfully adopted the technology. Others such as the aerospace sector are still more concerned about the loss in aerodynamic performance and the perceived safety issue. To this end, an active flow control represents an attractive alternative because the mechanical and control mechanisms can usually be "hidden" within the airfoil body, thus producing no profile drag. A sophisticated closed-loop and high response active control system can even widen the operational ranges in Reynolds number and Mach number, while still preserving the efficiency in the energy consumption. However, most of the mechanical system underpinning the active flow control can be heavy, bulky, and complex, which will increase the overall payload. This could be at odds against a current technological trend of weight slimming of both the civil aircraft and unmanned aerial vehicles.

The most representative method to execute an active flow control in aeroacoustics is to manipulate the hydrodynamic field through mass flow injection (blowing) or subtraction (suction). In the case of the rotor–stator stage of turbomachinery, turbulent leading-edge interaction noise can be mitigated by the so-called "wake-filling" method through the trailing edge blowing [158,270–272]. To implement this technique, the upstream rotor is usually configured by trailing-edge slots, or vent holes, so that externally supplied air jet can be blown out in a controlled manner to mix with the most deficit region of the wake. As a side note, although trailing edge configured with the air slot and vent holes will inevitably be slightly blunt, it is unlikely to produce significant bluntness-induced tone when blowing is in operation because the wake-filling would have already prevented the vortex shedding from happening. There are two direct consequences of the enhanced mixing by the trailing edge blowing. First is the reduction of turbulence intensity in the wake flow. Second is the faster dissipation of the large scale turbulence structure. These two turbulence properties are precisely the most dominant sources for the turbulent leading-edge interaction noise [8]. Therefore, trailing edge blowing is a powerful method to mitigate this particular noise source. However, there is no evidence that it is also effective for the reduction of turbulent broadband trailing-edge self-noise. After all, the most critical hydrodynamic source for the self-noise radiation is the turbulent boundary layer near the trailing edge, not the wake at downstream.

There are some published works on mass flow blowing, or suction, to target the turbulent boundary layer near the trailing edge to reduce the self-noise radiation. Winkler et al. [158] and later Gerhard et al. [273] facilitated near wall blowing at three different locations at the suction side of their asymmetric airfoil. The exit air jet was specially configured such that it followed the contour of the airfoil surface, which was designed to inject momentum directly to the near wall flow. The exit jet was 50% of the freestream velocity. The most optimal blowing location to achieve broadband noise reduction at low-to-mid frequencies was found to be the one closest to the trailing edge (at 90% chord). In their mean and fluctuating velocity boundary layer profiles, the near wall velocity excess by the blowing was accompanied by a much reduced level of turbulence intensity. The maxima of the turbulence intensity remained the same level, and sometimes even higher value than the untreated case. However, these maxima subjected to near wall blowing was displaced further away from the wall to coincide with the interface between the wall jet and the outer layer where a significant inflectional velocity profile occurs. Similar results have been reported

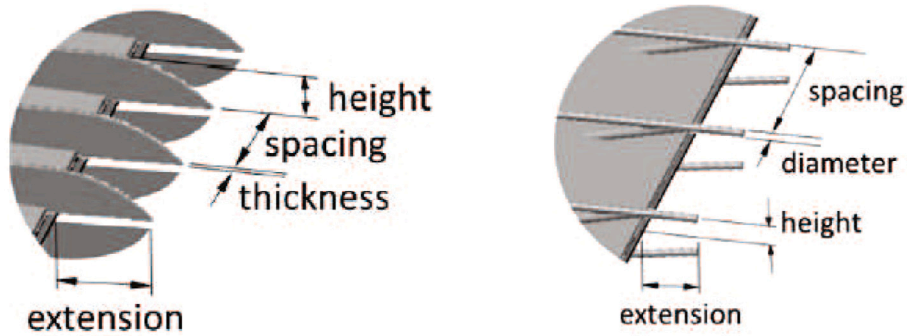


(a) (b)

**Fig. 32.** Treatment designs tested on a DU96-W180 airfoil: (a) finlet fence and (b) finlet rail (Clark et al. [267]).

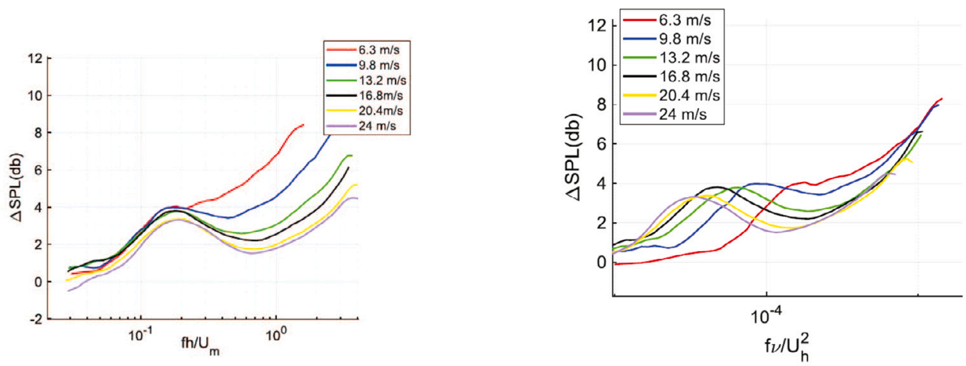


(a) (b)

**Fig. 33.** Sound Pressure Level reduction spectra at different flow speeds plotted against non-dimensional frequency scaled with (a) canopy height and (b) skin friction velocity (Gonzalez et al. [268]).

by Moreau et al. [229] on a modified CD airfoil. Szoke et al. [274] measured the wall pressure fluctuation spectra and spanwise coherence coefficients when their flat plate is subjected to inclined jet blowing near the trailing edge. Both the turbulence statistical quantities was reduced under a relatively high jet-to-freestream velocity ratio. Since both are the key components for the radiation of turbulent broadband trailing-edge noise [19], reduction of self-noise is expected.

Although applying suction from the wall surface over a long cycle period could attract deposition of foreign objects (dirt, dusts, etc.) to the slot/vent holes, the impact of wall-normal suction to the turbulent boundary layer has been positively demonstrated by Wolf et al. [275] in their flat plate experiments. Despite not measuring the far-field noise directly, the near-field measurements on the vertical integral length scale, velocity gradient, and vertical velocity fluctuation subjected to the wall-normal suction all exhibited lower values than the untreated flat plate. These parameters would later be substituted into the TNO-like models (Section 3.1.2) to calculate the wall pressure fluctuations, and then the far-field radiation. In particular, the mean velocity profiles subject to wall-normal suction are much fuller than the untreated one, and importantly the overall boundary layer thickness is also reduced. Predictably, wall-normal suction does not displace the turbulence maxima further away from the wall. Quite the opposite, they are drawn closer to the wall, but crucially with a much reduced turbulence level. The active flow control of boundary layer suction was later transferred to a generic wind turbine blade and studied numerically on its aerodynamic and aeroacoustics performances [276,277].

Both blowing and suction, if they exceed the required threshold for the blowing/suction-to-freestream velocity ratio, have a potential to change the turbulent boundary layer structure fundamentally. To some extents, they share the same principles as the passive devices (e.g. canopy or finlet) in targeting the turbulent sources and the unsteady wall pressure. For the active flow control, however, the very principles of mass flow injection/subtraction by blowing and suction, respectively, could promote extraneous noise sources to contaminate the far-field spectrum. These can be in the forms of additional noise produced by the propulsion of air mass through the slots/vents, vacuum-induced fluid–structure interaction noise in the case of suction, cavity noise and breakout noise from the mechanical component system. In the case of a blowing slot, as shown in Section 3.4, the blowing jet may increase the trailing-edge noise (see Fig. 10 in [158]), and an extraneous noise source at the slot lips was evidenced at high frequency by Winkler et al. [158].

### 4.3. *Outlook*

#### 4.3.1. *Hybrid methods*

The development of new approaches for the mitigation of airfoil self-noise, which is built upon the improved knowledge gained especially in the last decade, has emerged. The resurgence of the trailing edge serration has prompted the development of several non-conventional serration profiles. Other geometrical modification in the forms of brushes, elastic edges, slits and porous surfaces have been developed, respectively but not interactively. The introduction of the surface-mounted finlets represents a very effective means to suppress the noise sources by sheltering the trailing edge from large turbulent structures, and reducing spanwise coherence of these structures.

Naturally, a question can be asked: if one were to combine these passive devices together, can we see further improvements in terms of the level and frequency range for the trailing-edge broadband noise reduction? Perhaps, the "poro-serrated" trailing edge developed by Vathylakis et al. [243] and Chong and Dubois [245] already provides a positive hint to the above question. Another consideration, for example, can be applied to a combination of the finlet, whose main function is to control the source of the turbulent boundary layer, and the trailing edge serration, whose main function is to reduce the radiation efficiency due to the oblique edges. A new control strategy for the turbulent broadband self-noise is the simultaneous targeting of the source-radiation in the form of "finlet-serration", as depicted in Fig. 34. Based on a preliminary result also shown in Fig. 34, obtained at Brunel University London, the finlet-serration can exploit the serration effect at low frequencies, and, at the same time, retain a more superior noise performance by the finlet at higher frequencies of a finite range. This suggests that both the source-radiation targeting can co-exist without imposing adverse interference effects against each other. Although it was not demonstrated by this particular configuration of the finlet-serration, a further level of noise reduction can be anticipated if a comprehensive optimization study is performed in the future. Another hybrid device that exploits multiple noise reduction mechanisms is the "Double Rooted Trailing Edge Serration", or DRooTES [230,255]. The DRooTES combines the acoustical destructive interference mechanism from the slit trailing edge and the serration effect. It demonstrates a reduction in the level of broadband noise reduction, as well as the establishment of the frequency-tuning capability. Therefore, the DRooTES has a potential to leapfrog the serrated trailing edge and slit trailing edge.

As a concluding remark, the current technology in the airfoil broadband trailing-edge noise reduction has reached a saturated phase, where a further level of noise reduction would be difficult to be achieved when only a single mechanism is considered. Therefore, the combination of multiple devices that targets different areas could represent one of the future research trends for the airfoil noise reduction.

#### 4.3.2. Active control

Mechanical blowing or suction has laid the ground works for the application of active flow control to mitigate the airfoil self-noise radiation. In majority of cases, they would rely on a significant modification of the hydrodynamic flow field by injecting/subtracting mass flow to/from the turbulent boundary layer. In laboratory tests, these operations can be realized in a relatively straightforward setup by connecting the airfoil (with pre-fabricated internal flow channels and exit holes/slots near the trailing edge) to external sources (e.g. compressed air, centrifugal blower, vacuum pump and so on). When moved to the real-life industrial operations, however, three issues could become the design constraints. First, in a space limited environment, the placement of the blower or vacuum pump can represent a problem. One way to mitigate this is to miniaturize these power sources. Second, the scale of the flow underpinning the industrial operation could be much higher than in the laboratory test. In order to maintain the same blowing ratio or suction ratio (against the freestream flow), which is usually greater than unity, the blower or vacuum pump need to have a relatively high power rating to improve the control authority. This requirement contradicts the effort to miniaturize the power sources mentioned previously, as well as elevates the overall payload. Third, the flow channels within the airfoil could be complex and expensive to manufacture, and difficult for maintenance.

Apart from the mechanical blowing or suction, other active flow control technologies that have hitherto been overlooked in the aeroacoustics applications could be considered. For example, the synthetic jet actuators that utilize only the piezoelectricity can achieve an extremely high exit jet ($> 100\ \mathrm{ms}^{-1}$) with a low energy input requirement. Rathay et al. [278] instrumented a number of synthetic jet actuators along the span of a sub-scale vertical stabilizer of an aircraft, where a side force enhancement has been positively demonstrated. They also showed that the momentum coefficient produced by the synthetic jet is more important than the blowing ratio. Besides the thrust vectoring and flow separation control, synthetic jet actuators can also be adapted to reproduce the effect of moving wall in spanwise oscillation to reduce the skin friction of turbulent boundary layers despite the high turbulence level introduced to the main flow by the synthetic jets. Cannata et al. [279] reported that when synthetic jets are induced in tangential to the wall and orthogonal to the mean flow direction in a turbulent channel flow, an attenuation of the near wall turbulent structures is observed. Although not presented in the paper, the forced flow has a potential to reduce the wall pressure spectra, and subsequently the self-noise radiation in the case of trailing edge flow. However, it is necessary to point out that the synthetic jet actuator is an inherently noisy device. Therefore, research efforts to reduce the synthetic jet actuator noise should also be carried out in parallel.

The Dielectric Barrier Discharge (DBD) plasma actuators is highly energy efficient, simple in structure, straightforward for implementation, fast response to facilitate both steady and unsteady actuations, and not creating any profile drag when not in operation. In the case of a turbulent boundary layer passing over a sharp trailing edge, a series of symmetrical electrodes can be aligned to the direction of the mean flow to produce spanwise traveling waves, which can reduce the streamwise vorticity in the near-wall region [280]. This would hamper the stretching of the quasi-streamwise vortices, thus weakening the near-wall turbulence events such as the sweeps and ejections and resulting in a reduction of turbulence intensity and the wall pressure spectra. Again, it is necessary to point out that the control authority of plasma actuator is not very high, so that it might be more suitable for a low Mach number flow at present.

## 5. Applications

In this section, practical applications of trailing-edge noise are discussed. In particular, wind turbine noise, fan noise, and rotorcraft/propeller noise are selected as examples. Specific considerations in terms of noise characteristics and industrial design perspectives are also discussed.

### 5.1. Wind turbine noise

Trailing-edge noise is a key factor for wind turbine design when considering noise emissions. The reasons are that trailing-edge noise constitutes the most significant part of a wind turbine signature in the audible frequency range [223,281] and noise limit regulations are established accordingly using A-weighting of the noise spectra. The additional main noise sources include inflow noise (more predominant in the low-frequency range which is also less audible), tip noise (which can be minimized by a careful blade tip design), separation/stall noise (although this is usually avoided and mainly occurs during non-nominal transient operational periods such as an unexpected wind gust[9]), and mechanical noise (which may be dealt with using damping devices and/or adequate structural designs). Furthermore, most of the aerodynamic noise, including trailing-edge noise, is produced in the outer part of the blades, because it travels through the air at higher velocities (of the order of 70 m/s (250 km/h or 160 mph), and sometimes more for modern MW-size wind turbines). This results in very large Reynolds numbers for the air flow in this region of the blade (of the order of several millions). This prevents the occurrence of specific phenomena such as laminar boundary layer instability. Contrastingly, at these Reynolds numbers the airfoil boundary layer is bound to be turbulent, which in fact generates trailing-edge noise. A transition to turbulence,

[9] Note however that older wind turbine stall-regulated concepts, and smaller turbine concepts, for which a pitch regulation system is too costly, stall is used in order to regulate the generator maximum electrical output above rated power.

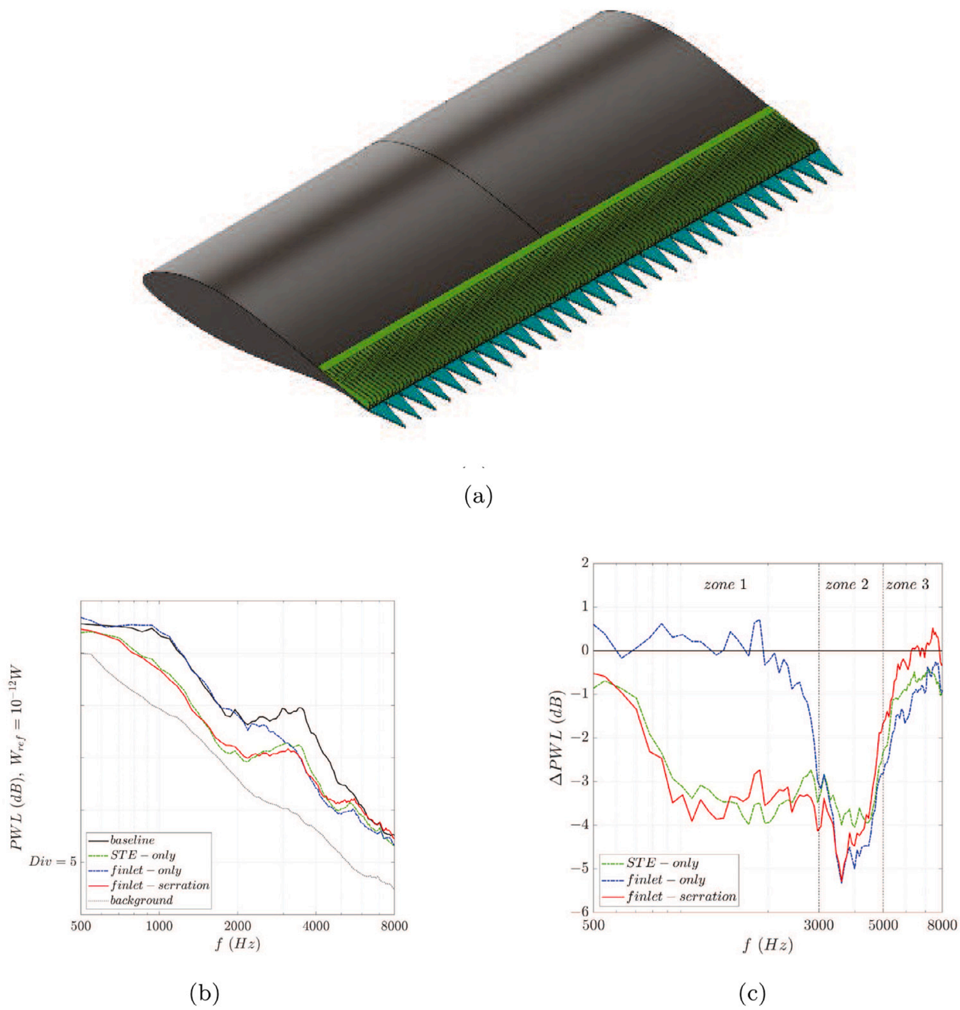


**Fig. 34.** (a) Schematic illustrating the finlet-serration configuration, (b) Sound Power Level (dB) for the baseline, finlet-only, STE (serrated trailing edge)-only, and finlet-STE airfoil, and (c) difference in Sound Power Level (dB) for the finlet-only, STE-only, and finlet-STE airfoil. All the test was conducted at $U$ = 30 m/s and the geometrical angle of attack = 0°.

and in particular its location on the blade airfoil sections, plays an important role on the noise emissions when the boundary layer reaches the trailing edge, e.g. by boundary layer thickening [282,283].

Although it has been recognized for a long time that trailing-edge noise is the main contributor to wind turbine noise in the audible frequency range, the study by Oerlemans et al. [223] provided a formal experimental evidence for this. Using a microphone array, they were able to isolate the regions of the rotor disk where noise at various frequencies is produced (see Fig. 35). Furthermore, they showed that the use of a mitigation technique for trailing-edge noise, here serration (see discussions in Section 3.4 and Section 4.2), reduces the noise emissions in these regions (see Fig. 36). Two additional important findings also emerged from this study. As can be observed in the picture in Fig. 35, higher noise emissions are observed: (1) in the outer part of the blade, and (2) when the blade is pointing upward and in its descending phase slightly after passing the vertical position during its rotation. The former finding can be expected since it is near the tip where the blade experiences its highest relative velocity. The latter fact is less well-understood and several mechanisms may play a role here. Firstly, it can be argued that the wind speed is larger at higher altitude due to the atmospheric wind shear. This should result in larger angles of attack and thereby more intense trailing-edge noise emission, in particular at lower frequencies, on the upper part of the rotor disk. Secondly, geometric factors related to the specific cardioid directivity pattern of trailing-edge noise emission can play a role. Finally, since the blade is a moving noise source, a convective amplification can also contribute to the pattern observed in Fig. 35. Note that the two latter mechanisms depend on the observer position relatively to the rotor disk. Thus, it may be possible to isolate the most significant mechanism (if indeed one of the above mechanisms is dominating) by changing the position of the observer.

Primarily, trailing-edge noise from wind turbine blades is driven by 2 factors: the rotational speed of the rotor and the blade pitch angle. The former mainly affects the relative inflow velocity impacting the blade, while the latter is the driving parameter determining the angle of attack at which the relative inflow velocity impinges the blade. At the same time, these parameters have a direct impact on the power production. Besides, due to the physical processes involved, increasing power production and reducing trailing-edge noise are antagonist goals during the design phase of a turbine. Thus, the main strategy for complying with noise regulations consists in an optimal design of the turbine operational conditions (through rotor speed and pitch control) that constrain noise emissions and maximize annual energy production simultaneously [285]. Most manufacturers have proposed different operational modes for their wind turbines, typically one or several low-noise modes and a full-power production mode [286].

**Fig. 35.** The noise source distribution in the rotor plane and measured using a microphone array (averaged over many revolutions) is projected on the picture.
*Source:* Oerlemans [284].

**Fig. 36.** A typical MW-class wind turbine blade with serrations at the trailing-edge.
*Source:* Oerlemans et al. [223].

These schemes can be applied selectively, e.g. during day and night time and/or depending on the proximity of dwellings.[10]

Since wind turbine manufacturers face stringent noise regulations in most countries, accurate predictions of trailing-edge noise is paramount in the design phase. In the industry, manufacturers have relied for a long time on semi-empirical models (BPM being one of the most popular, see Section 3.1.1) and these models were accurately tuned using the considerable amount of know-how and availability of field noise measurements [287]. Indeed, it is rare that totally innovative concepts, at least in term of blade aerodynamic design and associated aeroacoustic characteristics, are directly introduced into the market, at least without thorough prior testings. The use of simpler and faster prediction methods also responds to the requirement of fast turnover loops in the design process. Nevertheless, more advanced simulation methods are continuously being improved and introduced in wind turbine design, and these are used in conjunction with the development of more advanced technologies. A typical example is the use of CFD. A decade ago, it was started to be used in place of more empirical simulation methods. Nowadays, it has become an everyday industrial tool used for design, also in the context of aeroacoustics.

The above is specially true when developing and improving new mitigation devices as it is the case for serration. Although this technology originated from the aeronautical industry, early implementations within the wind turbine industry have heavily relied on empiricism. The trend in the industry is now to refine trailing-edge geometric designs. New concepts have emerged [244] (see Fig. 28) or are being investigated, such as finlets [267] (see Fig. 32), porous trailing edges, brushes, etc [288]. More advanced simulation and measurement methods are implemented and used to this end [234,289] (see also Sections 3.2, 3.3, and 4.2).

In the context of wind turbine technology, high-end solutions for trailing-edge noise mitigation such as jet injection or boundary layer suction devices [290–292] are still not viable options. Indeed, wind energy and wind turbine design are constrained by a strong economical competition with other energy sources. Therefore, maintenance costs must be kept to a minimum. More advanced technologies usually do not fulfill the required levels of sturdiness and durability for the relatively harsh environment experienced by wind turbine blades over their 20 years, or so, expected lifespan. But, it may be a question of time before these technologies have matured enough so that they can be applied on wind turbines.

An important factor to consider when designing wind turbine blades, and including noise in this process, is the 3-dimensional effects. Indeed, new airfoils and mitigation devices (e.g. serration) are typically developed in a 2-dimensional (2D) context. This is true both for modeling and experiments. In the former case, models often assume 2D homogeneity along the blade span to allow for the development of a theoretical frame (e.g. Howe/Amiet theories), or to adapt to existing computational resources (e.g. in CFD/CAA simulations). In the latter case, wind tunnel tests are mostly conducted on 2D airfoil sections as far as trailing-edge noise is concerned. However, the physics of the flow on a real wind turbine rotor blade may differ from these idealized conditions. The two main differences between the ideal conditions of a 2D flow versus real-life wind turbine blades originate from: (1) the varying blade geometry along its span and (2) transverse flow patterns induced by the centrifugal forces from the rotor rotation. These aspects are not considered in current wind turbine design, as far as the authors are aware of. Nevertheless, 3D CFD and CAA simulations are emerging as potential simulation tools for wind turbine blade design (see Section 3) and this situation may rapidly evolve in the near future.

Another specificity of wind turbine noise related to trailing-edge noise is the so-called Amplitude Modulation (AM) [293]. So far, there is no consensus on a single cause for this mechanism, and a number of scenarios, or combinations of them, can be considered. First, it is important to define what is meant by AM and from where it originates. In contrast to a sound source emitting at the same noise amplitude or level, a sound source can emit noise with a varying (or modulated)

[10] Note that control strategies for a wind turbine include noise emissions, alongside fatigue and maintenance issues. They are highly confidential as they have a large impact on the cost efficiency of a turbine during its life-time expectancy, which is in turn an important factor for marketing and sales, and ultimately for the investors.

strength (or amplitude). This is the case for a wind turbine when the passing of the, say 3, different blades can be distinctly heard when standing next to a wind turbine. This is often referred as 'swish'. The cause for this relates to the analysis conducted above for the noise map. As mentioned there, and assuming that trailing-edge noise is the dominant source of noise, which is an accepted fact, the cause can be a high wind shear, noise directivity effects, convective amplification (see earlier discussions). However, dwellings are always located at a certain distance from wind turbines and wind farms. In the case of a wind farm, for example, the AM of each turbine can cancel each other into a more continuous noise, which is less annoying in terms of human perception. However, certain atmospheric conditions (which may be intermittent, rendering the phenomenon even more audible by a change in the characteristics of noise) may enhance the generation, propagation or audibility of AM from a single or several wind turbines to the dwelling. Therefore, this is a topic that has been widely discussed in planning and post-installation phases of wind turbines/farms and is still a controversial subject in term of acceptance of wind energy. Note that this has led to studies on how to accurately quantify this phenomenon for regulation purposes [294]. To conclude, there may exist a solution to mitigate some of the AM noise impact from wind turbines, at least for the "swish"-type noise emission as discussed above. If the wind shear and/or directivity are proven to be the main causes for AM generation, the well-known directivity pattern of trailing-edge noise together with known or assumed atmospheric conditions (i.e. here the wind shear) could be used to operate the wind turbine more efficiently, at least in terms of AM strength reduction. Individual cyclic pitch of the, say 3, different blades with a varying period equal to one revolution of each blade, could be used to levelize the noise emission from each blade, thereby mitigating the overall AM emission from a turbine [295,296]. The basic idea is to regulate the angle of attack experienced by the outer part of the blade by a varying pitch of the blade into a more constant value, which in turn would produce more constant noise source emissions from the trailing edge as each individual blade rotates.

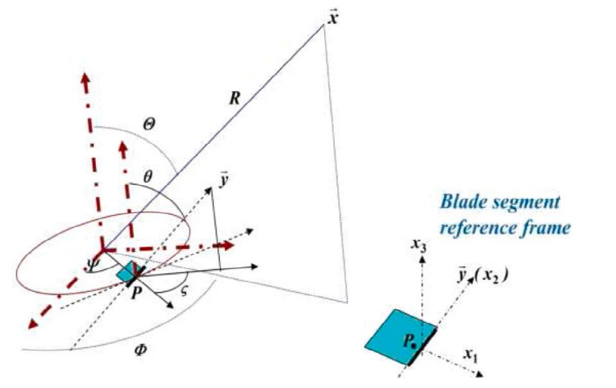


**Fig. 37.** Fan reference frames with a blade segment at trailing-edge point $P$. Observer's coordinates are $(R, \Theta, \Phi)$ with respect to rotor frame. A trailing-edge line is along the $\boldsymbol{y}$ axis. $(\theta, \zeta)$ are the orientation angles of the trailing-edge line with respect to rotor axes ($\zeta = 0$ and $\theta = \pi/2$ for axial and unswept blades).

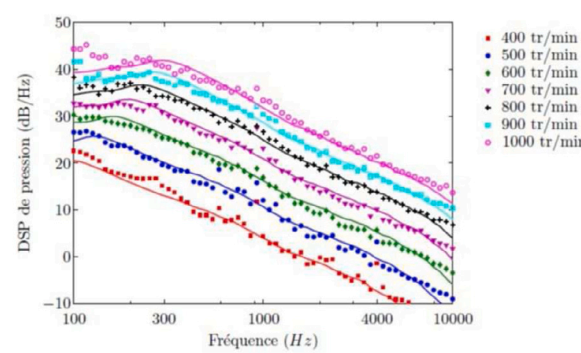


**Fig. 38.** Acoustic pressure PSD in the rotational plane ($\Theta = 90°$). Experimental results (symbols) and analytical results given by Eq. (80) (lines) [110].

## 5.2. Fan noise

Fan noise covers a wide range of applications from low speed machines with generally a low solidity (low pressure rise) to a high speed machines with high solidity (high pressure rise). Several reviews have been made recently, which cover both ranges and most noise sources [297–300]. In the present study, the focus is only on the self-noise or trailing-edge noise mechanism that corresponds to the minimum noise these machines will produce, free of any installation/interaction mechanisms. As pointed out by Roger and Moreau (Fig. 1 in [298]), cascade effects can become relevant when the solidity and the blade overlap becomes high. This additional effect is neglected here. Moreover, most of the present review neglects the possible effect of a duct and considers free-field applications. The corresponding information can be found in [298–300].

As originally noted by Schlinker and Amiet for high-speed blades of helicopter rotors [62], a fan blade segment in circular motion can be considered locally as moving in translation with its relative speed. This is actually valid only for sound frequencies higher than the rotational frequency. The sound heard at an angular frequency $\omega$ is then produced by sources on the rotating blade segment having different frequencies depending on their angular position. The resulting power spectral density (PSD) of the far-field acoustic pressure of a fan with $B$ uniformly spaced blades is decomposed in $N$ strips. $S_{pp}$ is then obtained by averaging over all possible angular locations $\Psi$ of all blade segments and all radial strips, and then weighted by the Doppler factor: $\omega_e(\Psi)/\omega = 1 + M \sin\Theta \sin\Psi$, where $M$ stands for the local relative Mach number. The various angles are defined in Fig. 37. It then reads:

$$S(\boldsymbol{x}, \omega) = \sum_{k=0}^{N} \frac{B}{2\pi} \int_0^{2\pi} \left(\frac{\omega_e(\Psi)}{\omega}\right)^2 S_{pp}^k\left(\boldsymbol{x}(\Psi), \omega_e(\Psi)\right)\, d\Psi \tag{80}$$

where $S_{pp}^k$ are the PSD of each segment in translation. They are therefore given by some of the models described in Section 2 (Amiet's model for instance). Provided that the three-dimensional aerodynamic effects due to inertial acceleration and radial pressure gradients are not too large and do not significantly modify what happens on an isolated airfoil, these PSD could be obtained on isolated airfoils from either wall-pressure measurements or numerical simulations as the LES and DNS described in Section 3. Such an assumption was verified on a specific instrumented fan blade termed Rotating Controlled Diffusion Blade (RCDB), which was designed to be built from hub to tip only with the controlled diffusion airfoil that had been previously tested and simulated (see Sections 3 and 4). Moreau et al. [301] showed that the actual mean blade loading was slightly modified by the rotation, but not the wall-pressure fluctuations significantly.

By comparing with the exact free-field formulation in rotation (Ffowcs Williams and Hawkings' analogy [302] in frequency domain [61]), such an approximate expression given by Eq. (80) was verified by Sinayoko et al. [303] to be valid up to transonic speeds, with even limited discrepancies (1–2 dB) in the latter regime. By measuring simultaneously wall-pressure statistics at two different blade radii and far-field sound on a large two-blade ventilator at different rotational speeds, Rozenberg et al. [110] obtained excellent agreement at all regimes between the model predictions with Eq. (80) and the experimental data, as shown by the acoustic spectra in the rotational plane ($\Theta = 90°$) in Fig. 38. Similar agreement on the directivity was found at all frequencies (Fig. 18 in [110]). The model was first applied to low-speed fans by Roger et al. [304], and applied to an automotive engine cooling fan with airfoil wall-pressure statistics coming from the above CD airfoil at 8° and 15°. Moreau and Roger [305] later confirmed by comparing turbulence-interaction and trailing-edge noise contributions that the trailing-edge noise could be the main noise contributor at high frequencies beyond 4 kHz. Recently, Sanjose and Moreau [106] applied the model systematically on an automotive ring fan (termed H380EC1), which had been tested in a reverberant wind tunnel at several flow rates along a performance curve as shown above in Fig. 14. Fig. 39 compares the sound power levels (PWLs) at three different flow rates covering the fan operating range, and the overall sound power levels (OAPWLs) between the model predictions and the experimental data. In Fig. 39(a), the trailing-edge contribution has been calculated using Rozenberg's wall-pressure model [86] and the leading-edge contribution has been fitted with an isotropic von Kàrmàn spectrum. All inputs of both models (boundary layer and turbulence parameters) have been extracted from a RANS simulation of the flush-mounted fan on the test-rig. As found before with more empirical inputs [305], the trailing-edge noise is found to dominate at high frequencies, with an increasing contribution with increasing flow rate. Indeed, in Fig. 39(a), trailing-edge noise covers most of the broadband noise envelope at 3500 $m^3/h$. This is further confirmed by the OAPWL shown in Fig. 39(b) (the two solid lines stand for the experimental spread among different mock-ups and prototypes): the trailing-edge noise becomes relevant beyond 2700 $m^3/h$ where it has an equal contribution to the overall fan noise. Note that at very high flow rate, the remaining difference of 5 dB in the OASPL is caused by a strong tonal contribution seen in Fig. 39(a), not accounted for in the models for this flow condition. Coutty et al. [306] recently applied the same methodology to a more complex full engine cooling module with promising results. Finally, this approach has also been recently applied to wind turbines by Cotté et al. [119,307]. Note also that alternative methods have also been proposed. For instance, Casalino et al. [308] proposed a stochastic method to predict the broadband noise generated by an automotive engine cooling axial fan system.

On the numerical side, very limited unsteady simulations properly resolving part of the turbulent scales have been achieved to yield reliable self-noise predictions. In 2006, Yamade et al. [309] were the first to achieve an incompressible LES on a low-speed axial-fan with the massively parallel FrontFlow/blue code developed by Kato. The Reynolds number based on the blade tip speed and the diameter of the blade tip, $Re_D$, was about $4\times10^6$. Even on the finer mesh with 33 million elements, the boundary layer was hardly resolved and no convergence on the wall-pressure fluctuations could be reached. The latter was then fed to the boundary element method code SYSNOISE to account for the actual ducted configuration of the experiment. Even though the acoustical resolution was also limited to a maximum frequency of 700 Hz, the agreement for the predicted sound pressure levels with measurements on the limited frequency range was reasonable. Note that their second prediction using Curle's analogy was quickly overpredicting the measured levels as seen above on airfoils. The first compressible prediction of fan noise was achieved in 2010 by Perot et al. [310] on the H380EC1 fan ($Re_D = 1.2\times10^6$) with a hybrid LBM/VLES method using PowerFLOW. This first study clearly showed that the broadband noise was dominated by the pressure fluctuations at the blade tips and on the rotating ring (suggesting some contributions from the tip gap flow), but did not have the proper grid resolution (minimum voxel size of 1 mm) to capture the oscillating shape of the experimental broadband spectrum (see spectra in Fig. 39). A grid convergence was subsequently achieved by Moreau and Sanjose [311] and both the shape and the levels of broadband noise were captured accurately, and the solution was becoming grid independent below a minimum voxel size of 0.25 mm. A similar excellent agreement with experiments was later achieved by Zhu et al. [312] with PowerFLOW on the USI-7 fan ($Re_D = 9.36\times10^5$), tested at Siegen universitat for two different tip gaps. Pogorelov et al. [313,314] simulated the same configuration using a fully conservative cut-cell method and a monotone integrated LES (MILES) approach of the compressible Navier–Stokes equations. They achieved a grid convergence of turbulence statistics with 1 billion cells and their study also followed the experimental trends when varying the tip gap size. Even though they matched the overall performances well, however, they did not manage to reproduce the experimental acoustic spectral shape and levels well. Finally, note that Moreau and Sanjose [311] also showed that, with the SAS model, similar good agreement could be achieved on the H380EC1 over a wide frequency range.

Moreover, as shown by Moreau and Sanjose [311], combining different numerical predictions namely unsteady RANS, SAS, and hybrid LBM/VLES simulation, the main contribution in a low-speed fan even in its simplest, cleanest set-up e.g. flushed mounted on a plenum without any upstream and downstream obstacles, is the tip noise coming from the turbulence created in the tip gap mixing with the incoming flow at the blade tip. Only at high frequencies again, trailing-edge noise can be evoked and shown to contribute as found with the above analytical model. Note that the resulting fan noise often has two broadband contributions, a bell-shaped smooth spectrum spread over a large range of frequencies and some narrower humps centered at some sub-harmonic of the blade passing frequencies, as shown in Fig. 39(a). The former comes from both the small-scale turbulence at the tip and at the trailing-edge, the latter from large coherent structures also forming in the tip gap as shown in both the H380EC1 and USI-7 fans [311,312]. Recently, several different unsteady methods have been reviewed on the H380EC1 fan [315], with increasingly more complex experimental set-ups, starting from the above flush-mounted fan-alone configuration [311] to the complete installed fan in its engine cooling module [316] and possibly with additional upstream periodic obstructions that can be set in rotation to mimic the necessary process to optimize their size and position [317]. Noticeably, the LBM is extremely accurate to predict the broadband noise spectra and becomes more and more computationally efficient as the complexity of the model increases (full engine cooling modules, fan systems with upstream obstructions to control its tonal noise etc.). It should be emphasized that such a study on axial ring fans could be transposed to any axial or radial fans [318].

Overall, for low-speed fans, most unsteady simulations that can resolve enough turbulent scales and the tip gap flow will provide some reasonable predictions of the broadband noise, and the hybrid LBM/VLES seems particularly efficient and accurate especially for the more complex flow conditions and set-ups. The trailing-edge contribution is, however, limited to the high frequency range and can be quickly masked by other installation effects. Finally, for high-speed turbomachines, fan noise has also been extensively studied, but it was mostly the dominant fan-Outlet Guiding Vane interaction mechanism and rarely the rotor-alone noise mechanisms. Glegg and Jochault [319] proposed a broadband self-noise model for ducted fans, which has been recently compared to the NASA Source Diagnostic Test (SDT) turbofan database by Sanjose et al. [320]. All wall-pressure spectra models derived from low-speed airfoil databases such as Rozenberg's [86] or Lee's extension [90] seem to underpredict the levels obtained numerically by a recent wall-modeled LES [58,321]. Only Gliebe's model tuned to high-speed turbofans was able to yield the proper levels [322]. As a result, most trailing-edge noise predictions significantly underestimated both the measured and LES-predicted noise levels. Only predictions based on Gliebe's inputs could partially retrieve the upstream power levels. Moreover, the recent high-order wall-modeled LES on the NASA Source Diagnostic Test turbofan seems to confirm that the trailing-edge noise mechanism as described above is not dominant, but rather the tip flow again [323,324]. Further efforts are needed to clarify such a contribution and to develop some adequate analytical models.

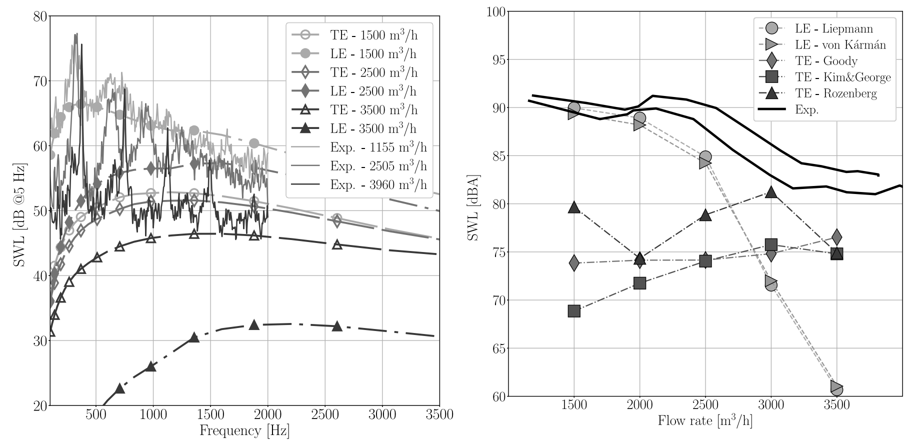


(a) (b)

**Fig. 39.** Comparison of the model predictions with measurements on the H380EC1 ring fan: (a) Sound Power Levels; (b) Overall Sound Power Levels (the two solid lines show the experimental range).

### 5.3. Rotorcraft and propeller noise

Most rotorcraft noise research has been focused on tonal noise including blade vortex interaction noise and high speed impulsive noise. One of the earliest publications on helicopter broadband noise based on the physics-based model is Schlinker and Amiet's NASA report [62]. They extended Amiet's airfoil trailing-edge noise model for helicopter rotor broadband noise, and found that trailing-edge noise from a full-scale helicopter contributes significantly to the total broadband noise spectrum at high frequencies. They used a flat plate turbulent boundary layer calculation to estimate the surface pressure spectrum. Kim and George [325] applied Ffowcs Williams and Hawkings equation for rotor trailing-edge noise predictions in hover. In their method, however, each blade was modeled as a point source of a flat plate, and the effect of an angle of attack was neglected. Blandeau and Joseph [326] showed that Amiet's model provides good agreement with the results from Ffowcs Williams and Hawkings equation, especially at high frequencies. In their paper, they used Goody's wall pressure spectrum model [85], which was developed for zero pressure gradient flows on a flat plate. In addition, they assumed that the observer and propeller were in the same vertical plane and neglected the effects of skewed gust. They also considered the noise source as a point source that is located at 75% of the blade radius. Recently, Li and Lee [327] combined the blade element momentum method (BEMT), XFOIL, Lee's wall pressure spectrum model, and Amiet's method to predict helicopter trailing-edge noise in hover. The equation of the averaged acoustic power spectral density is essentially the same as Eq. (80). In this paper, the noise source is located at the trailing-edge of the mid-span of the blade segment. Through BEMT, the induced velocities were included, which is essential for accurately predicing the angle of attack. The boundary layer flow properties for actual airfoil geometries were obtained through XFOIL. Lee's model provided more accurate turbulent wall pressure spectrum results for adverse pressure gradient flows. Since Amiet's method was used, the first principles acoustic scattering physics was well captured and the method could be extended for non-rectangular trailing edges such as serrated trailing edges using analytic solutions [42,43]. Using this code, named UCD-QuietFly, they analyzed the effect of rotor blade design parameters and operating conditions, including rotor tip Mach number, collective pitch angle, twist angle, blade chord length, rotor radius, on rotor broadband noise. In addition, they have incorporated coordinate transformations for general motions of rotor blades. They found a semi-analytic equation for far-field noise propagation from SPL at a reference position, which is one rotor diameter below the rotor hub. This semi-analytic equation enables fast calculations for a noise map that consists of several hundreds of observer locations. They have developed machine-learning-based fast predictions based on UCD-QuietFly [328]. UCD-QuietFly's rotor noise validation cases are shown in Fig. 40. The high-frequency trailing-edge noise was well captured by the UCD-QuietFly predictions against the measurement data for both helicopter noise and drone noise. The rotor configurations and operating conditions are shown in Tables 5 and 6. Recently, Li and Lee [329] used a dynamic inflow model [330] along with the blade element method (BET) to predict rotor trailing-edge noise in forward flight.

**Table 5**
Configuration of UH-1B Helicopter [335].

| Item | Value |
|---|---|
| Radius [m] | 6.7056 |
| Airfoil | NACA0012 |
| Number of blade | 2 |
| Linear twist [deg] | −10 |
| Solidity | 0.0506 |
| Collective pitch [deg] | 13.52 |
| $(X_2, Y_2, Z_2)$ [m] | (60.69, 0, −30.48) |
| $(R_o, \Psi)$ [m, deg] | (67.91, −26.7) |
| $C_T$ | 0.0036 |
| $M_{tip}$ | 0.67 |

**Table 6**
APC Slow Flyer 11X4.7 Rotor Parameters [336].

| Item | Value |
|---|---|
| Radius [m] | 0.14 |
| Number of blade | 2 |
| RPM | 3600 |
| Observer distance [m] | 1.095 |
| Observer elevation angle [deg] | −45 |
| Airfoil | E63(hub)/ClarkY(tip) |

The methods described in the previous paragraph are first principles acoustic scattering method. Another popular and simpler prediction method is the BPM semi-empirical model (see Section 3.1.1). Although this model was developed based on NACA 0012 airfoil noise data, it is widely used in rotorcraft community. Recent studies include the references [331–334].

In experimental research, Brooks et al. [337] tested DNW wind-tunnel tests to measure rotor noise including trailing-edge broadband noise. This paper includes extensive measurement data for a wide range of operating conditions including hover and forward flights

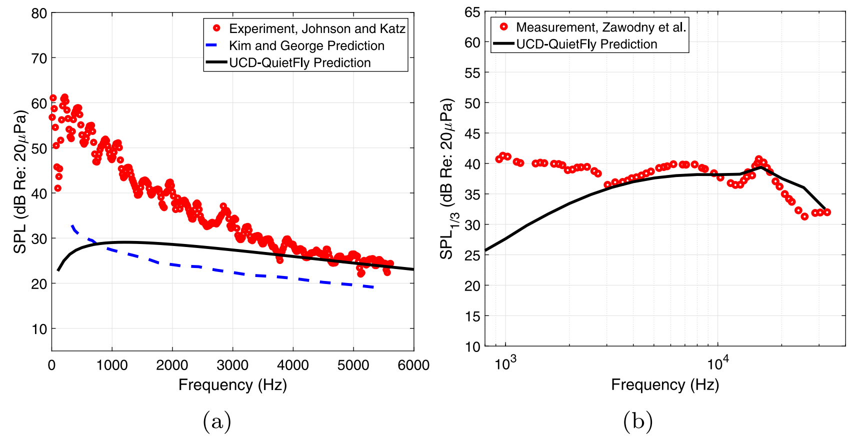


**Fig. 40.** Validation of UCD-QuietFly against measurement data [328]: (a) UH-1B helicopter noise (measurement data [335] and Kim and George's prediction [325]) and (b) APC drone noise (measurement data [336]).

with various advance ratios at different thrust conditions. Trailing-edge noise significantly varied with a change in the tip Mach number, but it did not change much with different rotor thrust values. For a small advance ratio in forward flight, trailing-edge noise was similar to that of hover. Low- and mid-frequency noise was dominated by wake induced leading-edge noise in hover. In general, trailing-edge noise became evident at mid- and high-frequencies in forward flight as blade wake induced leading-edge noise became weaker at these frequency ranges. Snider et al. [338] measured helicopter noise in flight and calculated Effective Perceived Noise Level (EPNL). They identified broadband noise is a main contributor to EPNL. They showed that high-frequency broadband noise is especially important when a helicopter is above the head and flies away.

Small-scaled multi-rotor drone noise has recently received a lot of attention. The acoustic measurements by Zawodny et al. [336] showed that the DJI quad-copter drone rotors generate considerable broadband noise above 1 kHz frequency and the A-weighted spectrum indicated increased importance of this noise in human hearing. They also showed that the laminar separation noise is important. Pettingill and Zawodny [339] measured SUI drone noise and used the BPM model [46] to predict airfoil self-noise. In this paper, they did not include the laminar separation noise. The role and relative importance of the laminar separation noise for drones are still questionable. They identified that the separation noise and trailing-edge noise is dominant at high frequencies. In their paper, the trailing-edge noise was separated from the separation noise since the original BPM paper considered the trailing-edge noise only at a zero angle of attack and the separation noise at a non-zero angle of attack. However, it should be noted that the separation noise at a non-zero angle of attack below the stall is still part of the trailing-edge noise in terms of flow physics. Therefore, this distinction between trailing-edge noise and separation noise could be misleading to readers. In fact, in Howe's or Amiet's models, both noise components are calculated as trailing-edge noise since the noise generation mechanism is the same. Intaratep et al. [340] measured multi-copter DJI Phantom rotor noise. They showed that trailing-edge noise is not only important at mid- and high-frequency ranges, but also considerably increases from a single rotor to multi-rotors. Zawodny and Boyd [341] investigated the effect of a fuselage on small-scaled rotor noise. They showed that the fuselage makes a large impact on tonal noise, but it does not change high-frequency broadband noise. It is anticipated that the pressure fluctuations on the fuselage due to rotor wake flow impingement would generate broadband noise, but this fuselage-induced broadband could be masked by the much stronger blade leading-edge noise and trailing-edge noise.

As an urban air mobility (UAM) concept becomes popular and many companies are building prototypes of electric vertical take-off and landing (eVTOL) aircraft, people are concerned about noise of this futuristic vehicles. When UAM aircraft takes off and lands nearby residential areas, high-frequency noise would be significantly annoying to people. Li and Lee [342] applied UCD-Quietly to predict multi-rotor trailing-edge noise particularly for urban air mobility (UAM) applications. They showed that the trailing-edge noise levels increase with a larger number of rotor blades. They compared UAM multi-rotor vehicle trailing-edge noise with conventional helicopter trailing-edge noise, as well as community background noise. They addressed that the UAM aircraft broadband noise could be a large concern in residential areas, especially when it is taking off or landing, compared to background noise [343]. They also addressed that multi-rotor vehicles are beneficial in terms of the amplitude modulation of broadband noise or noise annoyance levels compared to single rotor noise.

Recent passive noise reduction techniques were applied to rotorcraft or propeller. Halimi [344] used an analytical method [42] and Lattice Boltzmann method simulations for a propeller with straight and serrated trailing edges to reduce trailing-edge noise. Yang et al. [345] conducted an experimental research on wavy leading and trailing edges. They demonstrated that the destructive effects of the scattered pressure by the wavy trailing edge surfaces reduce trailing-edge noise. When the RPM was increased, the broadband noise reduction decreased due to the increased misalignment of the wavy surfaces with the shedding vortices.

### 5.4. Outlook

Wind turbine technology is currently developing quite rapidly in parallel with the increasing deployment of wind energy in response to the societal demand for clean energy sources. There are certainly the noise improvement needs and requirements for wind energy. As can be expected, the wind industry is taking advantage of earlier technical developments from the aeronautical and related industries in the field of aerodynamics and aeroacoustics. As an example, in order to reduce structural loads for the future generation of large wind turbines (in the range of 10 MW or more), aerodynamic control using trailing-edge flaps is investigated as a commercially viable option for increasing wind turbine blades' life-time and, thereby, reducing the levelized cost of energy [346–348]. Such concepts include classical flaps with pneumatic actuators as used on airplanes, morphing wing technology, and other technical solutions. In any case, such new concepts will certainly have an impact on trailing-edge noise emissions, and it can be expected that classical engineering models currently used for blade designs may fail to accurately predict wind turbine noise in these conditions. Engineers and researchers will be faced with the choice of either improving and extending the range of validity of existing engineering models, or using more advanced (but also more computationally demanding) methodologies such as LES or DNS (see Section 3). Other disruptive wind turbine concepts may also arise. A few examples can be mentioned: tip rotor, multi-rotor, multi-element blades, multi-section blades. All of these configurations may prove challenging for existing engineering trailing-edge noise models. Once again, more advanced prediction tools will probably need to be developed and/or implemented for the design of such new concepts.

In fan noise, trailing-edge noise remains relevant as it provides the minimal broadband noise levels that such a machine can achieve without any installation effect, and is also often the main contributor at high frequency. More and more detailed LES predictions of rotor self-noise such as the recent ones by Perez-Arroyo et al. [349] or Kholodov and Moreau [323,324] on the SDT turbofan configuration should be foreseen in the future to quantify trailing-edge noise relatively to tip noise. The efficient hybrid LBM/VLES simulations are already providing detailed insights into the noise mechanisms of installed fans, and more refined simulations particularly in the tip region should ease the proper separation of the different noise sources in these more complex, but more realistic configurations.

Conventional helicopter trailing-edge noise will be continuously important in terms of EPNL metrics or noise regulations. The effect of flight conditions during forward flight at different advance ratios on the generation and propagation of trailing-edge noise should be studied. As more drones and VTOL air taxi vehicles will be expected to fly near the community areas, trailing-edge broadband noise would be a great concern to people during hover, take-off, or landing of these vehicles near the ground as well as forward flight at low altitudes. Unless this noise is not significantly reduced, it would be challenging for UAM vehicles to take-off, land, or fly in the neighborhood. This indicates the noise improvement needs and requirements for UAM operations. Passive and active noise reduction techniques need to continue to be developed and applied to these vehicles. These broadband noise reduction techniques have not been studied much in rotorcraft community. It is expected that more research will be conducted in rotor trailing-edge noise reduction experimentally and computationally in the coming decades. Classical BPM models may not be applicable for non-straight trailing edge shapes. First principles trailing-edge noise theories, such as variants of Amiet's models, are more suitable to study rotor trailing-edge noise reduction with serrated edges as mentioned in Section 2. Airfoil design and optimization for low trailing-edge noise is also an important research topic. Fast predictions that can be embedded in an optimization loop will rely on analytical and semi-empirical models along with steady or unsteady RANS simulations. Therefore, the predictive accuracy of rotor trailing-edge noise will depend on the accuracy of the analytical and semi-empirical models in conjunction with RANS solutions. For high local blade angles of attack, or blade stall, the current prediction methods may not be accurate in terms of both RANS solutions and semi-empirical acoustic models. In addition, most prediction methods were developed on the strip theory so that these methods are not applicable for radially varying flows or cross-wind conditions. Traditional wall-resolved LES might be challenging for full rotor simulations due to the excessive computational cost. The wall-model LES or efficient hybrid LBM/VLES simulations in conjunction with acoustic analogy equations may open new avenues for rotor/propeller broadband noise predictions, but the accuracy of these simulations for the boundary layer turbulence near the trailing edge should be further validated.

## 6. Conclusions

This paper presented a comprehensive review of turbulent boundary layer trailing-edge noise over several decades in theoretical, computational, and experimental aspects. All three methods have significantly advanced our knowledge and understanding in fluid mechanics and acoustics and enabled us to make devices to reduce trailing-edge noise. Applications of trailing-edge noise have been discussed for wind turbine noise, fan noise, and rotorcraft/propeller noise.

Aeroacoustic theory in trailing-edge noise has been well developed over several decades. Amiet's model and Howe's model are widely used for trailing-edge noise predictions, and several variants of Amiet's model have been produced to deal with arbitrarily shaped trailing edges. The Wiener–Hopf technique has been advanced to solve the acoustic scattering in a finite chord length. There was a significant progress in theoretical approaches for trailing-edge noise reductions in recent years. These recent achievements include the development of analytical models for poroelasticity and serrations. These advanced models enable a quick assessment of design parameters. The theoretical models require turbulent surface pressure spectra as an input to the noise prediction. Therefore, the accuracy of the trailing-edge noise prediction depends on an accurate modeling of the surface pressure spectra.

In terms of computational methods, low- and high-fidelity models serve very well for each purpose. The low-fidelity models, such as BPM model, TNO model, or empirical wall pressure spectrum model, have been developed during the last decades and will be continually used for quick calculations and in industrial design cycle. Several RANS-based medium-fidelity statistical models were also developed. Parameter tuning for these low- and medium-fidelity models is essential to achieve accurate predictions. Hence, the validity of their prediction is typically limited within the calibrated range of parameters, although this range could be wide enough to cover most of operating conditions of interest. The usage of high-fidelity models, such as LES or DNS, is slowly growing to provide a better understanding of flow physics and complement experimental research. High-resolution data in spatial and temporal domains, which may not be available in experimental research, provide the unique power of these high-fidelity models. It is expected that LES/DNS will be more used in various noise control concepts to unravel the detailed flow physics and to provide proper guidance on RANS-based semi-empirical models.

Experimental research has played a key role in generating new ideas for noise reduction and evaluating the effectiveness of various noise reduction devices including serrations, slits, porous materials, finlets, and active control. With these devices, 5–10 dB noise reduction was achieved in laboratory environment and 2–5 dB noise reduction was achieved in real products. However, this noise reduction is typically apparent only in certain frequency regions, and no benefits or noise increase were often found in other frequency ranges. In order to achieve further noise reduction or achieve noise reduction in a whole frequency region, a combination of different noise reduction ideas/devices could be pursued. Passive noise control using geometrical modifications was preferred over active noise control due to high cost and maintenance issues associated with the latter. However, the clear advantages in active control over passive control in terms of aerodynamic performance and the range of the operating regime will pave the way for more research and development into active noise control.

The future research recommendations and development needs of each technical discipline and application area were also presented at the end of each section in the paper. Ultimately, the advanced knowledge in aeroacoustics and innovative noise reduction devices will find their home in the final products and help us live in a quiet environment. The research in trailing-edge noise will be continuously important and central part in aeroacoustic community. We hope that this review paper will be useful for readers, especially young engineers or novices who enter this area for the first time.

## Declaration of competing interest

The authors declare that they have no known competing financial interests or personal relationships that could have appeared to influence the work reported in this paper.

## References


[1] T. Colonius, S.K. Lele, Computational aeroacoustics: progress on nonlinear problems of sound generation, Prog. Aerosp. Sci. 40 (2004) 345–416, http://dx.doi.org/10.1016/j.paerosci.2004.09.001.

[2] A. Powell, On the aerodynamic noise of a rigid flat plate moving at zero incidence, J. Acoust. Soc. Am. 31 (1959) 1649–1653, http://dx.doi.org/10.1121/1.1907674.

[3] M. Howe, A review of the theory of trailing edge noise, J. Sound. Vib. 61 (1978) 437–465, http://dx.doi.org/10.1016/0022-460X(78)90391-7.

[4] C.J. Doolan, D.J. Moreau, A review of airfoil trailing edge noise with some implications for wind turbines, Int. J. Aeroacoust. 14 (2015) 811–832, http://dx.doi.org/10.1260/1475-472X.14.5-6.811.

[5] M.J. Lighthill, M.H.A. Newman, On sound generated aerodynamically I. General theory, Proc. R. Soc. Lond. A 211 (1107) (1952) 564–587, http://dx.doi.org/10.1098/rspa.1952.0060.

[6] J.F. Williams, L.H. Hall, Aerodynamic sound generation by turbulent flow in the vicinity of a scattering half plane, J. Fluid Mech. 40 (4) (1970) 657–670, http://dx.doi.org/10.1017/S0022112070000368.

[7] D. Crighton, Basic principles of aerodynamic noise generation, Prog. Aerosp. Sci. 16 (1) (1975) 31–96, http://dx.doi.org/10.1016/0376-0421(75)90010-X.

[8] R. Amiet, Acoustic radiation from an airfoil in a turbulent stream, J. Sound Vib. 41 (4) (1975) 407–420, http://dx.doi.org/10.1016/S0022-460X(75)80105-2.

[9] L. Ayton, M.J. Colbrook, T. Geyer, C. Paruchuri, E. Sarradj, Reducing aerofoil-turbulence interaction noise through chordwise-varying porosity, J. Fluid Mech. 906 (2020) A1: 1–28, http://dx.doi.org/10.1017/jfm.2020.746.

[10] D. Jones, Aerodynamic sound due to a source near a half-plane, IMA J. Appl. Math. 9 (1972) 114–122, http://dx.doi.org/10.1093/imamat/9.1.114.

[11] H.M. Macdonald, A class of diffraction problems, Proc. Lond. Math. Sic. 14 (1915) 410–427, http://dx.doi.org/10.1112/plms/s2_14.1.410.

[12] M. Roger, S. Moreau, K. Kucukcoskun, On sound scattering by rigid edges and wedges in a flow, with applications to high-lift device aeroacoustics, J. Sound Vib. 362 (2016) 252–275, http://dx.doi.org/10.1016/j.jsv.2015.10.004.

[13] P. Salas, G. Fauquembergue, S. Moreau, Direct noise simulation of a canonical high lift device and comparison with an analytical model, J. Acoust. Soc. Am. 140 (3) (2016) 2091–2100, http://dx.doi.org/10.1121/1.4963092.

[14] M. Howe, Contributions to the theory of aerodynamic sound, with application to excess jet noise and the theory of the flute, J. Fluid Mech. 71 (1975) 625–673, http://dx.doi.org/10.1017/S0022112075002777.

[15] N. Wiener, E. Hopf, Über eine klasse singulärer integralgleichungen, Sitzg.-Ber. Preuss. Akad. Wiss. Phys.-Math 31 (1931) 696–706.

[16] B. Noble, Methods Based on the Wiener-Hopf Technique, Pergamon Press, 1958.

[17] T. Chong, A. Vathylakis, On the aeroacoustic and flow structures developed on a flat plate with a serrated sawtooth trailing edge, J. Sound Vib. 354 (2015) 65–90, http://dx.doi.org/10.1016/j.jsv.2015.05.019.

[18] D.I. Baker, Acoustic Scattering in Sheared Flow (Ph.D. thesis), University of Cambridge, 2020, http://dx.doi.org/10.17863/CAM.44966.

[19] R. Amiet, Noise due to turbulent flow past a trailing edge, J. Sound. Vib. 47 (1976) 387–393, http://dx.doi.org/10.1016/0022-460X(76)90948-2.

[20] M. Roger, S. Moreau, Back-scattering correction and further extensions of amiet's trailing-edge noise model. Part i: Theory, J. Sound Vib. 286 (2005) 477–506, http://dx.doi.org/10.1016/j.jsv.2004.10.054.

[21] S. Moreau, M. Roger, Back-scattering correction and further extensions of amiet's trailing-edge noise model. Part II: Application, J. Sound Vib. 323 (1-2) (2009) 397–425, http://dx.doi.org/10.1016/j.jsv.2008.11.051.

[22] M. Howe, Edge-source acoustic Green's function for an airfoil of arbitrary chord, with application to trailing-edge noise, Q. J. Mech. Appl. Math. 54 (2001) 139–155, http://dx.doi.org/10.1093/qjmam/54.1.139.

[23] M. Abramowitz, I.A. Stegun, Handbook of Mathematical Functions with Formulas, Graphs, and Mathematical Tables, ninth Dover printing, tenth GPO printing, Dover, New York, 1964.

[24] M. Wang, S. Moreau, G. Iaccarino, M. Roger, LES Prediction of wall-pressure fluctuations and noise of a low-speed airfoil, Int. J. Aeroacoustics 8 (3) (2009) 177–197, http://dx.doi.org/10.1260/147547208786940017.

[25] J. Winkler, H. Wu, S. Moreau, T. Carolus, R. Sandberg, Trailing-edge broadband noise prediction of an airfoil with boundary-layer tripping, J. Sound Vib. 482 (2020) 115450:1–25, http://dx.doi.org/10.1016/j.jsv.2020.115450.

[26] S. Moreau, M. Roger, Effect of airfoil aerodynamic loading on trailing-edge noise sources, AIAA J. 43 (1) (2005) 41–52, http://dx.doi.org/10.2514/1.5578.

[27] S. Moreau, D. Neal, Y. Khalighi, M. Wang, G. Iaccarino, Validation of unstructured-mesh LES of the trailing-edge flow and noise of a controlled-diffusion airfoil, in: Proceedings of the Summer Program 2006, Center for Turbulence Research, NASA AMES, Stanford, 2006, pp. 519–531.

[28] M.J. Priddin, A.V. Kisil, L.J. Ayton, Applying an iterative method numerically to solve $n \times n$ matrix Wiener–Hopf equations with exponential factors, Phil. Trans. R. Soc. A 378 (2162) (2020) 20190241, http://dx.doi.org/10.1098/rsta.2019.0241, 1–18.

[29] M.J. Colbrook, M.J. Priddin, Fast and spectrally accurate numerical methods for perforated screens (with applications to robin boundary conditions), IMA J. Appl. Math. 85 (5) (2020) 790–821, http://dx.doi.org/10.1093/imamat/hxaa021.

[30] N. McLachlan, Theory and application of Mathieu functions, Dover Publications, 1964.

[31] D. Nigro, Prediction of Broadband Aero and Hydrodynamic Noise: Derivation of Analytical Models for Low Frequency (Ph.D. thesis), University of Manchester, 2017.

[32] M.J. Colbrook, A. Kisil, A mathieu function boundary spectral method for scattering by multiple variable poro-elastic plates, with applications to metamaterials and acoustics, Phil. Trans. R. Soc. A 476 (2020) 20200184, http://dx.doi.org/10.1098/rspa.2020.0184, 1–22.

[33] J. Jaworski, N. Peake, Aerodynamic noise from a poroelastic edge with implications for the silent flight of owls, J. Fluid Mech. 52 (2013) 395–420, http://dx.doi.org/10.1017/jfm.2013.139.

[34] D. Crighton, F.G. Leppington, Scattering of aerodynamic noise by a semi-infinite compliant plate, J. Fluid Mech. 43 (4) (1970) 721–736, http://dx.doi.org/10.1017/S0022112070002690.

[35] J.M. Scott, Acoustic scattering by a finite elastic strip, Phil. Trans. R. Soc. A 338 (1649) (1992) 145–167, http://dx.doi.org/10.1098/rsta.1992.0006.

[36] L. Ayton, Acoustic scattering by a finite rigid plate with a poroelastic extension, J. Fluid Mech. 791 (2016) 414–438, http://dx.doi.org/10.1017/jfm.2016.59.

[37] A.G. Cavalieri, W.R. Wolf, J.W. Jaworski, Numerical solution of acoustic scattering by finite perforated elastic plates, Proc. R. Soc. Lond. a 472 (2188) (2016) 20150767, http://dx.doi.org/10.1098/rspa.2015.0767.

[38] M. Howe, Noise produced by a sawtooth trailing edge, J. Acoust. Soc. Am. 90 (1) (1991) 482–487, http://dx.doi.org/10.1121/1.401273.

[39] M. Howe, Aerodynamic noise of a serrated trailing edge, J. Fluids Struct. 5 (1) (1991) 33–45, http://dx.doi.org/10.1016/0889-9746(91)80010-B.

[40] M. Azarpeyvand, M. Gruber, P.F. Joseph, An analytical investigation of trailing edge noise reduction using novel serrations, in: 19 Th AIAA/CEAS Aeroacoustics Conference, AIAA 2013-2009 paper, Berlin, Germany, 2013, doi:10.2514/6.2013-2009.

[41] M. Gruber, Airfoil noise reduction by edge treatments, (Ph.D. thesis), University of Southampton, 2012, http://eprints.soton.ac.uk/id/eprint/349012.

[42] B. Lyu, M. Azarpeyvand, S. Sinayoko, Prediction of noise from serrated trailing edges, J. Fluid. Mech. 793 (2016) 556–588, http://dx.doi.org/10.1017/jfm.2016.132.

[43] L.J. Ayton, Analytic solution for aerodynamic noise generated by plates with spanwise-varying trailing edges, J. Fluid Mech. 849 (2018) 448–466, http://dx.doi.org/10.1017/jfm.2018.431.

[44] M. Sanjosé, S. Moreau, B. Lyu, L.J. Ayton, Analytical, numerical and experimental investigation of trailing-edge noise reduction on a controlled diffusion airfoil with serrations, in: 25Th AIAA/CEAS Aeroacoustics Conference, in: AIAA 2019-2450 paper, Delft, Netherland, 2019, http://dx.doi.org/10.2514/6.2019-2450.

[45] S. Moreau, M. Sanjosé, B. Lyu, L.J. Ayton, Analytical, numerical and experimental investigation of trailing-edge noise reduction on a controlled diffusion airfoil with serrations, in: 25 Th AIAA/CEAS Aeroacoustics Conference, in: AIAA 2019-2450 paper, 2019, http://dx.doi.org/10.2514/6.2019-2450.

[46] T.F. Brooks, S.D. Pope, M.A. Marcolini, Airfoil self-noise and prediction, NASA Langley Research Center, Hampton (VA), 1989, (Accessed: 2020-04-08).

[47] M. Kingan, J.R. Pearse, Laminar boundary layer instability noise produced by an aerofoil, J. Sound Vib. 322 (4-5) (2009) 808–828, http://dx.doi.org/10.1016/j.jsv.2008.11.043.

[48] M. Sanjosé, A. Towne, P. Jaiswal, S. Moreau, S. Lele, Modal analysis of the laminar boundary layer instability and tonal noise of an airfoil at Reynolds number 150,000, Int. J. Aeroacoustics 18 (2–3) (2019) 317–350, http://dx.doi.org/10.1177/1475472X18812798.

[49] R.H. Kraichnan, Pressure fluctuations in turbulent flow over a flat plate, J. Acoust. Soc. Am. 28 (3) (1956) 378–390, http://dx.doi.org/10.1121/1.1908336.

[50] G.A. Gerolymos, D. Sénéchal, I. Vallet, Wall effects on pressure fluctuations in turbulent channel flow, J. Fluid Mech. 720 (2013) 15–65, http://dx.doi.org/10.1017/jfm.2012.633.

[51] G. Grasso, P. Jaiswal, H. Wu, S. Moreau, M. Roger, Analytical models of the wall-pressure spectrum under a turbulent boundary layer with adverse pressure gradient, J. Fluid Mech. 877 (2019) 1007–1062, http://dx.doi.org/10.1017/jfm.2019.616.

[52] R.L. Panton, J.H. Linebarger, Wall pressure spectra calculations for equilibrium boundary layers, J. Fluid Mech. 65 (2) (1974) 261–287, http://dx.doi.org/10.1017/S0022112074001388.

[53] S. Remmler, J. Christophe, J. Anthoine, S. Moreau, Computation of wall-pressure spectra from steady flow data for noise prediction, AIAA J. 48 (2010) 1997–2007, http://dx.doi.org/10.2514/1.J050206.

[54] W.K. Blake, Mechanics of flow-induced sound and vibration, Vol. I and II, in Applied Mathematics and Mechanics, Academic Press, 1986, http://dx.doi.org/10.1121/1.396227,

[55] B. Lyu, L.J. Ayton, P. Chaitanya, On the acoustic optimality of leading-edge serration profiles, J. Sound Vib. 462 (2019) 114923, http://dx.doi.org/10.1016/j.jsv.2019.114923.

[56] F. Avallone, W.C.P. van der Velden, D. Ragni, Benefits of curved serrations on broadband trailing-edge noise reduction, J. Sound Vib. 400 (2017) 167–177, http://dx.doi.org/10.1016/j.jsv.2017.04.007.

[57] P. Kholodov, S. Moreau, Optimization of serrations for broadband trailing-edge noise reduction using an analytical model, in: 25 Th AIAA/CEAS Aeroacoustics Conference, in: AIAA 2019-2655 paper, Delft, Netherland, 2019, http://dx.doi.org/10.2514/6.2019-2655.
[58] P. Kholodov, S. Moreau, Optimization of trailing-edge serrations with and without slits for broadband noise reduction, AIAA 2019-2655 paper, J. Sound Vib. 490 (2021) 115736: 1–26, http://dx.doi.org/10.1016/j.jsv.2020.115736.
[59] P. Kholodov, S. Moreau, Numerical study of optimized airfoil trailing-edge serrations for broadband noise reduction, in: 26 Th AIAA/CEAS Aeroacoustics Conference, in: AIAA2020-2541 paper, Virtual Event, 2020, http://dx.doi.org/10.2514/6.2020-2521.
[60] G. Grasso, M. Roger, S. Moreau, Effect of sweep angle and of wall-pressure statistics on the free-field directivity of airfoil trailing-edge noise, in: 25 Th AIAA/CEAS Aeroacoustics Conference, in: AIAA 2019-2612 paper, Delft, Netherland, 2019, http://dx.doi.org/10.2514/6.2019-2612.
[61] M. Lowson, J.B. Ollerhead, A theoretical study of helicopter rotor noise, J. Sound Vib. 9 (2) (1969) 197–222, http://dx.doi.org/10.1016/0022-460X(69)90028-5.
[62] R.H. Schlinker, R.K. Amiet, Helicopter rotor trailing edge noise, NASA Contractor Report 3470, Washington DC, USA, 1981.
[63] M. Drela, XFOIL: An analysis and design system for low Reynolds number airfoils, in: T. Mueller (Ed.), Low Reynolds Number Aerodynamics, in: Lecture Notes in Engineering, 54, Springer Berlin Heidelberg, 1989, pp. 1–12, http://dx.doi.org/10.1007/978-3-642-84010-4_1.
[64] T.P. Chong, P.F. Joseph, An experimental study of airfoil instability tonal noise with trailing edge serrations, J. Sound Vib. 332 (24) (2013) 6335–6358, http://dx.doi.org/10.1016/j.jsv.2013.06.033, https://www.sciencedirect.com/science/article/pii/S0022460X13005956.
[65] T.P. Chong, P.F. Joseph, P.O.A.L. Davies, Design and performance of an open jet wind tunnel for aero-acoustic measurement, Appl. Acoust. 70 (4) (2009) 605–614, http://dx.doi.org/10.1016/j.apacoust.2008.06.011, https://www.sciencedirect.com/science/article/pii/S0003682X08001485.
[66] T. Chong, P.F. Joseph, M.J. Kingan, An investigation of airfoil tonal noise at different Reynolds numbers and angles of attack, Appl. Acoust. 74 (2013) 38–48, http://dx.doi.org/10.1016/j.apacoust.2012.05.016.
[67] R. Parchen, Progress Report DRAW: a Prediction Scheme for Trailing-Edge Noise Based on Detailed Boundary-Layer Characteristics, TNO Rept. HAG-RPT-980023, TNO Institute of Applied Physics, The Netherlands, 1998.
[68] T. Brooks, T.H. Hodgson, Trailing edge noise prediction from measured surface pressures, J. Sound Vib. 78 (1) (1981) 69–117, http://dx.doi.org/10.1016/S0022-460X(81)80158-7.
[69] T. Lutz, A. Herrig, W. Würz, M. Kamruzzaman, E. Krämer, Design and wind-tunnel verification of low-noise airfoils for wind turbines, AIAA J. 45 (4) (2007) 779–785, http://dx.doi.org/10.2514/1.27658.
[70] M. Kamruzzaman, T. Lutz, W. Würz, W.Z. Shen, W.J. Zhu, M.O.L. Hansen, F. Bertagnolio, H.A. Madsen, Validations and improvements of airfoil trailing-edge noise prediction models using detailed experimental data, Wind Energy 15 (1) (2012) 45–61, http://dx.doi.org/10.1002/we.505.
[71] D. Coles, The law of the wake in the turbulent boundary layer, J. Fluid Mech. 1 (2) (1956) 191–226, http://dx.doi.org/10.1017/S0022112056000135.
[72] I. Marusic, K.A. Chauhan, V. Kulandaivelu, N. Hutchins, Evolution of zero-pressure-gradient boundary layers from different tripping conditions, J. Fluid Mech. 783 (2015) 379–411, http://dx.doi.org/10.1017/jfm.2015.556.
[73] R.P.J.O.M. Van Rooij, Modification of the Boundary Layer Calculation in RFOIL for Improved Airfoil Stall Prediction, Tech. rep., Institute for Wind Energy (IWE), Delft University, 1996, Tech. Rep. IW-96087R,.
[74] D. Marten, J. Wendler, G. Pechlivanoglou, C.N. Nayeri, C.O. Paschereit, QBlade: An open source tool for the design and simulation of horizontal and vertical axis wind turbines, Int. J. Emerg. Technol. Adv. Eng. 3 (3) (2013) 264–269, doi:10.1-1-414-5294.
[75] A. Fischer, F. Bertagnolio, H.A. Madsen, Improvement of TNO type trailing edge noise models, Eur. J. Mech. 61 (2017) 255–262, http://dx.doi.org/10.1016/j.euromechflu.2016.09.005.
[76] J. Mathieu, J. Scott, An Introduction To Turbulent Flow, Cambridge University Press, 2000, http://dx.doi.org/10.1017/CBO9781316529850.
[77] M. Kamruzzaman, T. Lutz, A. Herrig, Krämer, Semi-empirical modeling of turbulent anisotropy for airfoil self-noise predictions, AIAA J. 50 (1) (2012) 46–60, http://dx.doi.org/10.2514/1.J051075.
[78] F. Bertagnolio, A. Fischer, W.J. Zhu, Tuning of turbulent boundary layer anisotropy for improved surface pressure and trailing-edge noise modeling, J. Sound Vib. 333 (3) (2014) 991–1010, http://dx.doi.org/10.1016/j.jsv.2013.10.008.
[79] O. Stalnov, P. Chaitanya, P.F. Joseph, Towards a non-empirical trailing edge noise prediction model, J. Sound Vib. 372 (2016) 50–68, http://dx.doi.org/10.1016/j.jsv.2015.10.011.
[80] C. Hornung, T. Lutz, E. Krämer, A model to include turbulence-turbulence interaction in the prediction of trailing edge far field noise for high angles of attack or slightly separated flow, Renew. Energy 136 (2019) 945–954, http://dx.doi.org/10.1016/j.renene.2018.12.093.
[81] O. Ferret Gasch, S. Oerlemans, B.W. Faßmann, M. Herr, F. Bertagnolio, A. Fischer, B. Arnold, T. Lutz, Trailing edge noise prediction of wind turbine airfoils: A benchmark exercise, in: AIAA/CEAS 25 Th Aeroacoustics Conference, in: AIAA 2019-2675 paper, Delft, NL, 2019, http://dx.doi.org/10.2514/6.2019-2675.
[82] M. Herr, R. Ewert, C. Rautmann, M. Kamruzzaman, D. Bekiropoulos, A. Iob, R. Arina, P. Batten, S. Chakravarthy, F. Bertagnolio, Broadband Trailing-Edge Noise Predictions - Overview of BANC-III Results, in: AIAA/CEAS 21 StAeroacoustics Conference, AIAA Paper 2015-2847, Dallas, TX, 2015, doi:10.2514/6.2015-2847.
[83] M. Herr, M. Kamruzzaman, C. Bahr, BANC-IV-1: TBL-Trailing-edge noise, in: Fourth Workshop on Benchmark Problems for Airframe Noise Computations (BANC-IV), 22 nd AIAA-CEAS Aeroacoustics Conference (Workshop), Lyon, France, 2016.
[84] M. Choudhari, C. Bahr, M. Khorrami, D. Lockard, L. Lopes, N. Zawodny, M. Herr, M. Pott-Pollenske, M. Kamruzzaman, T.V. de Ven, E. Manoha, S. Redonnet, K. Yamamoto, T. Ikeda, T. Imamura, Simulations & measurements of airframe noise: A BANC workshops perspective, in: Proceedings of NATO STO-MP-AVT-246 Specialists Meeting on Progress and Challenges in Validation Testing for Computational Fluid Dynamics, NATO Science and Technology Organization (publisher), Avila, Spain, 2016.
[85] M. Goody, Empirical spectral model of surface pressure fluctuations, AIAA J. 42 (2004) 1788–1794, http://dx.doi.org/10.2514/1.9433.
[86] Y. Rozenberg, G. Robert, S. Moreau, Wall-pressure spectral model including the adverse pressure gradient effects, AIAA J. 50 (10) (2012) 2168–2179, http://dx.doi.org/10.2514/1.J051500.
[87] M. Kamruzzaman, D. Bekiropoulos, T. Lutz, W. Würz, E. Krämer, A semi-empirical surface pressure spectrum model for airfoil trailing-edge noise prediction, Int. J. Aeroacoust. 14 (2015) 833–882, http://dx.doi.org/10.1260/1475-472X.14.5-6.833.
[88] M.R. Catlett, J.M. Anderson, J.B. Forest, D.O. Stewart, Empirical modeling of pressure spectra in adverse pressure gradient turbulent boundary layers, AIAA J. 54 (2016) 569–587, http://dx.doi.org/10.2514/1.J054375.
[89] N. Hu, Empirical model of wall pressure spectra in adverse pressure gradients, AIAA J. 56 (2018) 3491–3506, http://dx.doi.org/10.2514/1.J056666.
[90] S. Lee, Empirical wall-pressure spectral modeling for zero and adverse pressure gradient flows, AIAA J. 56 (2018) 1818–1829, http://dx.doi.org/10.2514/1.J056528.
[91] M.S. Howe, Acoustics of Fluid-Structure Interactions, Cambridge University Press, 1998.
[92] W.W. Willmarth, F.W. Roos, Resolution and structure of the wall pressure field beneath a turbulent boundary layer, J. Fluid. Mech. 22 (1965) 81–94, http://dx.doi.org/10.1017/S0022112065000599.
[93] H. Wu, S. Moreau, R. Sandberg, On the noise generated by a controlled-diffusion aerofoil at $Re_c = 1.5 \times 10^5$, J. Sound Vib. 487 (2020) 115620: 1–25, http://dx.doi.org/10.1017/jfm.2019.129.
[94] X. Zhao, J. Lei, Improved technical for evaluation of wall pressure fluctuations from turbulent boundary layer, AIAA J. 58 (2020) 3320–3331, http://dx.doi.org/10.2514/1.J059164.
[95] A. Garcia-Sagrado, T. Hynes, Wall pressure sources near an airfoil trailing edge under turbulent boundary layers, J. Fluid. Struc. 30 (2012) 3–34, http://dx.doi.org/10.1016/j.jfluidstructs.2011.12.007.
[96] L. Maestrello, Radiation from panel response to a supersonic turbulent boundary layer, J. Sound. Vib. 10 (1969) 261–295, http://dx.doi.org/10.1016/0022-460X(69)90200-4.
[97] J. Cockburn, J.E. Robertson, Vibration response of spacecraft shrouds to in-flight fluctuating pressures, J. Sound. Vib. 33 (1974) 399–425, http://dx.doi.org/10.1016/S0022-460X(74)80226-9.
[98] D. Chase, Modeling the wavevector-frequency spectrum of turbulent boundary layer wall pressure, J. Sound. Vib. 70 (1980) 29–67, http://dx.doi.org/10.1016/0022-460X(80)90553-2.
[99] Y.F. Hwang, W.K. Bonness, A. Hambric, Comparions of semi-empirical models for turbulent boundary layer wall pressure spectra, J. Sound. Vib. 319 (2009) 199–217, http://dx.doi.org/10.1016/j.jsv.2008.06.002.
[100] F.H. Clauser, Turbulent boundary layers in adverse pressure gradients, J. Aeronaut. Sci. 21 (1954) 91–108, http://dx.doi.org/10.2514/8.2938.
[101] A. Suryadi, M. Herr, Wall pressure spectra on a DU96-W-180 profile from low to pre-stall angles of attack, in: AIAA/CEAS 21 St Aeroacoustics Conference, in: AIAA 2015-2688 paper, Dallas, TX, 2015, http://dx.doi.org/10.2514/6.2015-2688.
[102] M. Sanjosé, D. Lallier-Daniels, S. Moreau, Aeroacoustics analysis of a low subsonic axial fan, in: ASME Turbo Expo 2015 Conference, no. ASME GT2015-12345, Montreal, Canada, 2015.
[103] N. Hu, M. Herr, Characteristics of wall pressure fluctuations for a flat plate turbulent boundary layer with pressure gradients, in: AIAA/CEAS 22 Nd Aeroacoustics Conference, AIAA Paper 2016-2749, Lyon, France, 2016, http://dx.doi.org/10.2514/6.2016-2749.
[104] M. Drela, XFOIL: An Analysis and Design System for Low Reynolds Number Airfoils, Low Reynolds Number Aerodynamics, Springer-Verlag, 1989.

[105] Y.C. Küçükosman, J. Christophe, C. Schram, Trailing edge noise prediction based on wall pressure spectrum models for NACA0012 airfoil, J. Wind. Eng. Ind. Aerod. 175 (2018) 305–316, http://dx.doi.org/10.1016/j.jweia.2018.01.030.

[106] M. Sanjosé, S. Moreau, Fast and accurate analytical modeling of broadband noise for a low-speed fan, J. Acoust. Soc. Am. 143 (5) (2018) 3103–3113, http://dx.doi.org/10.1121/1.5038265.

[107] S. Lee, J.G. Shum, Prediction of airfoil trailing edge noise using empirical wall pressure spectrum models, AIAA J. 57 (2019) 888–897, http://dx.doi.org/10.2514/1.J057787.

[108] G.M. Corcos, The structure of the turbulent pressure field in boundary-layer flows, J. Fluid Mech. 18 (1964) 353–378.

[109] M. Roger, S. Moreau, Broadband self noise from loaded fan blades, AIAA J. 42 (3) (2004) 536–544, http://dx.doi.org/10.2514/1.9108.

[110] Y. Rozenberg, M. Roger, S. Moreau, Rotating blade trailing-edge noise: experimental validation of analytical model, AIAA J. 48 (5) (2010) 951–962, http://dx.doi.org/10.2514/1.43840.

[111] M. Karimi, P. Croaker, A. Skvortsov, D. Moreau, N. Kessissoglou, Numerical prediction of turbulent boundary layer noise from a sharp-edged flat plate, Int. J. Numer. Mech. Fluids. 90 (2019) 522–543, http://dx.doi.org/10.1002/fld.4733.

[112] D. Chase, The character of the turbulent wall pressure spectrum at subconvective wavenumbers and a suggested comprehensive model, J. Sound. Vib. 112 (1987) 127–147, http://dx.doi.org/10.1016/S0022-460X(87)80098-6.

[113] G. Corcos, Resolution of pressure in turbulence, J. Acousst. Soc. Am. 35 (1963) 192–199, http://dx.doi.org/10.1121/1.1918431.

[114] A. Caiazzo, R. Amico, W. Desmet, A generalized corcos model for modelling turbulent boundary layer wall pressure fluctuations, J. Sound. Vib. 372 (2016) 192–210, http://dx.doi.org/10.1016/j.jsv.2016.02.036.

[115] K. Volkmer, T. Carolus, Aeroacoustic airfoil shape optimization utilizing semi-empirical models for trailing edge noise prediction, in: AIAA/CEAS 24 Th Aeroacoustics Conference, in: AIAA 2018-3130 paper, Atlanta, GA, 2018, http://dx.doi.org/10.2514/6.2018-3130.

[116] N. Ricks, P. Tsirikoglou, F. Contino, G. Ghorbaniasl, A CFD-based methodology for aerodynamic-aeroacoustic shape optimization of airfoils, in: AIAA Scitech, in: AIAA Paper 2016-2749, Orland, FL, 2020, http://dx.doi.org/10.2514/6.2020-1729.

[117] C. Liu, S. Lee, Parametric airfoil design for trailing-edge noise reduction, in: AIAA/CEAS 26 Th Aeroacoustics Conference, AIAA Paper 2020-2536, Virtual Event, 2020, http://dx.doi.org/10.2514/6.2020-2536.

[118] C. Liu, S. Lee, Surrogate-based optimization for airfoil trailing-edge noise reduction using morphed trailing-edge shapes, in: Inter-Noise 2020, Seoul, Korea, 2020.

[119] Y. Tian, B. Cotté, Wind turbine noise modeling based on Amiet's theory: effects of wind shear and atmospheric turbulence, Acta Acust. United Acust. 102 (2016) 626–639, http://dx.doi.org/10.3813/AAA.918979.

[120] Y. Rozenberg, Modélisation Analytique Du Bruit Aérodynamique À Large Bande Des Machines Tournantes : Utilisation De Calculs Moyennés De Mécanique Des Fluides (Ph.D. thesis), Ecole Centrale de Lyon, 2007, https://tel.archives-ouvertes.fr/tel-00678225.

[121] J. Christophe, Application of Hybrid Methods to High Frequency Aeroacoustics (Ph.D. thesis), von Karman Institute for Fluid Dynamics / Universite Libre de Bruxelles, 2011.

[122] J. Christophe, S. Moreau, C.W. Hamman, J.A.S. Witteveen, G. Iaccarino, Uncertainty quantification for the trailing-edge noise of a controlled-diffusion airfoil, AIAA J. 53 (1) (2015) 42–54, http://dx.doi.org/10.2514/1.J051696.

[123] J. Christophe, M. Sanjose, J.A.S. Witteveen, S. Moreau, Uncertainty quantification applied to aeroacoustics of wall-bounded flows, in: J.A.S.W. S. Sarkar (Ed.), Uncertainty Quantification in Computational Science: Theory and Application in Fluids and Structural Mechanics, World Scientific, 2016, http://dx.doi.org/10.1142/9789814730587_0001.

[124] S.L. Glegg, B. Morin, O. Atassi, R. Reba, Using Reynolds-averaged Navier-Stokes calculations to predict trailing-edge noise, AIAA J. 48 (2010) 1290–1301, http://dx.doi.org/10.2514/1.38836.

[125] L. Chen, I.R. MacGillivray, Prediction of trailing-edge noise based on Reynolds-averaged Navier-Stokes solution, AIAA J. 52 (2014) 2673–2682, http://dx.doi.org/10.2514/1.J052827.

[126] G. Grasso, J. Christophe, C. Schram, Prediction of low-speed fan trailing-edge noise based on RANS and on scale resolved simulations, in: AIAA/CEAS 21 St Aeroacoustics Conference, AIAA Paper 2015-2669, Dallas, TX, 2015, http://dx.doi.org/10.2514/6.2015-2669.

[127] R. Ewert, A. Dierke, M. Herr, RANS/CAA based prediction of NACA 0012 broadband trailing edge noise and experimental validation, in: AIAA/CEAS 15 Th Aeroacoustics Conference, AIAA Paper 2009-3269, Miami, FL, 2009, http://dx.doi.org/10.2514/6.2009-3269.

[128] I. Cozza, A. Iob, R. Arina, Broadband trailing-edge noise prediction with a stochastic source model, Comput. Fluids. 57 (2012) 98–109, http://dx.doi.org/10.1016/j.compfluid.2011.12.011.

[129] B. Bai, X. Li, Study of the impact of turbulent anisotropy on the airfoil turbulent boundary layer trailing edge noise, in: AIAA/CEAS 22 Nd Aeroacoustics Conference, AIAA Paper 2016-2813, Lyon, France, 2016, http://dx.doi.org/10.2514/6.2016-2813.

[130] C.W. Tam, L. Auriault, Jet mixing noise from fine scale turbulence, AIAA J. 37 (1999) 145–153, http://dx.doi.org/10.2514/2.691.

[131] C.A. Albarracin, C.J. Doolan, R.F. Jones, C.H. Hansen, L.A. Brooks, A RANS-based statistical noise model for trailing edge noise, in: AIAA/CEAS 18 Th Aeroacoustics Conference, AIAA Paper 2012-2181, Colorado Springs, CO, 2012, http://dx.doi.org/10.2514/6.2012-2181.

[132] P.J. Morris, F. Farassat, Acoustic analogy and alternative theories for jet noise prediction, AIAA J. 40 (2002) 671–680, http://dx.doi.org/10.2514/2.1699.

[133] M.P. Rumpfkeil, Using steady flow analysis for noise predictions, Comput. Fluids. 154 (2017) 347–357, http://dx.doi.org/10.1016/j.compfluid.2017.03.003.

[134] F.R. Menter, M. Kuntz, R. Langtry, Ten years of industrial experience with the SST turbulence model, in: K. Hanjalic, Y. Nagano, M. Tummers (Eds.), Turbul. Heat Mass Transf. 4 (1) (2003) 625–632.

[135] E. Manoha, B. Troff, P. Sagaut, Trailing edge noise prediction using large eddy simulation and acoustic analogy, AIAA J. 38 (4) (2000) 575–583, http://dx.doi.org/10.2514/2.1015.

[136] B.A. Singer, K.S. Brentner, D.P. Lockard, G.M. Lilley, Simulation of acoustic scattering from a trailing-edge, J. Sound Vib. 230 (3) (2000) 541–560, http://dx.doi.org/10.1006/jsvi.1999.2628.

[137] J. Casper, F. Farassat, A new time domain formulation for broadband noise predictions, Int. J. Aeroacoustics 1 (3) (2002) 207–240, http://dx.doi.org/10.1260/147547202320962574.

[138] M. Wang, P. Moin, Computation of trailing-edge flow and noise using Large-Eddy simulation, AIAA J. 38 (12) (2000) 2201–2209, http://dx.doi.org/10.2514/2.895.

[139] W.K. Blake, A statistical description of pressure and velocity fields at the trailing edge of a flat strut, Tech. rep., David Taylor Naval Ship R & D Center, Bethesda, Maryland, December 1975., 1975.

[140] A.A. Oberai, F. Roknaldin, T.J. R. Hughes, Computation of trailing-edge noise due to turbulent flow over an airfoil, AIAA J. 40 (11) (2002) 2206–2216, http://dx.doi.org/10.2514/2.1582.

[141] T.F. Brooks, M.A. Marcollini, D.S. Pope, Airfoil trailing edge flow measurements, AIAA J. 24 (1986) 1245–1251, http://dx.doi.org/10.2514/3.9426.

[142] S. Moreau, M. Henner, G. Iaccarino, M. Wang, M. Roger, Analysis of flow conditions in freejet experiments for studying airfoil self-noise, AIAA J. 41 (10) (2003) 1895–1905, http://dx.doi.org/10.2514/2.1905.

[143] C. Kato, M. Ikegawa, Large eddy simulation of unsteady turbulent wake of a circular cylinder using the finite element method, in: Advances in Numerical Simulation of Turbulent Flows, Vol. 1, 1991, pp. 49–56.

[144] M. Breuer, Large eddy simulation of the subcritical flow past a circular cylinder: numerical and modeling aspects, Int. J. Numer. Meth. Fl. 28 (1998) 1281–1302, http://dx.doi.org/10.1002/(SICI)1097-0363(19981215)28:91281::AID-FLD7593.0.CO;2-%23.

[145] P. Sagaut, Large Eddy Simulation for Incompressible Flows: An Introduction, Springer Science & Business Media, 2006.

[146] M. Wang, S. Moreau, G. Iaccarino, M. Roger, Pressure fluctuations on a low speed airfoil, in: Annual Research Briefs, 2004, pp. 183–193.

[147] J. Christophe, J. Anthoine, S. Moreau, Trailing edge noise of a controlled-diffusion airfoil at moderate and high angle of attack, in: 15 Th AIAA/CEAS Aeroacoustics Conference, in: AIAA Paper 2009-3196, 2009, http://dx.doi.org/10.2514/6.2009-3196.

[148] J. Winkler, S. Moreau, T. Carolus, Large-eddy simulation and trailing-edge noise prediction of an airfoil with boundary-layer tripping, in: 15 Th AIAA/CEAS Aeroacoustics Conference, Miami, FL, in: AIAA 2009-3197 paper, 2009, http://dx.doi.org/10.2514/6.2009-3197.

[149] S. Moreau, M. Roger, J. Christophe, Flow features and self-noise of airfoils near stall or in stall, in: 15 Th AIAA/CEAS Aeroacoustics Conference, Miami, FL, no. 2009–3198, 2009, http://dx.doi.org/10.2514/6.2009-3198.

[150] J. Winkler, S. Moreau, T. Carolus, Airfoil trailing edge noise prediction from large-eddy simulation influence of grid resolution and noise model formulation, in: 16 Th AIAA/CEAS Aeroacoustics Conference, Stockholm, Sweden, in: AIAA 2010-3704 paper, 2010, http://dx.doi.org/10.2514/6.2010-3704.

[151] R. Martinez-Lera, J. Christophe, C. Schram, Computation of the self-noise of a controlled-diffusion airfoil based on the acoustic analogy, Int. J. Aeroacoustics 16 (1–2) (2017) 1049–1070, http://dx.doi.org/10.1177/1475472X16680447.

[152] H. Wu, Direct Numerical Simulation of Airfoil Self-Noise at High Reynolds Numbers (Ph.D. thesis), Université de Sherbrooke, 2019.

[153] Y. Addad, R. Prosser, D. Laurence, S. Moreau, F. Mendonca, On the use of embedded meshes in the LES of external flow, Flow, Turb. Comb. 80 (2008) 393–403, http://dx.doi.org/10.1007/s10494-007-9131-1.

[154] R. Matouk, J. Christophe, G. Degrez, Aerodynamics and aeroacoustics study of the flow around an automotive fan airfoil, Int. J. Aeroacoustics 14 (7) (2015) 1049–1070, http://dx.doi.org/10.1260/1475-472X.14.7.1049.

[155] N. Ricks, C. Nixarlidis, A. Kalfas, G. Ghorbaniasl, A hybrid computational aeroacoustic methodology for broadband noise prediction, J. Acoust. Soc. Am. 146 (2) (2019) 1438–1447, http://dx.doi.org/10.1121/1.5123142.

[156] L. Soulat, P. Ferrrand, S. Moreau, S. Aubert, M. Buisson, Efficient optimisation procedure for design problems in fluid mechanics, Comp. Fluids 82 (2013) 73–86, http://dx.doi.org/10.1016/j.compfluid.2013.04.009.
[157] STURM4 project, High Reynolds Turbulence Simulations with Multi-Mesh and Multi-Models, Tech. rep., Agence Nationale de la Recherche, http://cfd.mace.manchester.ac.uk/twiki/bin/view/Main/Sturm4Project, 2009.
[158] J. Winkler, S. Moreau, T. Carolus, Airfoil trailing-edge blowing: broadband noise prediction from Large-Eddy Simulation, AIAA J. 50 (2) (2012) 294–303, http://dx.doi.org/10.2514/1.J050959.
[159] J. Christophe, K. Kucukcoskun, C. Schram, A. Idier, P. Laffay, S. Moreau, Experimental validation of a semi-analytical trailing-edge noise model including broadband scattering, in: 21 Th AIAA/CEAS Aeroacoustics Conference, Dallas, TX, in: AIAA2015-2531 paper, 2015, http://dx.doi.org/10.2514/6.2015-2531.
[160] K. Kucukcoskun, Prediction of free and scattered acoustic fields of low-speed fans, (Ph.D. thesis), von Karman Institute for Fluid Dynamics / Ecole Centrale de Lyon, 2012.
[161] W.Z. Shen, J.N. Sørensen, Aero-acoustic modeling of turbulent airfoil flows, AIAA J. 39 (6) (2001) 1057–1064, http://dx.doi.org/10.2514/2.1446.
[162] W.Z. Shen, W. Zhu, J.N. Sørensen, Aeroacoustic computations for turbulent airfoil flows, AIAA J. 47 (6) (2009) 1518–1527, http://dx.doi.org/10.2514/1.40399.
[163] Y.J. Moon, J.H. Seo, Y.M. Bae, M. Roger, S. Becker, A hybrid prediction method for low-subsonic turbulent flow noise, Comp. Fluids 39 (8) (2010) 1125–1135, http://dx.doi.org/10.1016/j.compfluid.2010.02.005.
[164] J. Seo, Y.J. Moon, Perturbed compressible equations for aeroacoustic noise prediction at low Mach numbers, AIAA J. 43 (8) (2005) 1716–1724, http://dx.doi.org/10.2514/1.3001.
[165] H. Wu, S. Moreau, R. Sandberg, Effects of pressure gradient on the evolution of velocity-gradient tensor invariant dynamics on a controlled-diffusion aerofoil at $Re_c = 150000$, J. Fluid Mech. 868 (2019) 584–610, http://dx.doi.org/10.1017/jfm.2019.129.
[166] M. Sanjosé, S. Moreau, M.S. Kim, F. Pérot, Direct self-noise simulation of the installed controlled diffusion airfoil, in: 17 Th AIAA/CEAS Aeroacoustics Conference, in: AIAA 2011-2716 paper, Portland, OR, 2011, http://dx.doi.org/10.2514/6.2011-2716, AIAA-2011-2716.
[167] W.R. Wolf, S.K. Lele, Trailing-edge noise predictions using compressible Large-Eddy Simulation and acoustic analogy, AIAA J. 50 (11) (2012) 2423–2434, http://dx.doi.org/10.2514/1.J051638.
[168] W.R. Wolf, J.L. Azevedo, S.K. Lele, Convective effects and the role of quadrupole sources for aerofoil aeroacoustics, J. Fluid Mech. 708 (2012) 502–538, http://dx.doi.org/10.1017/jfm.2012.327.
[169] M. Deuse, R.D. Sandberg, Parametric study of multiple aerofoil self-noise sources using direct noise computation, in: 25 Th AIAA/CEAS Aeroacoustics Conference, in: AIAA 2019-2681 paper, Delft, Netherland, 2019, http://dx.doi.org/10.2514/6.2019-2681.
[170] R. Boukharfane, J. Bodart, M.C. Jacob, L. Joly, T. Bridel-Bertomeu, T. Node-Langlois, Characterization of the pressure fluctuations within a controlled-diffusion airfoil boundary layer at large Reynolds numbers, in: 25th AIAA/CEAS Aeroacoustics Conference, in: AIAA 2019-2722 paper, Delft, Netherland, 2019, http://dx.doi.org/10.2514/6.2019-2722.
[171] M. Deuse, R.D. Sandberg, Different noise generation mechanisms of a controlled diffusion aerofoil and their dependence on Mach number, J. Sound Vib. 476 (2020) 115317: 1–18, http://dx.doi.org/10.1016/j.jsv.2020.115317.
[172] P. Salas, S. Moreau, Aeroacoustic simulations of a simplified high-lift device accounting for some installation effects, AIAA J. 55 (3) (2017) 774–789, http://dx.doi.org/10.2514/1.J055104.
[173] H. Chen, S.A. Orszag, I. Staroselsky, S. Succi, Expanded analogy between Boltzmann kinetic theory of fluids and turbulence, J. Fluid Mech. 519 (2004) 301–314, http://dx.doi.org/10.1017/S0022112004001211.
[174] G.A. Brès, F. Pérot, D. Freed, Properties of the lattice-Boltzmann method for acoustics, in: 16th AIAA/CEAS Aeroacoustics Conference, in: AIAA 2009-3395 paper, Miami, Florida, 2009, http://dx.doi.org/10.2514/6.2009-3395,
[175] G.A. Brès, D. Freed, M. Wessels, S. Noelting, F. Pérot, Flow and noise predictions for the tandem cylinder aeroacoustic benchmark, Phys. Fluids 24 (3) (2012) 036101–1–5, http://dx.doi.org/10.1063/1.3685102.
[176] A. Mann, M.S. Kim, J. Wu, F. Pérot, J. Grilliat, M.C. Jacob, M. Colman, Airfoil tip leakage aeroacoustics predictions using a lattice Boltzmann based method, in: 22 Th AIAA/CEAS Aeroacoustics Conference, in: AIAA 2016-2825 paper, Lyon, France, 2016, http://dx.doi.org/10.2514/6.2016-2825.
[177] M. Jacob, J. Grilliat, R. Camussi, G. Caputi Gennaro, Aeroacoustic investigation of a single airfoil tip leakage flow, Int. J. Aeroacoustics 9 (3) (2010) 253–272, http://dx.doi.org/10.1260/1475-472x.9.3.253.
[178] F. Avallone, W.C.P. van der Velden, D. Ragni, D. Casalino, Noise reduction mechanisms of sawtooth and combed-sawtooth trailing-edge serrations, J. Fluid Mech. 848 (2018) 560–591, http://dx.doi.org/10.1017/jfm.2018.377.
[179] R.D. Sandberg, N.D. Sandham, P.F. Joseph, Direct numerical simulations of trailing-edge noise generated by boundary-layer instabilities, J. Sound Vib. 304 (3–5) (2007) 677–690, http://dx.doi.org/10.1016/j.jsv.2007.03.011.
[180] R.D. Sandberg, N.D. Sandham, Direct numerical simulation of turbulent flow past a trailing edge and the associated noise generation, J. Fluid Mech. 596 (3–5) (2008) 353–385, http://dx.doi.org/10.1017/S0022112007009561.
[181] L.E. Jones, N.D. Sandham, R.D. Sandberg, Acoustic source identification for transitional airfoil flows using cross correlations, AIAA J. 48 (10) (2010) 2299–2312, http://dx.doi.org/10.2514/1.J050345.
[182] R.D. Sandberg, Compressible-flow DNS with application to airfoil noise, Flow Turb. Comb. 95 (2015) 211–229, http://dx.doi.org/10.1007/s10494-015-9617-1.
[183] T. Poinsot, S. Lele, Boundary conditions for direct simulations of compressible viscous flows, J. Comp. Phys. 101 (1) (1992) 104–129, http://dx.doi.org/10.1016/0021-9991(92)90046-2.
[184] C. Tam, Z. Dong, Radiation and outflow boundary conditions for direct computation of acoustic and flow disturbances in a nonuniform mean flow, J. Comp. Phys. 4 (2) (1996) 175–201, http://dx.doi.org/10.1142/S0218396X96000040.
[185] R.D. Sandberg, N.D. Sandham, Nonreflecting zonal characteristic boundary condition for direct numerical simulation of aerodynamic sound, AIAA J. 44 (2) (2006) 402–405, http://dx.doi.org/10.2514/1.19169.
[186] T. Padois, P. Laffay, A. Idier, S. Moreau, Tonal noise of a controlled-diffusion airfoil at low angle of attack and Reynolds number, J. Acoust. Soc. Am. 140 (1) (2016) EL:113–118, http://dx.doi.org/10.1121/1.4958916.
[187] J.M. Turner, J.W. Kim, Effect of spanwise domain size on direct numerical simulations of airfoil noise during flow separation and stall, Phys. Fluids 32 (2020) 065103:1–15, http://dx.doi.org/10.1063/5.0009664.
[188] J. Winkler, Investigation of trailing-edge blowing on airfoils for turbomachinery broadband noise reduction (Ph.D. thesis), Universität Siegen, 2011.
[189] R. Arina, R. Della Ratta Rinaldi, A. Iob, Numerical study of self-noise produced by an airfoil with trailing-edge serrations, in: 18th AIAA/CEAS Aeroacoustics Conference, Colorado Springs, CO, in: AIAA 2012-2184 paper, 2012, http://dx.doi.org/10.2514/6.2009-3197.
[190] L. Ji, W. Qiao, L. Wang, F. Tong, W. Chen, Experimental and numerical study on noise reduction mechanisms of an airfoil with serrated trailing edge, in: 20th AIAA/CEAS Aeroacoustics Conference, Atlanta, GA, in: AIAA 2014-3297 paper, 2014, http://dx.doi.org/10.2514/6.2009-3197.
[191] R.D. Sandberg, L.E. Jones, Direct numerical simulations of low Reynolds number flow over airfoils with trailing-edge serrations, J. Sound Vib. 330 (2011) 3818–3831, http://dx.doi.org/10.1016/j.jsv.2011.02.005.
[192] L.E. Jones, R.D. Sandberg, Acoustic and hydrodynamic analysis of the flow around an aerofoil with trailing-edge serrations, J. Fluid Mech. 706 (2012) 295–322, http://dx.doi.org/10.1017/jfm.2012.254.
[193] M. Sanjosé, C. Meon, V. Masson, S. Moreau, Direct numerical simulation of acoustic reduction using serrated trailing-edge on an isolated airfoil, in: 20th AIAA/CEAS Aeroacoustics Conference, in: AIAA 2014-2324 paper, Atlanta, GA, 2014, http://dx.doi.org/10.2514/6.2014-2324.
[194] F. Avallone, S. Pröbsting, D. Ragni, Three-dimensional flow field over a trailing-edge serration and implications on broadband noise, Phys. Fluids 28 (2016) 117101, http://dx.doi.org/10.1063/1.4966633.
[195] Y. Bae, Y.J. Moon, Effect of passive porous surface on the trailing-edge noise, Phys. Fluids 23 (12) (2011) 126101, http://dx.doi.org/10.1063/1.3662447.
[196] S. Ergun, Fluid flow through packed columns, Chem. Eng. Prog. 48 (2–3) (1952) 89–94.
[197] D.A. Nield, A. Bejan, Convection in Porous Media, Springer, New York, 1999.
[198] S.-R. Koh, M. Meinke, W. Schröder, Numerical analysis of the impact of permeability on trailing-edge noise, AIAA 2019-2655 paper, J. Sound Vib. Vol. 421 (2018) 348–376, http://dx.doi.org/10.1016/j.jsv.2018.02.017.
[199] V.B. Ananthan, P. Bernicke, R.A.D. Akkermans, T. Hu, P. Liu, Effect of porous material on trailing edge sound sources of a lifting airfoil by zonal overset-LES, J. Sound Vib. 480 (2020) 115386:1–19, http://dx.doi.org/10.1016/j.jsv.2020.115386.
[200] R. Zamponi, S. Satcunanathan, S. Moreau, D. Ragni, M. Meinke, W. Schröder, C. Schram, On the role of turbulence distortion on leading-edge noise reduction by means of porosity, J. Sound Vib. 485 (2020) 115561:1–22, http://dx.doi.org/10.1016/j.jsv.2020.115561.
[201] D.M. Freed, Lattice-Boltzmann method for macroscopic porous media modeling, Internat. J. Modern Phys. C 9 (8) (1998) 1491–1503, http://dx.doi.org/10.1142/S0129183198001357.
[202] C. Teruna, F. Manegar, F. Avallone, D. Ragni, D. Casalino, T. Carolus, Noise reduction mechanisms of an open-cell metal-foam trailing edge, J. Fluid Mech. 898 (2020) A18: 1–37, http://dx.doi.org/10.1017/jfm.2020.363.
[203] A. Rubio Carpio, R.M. Martinez, F. Avallone, D. Ragni, M. Snellen, S. van der Zwaag, Experimental characterization of the turbulent boundary layer over a porous trailing edge for noise abatement, J. Sound Vib. 443 (2019) 537–558, http://dx.doi.org/10.1016/j.jsv.2018.12.010.
[204] J.W. Jaworski, N. Peake, Aeroacoustics of silent owl flight, Ann. Rev. Fluid Mech. 723 (2020) 456–479, http://dx.doi.org/10.1146/annurev-fluid-010518-040436.
[205] M. Nardini, R.D. Sandberg, S.C. Schlanderer, Computational study of the effect of structural compliance on the noise radiated from an elastic trailing-edge, J. Sound Vib. 485 (2020) 115533:1–27, http://dx.doi.org/10.1016/j.jsv.2020.115533.
[206] A. Bodling, A. Sharma, Numerical investigation of low-noise airfoils inspired by the down coat of owls, Bioinspiration Biomim. 14 (2018) 016013, http://dx.doi.org/10.1088/1748-3190/aaf19c.

[207] A. Bodling, A. Sharma, Numerical investigation of noise reduction mechanisms in a bio-inspired airfoil, J. Sound. Vib. 453 (2020) 314–327, http://dx.doi.org/10.1016/j.jsv.2019.02.004.
[208] I.A. Clark, W.N. Alexander, W.J. Devenport, S.A.L. Glegg, J.W. Jaworski, C.A. Daly, N. Peake, Bioinspired trailing-edge noise control, AIAA J. 55 (2017) 740–754, http://dx.doi.org/10.2514/1.J055243.
[209] Y. Shi, S. Lee, Numerical study of 3-D finlets using RANS CFD for trailing edge noise reduction, Int. J. Aeroacoust. 19 (2020) 95–118, http://dx.doi.org/10.1177/1475472X20905053.
[210] Y. Shi, S. Lee, Airfoil trailing edge noise reduction using a boundary-layer bump, Acta. Acust. United. Ac. 105 (2019) 814–826, http://dx.doi.org/10.3813/AAA.919362.
[211] D.M. Chase, Sound radiated by turbulent flow off a rigid half-plane as obtained from a wavevector spectrum of hydrodynamic pressure, J. Acoust. Soc. Am. 52 (3B) (1972) 1011–1023, http://dx.doi.org/10.1121/1.1913170.
[212] K. Chandiramani, Diffraction of evanescent waves with applications to aerodynamically scattered sound and radiation from unbaffled plates, J. Acoust. Soc. Am. 55 (1) (1974) 19–29, http://dx.doi.org/10.1121/1.1919471.
[213] R.W. Paterson, P.G. Vogt, M.R. Fink, C.L. Munch, Vortex noise of isolated airfoils, J. Aircraft. 10 (1973) 296–302, http://dx.doi.org/10.2514/3.60229.
[214] J.C. Yu, M.C. Joshi, On sound radiation from the trailing edge of an isolated airfoil in a uniform flow, in: 5th AIAA Aeroacoustics Conference, in: AIAA 1979-603 paper, Seattle, WA, 1979, http://dx.doi.org/10.2514/6.1979-603.
[215] R.K. Amiet, Correction of open jet wind tunnel measurements for shear layer refraction, in: 2nd AIAA Aeroacoustics Conference AIAA 1975-0532. http://dx.doi.org/10.2514/6.1975-532.
[216] S. Moreau, D. Neal, J. Foss, Hot-wire measurements around a controlled diffusion airfoil in an open-jet anechoic wind tunnel, J. Fluid Eng. 128 (4) (2006) 699–706, http://dx.doi.org/10.1115/1.2201644.
[217] T. Padois, P. Laffay, A. Idier, S. Moreau, Detailed experimental investigation of the aeroacoustic field around a controlled-diffusion airfoil, in: 21st AIAA/CEAS Aeroacoustics Conference, in: AIAA 2015-2205 paper, Dallas, TX, 2015, http://dx.doi.org/10.2514/6.2015-2205.
[218] D.W. Shannon, S.C. Morris, Trailing edge noise measurements using a large aperture phased array, Int. J. Aeroacoust. 7 (2008) 147–176, http://dx.doi.org/10.1260/147547208784649446.
[219] W.K. Blake, J.L. Gershfeld, The aeroacoustics of trailing edges, Front. Exp. Fluid Mech. (1988) http://dx.doi.org/10.1007/978-3-642-83831-6_10.
[220] D.W. Shannon, S.C. Morris, T.J. Mueller, Trailing edge flow physics and acoustics, in: 11th AIAA/CEAS Aeroacoustics Conference, in: AIAA 2005-2957 paper, 2005, http://dx.doi.org/10.2514/6.2005-2957.
[221] S. Oerlemans, P. Sijtsma, Effects of wind tunnel side-plates on airframe noise measurements with phased arrays, NLR Technical Report NLR-TP-2000-169, 2000.
[222] T. Dassen, R. Parchen, J. Bruggeman, F. Hagg, Results of a wind tunnel study on the reduction of airfoil self-noise by the application of serrated blade trailing edges, NLR Technical Report NLR-TP-1996-350.
[223] S. Oerlemans, M. Fisher, T. Maeder, K. Kögler, Reduction of wind turbine noise using optimized airfoils and trailing-edge serrations, AIAA J. 47 (6) (2009) 1470–1481, http://dx.doi.org/10.2514/1.38888.
[224] J. Hurault, A. Gupta, E. Sloth, N.C. Nielsen, A. Borgoltz, P. Ravetta, Aeroacoustic wind tunnel experiment for serration design optimisation and its application to a wind turbine rotor, in: Proceedings of the 6th International Meeting on Wind Turbine Noise, Glasgow, UK, 2015.
[225] M. Gruber, P.F. Joseph, T.P. Chong, Experimental investigation of airfoil self noise and turbulent wake reduction by the use of trailing edge serrations, in: 16th AIAA/CEAS Aeroacoustics Conference, in: AIAA 2010-3803 paper, 2010, http://dx.doi.org/10.2514/6.2010-3803.
[226] D.J. Moreau, C.J. Doolan, Noise-reduction mechanism of a flat-plate serrated trailing edge, AIAA J. 51 (2013) 2513–2522, http://dx.doi.org/10.2514/1.J052436.
[227] M. Gruber, P.F. Joseph, T.P. Chong, On the mechanisms of serrated airfoil trailing edge noise reduction, in: 17th AIAA/CEAS Aeroacoustics Conference, in: AIAA 2011-2781 paper, 2011, http://dx.doi.org/10.2514/6.2011-2781.
[228] W.Y. Qiao, L. Ji, K.B. Xu, W.J. Cheng, F. Tong, An investigation on the near-field turbulence and radiated sound for an airfoil with trailing edge serrations, in: 19th AIAA/CEAS Aeroacoustics Conference, in: AIAA 2013-2112 paper, 2013, http://dx.doi.org/10.2514/6.2013-2112.
[229] S. Moreau, P. Laffay, A. Idier, N. Atalla, Several noise controls of the trailing-edge noise of a controlled-diffusion airfoil, in: 22nd AIAA/CEAS Aeroacoustics Conference, in: AIAA 2016-2816 paper, Lyon, France, 2016, http://dx.doi.org/10.2514/6.2016-2816.
[230] P.C. Woodhead, T.P. Chong, P.J. Joseph, J. Wissink, On the double-rooted trailing edge serration, in: 25th AIAA/CEAS Aeroacoustics Conference, in: AIAA 2019-2436 paper, Delft, Netherland, 2019, http://dx.doi.org/10.2514/6.2019-2436.
[231] B. Lyu, L. Ayton, P. Chaitanya, Leading- and trailing-edge noise reduction using serrations of new geometry, in: 23rd International Congress on Acoustics, 2019.
[232] T.P. Chong, T.M. Biedermann, O. Koster, S.M. Hasheminejad, On the effect of leading edge serrations on aerofoil noise production, in: 24th AIAA/CEAS Aeroacoustics Conference AIAA 2018-3289, 2018, http://dx.doi.org/10.2514/6.2018-3289.
[233] T.M. Biedermann, Aeroacoustic transfer of leading edge serrations from single aerofoils to low-pressure fan applications, (Ph.D. Thesis), TU Berlin, 2019, http://dx.doi.org/10.14279/depositonce-9075.
[234] C. Arce León, D. Ragni, S. Pröbsting, F. Scarano, F. Madsen, Flow topology and acoustic emissions of trailing edge serrations at incidence, Exp. Fluids 57 (5) (2016) 1–17, http://dx.doi.org/10.1007/s00348-016-2181-1.
[235] A. Vathylakis, T.P. Chong, P. Chaitanya, P.F. Joseph, Sensitivity of aerofoil self noise reductions to serration flap angles, in: 22nd AIAA/CEAS Aeroacoustics Conference, in: AIAA 2016-2837 paper, Lyon, France, 2016, http://dx.doi.org/10.2514/6.2016-2837.
[236] P.C. Woodhead, T.P. Chong, P.F. Joseph, A. Vathylakis, Aerofoil self-noise radiations subjected to serration flap angles, Exp. Fluids in press (2021) http://dx.doi.org/10.1007/s00348-021-03239-y.
[237] P.C. Woodhead, T.P. Chong, J.G. Wissink, Exploiting the misalignment of the serrated trailing edges for improved aerofoil broadband noise reduction, in: 23rd AIAA/CEAS Aeroacoustics Conference, in: AIAA 2017-4175 paper, Denver, CO, 2017, http://dx.doi.org/10.2514/6.2017-4175.
[238] T.P. Chong, A. Vathylakis, P.F. Joseph, M. Gruber, Self-noise produced by an airfoil with nonflat plate trailing-edge serrations, AIAA J. 51 (2013) 2665–2677, http://dx.doi.org/10.2514/1.J052344.
[239] T.P. Chong, P.F. Joseph, M. Gruber, Airfoil self noise reduction by non-flat plate type trailing edge serrations, Appl. Acoust. 74 (2013) 607–613, http://dx.doi.org/10.1016/j.apacoust.2012.11.003.
[240] J. Nedić, J.C. Vassilicos, Vortex shedding and aerodynamic performance of airfoil with multiscale trailing-edge modifications, AIAA J. 53 (2015) 3240–3250, http://dx.doi.org/10.2514/1.J053834.
[241] S.L. Prigent, O.R.H. Buxton, P.J.K. Bruce, Coherent structures shed by multiscale cut-in trailing edge serrations on lifting wings, Phys. Fluids 29 (2017) 075107, http://dx.doi.org/10.1063/1.4995467.
[242] S.M. Hasheminejad, T.P. Chong, P.F. Joseph, G. Lacagnina, Airfoil self-noise produced by fractal-serrated trailing edge, in: 24th AIAA/CEAS Aeroacoustics Conference AIAA 2018-3132, 2018, http://dx.doi.org/10.2514/6.2018-3132.
[243] A. Vathylakis, T.P. Chong, P.F. Joseph, Poro-serrated trailing-edge devices for airfoil self-noise reduction, AIAA J. 11 3379–3394, http://dx.doi.org/10.2514/1.J053983.
[244] S. Oerlemans, Reduction of wind turbine noise using blade trailing edge devices, in: Proc. of the 22nd AIAA/CEAS Aeroacoustics Conf., in: AIAA Paper 2016-3018, Lyon, France, 2016, http://dx.doi.org/10.2514/6.2016-3018.
[245] T.P. Chong, E. Dubois, Optimization of the poro-serrated trailing edges for broadband noise reduction, JASA 140 (2016) 1361–1373, http://dx.doi.org/10.1121/1.4961362.
[246] C. Jiang, J.R. Fischer, D.J. Moreau, C.J. Doolan, Experimental investigation of novel porous-serrated treatments on airfoil trailing edge noise reduction, in: 25th AIAA/CEAS Aeroacoustics Conference, AIAA 2019-2435 paper. http://dx.doi.org/10.2514/6.2019-2435.
[247] H. Liu, N. Chen, Y. Wang, Z. Hu, Modification of flow structure and sound source by hybrid porous-serrated trailing edge, J. Bionic Eng. 17 (2020) 539–552, http://dx.doi.org/10.1007/s42235-020-0043-2.
[248] M. Gruber, P.F. Joseph, M. Azarpeyvand, An experimental investigation of novel trailing edge geometries on airfoil trailing edge noise reduction, in: 19th AIAA/CEAS Aeroacoustics Conference, in: AIAA 2013-2011 paper, 2013, http://dx.doi.org/10.2514/6.2013-2011.
[249] C. Arce León, R. Merino-Martinez, S. Pröbsting, D. Ragni, F. Avallone, Acoustic emissions of semi-permeable trailing edge serrations, Acoust. Aust. 46 (2018) 111–117, http://dx.doi.org/10.1007/s40857-017-0093-8.
[250] M. Herr, W. Dobrzynski, Experimental investigations in low-noise trailing-edge design, AIAA J. 43 (2005) 1167–1175, http://dx.doi.org/10.2514/1.11101.
[251] A. Finez, M. Jacob, E. Jondeau, M. Roger, Broadband noise reduction with trailing edge brushes, in: 16th AIAA/CEAS Aeroacoustics Conference AIAA 2010-3980, 2010, http://dx.doi.org/10.2514/6.2010-3980.
[252] C. Das, A. Mimani, R. Yang Porteous, C.J. Doolan, An experimental investigation of flow-induced noise mechanism of a flexible flat-plate trailing-edge, in: Acoustics 2015 Hunter Valley Conference, 2015.
[253] E. Talboys, T.F. Geyer, C. Brucker, An aeroacoustic investigation into the effect of self-oscillating trailing edge flaplets, J. Fluid. Struct. 91 (2019) 102598, http://dx.doi.org/10.1016/j.jfluidstructs.2019.02.014.
[254] W.C. van der Velden, F. Avallone, D. Ragni, Numerical analysis of noise reduction mechanisms of serrated trailing edges under zero lift condition, in: 23rd AIAA/CEAS Aeroacoustics Conference, in: AIAA 2017-4173 paper, Denver, CO, 2017, http://dx.doi.org/10.2514/6.2017-4173.
[255] P.C. Woodhead, Aerofoil self noise reduction by innovative trailing edge treatment (Ph.D. Thesis), Brunel University London, 2020.
[256] T. Geyer, E. Sarradj, C. Fritzsche, Measurement of the noise generation at the trailing edge of porous airfoils, Exp. Fluids 48 (2010) 291–308, http://dx.doi.org/10.1007/s00348-009-0739-x.

[257] M. Herr, K.S. Rossignol, J. Delfs, M. Mossner, N. Lippitz, Specification of porous materials for low-noise trailing-edge applications, in: 20th AIAA/CEAS Aeroacoustics Conference, in: AIAA 2014-3041 paper, 2014, http://dx.doi.org/10.2514/6.2014-3041.

[258] T. Geyer, E. Sarradj, Trailing edge noise of partially porous airfoils, in: 20th AIAA/CEAS Aeroacoustics Conference AIAA 2014-3039, 2014, http://dx.doi.org/10.2514/6.2014-3039.

[259] M. Zhang, T.P. Chong, Effects of porous trailing edge on aerodynamic noise characteristics, Int. J. Aeroacoust. 19 (2020) 254–271, http://dx.doi.org/10.1177/1475472X20937941.

[260] M. Zhang, T.P. Chong, Experimental investigation of the impact of porous parameters on trailing-edge noise, J. Sound Vib. 489 (2020) 1–21, http://dx.doi.org/10.1016/j.jsv.2020.115694, 115694.

[261] C. Jiang, D.J. Moreau, Y. Yauwenas, J.R. Fischer, C.J. Doolan, J. Gao, W. Jiang, R. McKay, M. Kingan, Control of rotor trailing edge noise using porous additively manufactured blades, in: 24th AIAA/CEAS Aeroacoustics Conference, AIAA 2018-3792 paper. http://dx.doi.org/10.2514/6.2018-3792.

[262] G. Yakhina, B. Dignou, B. Jaiswal, P. Guilleminot-Simon, Y. Pasco, S. Moreau, Acoustic and aerodynamic investigation of passive trailing edge treatments for the controlled-diffusion airfoil, in: 25th AIAA/CEAS Aeroacoustics Conference, in: AIAA 2019-2451 paper, Delft, Netherland, 2019, http://dx.doi.org/10.2514/6.2019-2451.

[263] S. Moreau, B. Dignou, B. Jaiswal, G. Yakhina, Y. Pasco, M. Sanjosé, B. Alstrom, N. Atalla, Trailing-edge noise of a flat plate with several liner-type porous appendices, in: 24th AIAA/CEAS Aeroacoustics Conference, in: AIAA 2018-3119 paper, Atlanta, GA, 2018, http://dx.doi.org/10.2514/6.2018-3119.

[264] G. Yakhina, B. Dignou, B. Jaiswal, P. Guilleminot-Simon, Y. Pasco, S. Moreau, Liner-type porous treatments for the flat plate trailing edge, in: 25th AIAA/CEAS Aeroacoustics Conference, in: AIAA 2019-2452 paper, Delft, Netherland, 2019, http://dx.doi.org/10.2514/6.2019-2452.

[265] J. Jimenez, M. Uhlmann, A. Pinelli, G. Kawahara, Turbulent shear flows over active and passive porous walls, J. Fluid Mech. 442 (2001) 89–117, http://dx.doi.org/10.1017/S0022112001004888.

[266] M. Rosti, L. Brandt, A. Pinelli, Turbulent channel flow over an anisotropic porous wall - drag increase and reduction, J. Fluid Mech. 842 (2018) 381–394, http://dx.doi.org/10.1017/jfm.2018.152.

[267] I. Clark, C.A. Daly, W.J. Devenport, W.N. Alexander, N. Peake, J.W. Jaworski, S.A.L. Glegg, Bio-inspired canopies for the reduction of roughness noise, J. Sound Vib. 385 (2016) 33–54, http://dx.doi.org/10.1016/j.jsv.2016.08.027.

[268] A. Gonzalez, S.A.L. Glegg, N. Hari, M. Ottman, W.J. Devenport, Fundamental studies of the mechanisms of pressure shielding, in: 25th AIAA/CEAS Aeroacoustics Conference, in: AIAA 2019-2403 paper, 2019, http://dx.doi.org/10.2514/6.2019-2403.

[269] I. Jimenez, S. Glegg, W. Devenport, The effect of shear sheltering on trailing edge noise, in: AIAA/CEAS 26th Aeroacoustics Conference, AIAA Paper 2020-2515, Virtual Event, 2020, http://dx.doi.org/10.2514/6.2020-2515.

[270] D.L. Sutliff, D.L. Tweedt, E.B. Fite, E. Envia, Low-speed fan noise reduction with trailing edge blowing, Int. J. Aeroacoust. 1 (3) (2002) 275–305, http://dx.doi.org/10.1260/147547202320962592.

[271] C. Halasz, D. Arntz, R. Burdisso, W. Ng, Fan flow control for noise reduction part 1: advanced trailing edge blowing concepts, in: 11th AIAA/CEAS Aeroacoustics Conference, in: AIAA 2005-3025 paper, 2005, http://dx.doi.org/10.2514/6.2005-3025.

[272] A. Borgoltz, W.J. Devenport, L. Craig, Space-time correlations and trailing edge flow structure in fan-blade wakes with trailing edge blowing, in: AIAA/CEAS 12th Aeroacoustics Conference, in: AIAA 2006-2480 paper, Cambridge, MA, 2006, http://dx.doi.org/10.2514/6.2006-2480.

[273] T. Gerhard, S. Erbsloh, T. Carolus, Reduction of airfoil trailing edge noise by trailing edge blowing, J. Phys.: Conf. Ser. 524 (2014) 012123, http://dx.doi.org/10.1088/1742-6596/524/1/012123.

[274] M. Szoke, D. Fiscaletti, M. Azarpeyvand, Effect of inclined transverse jets on trailing-edge noise generation, Phys. Fluids 30 (2018) 085110, http://dx.doi.org/10.1063/1.5044380.

[275] A. Wolf, T. Lutz, W. Würz, E. Krämer, O. Stalnov, A. Seifert, Trailing edge noise reduction of wind turbine blades by active flow control, Wind Energy 18 (2015) 909–923, http://dx.doi.org/10.1002/we.1737.

[276] B. Arnold, T. Lutz, E. Krämer, C. Rautmann, Wind-turbine trailing-edge noise reduction by means of boundary-layer suction, AIAA J. 56 (2018) 1843–1854, http://dx.doi.org/10.2514/1.J056633.

[277] B. Arnold, T. Lutz, E. Krämer, Design of a boundary-layer suction system for turbulent trailing-edge noise reduction of wind turbines, Renew. Energ. 123 (2018) 249–262, http://dx.doi.org/10.1016/j.renene.2018.02.050.

[278] N. Rathay, M. Boucher, M. Amitay, E. Whalen, Performance enhancement of a vertical stabilizer using synthetic jet actuators: non-zero sideslip, in: 6th AIAA/CEAS Aeroacoustics Conference, in: AIAA 2012-2657 paper, 2012, http://dx.doi.org/10.2514/6.2012-2657.

[279] M. Cannata, G. Cafiero, G. Iuso, Large-scale forcing of a turbulent channel flow through spanwise synthetic jets, AIAA J. 58 (2020) 2042–2052, http://dx.doi.org/10.2514/1.J059047.

[280] Y. Du, G.E. Karniadakis, Suppressing of wall turbulence by means of a transverse traveling wave, Science 288 (2000) 1230–1234, http://dx.doi.org/10.1126/science.288.5469.1230.

[281] S. Wagner, R. Bareiß, G. Guidati, Wind Turbine Noise, Springer-Verlag, Berlin, 1996, http://dx.doi.org/10.1007/978-3-642-88710-9.

[282] S. Oerlemans, P. Sijtsma, B.M. López, Location and quantification of noise on a wind turbine, J. Sound Vib. 299 (5-6) (2007) 869–883, http://dx.doi.org/10.1016/j.jsv.2006.07.032.

[283] A. Garcia-Sagrado, T. Hynes, H. Hodson, Experimental investigation into trailing edge noise sources, in: 12th AIAA/CEAS Aeroacoustics Conference (27th AIAA Aeroacoustics Conference), 2006, http://dx.doi.org/10.2514/6.2006-2476.

[284] S. Oerlemans, Wind turbine noise: primary noise sources, in: R. Bowdler, G. Leventhall (Eds.), Wind Turbine Noise, Multi-Science Publishing Co Ltd, 2011.

[285] I. Romero-Sanz, A. Matesanz, Noise management on modern wind turbines, Wind Eng. 32 (1) (2008) 27–44, http://dx.doi.org/10.1260/030952408784305886.

[286] K. Kinzie, R. Drobietz, B. Petitjean, S. Honhoff, Concepts for wind turbine sound mitigation, in: AWEA Windpower Conference and Exhibition 2013 (Proceedings), 2013.

[287] A.S.H. Lau, J.W. Kim, J. Hurault, T. Vronsky, A study on the prediction of aerofoil trailing-edge noise for wind-turbine applications, Wind Energy 20 (2) (2017) 233–252, http://dx.doi.org/10.1002/we.2003.

[288] M.F. Barone, Survey of techniques for reduction of wind turbine blade trailing edge noise, Technical Report SAND2011-5252, Sandia National Laboratories (US), 2011, http://dx.doi.org/10.2172/1029824.

[289] B. Faßmann, C. Rautmann, R. Ewert, J. Delfs, Efficient prediction of broadband trailing edge noise and application to porous edge treatment, 2018, http://arxiv.org/abs/1810.02642.

[290] J. Yu, S.R. Koh, M.H. Meinke, W. Schröder, Noise reduction via jet injection near the trailing edge, in: 22nd AIAA/CEAS Aeroacoustics Conference, in: AIAA 2016-2831 paper, Lyon, France, 2016, http://dx.doi.org/10.2514/6.2016-2831.

[291] B. Arnold, T. Lutz, E. Krämer, C. Rautmann, Design of a boundary-layer suction system for trailing-edge noise reduction of an industrial wind turbine, in: 35th Wind Energy Symposium (AIAA SciTech Forum), 2017, http://dx.doi.org/10.2514/6.2017-1380.

[292] L.M. Cesar, H.K. Jawahar, M. Azarpeyvand, Airfoil trailing-edge noise reduction using flow suction, in: 2018 AIAA/CEAS Aeroacoustics Conference, in: AIAA 2018-2814 paper, 2018, http://dx.doi.org/10.2514/6.2018-2814.

[293] S. Oerlemans, M.G. Smith, P. White, S. von Hübernein, A. King, B. Piper, M. Cand, A. Bullmore, B. Wilson, H.A. Madsen, A. Fischer, K.A. Kragh, Wind turbine amplitude modulation: Research to improve understanding as to its cause and effect, Tech. rep., RenewableUK, UK, 2013, Accessed: 2020-06-28.

[294] R.A. Perkins, M.J. Lotinga, A method to control amplitude modulation in wind turbine noise within the UK planning regime, in: 24th International Congress on Sound and Vibration (ICSV 24), 2017, pp. 1512–1519.

[295] A. Fischer, H.A. Madsen, K. Abildgaard, F. Bertagnolio, Analyses of the mechanisms of amplitude modulation of aero-acoustic wind turbine sound, in: EWEA 2014, Proceedings of the European Wind Energy Association Conference and Exhibition, 2014, Barcelona, Spain.

[296] F. Bertagnolio, H.A. Madsen, A. Fischer, C. Bak, Cyclic pitch for the control of wind turbine noise amplitude modulation, in: Internoise 2014, in: Proceedings of the 43rd International Congress on Noise Control Engineering, The Australian Acoustical Society, Melbourne, Australia, 2014.

[297] N. Peake, A. Parry, Modern challenges facing turbomachinery aeroacoustics, Ann. Rev. Fluid Mech. 44 (2012) 227–248, http://dx.doi.org/10.1146/annurev-fluid-120710-101231.

[298] S. Moreau, M. Roger, Advanced noise modeling for future propulsion systems, Int. J. Aeroacoust. 17 (6–8) (2018) 576–599, http://dx.doi.org/10.1260/1475-472X.10.1.i.

[299] S. Moreau, Turbomachinery noise predictions: present and future, Acoustics 1 (2019) 92–116, http://dx.doi.org/10.3813/AAA.918372.

[300] S. Moreau, A review of turbomachinery noise: from analytical models to high-fidelity simulations, in: R. Radespiel, R. Semaan (Eds.), Proceedings of the SF880 Symposium, in: Fundamentals of High Lift for Future Civil Aircraft, Springer Nature Switzerland AG, 2020, http://dx.doi.org/10.3813/AAA.918372.

[301] S. Moreau, J. Foss, S. Morris, A numerical and experimental test-bed for low-speed fans, Proc. Inst. Mech. Eng., Part A: J. Power Energy 230 (5) (2016) 456–466, http://dx.doi.org/10.1177/0957650915623669.

[302] J.E. Ffowcs Williams, D.L. Hawkings, Theory relating to the noise of rotating machinery, J. Sound Vib. 10 (1) (1969) 10–21, http://dx.doi.org/10.1016/0022-460X(69)90125-4.

[303] S. Sinayoko, M. Kingan, A. Agarwal, Trailing edge noise theory for rotating blades in uniform flow, Proc. R. Soc. Lond. A 469 (2125) (2013) 1–21, http://dx.doi.org/10.1098/rspa.2013.0065.

[304] M. Roger, S. Moreau, A. Guedel, Broadband fan noise prediction using single-airfoil theory, Noise Control Eng. J. 54 (1) (2006) 5–14.

[305] S. Moreau, M. Roger, Competing broadband noise mechanisms in low-speed axial fans, AIAA J. 45 (1) (2007) http://dx.doi.org/10.2514/1.14583.

[306] B. Coutty, S. Moreau, Aeroacoustic modeling of an automotive engine cooling module, in: AIAA Paper, 26th International Congress on Noise and Vibration, Montreal, Canada, paper 525, Montreal, Canada, 2019.

[307] B. Cotte, Coupling of an aeroacoustic model and a parabolic equation code for long range wind turbine noise propagation, J. Sound Vib. 422 (2018) 343–357, http://dx.doi.org/10.1016/j.jsv.2018.02.026.
[308] D. Casalino, S. Moreau, M. Roger, One, no one and one hundred thousand methods for low-speed fan noise prediction, Int. J. Aeroacoust. 9 (3) (2010) 307–327, http://dx.doi.org/10.1260/1475-472X.9.3.307.
[309] Y. Yamade, C. Kato, H. Shimizu, T. Nishioka, Large eddy simulation and acoustical analysis for prediction of aeroacosutics noise radiated from an axial-flow fan, in: 2006 ASME Joint U.S.-European Fluids Engineering Summer Meeting, in: FEDSM2006-98303 paper, Miami, FL, 2006.
[310] F. Pérot, M.-S. Kim, S. Moreau, M. Henner, D. Neal, Direct aeroacoustics prediction of a low-speed axial fan, in: 16th AIAA/CEAS Aeroacoustics Conference, in: AIAA 2010-3887 paper, Stockholm, Sweden, 2010, http://dx.doi.org/10.2514/6.2010--3887.
[311] S. Moreau, M. Sanjosé, Sub-harmonic broadband humps and tip noise in low-speed ring fans, J. Acoust. Soc. Am. 139 (1) (2016) 118–127, http://dx.doi.org/10.1121/1.4939493.
[312] T. Zhu, D. Lallier-Daniels, M. Sanjosé, S. Moreau, T. Carolus, Rotating coherent flow structures as a source for narrow band tip clearance noise from axial fans, J. Sound Vib. 418 (2018) 198–215, http://dx.doi.org/10.1016/j.jsv.2017.11.014.
[313] A. Pogorelov, M. Meinke, W. Schröder, Cut-cell method based large-eddy simulation of tip-leakage flow, Phys. Fluids 27 (4) (2015) 075106: 1–20, http://dx.doi.org/10.1063/1.4926515.
[314] S.M.A. Moghadam, M. Meinke, W. Shröder, Numerical analysis of the acoustic field of a ducted axial fan at varying tip clearances, Acta Acust. United Acust. 105 (1) (2019) 43–55, http://dx.doi.org/10.3813/AAA.918372.
[315] S. Moreau, Direct noise computation of low-speed ring fans, Acta Acust. United Acust. 105 (1) (2019) 1–13, http://dx.doi.org/10.3813/AAA.918372.
[316] D. Lallier-Daniels, M. Sanjosé, S. Moreau, M. Piellard, Aeroacoustic study of a ring-shrouded axial fan using Lattice-Boltzmann simulations, Eur. J. Mech. B/Fluids 61 (2017) 244–254, http://dx.doi.org/10.1016/j.euromechflu.2016.10.008.
[317] S. Moreau, M. Sanjosé, S. Magne, Optimization of tonal noise control with flow obstruction, J. Sound Vib. 437 (2018) 264–275, http://dx.doi.org/10.1016/j.jsv.2008.11.051.
[318] M. Sanjosé, S. Moreau, Direct noise prediction and control of an installed large low-speed radial fan, Eur. J. Mech. B/Fluids 61 (2017) 235–243, http://dx.doi.org/10.1016/j.euromechflu.2016.10.004.
[319] S.A.L. Glegg, C. Jochault, Broadband self-noise from a ducted fan, AIAA J. 36 (8) (1998) 1387–1395, http://dx.doi.org/10.2514/2.559.
[320] M. Sanjosé, P. Kholodov, C.P. Arroyo, S. Moreau, CFD modeling of a realistic turbofan for noise prediction. Part 2: Analytical acoustic predictions, in: Proceedings of Global Power and Propulsion Society, GPPS-BJ-2019-224 paper, Beijing, China, 2019.
[321] C. Pérez Arroyo, T. Leonard, M. Sanjose, S. Moreau, F. Duchaine, Large eddy simulation of a scale-model turbofan for fan noise source diagnostic, J. Sound Vib. 445 (2019) 64–76, http://dx.doi.org/10.1016/j.jsv.2019.01.005.
[322] P. Gliebe, R. Mani, H. Shin, B. Mitchell, G. Ashford, S. Salamah, S. Connell, Aeroacoustic prediction codes, Tech. Rep. CR-2000-210244, NASA, Glenn Research Center, 2000.
[323] P. Kholodov, S. Moreau, Tip flow evolution in a turbofan rotor for broadband noise diagnostic, in: 26th AIAA/CEAS Aeroacoustics Conference, in: AIAA2020-2521 paper, Virtual Event, 2020, http://dx.doi.org/10.2514/6.2020-2521.
[324] P. Kholodov, S. Moreau, Identification of noise sources in a realistic turbofan rotor using Large Eddy Simulation, Acoustics 2 (2020) 691–706, http://dx.doi.org/10.3390/acoustics2030037.
[325] Y. Kim, A. George, Trailing-edge noise from hovering rotors, AIAA J. 20 (1982) 1167–1174, http://dx.doi.org/10.2514/3.51176.
[326] V. Blandeau, P.J. Joseph, Validity of Amiet's model for propeller trailing-edge noise, AIAA J. 49 (2011) 1057–1066, http://dx.doi.org/10.2514/1.J050765.
[327] S. Li, S. Lee, Prediction of rotorcraft broadband trailing-edge noise and parameter sensitivity, J. Am. Helicopter Soc. 65 (2020) 042006, http://dx.doi.org/10.4050/JAHS.65.042006.
[328] S. Li, S. Lee, A machine learning-based fast prediction of rotorcraft broadband noise, in: AIAA/CEAS 26th Aeroacoustics Conference, AIAA Paper 2020-Xxxx, Virtual Event, 2020, http://dx.doi.org/10.2514/6.2020-2588.
[329] S. Li, S. Lee, Acoustics Analysis of a Quiet Helicopter for Air Taxi Operations, in: Proceeding of the 77th VFS Annual Forum, Virtual Event, 2021.
[330] D. Peters, D. Boyd, C. He, Finite-state induced-flow model for rotors in hover and forward flight, J. Am. Helicopter Soc. 34 (1989) 5–17, http://dx.doi.org/10.4050/JAHS.34.5.
[331] C. Johnson, J. Sirohi, G. Jacobellis, R. Singh, Experimental and Computational Investigation of Stacked Rotor Broadband Noise in Hover, in: Proceeding of the 77th VFS Annual Forum, Virtual Event, 2021.
[332] C. He, J. Kim, C. Ware, S. Yang, J. Baeder, Y.S. Jung, eVTOL Rotor Noise Study Using Combined Comprehensive Modeling with Acoustic Analysis, in: Proceeding of the 77th VFS Annual Forum, Virtual Event, 2021.
[333] Y.S. Jung, J. Baeder, C. He, Investigation of Empirical Rotor Broadband Prediction using CFD Boundary Layer Parameters Extraction, in: Proceeding of the 77th VFS Annual Forum, Virtual Event, 2021.
[334] Z.F. Gan, K.S. Brentner, E. Greenwood, Time variation of rotor broadband noise, in: Proceeding of 9th Biennial Autonomous VTOL Technical Meeting and 8th Annual Electric VTOL Symposium, Virtual Event, 2021.
[335] H. Johnson, W. Katz, Investigation of the vortex noise produced by a helicopter rotor, Tech. rep. USAAMRDL RP 72-2, 1972.
[336] N. Zawodny, D. Boyd, C. Burley, Acoustic characterization and prediction of representative, small-Scale rotary-wing unmanned aircraft system components, in: Proceeding of the 72th AHS Annual Forum, West Palm Beach, FL, 2016.
[337] T.F. Brooks, M. Marcolini, D.S. Pope, Main rotor broadband noise study in the DNW, J. Am. Helicopter Soc. 34 (1989) 3–12, http://dx.doi.org/10.4050/JAHS.34.2.3.
[338] R. Snider, T. Samuels, B. Goldman, K. Brentner, Full-scale rotorcraft broadband noise prediction and its relevance to civil noise certification criteria, in: Proceeding of the 69th AHS Annual Forum, Phoenix, AZ, 2013.
[339] N. Pettingill, N. Zawodny, Acoustic characterization and prediction of representative, small-scale rotary-wing unmanned aircraft system components, in: Proceeding of the 75th VFS Annual Forum, Philadelphia, PA, 2019.
[340] N. Intaratep, W.N. Alexander, W.J. Devenport, S.M. Grace, A. Dropkin, Experimental study of quadcopter acoustics and performance at static thrust conditions, in: 22nd AIAA/CEAS Aeroacoustics Conference, AIAA Paper 2016-2873, Lyon, France, 2016, http://dx.doi.org/10.2514/6.2016-2873.
[341] N. Zawondy, D.D. Boyd, Investigation of rotor-airframe interaction noise associated with small-scale rotary-wing unmanned aircraft systems, J. Am. Helicopter Soc. 65 (2020) 012007, http://dx.doi.org/10.4050/JAHS.65.012007.
[342] S. Li, S. Lee, UCD-QuietFly: a new program to predict multi-rotor eVTOL broadband noise, in: Proceeding of the 2020 VFS Aeromechanics for Advanced Vertical Flight Technical Meeting, San Jose, CA, 2020.
[343] D. Begault, Overview of metrics pertinent to human response to UAM noise, in: Acoustics and Urban Air Mobility Technical Working Group Meeting, Cleveland, OH, 2018.
[344] A. Halimi, B.G. Marinus, S. Larbi, Analytical prediction of broadband noise from mini-RPA propellers with serrated edges, Int. J. Aeroacoust. 18 (2019) 517–535, http://dx.doi.org/10.1177/1475472X19859889.
[345] Y. Yang, Y. Liu, H. Hu, X. Liu, Y. Wang, E.J.G. Arcondoulis, Z. Li, Experimental study on noise reduction of a wavy multi-copter rotor, Appl. Acoust. 165 (2020) 107311, http://dx.doi.org/10.1016/j.apacoust.2020.107311.
[346] I. Couchman, D. Castaignet, N.K. Poulsen, T. Buhl, J.J. Wedel-Heinen, N.A. Olesen, Active load reduction by means of trailing edge flaps on a wind turbine blade, in: 2014 American Control Conference, IEEE, 2014, pp. 3722–3727, http://dx.doi.org/10.1109/ACC.2014.6859046.
[347] H.A. Madsen, A. Barlas, T.L. Andersen, A morphing trailing edge flap system for wind turbine blades, in: A.L. Araújo, C.A. Mota Soares (Eds.), Proceedings of the 7th ECCOMAS Thematic Conference on Smart Structures and Materials (SMART 2015), IDMEC, 2015.
[348] E. Jost, M.F. Beckers, T. Lutz, E. Krämer, CFD study of trailing edge flaps for load control on wind turbines, in: A. Dillmann, G. Heller, E. Krämer, C. Wagner, S. Bansmer, R. Radespiel, R. Semaan (Eds.), New Results in Numerical and Experimental Fluid Mechanics XI, Springer International Publishing, Cham, 2018, pp. 741–751.
[349] C. Pérez Arroyo, T. Leonard, M. Sanjosé, S. Moreau, F. Duchaine, Large eddy simulation of a rotor stage for fan noise source diagnostic, in: Global Power and Propulsion Forum, Montreal, Canada, 2018.